Air quality modeling : evaluation of chemical and meteorological parameterizations

Youngseob Kim

Thèse de doctorat de l'Université Paris-Est

Présentée et soutenue publiquement le 15 décembre 2011 par

Youngseob KIM

pour l'obtention du diplôme de docteur
de l'Université Paris-Est

Spécialité : Sciences et techniques de l'environnement

Modélisation de la qualité de l'air: Évaluation des paramétrisations chimiques et météorologiques

---

Jury composé de

Pr Bernard Aumont	Université Paris-Est	président
Dr Olivier Boucher	CNRS, Université Pierre et Marie Curie	examinateur
Pr émérite Robert Rosset	Université Paul Sabatier	examinateur
Dr Yves Balkanski	IPSL/LSCE	rapporteur
Dr Sylvain Dupont	INRA	rapporteur
Mme Deborah Luecken	US EPA	examinatrice
Dr Karine Sartelet	CEREA	co-directrice de thèse
Pr Christian Seigneur	École des Ponts ParisTech, CEREA	directeur de thèse

Le commencement de la sagesse, c'est la crainte de l'Éternel ;
Et la science des saints, c'est l'intelligence.
Proverbes 9 :10

Remerciements

Je me dois de remercier en premier lieu Karine Sartelet, qui a sincèrement suivi mes études au CEREA. Ses multiples qualités scientifiques ont été essentielles pour faire aboutir cette thèse. Sans son évaluation positive de ma candidature au sujet de thèse, je n'aurais pu commencer la thèse. Aussi les discussions incomptables, la patience, l'encouragement sont inoubliables.

Le remerciement est vraiment dû à Christian Seigneur, qui est le directeur de thèse. Sa direction a été toujours claire. Il ne laisse jamais seul son élève qui a des difficultés dans sa recherche pour des affaires administratives. Il pousse son élève à avancer ses recherches avec pertinence et cela permet d'arriver jusqu'au perfectionnement d'une œuvre.

Je remercie les rapporteurs, Sylvain Dupont et Yves Balkanski, de même que les autres membres du jury, d'avoir accepté d'évaluer mon travail. Ils ont bien évalué la qualité de la thèse. Surtout, depuis le début de mon travail, Deborah Luecken m'a permis de communiquer sur les questions concernant le mécanisme chimique CB05.

Je remercie Jean-Christophe Raut pour les données de mesure lidar qui sont essentielles pour la deuxième partie de thèse. Ses coopérations favorables sont tellement utiles et finalement il devient un co-auteur pour les articles.

Les expériences durant ces quelques années au CEREA sont très impressionnantes sur le plan scientifique, mais aussi sur le plan humain à travers les multiples échanges et rencontres. Je citerai en particulier mes différents collègues de bureau, passés et présents, Hossein Malakooti, Damien Garaud et Jérôme Drevet qui ont partagé la vie au CEREA. Des soutiens inoubliables ont été offerts par Pierre Tran, Victor Winiarek et Yelva Roustan. La vie au CEREA a été riche grâce aux rencontres avec Elsa Real, Maya Milliez, Denis Wendum (pour la carte extraordinaire à la naissance de mon fils), Vivien Mallet, Nora Duhanyan, Laëtitia Girault, Lin Wu (pour l'histoire chinoise intéressante), Yiguo Wang, Nicolas Cherin, Eve Lecoeur, Antoine Waked, Florian Couvidat (pour devenir un co-auteur d'un article), Régis Briant, Marion Devilliers, Hilel Dergaoui, Yongfeng Qu, Janusz Zysk, Rachid Abida, Mohammad Taghavi, etc.

Je remercie tous les membres de l'Église Sonnan de Paris, et particulièrement le pasteur Weonyong Seong et Woojung Kim. Ils ont toujours prié pour mon travail et ma famille.

Enfin, Je peux terminer en adressant mes chaleureux remerciements aux membres de ma famille, et en particulier à ma femme Soojung Kim qui m'a encouragé et supporté dans le champs de bataille avec mes deux trésors, Minjou et Minu. Mes parents, Kiwun Kim et Yunja Lee, ont pris un vol pour venir me soutenir pendant la soutenance de thèse du pays lointain.

Table des matières

Chapitre 1

Introduction

Sommaire

1.1 Modélisation de la qualité de l'air

Au début du XXe siècle, la combinaison de la fumée (*smoke*) et du brouillard (*fog*) a été observée et appelée *smog*. Ce *smog* était dû à la combustion du charbon et aux émissions des usines chimiques. Le grand *smog* de Londres du 5 au 9 décembre 1952 pourrait avoir causé jusqu'à 12 000 morts. La pollution due au charbon et aux usines contient du dioxyde de soufre (SO_2) et en présence de brouillard est communément appelée le *smog* de Londres.

L'utilisation généralisée de l'automobile et l'augmentation de l'activité industrielle ont augmenté la prévalence d'un autre type de pollution de l'air, le *smog* photochimique. Cette pollution était formée presque quotidiennement à Los Angeles, en Californie aux États-Unis. Elle est devenue si grave qu'un organisme, "*Air Pollution Control District*", a été formé à Los Angeles en 1947 pour lutter contre ce fléau. La composition du *smog* photochimique a été élucidée en 1951, quand Arie Haagen-Smit, professeur de biologie (chimie bio-organique) au California Institute of Technology (Caltech), a produit de l'ozone dans un laboratoire à partir d'oxydes d'azote et de gaz organiques réactifs, en présence de lumière et a suggéré que les gaz produits

étaient les principaux constituants de la pollution atmosphérique à Los Angeles. Le *smog* photochimique a été observé dans la plupart des villes du monde. Suite aux travaux de laboratoire menés dans les années 1950 pour mieux comprendre la formation du *smog* photochimique, des modèles "boîte" pour simuler des réactions chimiques dans l'atmosphère ont été mis en œuvre. Dans les années 1960 et 1970, les modèles de pollution atmosphérique, appelés modèles de qualité de l'air, ont été élargis à deux et trois dimensions [Jacobson, 2005].

Les modèles de qualité de l'air sont des implémentations numériques de modèles mathématiques de la physico-chimie de l'atmosphère qui décrivent l'évolution des polluants atmosphériques. L'évolution de la concentration de polluants est donnée par une équation de type advection-diffusion-réaction, i.e., l'équation de dispersion réactive. L'advection correspond au transport par le champ de vent, la diffusion au mélange turbulent et la réaction aux processus physico-chimiques des transformations des polluants. Les modèles numériques tridimensionnels qui résolvent cette équation sont généralement appelés modèles de chimie-transport (CTM, "Chemical-transport models").

Les CTM sont utilisés de manière opérationnelle pour la prévision de qualité de l'air (e.g., PREV'AIR, ESMERALDA, AIRPARIF, AIRNOW, etc[1]). Ils permettent également de tester l'impact de mesures affectant la qualité de l'air. Ils sont largement utilisés par les organismes (EEA, AASQA, US EPA, NOAA, NCAR, etc[2]) chargés de lutter contre la pollution à la fois pour identifier la contribution de différentes sources aux problèmes de qualité de l'air et pour contribuer à la conception de stratégies efficaces pour réduire les concentrations de polluants atmosphériques nocifs. Les CTM peuvent également être utilisés pour prédire les concentrations futures de polluants après la mise en œuvre d'un nouveau programme de réglementations, afin d'estimer l'efficacité du programme pour réduire les concentrations (étude de prospective).

1.1.1 Prévision de la qualité de l'air

L'année 2003 a été marquée par un épisode de canicule au cours de l'été doublé d'une pollution à l'ozone exceptionnelle, qui a touché l'ensemble de l'Europe. De forts niveaux de pollution ont été observés au sud du Royaume-Uni, sur la majeure partie de l'Allemagne, au nord de la Suisse et en Italie du Nord. Toute la France était concernée par la vague d'ozone. La pollution était forte en Île de France, en région Centre et dans la région Provence Alpes Côte d'Azur (PACA). Les épisodes de pollution peuvent être liés à d'autres facteurs que la canicule. Ils peuvent être dus par exemple à une configuration météorologique qui conduit à l'accumulation de polluants dans la couche limite et proche de zone peuplée, à une soudaine augmentation des rejets de polluants dans l'atmosphère, ou à du transport longue-distance de polluants. Les épisodes de forte pollution peuvent remettre en cause les pratiques quotidiennes de gestion de la ville (par la mise en place d'une circulation alternée ou par la réduction des émissions industrielles) et exposent brusquement ces habitants à des dangers sanitaires. Lors d'un pic de pollution, différents symptômes peuvent survenir notamment chez les personnes sensibles (les enfants, les personnes âgées, les asthmatiques, les insuffisants respiratoires, les personnes atteintes de problème cardiaque). Selon les concentrations, des seuils d'alertes et de recom-

[1] PREV'AIR (`www.prevair.org`), ESMERALDA (`www.esmeralda-web.fr`), AIRPARIF (`www.airparif.asso.fr`) et AIRNOW (`airnow.gov`)

[2] EEA (European Environment Agency), AASQA (Association Agréée de Surveillance de la Qualité de l'Air), US EPA (United States Environmental Protection Agency), NOAA (National Oceanic and Atmospheric Administration) et NCAR (The National Center for Atmospheric Research)

mandation et d'information sont définis. Par exemple, pour les particules, le seuil d'alerte à la population est de 125 μg m^{-3} sur 24 heures glissantes. Il enclenche des mesures d'urgence prises par le préfet. Le seuil de recommandation et d'information est de 80 μg m^{-3}. Quand ce seuil est dépassé, les pouvoirs publiques mettent en garde les personnes sensibles et recommandent des mesures destinées à la limitation des émissions. Les AASQA ont pour mission d'informer la population en cas d'épisode de forte pollution afin de permettre aux habitants et à la ville de s'adapter à cette situation (`http://www.developpement-durable.gouv.fr/IMG/ecologie/pdf/Note-bilan-ete2003-ozone.pdf`).

Ces missions de surveillance et d'information du public des AASQA s'appuient sur des prévisions de qualité de l'air. Les concentrations de polluants sont prévues quotidiennement sur quelques jours. Une prévision est généralement initialisée par la prévision du jour précédent. Par exemple, les plates-formes de prévision nationale PREV'AIR (`www.prevair.org`) et inter-régionale ESMERALDA (`www.esmeralda-web.fr`) proposent quotidiennement des simulations sur quatre jours (depuis la veille jusqu'au surlendemain) sur l'Europe et la France. Les prévisions sont fournies pour l'ozone (O_3), le dioxyde d'azote (NO_2) et les matières particulaires (PM), trois polluants réglementés en raison de leurs impacts sanitaire et environnemental. Les informations liées aux particules sont séparées en deux classes, les PM_{10} (particules de diamètre aérodynamique inférieur à 10 μm), et les $PM_{2.5}$ (particules de diamètre aérodynamique inférieur à 2,5 μm).

Des prévisions de la qualité de l'air sont également utilisées par certains industriels pour diminuer leur production en cas de prévision de dépassement de seuil (e.g., Poulet *et al.*, 2008, pour SO_2).

Pour des risques accidentels (e.g., l'accident nucléaire de Fukushima-Daiichi), des prévisions de la dispersion atmosphérique de radionucléides (césium-137, iode-131/132) sont réalisées par des organismes français tel que l'IRSN[3]) afin d'estimer au mieux l'impact potentiel sur les populations.

1.1.2 Études d'impact et de prospective

Les études d'impact permettent d'estimer l'impact sur les concentrations de mesures affectant la qualité de l'air. Par exemple, les émissions de polluants dans une ville peuvent être modifiées par la construction d'un nouvel axe routier, le développement d'une nouvelle industrie ou d'une nouvelle technologie. Une étude d'impact permet de quantifier la réponse sur les concentrations de cette variation des émissions.

En Chine, un contrôle systématique de la pollution atmosphérique a été effectué pendant les Jeux Olympiques de Pékin en 2008 et des mesures ont été conçues et mises en œuvre pour améliorer la qualité de l'air. Ces mesures concernaient des restriction de circulation des véhicules. Les jours pairs, seules les voitures dont la plaque d'immatriculation se termine par un chiffre pair étaient autorisées à rouler et l'inverse les jours impairs. Une étude d'impact de ces mesures sur la qualité de l'air à Pékin a été présentée par Cai et Xie [2010].

La définition de l'étude de prospective pour la modélisation de la qualité de l'air est proche de celle de l'étude d'impact. Tandis que l'étude d'impact cible une source spécifique, l'étude de prospective peut évaluer différentes mesures de réduction des émissions pour atteindre un seuil réglementaire de concentrations.

[3]IRSN (Institut de Radioprotection et de Sûreté Nucléaire)

Par exemple, l'Agence de l'Environnement et de la Maîtrise de l'Energie (ADEME) a lancé une évaluation prospective dont l'objectif est d'identifier les solutions et les coûts induits pour développer le chauffage à bois domestique et les chaufferies à biomasse tout en préservant la qualité de l'air (`http://www.ademe.fr/htdocs/publications/dossier/av32/p3.htm`).

L'impact des émissions de véhicules sur la qualité de l'air parisien a été examiné par Roustan *et al.* [2010a]. Différents scénarios pour les émissions de PM, composés organiques volatils (COV) et oxyde d'azote (NO_x) pour les années de 2000 au 2020 ont été utilisés pour modéliser les concentrations de polluants photochimiques (O_3, NO_2 et PM).

L'impact du changement climatique futur sur les polluants (O_3 et $PM_{2.5}$) dans l'hémisphère nord [e.g., Hedegaard, 2007], aux États-Unis [e.g., Lam *et al.*, 2011] et en Europe [e.g., Carvalho *et al.*, 2010] a été présenté d'ici la fin du 21ème siècle. Les simulations sur les scénarios du changement climatique ont été effectuées en examinant l'impact du changement sur les émissions biogéniques.

1.2 Description du modèle

On cherche à décrire l'évolution dans l'atmosphère de la concentration d'un ensemble d'espèces chimiques, radioactives ou biologiques, qui réagissent éventuellement entre elles. En toute rigueur, l'évolution du système couplé (fluide et espèces) est donnée par les équations de Navier-Stokes réactives. On parle alors de modèle intégré "*on line*" (MM5-CHEM [Grell *et al.*, 2000], WRF-CHEM [Grell *et al.*, 2005], GEM-MACH [Ménard, 2007], GATOR-GCMM [Jacobson, 2001], etc.[4]). Ce système de modélisation intégré permet de prendre en compte les rétroactions de la météorologie avec les constituants chimiques. Une approche plus commune parce que plus simple consiste à résoudre séparément la dynamique du fluide et les concentrations chimiques. Ce système de modélisation est appelé en série ("*one-way*") car la météorologie influence les concentrations des espèces chimiques mais la réciproque n'est pas vraie.

Dans le cadre de l'approche en série, les champs dynamiques (vent, température, densité et humidité de l'air, diffusion, etc.) sont donc paramétrisés ou précalculés indépendamment par un code météorologique. Ils sont ensuite utilisés comme données d'entrée dans l'équation de dispersion pour les espèces étudiées. On parle souvent de couplage "*off line*" (e.g., CMAQ [Byun et Schere, 2006], CAMx [Morris *et al.*, 2003], Chimere [Bessagnet *et al.*, 2008], Polyphemus [Mallet *et al.*, 2007], etc.[5]) [Sportisse, 2008].

Les systèmes de modélisation "*on line*" ou "*off line*" comprennent les processus qui pilotent l'évolution des espèces ; ceux-ci sont présentés dans la figure 1.1.

1.2.1 Les différents processus

Les CTM reconstituent l'information de la composition chimique de l'air en tout point d'une grille maillant le domaine d'étude grâce à la résolution des équations mathématiques pour re-

[4]MM5-CHEM (the Fifth generation NCAR/Penn State Mesoscale Model coupled with Chemistry), WRF-CHEM (the Weather Research and Forecasting model coupled with Chemistry), GEM-MACH (Global Environmental Multi-scale - Modelling Air quality and CHemistry) et GATOR-GCMM (Gas, Aerosol, Transport, Radiation, General Circulation and Mesocale Meteorological)

[5]CMAQ (Community Multiscale Air Quality model) et CAMx (the Comprehensive Air Quality Model with extensions)

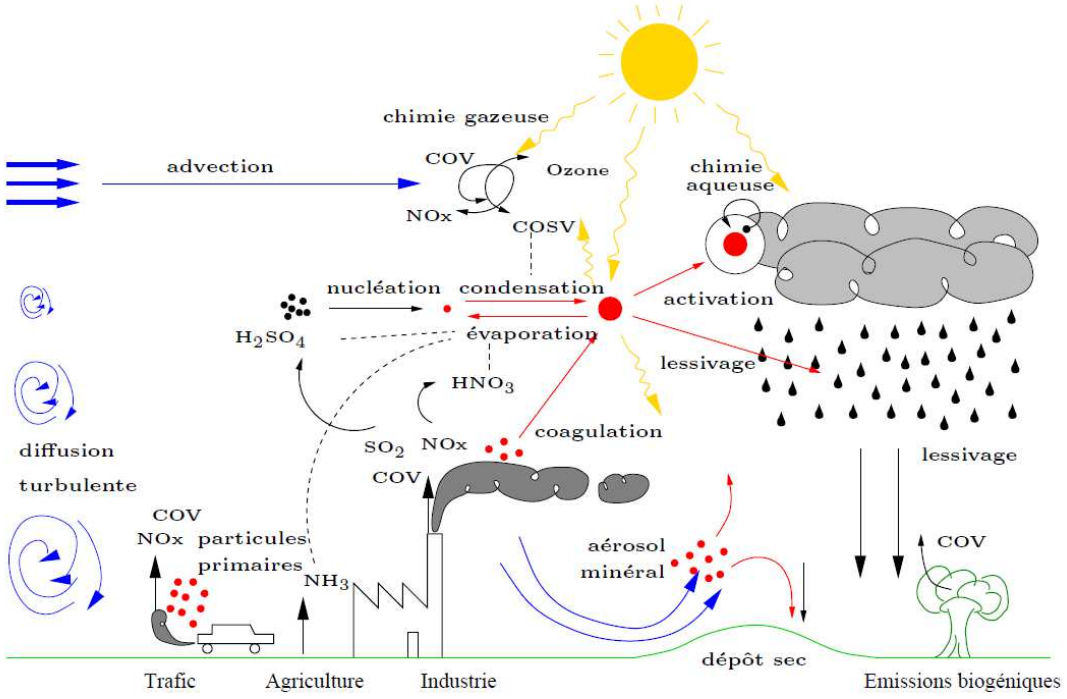

FIGURE 1.1 – Processus décrits dans un modèle de chimie-transport [Sportisse, 2008].

produire les processus physiques et chimiques qui décrivent les phénomènes liés au transport, aux réactions en phase gazeuse et particulaire, ainsi qu'aux dépôts sec et humide. Les modèles découlent d'un système d'équations aux dérivées partielles décrit dans l'équation 1.1 et appelé plus communément équation d'advection-diffusion-réaction. Cette équation décrit le cycle de vie d'une espèce chimique i et représente les phénomènes physico-chimiques. L'évolution spatio-temporelle de la concentration de cette espèce i est

$$\frac{\partial c_i}{\partial t} = -\underbrace{\mathrm{div}(Vc_i)}_{\text{advection}} - \underbrace{\mathrm{div}\left(\overline{V'c'_i}\right)}_{\text{diffusion}} + \underbrace{\chi_i(c_i)}_{\text{réaction}} + S_i - P_i \tag{1.1}$$

où c_i est la concentration de l'espèce i en moyenne, c'_i est la pertubation de la concentration de l'espèce i, V le champ de vent moyen, V' des perturbations du vent moyen, χ_i les réactions chimiques associées à l'espèce considérée, S_i le terme source (émission naturelle ou liée à une activité humaine) et P_i le terme perte (dépôts secs et humides).

Le terme d'advection $\mathrm{div}(Vc_i)$ représente le transport tridimensionnel par le vent, le terme de diffusion $\mathrm{div}\left(\overline{V'c'_i}\right)$ régit principalement le transport vertical en limite de zone de convection.

Les quatre principaux modules qui constituent les CTM sont maintenant présentés en détails.

1.2.1.1 Transport

Lorsqu'il s'agit du transport de polluants, on distingue généralement le transport dû à la convection thermique (diffusion) et celui dû aux vents (advection). Les principales composantes du vent sont horizontales. Dans la couche limite atmosphérique (CLA) - la partie de la troposphère directement soumise à l'influence de la surface terrestre et surtout du cycle diurne - les vents horizontaux sont typiquement de l'ordre de 2 à 10 m/s. En revanche, les vents verticaux sont très faibles et habituellement de l'ordre de quelques millimètres à quelques centimètres par seconde [Stull, 1988]. Ils sont donc généralement négligeables par rapport à la turbulence quand la surface est plate et uniforme.

Turbulence

On peut représenter les mouvements turbulents par des tourbillons qui ont des dimensions couvrant un large spectre de taille et dont l'amplitude peut aller jusqu'à la hauteur de la couche limite (entre 100 et 3000 mètres). La turbulence naît d'une part de l'agitation de l'air due au frottement avec le sol (effet de cisaillement) : i.e., la turbulence mécanique. D'autre part, son origine peut être également le gradient vertical de température qui lui-même dépend des capacités d'absorption du rayonnement solaire par la surface. Le réchauffement au sol élève les masses d'air réchauffées au contact du sol : i.e., la turbulence thermique.

Fermeture turbulente

Le nombre d'inconnues dans l'ensemble d'équations pour un écoulement turbulent est plus grand que le nombre d'équations. Quand les équations sont incluses pour ces inconnues, on découvre encore davantage de nouvelles inconnues. Donc, la description de la turbulence n'est pas fermée. Les paramétrisations utilisés afin de fermer les equations turbulentes sont classifiées par leur ordre (premier, second, etc.). Une paramétrisation qui a le premier ordre de la fermeture, utilise l'approximation des variables turbulentes ayant la double corrélation (e.g., $\overline{V'c_i'}$ où V' représente les perturbations du vent, c_i' est la perturbation des concentrations de l'espèce i et $\overline{V'c_i'}$ est la moyenne de $V'c_i'$.). Les paramétrisations sont classifiées aussi comme la fermeture locale (une inconnue à un point paramétrisée par les valeurs connues à ce point) et la fermeture nonlocale (une inconnue à un point paramétrisée par les valeurs connues à plusieurs points).

Si on utilise le premier ordre et la fermeture locale pour fermer le terme de diffusion dans l'equation 1.1, une fermeture possible et simple est

$$\overline{V'c_i'} = -\rho K \nabla \frac{c_i}{\rho} \tag{1.2}$$

où ρ est la densité de l'air, K est une matrice de diffusion turbulente et c_i est la concentration moyenne.

Si on reporte l'équation 1.2 dans l'équation 1.1, on obtient

$$\frac{\partial c_i}{\partial t} = -\underbrace{\operatorname{div}(V c_i)}_{\text{advection}} + \underbrace{\operatorname{div}\left(\rho K \nabla \frac{c_i}{\rho}\right)}_{\text{diffusion}} + \underbrace{\chi_i(c_i)}_{\text{réaction}} + S_i - P_i \tag{1.3}$$

La matrice K est prise diagonale : on note en général K_x, K_y et K_z les termes associés à la diffusion turbulente selon les directions x, y et z, respectivement. Les termes de diffusion

horizontaux sont *a priori* négligeables par rapport à l'advection. Donc, on ne prend souvent en compte que la diffusion verticale, décrite par K_z. La diffusion verticale K_z est prépondérante et doit être paramétrisée en fonction de l'écoulement.

1.2.1.2 Photochimie

$\chi_i(c_i)$ dans l'équation 1.3 est le terme du bilan des productions et pertes par réactions chimiques de l'espèce i.

$$\chi_i(c_i) = P_i - L_i(c_i) \tag{1.4}$$

où c_i est la concentration de l'espèce i, P_i et L_i sont respectivement les termes de production et consommation (qui dépendent de l'ensemble des réactions). L_i est proportionnel à c_i (et parfois à c_i^2).

En raison des nombreuses reactions et espèces chimiques impliquées dans la chimie atmosphèrique, un mécanisme cinétique chimique complet et détaillé n'est pas envisagé pour des simulations de qualité de l'air. Par conséquent, on utilise souvent un ensemble de réactions simplifié pour les espèces chimiques considérées. Le nombre des réactions dans les mécanismes peut varier de quelques centaines à plusieurs milliers. Les mécanismes chimiques avec quelques centaines de réactions sont souvent adaptés pour la formation des polluants atmosphériques dans les CTM.

La production photochimique d'ozone résulte de la photo-oxydation des COV en présence de NO_x. La seule réaction de production de l'ozone est donnée par

$$\mathrm{O_2 + O \rightarrow O_3} \tag{1.5}$$

Dans la troposphère, la source disponible d'oxygène atomique est la dissociation photolytique de NO_2,

$$\mathrm{NO_2 + h\nu\ (300\ nm \leq \lambda \leq 400\ nm) \rightarrow NO + O} \tag{1.6}$$

L'oxydation des COV par OH va conduire à la formation des radicaux péroxyles (RO_2) qui oxydent NO en NO_2. Cette chaine contibue à la formation d'ozone par la formation de NO_2.

$$\mathrm{COV + OH \xrightarrow{O_2} RO_2 + H_2O,} \tag{1.7}$$

$$\mathrm{RO_2 + NO \rightarrow RO + NO_2} \tag{1.8}$$

où $\mathrm{RO_2}$ et RO sont des radicaux organiques péroxyles et alcoxyle.

Il exist un grand nombre de COV dans la nature avec différents vitesses de réaction par rapport à OH et des nombres de carbones et structures différents. La méthode de la classification des COV dans le mécanisme est importante et elle permet de diversifier le caractère des mécanismes. Par exemple, dans un mécanisme d'espèces moléculaires regroupées, un composé organique particulier ou une espèce chimique suppléante ("*surrogate species*") est utilisée afin de représenter plusieurs composés organiques de la même classe. Mais dans un mécanisme de structures regroupées, les composées organiques sont divisés en plus petits éléments (groupes fonctionnels) basés sur les types de liaisons carbones ("*carbon-bond*") dans chaque espèce. L'évolution de ces groupes fonctionnels lors de l'oxydation des COV est alors représentée afin de reproduire l'évolution de la composition chimique organique.

1.2.1.3 Dépôts

On dit que les polluants se déposent au sol lorsqu'ils sont absorbés par l'eau, le sol ou la végétation. Ce phénomène constitue un terme de perte. Son intensité dépend des polluants, des conditions météorologiques, du rayonnement, du lieu (type et densité de végétation), de la saison (état de la végétation). Le dépôt est plus fort en journée et il est accru par le rayonnement qui augmente le transport vertical turbulent. Au-dessus des masses d'eau, il croît avec la solubilité de l'espèce considérée.

Dépôt sec

Le flux de dépôt sec est directement proportionnel à la concentration au-dessus du sol de l'espèce qui se dépose.

$$F = -v_d C \tag{1.9}$$

où F représente le flux vertical de dépôt sec, i.e. la quantité de matière qui se dépose par unité de surface et unité de temps. La constante de proportionnalité, v_d, entre le flux et la concentration C a des unités de longueur par unité de temps et est appelée la vitesse de dépôt. Puisque C est une fonction de la hauteur z au-dessus du sol, v_d est également une fonction de z et doit être liée à une hauteur de référence à laquelle C est spécifiée [Seinfeld et Pandis, 2006].

L'approximation classique consiste en une analogie électrique où apparaît une résistance de transfert, composée de trois résistances en série :

$$v_d = \frac{1}{R_a + R_b + R_c} \tag{1.10}$$

où R_a est la résistance aérodynamique, R_b la résistance de couche quasi-laminaire et R_c la résistance de surface (végétation, sol, eau, etc.) [Wesely, 1989; Sportisse, 2007].

Dépôt humide

On qualifie de dépôt humide ou de lessivage la perte due aux transferts de masse avec la phase aqueuse (nuages ou pluies). Les polluants solubles peuvent pénétrer les gouttes de pluie lors de leur chute et sont ainsi précipités au sol (*below-cloud scavenging*). Le taux de transfert d'un gaz à la surface d'une goutte en suspension ou en chute libre peut être calculée par

$$W_t(z,t) = K_c(C_g(z,t) - C_{eq}(z,t)) \tag{1.11}$$

où K_c est le coefficient de transfert de masse des espèces (m/s), C_g est la concentration de l'espèce dans la phase gazeuse, et C_{eq} est la concentration de l'espèce à la surface des gouttes en équilibre avec la concentration en phase aqueuse du gaz dissous [Seinfeld et Pandis, 2006].

Une autre forme de lessivage a lieu dans les nuages où les polluants solubles ont des échanges (transferts de masse) avec les gouttes d'eau (*in-cloud scavenging*). Les gaz comme HNO_3, NH_3 et SO_2 peuvent être dissous partiellement dans les gouttes des nuages. Le taux local du lessivage d'un gaz soluble avec la concentration C_g est donnée par

$$W_{ic} = \Lambda C_g \tag{1.12}$$

où Λ est le coefficient de lessivage (s^{-1}). Pour le lessivage d'un gaz très soluble comme HNO_3 dans un nuage typique, Λ est une fonction de K_c et de la distribution des gouttes de nuage. Par contre, pour un gaz modérément soluble comme SO_2, il faut tenir compte des variables supplémentaires pour calculer Λ (e.g., le pH).

Le lessivage des particules est une fonction des tailles des particules et des tailles des gouttes de pluie [Seinfeld et Pandis, 2006; Duhanian et Roustan, 2011].

1.2.1.4 Aérosol

Un aérosol est un ensemble de particules en suspension dans l'air. La phase d'une particule peut être liquide ou solide. De nombreuses classifications sont utilisées pour la description des aérosols : en fonction de leur origine (naturelle ou anthropique), de leur nature (minérale ou organique), de leur histoire chimique (aérosol primaire ou secondaire), de leur taille (distribution en nombre, surface et en masse). L'évolution de la distribution en taille et de la compostion chimique des aérosols est gouvernée par de nombreux processus [Debry *et al.*, 2007a].

Nucléation

De très petits aérosols, de diamètre de l'ordre du nanomètre, se forment à partir de l'agrégation de molécules gazeuses menant à des agrégats stables thermodynamiquement. Le mécanisme et les espèces en jeux ne sont pas encore bien élucidés et des paramétrisations sont nécessaires pour représenter la nucléation binaire homogène de l'acide sulfurique et de l'eau (H_2O-H_2SO_4) ou la nucléation ternaire en incluant l'ammoniac (H_2O-H_2SO_4-NH_3) [Zhang *et al.*, 2010a, b].

Condensation/évaporation

Des composés gazeux à faible pression de vapeur saturante peuvent condenser sur les aérosols existants. À l'inverse, des composés condensés dans la matière particulaire peuvent s'évaporer. Ce transfert de masse est déterminé par le gradient entre la concentration moyenne en phase gazeuse et la concentration de l'espèce gazeuse à la surface des particules qui est en équilibre thermodynamique avec la concentration de l'espèce considérée [Pilinis *et al.*, 2000].

Coagulation

La coagulation des aérosols est principalement brownienne, c'est-à-dire elle est due à l'agitation thermique des aérosols. D'autres processus (turbulence, force de van der Waals et thermophorèse) ne sont importants que dans des cas particuliers. La coagulation est souvent négligée parce que son effet sur la distribution en masse est petit par rapport à l'effet de la condensation/évaporation loin des sources de particules. Mais la coagulation peut avoir un impact substantiel sur la distribution en taille pour les particules ultrafines après leur génération [Finlayson-Pitts et Pitts, Jr., 2000].

Thermodynamique des composés minéraux

L'état de l'aérosol, liquide ou solide, est déterminé par l'humidité relative (HR). Lorsque l'humidité augmente, l'aérosol solide peut devenir liquide (déliquescence) puis croître absorbant de l'eau quand HR augmente (hygroscopicité). La résolution du transfert de masse entre la phase

particulaire et la phase gazeuse nécessite donc le calcul des concentrations à l'équilibre thermodynamique. Par exemple, à l'équilibre thermodymique, le nitrate d'ammonium est formé à partir de

$$\mathrm{NH_3 + HNO_3 \rightleftharpoons NH_4NO_3(s) \text{ ou } (aq) \text{ selon HR}} \tag{1.13}$$

Le nitrate d'ammonium est formé dans les zones caractérisées par des concentrations élevées de l'ammoniac et de l'acide nitrique et des concentrations de sulfate faible (voir ci-dessous). Selon l'HR ambiante, le nitrate d'ammonium peut exister en phase solide, NH_4NO_3(s), ou en phase aqueuse de NH_4^+ et NO_3^-. Les concentrations à l'équilibre de NH_3 et HNO_3 en phase gazeuse, et la concentration résultante de NH_4NO_3 solide ou aqueuse, peuvent être calculées à partir de principes thermodynamiques fondamentaux [Seinfeld et Pandis, 2006].

La composition de l'aérosol minéral continental est fortement pilotée par l'interaction entre le sulfate, le nitrate et l'ammonium. Au sein des aérosols, le nitrate et le sulfate sont en compétition à l'égard de l'ammonium, pour la formation du nitrate d'ammonium et du sulfate d'ammonium ($(NH_4)_2SO_4$). On distingue en général deux régimes en fonction de la richesse en ammonium du milieu [Saxena *et al.*, 1986; Ansari et Pandis, 1998; Blanchard *et al.*, 2000] :

- si le milieu est riche en ammonium, le sulfate d'ammonium se forme, puis avec l'excès d'ammonium, le nitrate d'ammonium. L'aérosol est en général peu acide, voire neutre.
- si le milieu est pauvre en ammonium, il n'y a pas assez d'ammonium pour neutraliser le sulfate et l'aérosol est fortement acide. Le nitrate d'ammonium ne peut alors pas se former. Une faible quantité d'acide nitrique peut cependant se dissoudre dans les particles aqueuses.

Aérosol organique secondaire (AOS)

L'oxydation des COV peut conduire à des espèces à pression de vapeur saturante plus faible, les composés organiques semi-volatils (COSV). Les COSV se forment par des réactions d'oxydation des COV par OH, O_3 et NO_3 (voir l'équation 1.14). Les COSV sont souvent d'origine biogénique (terpènes et isoprène) ou d'origine anthropique (composés aromatiques).

$$\mathrm{COV + oxydant \rightarrow \alpha_1 COSV_1 + \alpha_2 COSV_2 + ...} \tag{1.14}$$

Les coefficients stœchiométriques α_i sont en général calculés à partir d'expériences en chambres atmosphériques, et selon la méthode empirique de Odum [Odum *et al.*, 1996], on se limte seulement à deux espèces suppléantes d'AOS par réaction pour paramétriser les résultats expérimentaux.

La répartition des COSV entre phase gazeuse et phase particulaire est calculée selon la loi de Raoult par

$$(q_i)_g = \gamma_i (x_i)_a q_i^{sat} \tag{1.15}$$

où $(q_i)_g$ est la concentration massique de l'espèce i en phase gazeuse, q_i^{sat} est la concentration massique saturante de l'espèce i dans un mélange pur, $(x_i)_a$ est la fraction molaire de l'espèce i dans le mélange organique particulaire, et γ_i est le coefficient d'activité dans le mélange organique. La concentration massique en phase particulaire, $(q_i)_a$, est calculée par l'équation 1.15 et la conservation de la masse :

$$(q_i)_a + (q_i)_g = (q_i)_{tot} \tag{1.16}$$

où $(q_i)_{tot}$ est la masse totale pour la phase gazeuse et la phase particulaire.

1.2.2 Données d'entrée

De nombreuses données d'entrées sont nécessaires pour initier les processus précédemment exposés. Les résultats de simulation sont très sensibles à certaine de ces données. Or la plupart d'entre elles sont fortement entachées d'incertitudes. Elles jouent donc un rôle important dans la qualité des résultats. Certaines données d'entrée sont fixes et d'autres données varient dans l'espace et le temps. Les principales données sont listées dans cette section.

1.2.2.1 Données topographiques

Les données topographiques sont fixes dans l'espace et le temps. Elles sont utilisées pour spécifier la hauteur géopotentielle à la surface.

1.2.2.2 Occupation des sols

L'occupation des sols, souvent appelé avec l'acronyme anglais LUC (*Land use cover*), décrit les différents types de terrain, souvent avec une résolution de l'ordre du kilomètre carré. Cette donnée permet de distinguer les terres des étendues d'eau. Sur terre, plusieurs types de terrain sont aussi identifiés, selon le type de culture agricole, le type de forêt, l'étendue urbaine. L'occupation des sols est aussi utilisée pour estimer la longueur de rugosité de surface pour la vitesse du vent, la chaleur spécifique du sol, la densité du sol, la porosité du sol, etc. Elle peut varier avec le mois ou la saison.

1.2.2.3 Données chimiques

Constantes cinétiques de réaction

Les constantes cinétiques de réaction des mécanismes chimiques sont de deux natures. Il y a d'une part les réactions dont les constantes sont estimées à partir de quelques coefficients et quelques variables météorologiques (température et pression) ; un exemple concerne les réactions dont les constantes suivent la loi d'Arrhenius.

$$k = Ae^{\left(\frac{-E_a}{RT}\right)} \tag{1.17}$$

où k est le constant cinétique, A le facteur pré-exponentiel, E_a l'énergie d'activation et R la constante des gaz parfaits.

Ces données incluent les coefficients uni-, bi- et termoléculaire pour les réactions en phase gazeuse ou en phase aqueuse et aussi les données de coefficients d'équilibre pour les réactions réversibles.

D'autre part, il faut estimer les constantes photolytiques. La section efficace d'absorption et le rendement quantique sont utilisés pour calculer les constantes photolytiques des gaz et liquides.

Coefficient d'activité

Le coefficient d'activité est un facteur utilisé en thermodynamique pour rendre compte de l'activité d'une substance chimique dans un mélange de substances chimiques. Le coefficient d'activité est utilisé dans les CTM pour simuler la chimie particulaire pour la formation d'aérosol secondaire (voir Section 1.2.1.4).

1.2.2.4 Émissions

Les émissions biogéniques sont issues de la biomasse. On considère que les polluants sont émis à la surface. Les principaux polluants concernés sont l'isoprène, les terpènes et le monoxyde d'azote. Bien qu'une grosse partie des émissions en Europe proviennent des activités humaines, les émissions naturelles, y compris biogéniques, peuvent être importantes selon les saisons. Par exemple, les émissions de soufre en Italie sont dominées par des sources volcaniques, les émissions de COV dans la région méditerranéenne sont dominées par les émissions provenant de forêts pendant l'été, et les émissions de méthane en Scandinavie par les zones humides [Simpson *et al.*, 1999].

Le traitement des émissions anthropiques diffère selon les données disponibles. À l'échelle européenne, ces émissions sont fournies par l'organisme européen, European Monitoring and Evaluation Programme (EMEP) sur un maillage de 50 km par 50 km sous forme de taux annuels pour les catégories de polluants NO_x, COV, SO_2 et CO, et pour dix types d'émetteurs (dont le trafic et diverses industries) réparties en classes SNAP (*Selected Nomenclature for Air Pollution*). Les émissions sont réparties temporellement par mois, par type de jour, et puis par heure. Les facteurs appliqués dépendent du pays et de la classe SNAP.

Une répartition verticale peut aussi être appliquée, surtout pour les émissions des cheminées d'usine, les émissions volcaniques et les feux de végétation.

1.2.2.5 Données météorologiques

Pour mener à bien une simulation, il faut disposer d'une vingtaine ou d'une trentaine de variables météorologiques. Parmi les plus importantes, on trouve bien sûr le vent, la température, les flux de surface, la hauteur de couche limite ou encore l'intensité du rayonnement solaire. Les modèles météorologiques ne proposent pas toujours les variables nécessaires à la simulation. En conséquence, quelques paramétrisations sont proposées pour diagnostiquer les variables indisponibles (diffusion verticale, atténuation du rayonnement, longueur de Monin-Obukhov, etc.).

1.2.2.6 Concentrations de polluants

Les concentrations de polluants sont nécessaires pour initialiser les simulations et surtout pour fournir des conditions aux limites du domaine de modélisation. Par exemple, les simulations à l'échelle régionale utilisent généralement des concentrations issues d'un modèle de chimie-transport global.

1.3 Incertitudes du modèle

L'incertitude correspond aux variations des concentrations en sortie du CTM. Elle est estimée indépendamment des observations. L'origine de l'incertitude est triple [Mallet et Sportisse, 2006] :

- les données d'entrées (occupation des sols, inventaires d'émissions, champs de forçage météorologiques, constantes cinétiques de réaction, etc).
- les paramétrisations physiques ou chimiques (vitesse de dépôt, émissions biogéniques, fermeture turbulente, etc).
- les approximations numériques (maillage, pas de temps, mécanisme chimique réduit, etc).

Selon des études précédentes, la fermeture turbulente, le mécanisme chimique et la formulation de la vitesse de dépôt introduisent la plus grande incertitude pour l'ozone [Mallet et Sportisse, 2006; Tang *et al.*, 2011]. Par ailleurs, le mélange vertical par la fermeture turbulente et le choix des niveaux verticaux a un grand impact sur les concentrations de nombreux polluants (O_3, NO_2, SO_2, NH_3 et PM) [Roustan *et al.*, 2010b].

1.3.1 Incertitudes liées aux mécanismes chimiques

Les mécanismes chimiques utilisés dans les CTM sont simplifiés, ils ne prennent pas en compte toutes les espèces chimiques. Les mécanismes chimiques peuvent être conçus dans des buts différents. Par exemple, un mécanisme est conçu pour être utilisé uniquement dans la couche limite atmosphérique, tandis qu'un autre est développé pour simuler la chimie dans toute la troposphère et la basse stratosphère.

De plus, les mécanismes simplifiés utilisent des hypothèses différentes pour l'agrégation des COV (voir Section 1.2.1.2). La formation des espèces intermédiaires, e.g., des radicaux péroxyles, est fortement influencée par ces hypothèses ainsi que la formation des polluants secondaires (O_3 et PM). En revanche, les différences entre les mécanismes sont très limitées dans les zones rurales, où la chimie est principalement contrôlée par les espèces minérales dont la chimie varie peu d'un mécanisme à l'autre [Gross et Stockwell, 2003].

Les mécanismes sont évalués par des études en chambre atmosphérique pour les cinétiques et les coefficients stœchiométriques. Mais ces évaluations ont un degré important d'incertitude. Par exemple, les parois de la chambre peuvent servir de source et de puits pour O_3, NO_x, aldéhydes, cétones et OH. Un autre problème est que la plupart des chambres atmosphériques fonctionnent avec des concentrations initiales plus élevées de COV et de NO_x que dans l'atmosphère réelle. Cette incertitude d'évaluation induit une incertitude sur les produits formés pendant les réactions.

1.3.2 Incertitudes liées au mélange vertical

L'incertitude liée au mélange vertical est due à la paramétrisation de la diffusion verticale et de la vitesse de dépôt [Tang *et al.*, 2011]. Il exist différentes paramétrisations pour la diffusion verticale. Elles sont classifiées en fonction de l'hypothèse de fermeture (locale ou non-locale), de la stabilité dans la couche limite (stable, neutre, instable et adiabatique), de l'ordre de la

fermeture (premier, second, troisième, etc.) et de la dépendance de la discrétisation verticale [Stull, 1988].

La diversité des paramétrisations de diffusion verticale induit une grande incertitude sur le coefficient et ainsi une grande incertitude sur le mélange vertical des polluants dans la couche limite.

1.4 Objectifs de la thèse

Cette thèse se compose en deux parties : une partie concernant les incertitudes liées aux mécanismes chimiques et une autre partie concernant les incertitudes liées au mélange vertical.

Dans sa première partie, cette thèse vise à évaluer l'impact de mécanismes chimiques à la formation de O_3 et PM sur l'Europe. Les différents mécanismes sont implémentés dans le CTM Polair3D/Polyphemus et les mécanismes sont associés au modèle d'aérosol SIREAM/ Polyphemus. Les différents modules d'AOS sont aussi associés aux mécanismes afin d'évaluer leur impact sur la formation de PM sur l'Europe. Les impacts de mécanismes chimiques et modules d'AOS sont quantitativement évalués en considérant les caractères chimiques (catégorie des espèces moléculaires, cinétiques des réactions, voies d'oxydation chimique et oligomérisation) et physico-chimique (vaporisation, solubilité des espèces et coefficients d'activité).

Les chapitres 2 et 3 sont des études sur l'impact du traitement de la chimie en phase gazeuse sur la formation de O_3 (le chapitre 2) et $PM_{2.5}$ (le chapitre 3).

Le chapitre 4 traite de l'impact du module d'AOS sur la formation de $PM_{2.5}$. Il s'agit aussi d'études de sensibilité pour l'impact conjugué de mécanisme chimique et module d'AOS sur la concentration de $PM_{2.5}$.

Dans sa deuxième partie, cette thèse est consacrée à l'évaluation de l'impact de paramétrisation météorologique sur la concentration de PM_{10}. D'abord, l'impact de la fermeture turbulente et le module urbain sur les champs météorologiques dans la CLA est évalué sur l'Île-de-France. Ensuite, la modélisation de PM_{10} est évaluée concernant cet impact sur les champs météorologiques. L'évaluation de la distribution verticale de PM_{10} est l'objectif final dans cette partie de la thèse. La distribution verticale de PM_{10} sur l'Île-de-France est évaluée pendant la nuit et le petit matin selon la comparaison avec la mesure.

Le chapitre 5 est une étude de l'évaluation des champs météorologiques par WRF sur l'Île-de-France.

Enfin, le chapitre 6 traite de la sensibilité de la dispersion verticale des polluants aux champs météorologiques.

Chapitre 2

Influence des mécanismes chimiques sur les concentrations d'ozone

Résumé

Le mécanisme chimique est une composante essentielle des modèles de qualité de l'air (MQA), parce que les polluants secondaires comme l'ozone sont formés par la dégradation en phase gazeuse de composés anthropiques et biogéniques.

Comme il existe plusieurs millions d'espèces organiques réactives, il n'est pas possible de simuler la chimie atmosphérique dans un MQA avec un mécanisme détaillé de toutes ces espèces. Par conséquent, des mécanismes réduits sont utilisés dans les MQAs. Ces différents mécanismes chimiques ont été développés qui redistribuent les espèces organiques en "espèces modèle". La chimie minérale atmosphérique inclut un nombre limité d'espèces chimiques et, par conséquent, un mécanisme détaillé de ces espèces peut être utilisé. Il existe cependant des incertitudes notables sur la cinétique des réactions minérales. Par conséquent, des différences existent entre divers mécanismes dans la modélisation des réactions minérales et organiques, et différents mécanismes peuvent produire des concentrations différentes pour certains polluants. Il est donc utile de comparer différents mécanismes chimiques implémentés dans les MQAs et d'évaluer leur influence sur les concentrations simulées.

Les mécanismes chimiques sont souvent classifiés pour la chimie organique soit en mécanismes de structures regroupées, soit en mécanismes d'espèces moléculaires regroupées. Dans les mécanismes de structures regroupées, les espèces organiques chimiques sont divisées en plus petits éléments (groupes fonctionnels) basés sur les types de liaisons carbones. Dans un mécanisme d'espèces moléculaires regroupées, une espèce suppléante est utilisée pour représenter plusieurs espèces organiques de la même classe (e.g., alcanes, alcènes et aromatiques). Ces espèces peuvent être regroupées selon leur réactivité par rapport à OH, par exemple. Certaines espèces organiques peuvent être traitées de manière individuelle, c'est-à-dire sans être groupées avec d'autre espèces. Deux mécanismes, un de chaque catégorie, ont été choisis pour les comparaisons dans cette thèse. L'un est le mécanisme de structures regroupées CB05 (*Carbon Bond chemical mechanism 2005*) et l'autre est le mécanisme d'espèces moléculaires regroupées RACM2 (*Regional Atmospheric Chemistry Mechanism, version 2*).

RACM2 est un mécanisme récent développé à partir de RACM. Les nouveaux développements dans RACM2 comprennent un nouveau schéma pour le benzène, la destruction de

l'ozone avec des atomes d'oxygène et les réactions d'atomes d'oxygène avec l'azote et l'oxygène moléculaire.

CB05 est le mécanisme le plus récent de la série "Carbon Bond" et c'est une version mise à jour de CBM-IV. Dans CB05, des réactions des radicaux nitrates (NO_3), l'oxydant principal pour la chimie atmosphérique pendant la nuit, ont été ajoutées afin d'améliorer la chimie nocturne. Une nouvelle espèce biogénique, TERP a été ajoutée pour représenter les monoterpènes (dans RACM2, les monoterpènes sont représentés par deux espèces suppléantes, API et LIM).

Les deux mécanismes ont été incorporés dans le MQA tri-dimensionnel (3-D) Polair3D de la plateforme Polyphemus (`http://cerea.enpc.fr/polyphemus/index.html`) pour modéliser la qualité de l'air. Une période d'un mois (du 15 juillet au 15 août 2001) a été simulée avec une période de deux semaines pour le pré-calcul. Le but de ce pré-calcul est de générer des conditions initiales raisonnables. Le domaine du modèle couvre l'Europe de l'ouest et une partie de l'Europe de l'est. Il couvre une zone de 33,5° en longitude $\times$ 23° en latitude avec un pas de 0,5° en longitude et en latitude. Cinq niveaux verticaux sont considérés à partir de la surface jusqu'à 3 000 m, avec une résolution plus fine près de la surface. Les champs météorologiques ont été obtenus de la réanalyse fournie par ECMWF (European Centre for Medium-Range Weather Forecasts). Les émissions anthropiques ont été générées à partir de l'inventaire d'EMEP (European Monitoring and Evaluation Programme) pour l'année 2001. Les émissions biogéniques sont calculées avec une paramétrisation qui dépend de la météorologie et des données disponibles sur la végétation.

La performance du modèle est satisfaisante pour chacun des deux mécanismes. Globalement, les deux mécanismes donnent des résultats similaires avec une différence moyenne sur le domaine de seulement 5% (moins de 3 ppb) pour les concentrations journalières des maximums d'ozone sur 8 h moyennées sur le mois. Cette différence résulte de traitements différents dans les deux mécanismes de la chimie organique et minérale.

D'abord, nous comparons les deux mécanismes pour la chimie minérale seulement. Ensuite, nous étudions l'effet de la chimie organique sur la formation d'ozone. Les différentes catégories de composés organiques volatils (COV) (c'est-à-dire les "espèces modèle") ont des réactivités différentes pour la formation d'ozone. Il semble approprié d'examiner la formation d'ozone dans chacun des deux mécanismes par catégorie de COV. Deux méthodes distinctes sont utilisées pour étudier l'influence du CO ou une catégorie de COV sur la formation d'ozone : (1) le CO ou une catégorie de COV est retiré de la simulation et son effet est estimé en comparant la simulation de base (avec toutes les espèces) avec la simulation où le CO ou la catégorie de COV a été retirée, (2) le CO ou la catégorie de COV est ajouté à une simulation de base ne contenant que des espèces minérales (c'est-à-dire, les espèces d'azote et de soufre, NO_y et SO_x) et son effet est estimé en comparant la simulation de base avec la simulation où le CO ou la catégorie de COV a été ajouté.

Les différences dans le traitement de la chimie minérale sont principalement dues à des différences dans la cinétique des deux réactions majeures de l'oxydation du monoxyde d'azote (NO) : $NO + O_3 \longrightarrow NO_2 + O_2$ et $NO + HO_2 \longrightarrow NO_2 + OH$. La cinétique de $NO + O_3$ est plus rapide dans CB05 que dans RACM2 alors que la cinétique de $NO + HO_2$ est plus rapide dans RACM2 que dans CB05 (les différences de constantes cinétiques sont d'environ 10% à 298 K). Ces différences conduisent à une différence de concentration moyenne d'ozone sur tout le domaine de 5%. Les concentrations d'ozone sont supérieures dans RACM2 que dans CB05 car les cinétiques de RACM2 sont plus favorables à la formation d'ozone.

Bien que la cinétique du CO avec OH est identique dans les deux mécanismes, des concen-

trations différentes de OH en raison des incertitudes sur la chimie de l'azote conduisent à des différences importantes des concentrations d'ozone selon si le CO est pris en compte ou pas.

Les différences entre RACM2 et CB05 de traitement de la chimie organique conduisent à une différence de la concentration moyenne d'ozone sur tout le domaine de 3%, CB05 étant plus favorable à la formation d'ozone. La différence moyenne est faible car les effets de diverses catégories de COV se compensent. Cependant des différences significatives sont simulées localement et/ou pour des catégories spécifiques de COV.

Pour certaines catégories de COV, tels que les aldéhydes et les alcènes biogèniques, les traitements sont plus détaillés et explicites dans RACM2, qui utilise plus d'espèces modèle que CB05. Par exemple, pour les aldéhydes, le benzaldéhyde, la méthacroléine et le glyoxal contribuent 20%, 9% et 1%, respectivement, des émissions totales d'aldéhydes . Les trois espèces sont explicitement représentées dans RACM2, alors qu'elles sont agrégées dans CB05. Elles ont des réactivités avec OH relativement élevées dans RACM2, alors que les espèces agrégées dans CB05 ont des réactivités avec OH plus faibles. Pour les alcènes biogéniques, la cinétique de l'isoprène est identique dans les deux mécanismes, mais les produits primaires d'isoprène sont différents ; CB05 comprend un seul produit de l'isoprène (ISPD) tandis que RACM2 en comprend deux : la méthacroléine (MACR) et la méthyl vinyl cétone (MVK). Les taux de réactions pour les réactions de ISPD et MACR avec OH sont identiques à 298 K, cependant, le taux de MVK est inférieur à celui d'ISPD. Ainsi, l'impact de l'isoprène sur la formation d'ozone est plus grand dans CB05 que dans RACM2. De même, CB05 représente les monoterpènes avec une seule espèce (TERP), alors que RACM2 en utilise deux (API et LIM). Le taux de réaction de TERP avec OH à 298 K se situe entre les taux de réactions d'API et LIM avec OH ; i.e., $k_{API,OH} < k_{TERP,OH} < k_{LIM,OH}$. Cependant, la formation de HO_2 et NO_2 par l'oxydation des monoterpènes par OH diffère et les concentrations sont d'environ 15% plus élevées dans CB05 que dans RACM2. Ainsi, CB05 conduit à environ 10% de plus de formation de l'ozone que RACM2 en comprenant les émissions de monoterpènes.

Pour les autres espèces de COV, tels que les aromatiques (toluène, xylènes, benzène, etc.), les hypothèses faites sur les principales voies d'oxydation chimique affectent la formation de l'ozone de manière significative. Les composés aromatiques après réactions avec OH réagissent avec O_2, soit pour mener à l'abstraction d'un atome d'hydrogène afin de former un crésol, soit pour ajouter O_2 afin de former un radical peroxyle qui par la suite entraîne la formation de produits de scission. RACM2 suppose que la majorité des produits de réaction du toluène sont des espèces très réactives associées aux produits de scission (dicarbonyle et époxyde). Par contre, CB05 a une fraction plus grande de produits retenant le cycle aromatique (crésol). Des comparaisons entre les concentrations d'ozone et de crésol simulées avec CB05 et RACM2 montrent que de fortes concentrations de crésol correspondent à de faibles concentrations d'ozone.

Les différences dans la chimie des alcanes et alcènes anthropiques résultent principalement des différences de représentations des catégories de COV dans les deux mécanismes, par structures regroupées et par molécules regroupées. Par exemple, le propène est representé par PAR (espèce paraffine) + OLE (oléfine terminale avec deux carbones) dans CB05 et par OLT (oléfine terminale avec quatre carbones) dans RACM2. Les différences induites pour les concentrations d'ozone, ne sont pas plus grandes que celles obtenues pour d'autres catégories d'espèces des mécanismes, et suggèrent que les représentations regroupées ont été optimisées dans la mesure du possible.

Les résultats obtenus dans cette comparaison de deux mécanismes chimiques en phase gazeuse pour la formation d'ozone sont encourageants, car (1) les différences sont faibles en

moyenne et (2) les différences identifiées par catégories d'espèces chimiques spécifiques sont dues essentiellement à des incertitudes dans nos connaissances en chimie (par exemple, la cinétique des réactions d'oxydation de NO et l'importance relative des produits résultant de l'oxydation de composés aromatiques). Il convient de noter que dans un MQA l'incertitude due à la chimie minérale est comparable à celle due à la chimie organique. Les différences induites par les approximations nécessaires pour représenter les COV en un nombre limité de catégories (par exemple, en structures regroupées ou en molécules regroupées) ne sont pas plus grandes que celles d'autres facteurs (constantes cinétiques et voies d'oxydation). Par conséquent, les améliorations futures des mécanismes chimiques en phase gazeuse nécessitent des données expérimentales pour réduire les incertitudes actuelles. Ces données expérimentales devront concerner aussi bien la chimie minérale que la chimie organique. Ces améliorations bénéficieront aussi bien les mécanismes en structures regroupées que ceux en molécules regroupées.

Ce chapitre est constitué de
Kim, Y., Sartelet, K. et Seigneur, C. (2009). **Comparison of two gas-phase chemical kinetic mechanisms of ozone formation over Europe.** *J. Atmos. Chem.*, 62 :89-119.

Sommaire

2.1 Introduction

The gas-phase chemical mechanisms are an important component of air quality models (AQMs), because secondary pollutants such as ozone and particulate matter are formed during the gas-phase degradation of anthropogenic and biogenic compounds [Seinfeld et Pandis, 1998; Finlayson-Pitts et Pitts, Jr., 2000]. A mechanism that treats oxidant formation explicitly would require several millions of organic reactants and products and even more reactions [Aumont *et al.*, 2005]. Hence the chemical mechanisms used in three-dimensional AQMs must strike a balance between the complexity of the mechanism and its computational efficiency [Dodge, 2000]. For example, Dennis *et al.* [1996] showed that the majority of the computing time for tropospheric gas-phase modeling (80 to 90%) was consumed integrating the chemical rate equations. Condensing a chemical kinetic mechanism to minimize computational requirements necessarily introduces approximations that are reflected as uncertainties in the mechanism simulations. Therefore, it is useful to compare different chemical mechanisms implemented in AQMs and assess their influence on the predictions of AQMs. Several previous studies have been dedicated to the comparisons of the chemical mechanisms implemented in AQMs [Kuhn *et al.*, 1998; Junier *et al.*, 2005; Arteta *et al.*, 2006; Faraji *et al.*, 2008; Luecken, 2008; Luecken *et al.*, 2008; Pan *et al.*, 2008; Sarwar *et al.*, 2008]. Most comparisons have addressed applications to North America or box model (0-D) simulations; only one comparison over Europe was identified [Arteta *et al.*, 2006]. Reported ozone differences among chemical mechanisms vary from less than 1% to 8% over the whole calculation domain.

We examine here differences in ozone concentrations simulated with two recent chemical mechanisms, CB05 and RACM2. The mechanisms were incorporated within a three-dimensional (3-D) AQM, which was applied over Europe. First, a brief description of the models used in this study is given, including the chemical mechanisms, the host air quality model, the modeling domain, model setup and some preliminary assessements. Next, the methodology used for the comparison is introduced. The analysis of the effect of the mechanism formulation on ozone concentrations is conducted by considering eight distinct species groups: non-carbonaceous inorganic species (nitrogen oxides and sulfur oxides), carbon monoxide, alkanes, anthropogenic alkenes, biogenic alkenes, aldehydes, alcohols and aromatic compounds. The analysis of differences in ozone concentrations is conducted for the whole domain and at specific locations including 8 urban sites and 4 remote areas. Among urban sites, some are NO_x-sensitive for ozone formation and some are VOC-sensitive. Three other sites are also included to characterize a high biogenic emissions region. The results are discussed in a diagnostic fashion to identify the causes of the discrepancies. Concluding remarks summarize the major differences between these two mechanisms.

2.2 Model descriptions

2.2.1 Chemical kinetic mechanisms

Condensed chemical mechanisms are mostly classified as lumped structure mechanisms and lumped species mechanisms. In a lumped structure mechanism, chemical organic compounds are divided into smaller species elements (functional groups) based on the types of carbon bonds in each species. In a lumped species mechanism, a particular organic compound or a surrogate species is used to represent several organic compounds of a same class (e.g., alka-

Table 2.1: General characteristics of CB05 and RACM2.

	CB05	RACM2
Date of last major update	2005	2008
Total number of reactions	156	349
Number of inorganic reactions	53	45
Number of organic reactions	103	304
Number of photolysis reactions*	23	34
Total number of species	52**	113**
Number of stable inorganic species	12***	12***
Number of inorganic intermediates	4	4
Number of stable organic species	29	56
Number of organic intermediates	7	41

*: included above, **: including XO2 and XO2N, ***: excluding CO2, H2, H2O, N2 and O2.

nes, alkenes and aromatics) which, for example, have similar reactivity with hydroxy radicals [Dodge, 2000]. We have chosen two mechanisms, one from each category, for this study. One is the lumped structure mechanism CB05 [Yarwood *et al.*, 2005] and the other is the lumped species mechanism RACM2 [Goliff et Stockwell, 2008, 2010]. These two chemical mechanisms have been developed recently for regional scale applications. These mechanisms and their predecessors are widely used in AQMs. For example, CB05 and its previous versions are used in CMAQ (Community Multi-scale Air Quality), CAMx (the Comprehensive Air Quality Model with extensions), UAM-V (the Variable grid Urban Airshed Model), WRF/Chem (Weather Research and Forecasting model coupled with Chemistry). RACM2 and its previous versions (RACM and RADM2) are used for example in CMAQ, WRF/Chem, MM5/Chem (the Meteorological Mesoscale model, version 5 with Chemistry), EURAD (EURopean Air pollution Dispersion model) and POLAIR3D. General characteristics of the mechanisms are summarized in Table 2.1.

RACM2 is a new mechanism developed via various improvements made to RACM [Stockwell *et al.*, 1997]. Reaction rate constants were updated from different sources, e.g., NASA/JPL [Sander *et al.*, 2006], IUPAC [Atkinson *et al.*, 2006] and MCM 3.1 [Bloss *et al.*, 2005]. New developments in RACM2 include a new benzene scheme and new photolysis reactions for benzaldehyde and glyoxal. In the benzene scheme, phenol is explicitly speciated as a product of benzene oxidation [Goliff et Stockwell, 2010]. In RACM2, ozone destruction with oxygen atoms is included exclusively, though this reaction is important mostly near the tropopause. Furthermore, RACM2 treats reactions of oxygen atoms with molecular nitrogen and oxygen separately so that the altitude dependence due to different activation energies is considered [Stockwell, 2009].

CB05 is an updated version of CBM-IV [Gery *et al.*, 1989]. In CB05, reaction rate constants were updated from the evaluations by IUPAC [Atkinson *et al.*, 2005] and NASA/JPL [Sander *et al.*, 2003]. Additional inorganic reactions were included and 10 organic species were

added to better represent stable organic species and radicals in the atmosphere [Luecken *et al.*, 2008]. CB05 has fewer species than RACM2, which makes it attractive for computational requirements; however, CB05 has more inorganic reactions than RACM2. Recent inorganic updates in CB05 include molecular hydrogen and oxygen atom reactions, more NO_3 radical reactions, N_2O_5 photolysis and odd-oxygen and odd-hydrogen reactions, though most of these reactions are important only in the upper troposphere. In particular, NO_3 radical reactions, the main driver for atmospheric chemistry at night, were added to improve nighttime chemistry [Yarwood *et al.*, 2005]. By this addition, NO_3 destruction reactions in CB05 became similar to those in RACM2. Table 2.2 summarizes the inorganic reactions that differ between the two mechanisms.

To better represent aldehyde species, the two mechanisms include a new higher aldehyde species in common. These are ALDX in CB05 and ALD in RACM2, so that acetaldehyde (ALD2 in CB05, ACD in RACM2) chemistry is explicitly represented. It was treated with other higher aldehydes previously in CBM-IV and RACM. In CB05, a new species TERP was added to represent monoterpenes; in RACM2, monoterpenes are represented by two surrogate species API and LIM [Yarwood *et al.*, 2005; Goliff et Stockwell, 2010].

2.2.2 The Polyphemus air quality modeling system

Polyphemus version 1.3.1 and its AQM Polair3D were used for this study (`http://cerea.enpc.fr/polyphemus/index.html`). To generate chemistry modules that allow using new chemical mechanisms in the Polyphemus platform, we applied an automatic preprocessor,

Table 2.2: Different inorganic reactions in CB05 and RACM2.

Type	Reaction*	Reaction no. in CB05**	Reaction no. in RACM2**
Molecular hydrogen reaction	O1D + H2 → OH + HO2	R38	X
NO_3 radical reactions	NO3 + O3P → NO2	R46	X
	NO3 + O3 → NO2	R49	X
NO_x recycling reaction	N2O5 → NO2 + NO3 photolysis	R53	X
Odd-oxygen and	OH + O3P → HO2	R40	X
odd-hydrogen reactions	OH + OH → O3P	R41	X
	OH + OH → H2O2	R42	X
	HO2 + O3P → OH	R44	X
	H2O2 + O3P → OH + HO2	R45	X
	O3P + O3 → 2 O2	X	R36
	O1D + N2/O2 → O3P	X	R37, R38
	O1D + M → O3P	R10	X

*: written with model species notation, **: X means that the reaction is not treated in the mechanisms.

SPACK (Simplified Preprocessor for Atmospheric Chemical Kinetics). This preprocessor converts a symbolic notation of chemical reactions to a mathematical set of ordinary differential equations and a large numbers of chemical equations can easily be treated [Djouad *et al.*, 2002]. A detailed description of Polyphemus is provided by Mallet *et al.* [2007].

2.2.3 Modeling domain, episode and setup

The modeling domain is identical to the one in Sartelet *et al.* [2007] and covers western and part of eastern Europe. The coordinates of the southwestern point are (10.75°W, 34.75°N) in longitude/latitude. The domain of simulation covers an area of $33.5^\circ \times 23^\circ$ with a step of 0.5° along both longitude and latitude. Five vertical levels are considered from the ground to 3000 m. The heights of the cell interfaces are 0, 50, 600, 1200, 2000 and 3000 m. The simulations were carried out for one month from 15 July to 15 August 2001, with a two-week spin-up period. The aim of the spin-up period is to get realistic initial conditions. Because of the greater number of species treated in RACM2, a model simulation took about twice more computational time with RACM2 than with CB05.

Photolysis rates were computed off-line by the photolysis preprocessor Fast-J, which calculates photolysis rates in the presence of an arbitrary mix of cloud and aerosol layers [Wild *et al.*, 2000]. The dry deposition velocities were preprocessed using the parameterization scheme for the gaseous dry deposition in AURAMS [Zhang *et al.*, 2002]. Meteorological inputs were obtained from reanalyses provided by the European Centre for Medium-Range Weather Forecasts (ECMWF), and vertical diffusion was computed using the Troen-Mahrt [1986] parameterization and the Louis [1979] parameterization.

Anthropogenic emissions were generated with the European Monitoring and Evaluation Programme (EMEP) inventory for 2001. The inventory is provided as total non-methane hydrocarbon (NMHC) and was subsequently disaggregated into molecular volatile organic compound (VOC) species using Passant's speciation coefficients [Passant, 2002]. Model species emissions were derived from the molecular species, according to speciation rules available for each mechanism [Yarwood *et al.*, 2005; Goliff et Stockwell, 2010]. Although the mechanism developers' own databases are also available, Carter's speciation database [Carter, 2008] was used here for the two mechanisms to maintain consistency for emission speciation. In any case, differences between Carter's speciation database and the mechanism developers' databases appear to be minor. Biogenic emissions were computed as in Simpson *et al.* [1999]. Two-thirds of monoterpene emissions were allocated to α-pinene and one-third to limonene in RACM2 [Johnson *et al.*, 2006], whereas all monoterpenes were simply allocated to model species TERP in CB05.

2.2.4 Preliminary assessements

Model performance was evaluated using the EMEP ozone concentration data available hourly at 92 stations. The mean normalized error and bias (using a 30 ppb threshold) were 23% and 9%, respectively, for RACM2 and 21% and 4%, respectively, for CB05. These results compare favorably with performance standards, typically $\leqslant$ 35% for error and $\leqslant$ 15% for bias [Russell et Dennis, 2000]. Root-mean square errors are 17 and 16 ppb and correlations of hourly ozone concentrations are 0.56 and 0.55 for RACM2 and CB05, respectively. Such

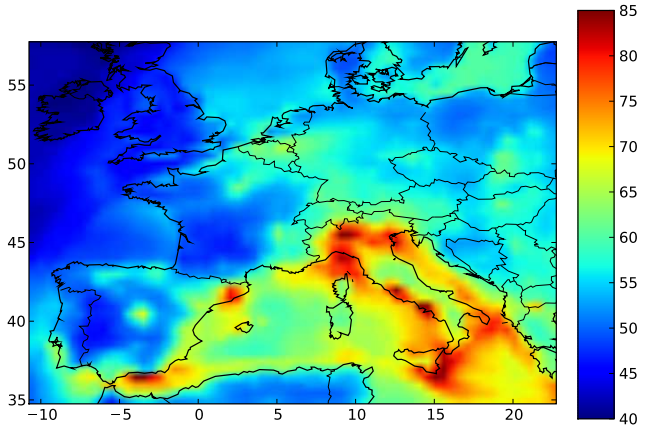

(a) **CB05**

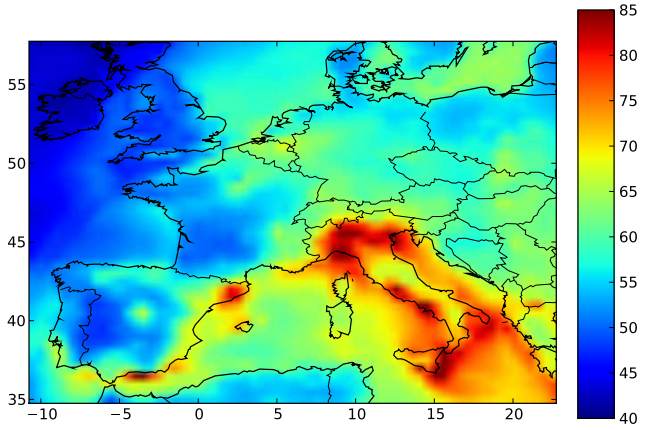

(b) **RACM2**

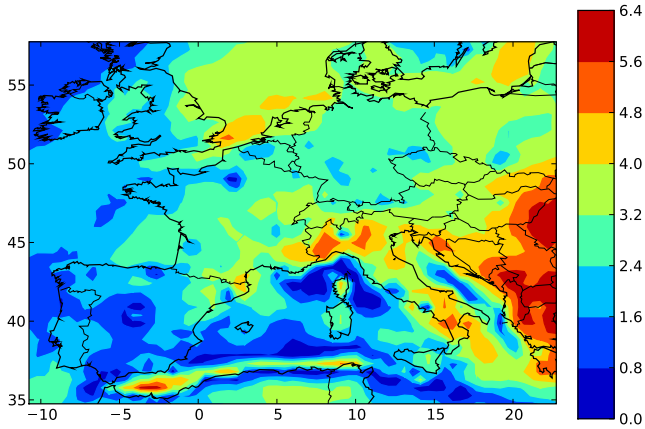

(c) **CB05 - RACM2**

Figure 2.1: Monthly average of daily maximum 8h-average ozone concentrations (ppb) modeled with (a) CB05 and (b) RACM2, and differences between the two model simulations by modulus (c) CB05 - RACM2.

results are commensurate with earlier model performance results for Europe (e.g., van Loon *et al.*, 2007; Sartelet *et al.*, 2007; Honoré *et al.*, 2008).

Monthly averages of daily maximum 8h-average ozone concentrations (8h-maximum below) are not significantly different between the two chemical mechanisms. Using mean fractional absolute difference defined by

$$\frac{1}{n}\sum_{i=1}^{n}\frac{\mid [O_3]_{CB05} - [O_3]_{RACM2} \mid}{([O_3]_{CB05} + [O_3]_{RACM2})/2} \tag{2.1}$$

the difference between CB05 and RACM2 is 5% over the entire domain and the mean value of those O_3 concentrations in CB05 is lower than that in RACM2 by 2.6 ppb. The maximum local differences between the two mechanisms are 6.1 ppb (9%) for locations where O_3 concentrations predicted by RACM2 are greater and 5.9 ppb (9%) for locations where O_3 concentrations predicted by CB05 are greater. Figure 2.1 presents the modeled ozone concentrations over the entire domain for the two mechanisms and monthly average of the corresponding differences by modulus. Differences are large (> 4 ppb) along the coastline of northern Africa (9%) and in eastern Europe (9%). The difference along the coastline of northern Africa disappears when the biogenic VOC emissions are not included (not shown here). Ozone formation in that area results mostly from the interaction of biogenic emissions from land with NO_x emissions from marine traffic along the North African coast. Therefore, the difference in ozone concentration results from different treatments of the biogenic VOC chemistry and NO_x kinetics between the two mechanisms. Smaller differences are obtained in some large cities (about 3% in Paris, Madrid, Rome, Milan and Barcelona) and in some marine region (2.5% in the Ligurian Sea and the Adriatic Sea) but those differences stand out against the regional background as shown in Figure 2.1c. The ozone concentration in the Italian Peninsula is the highest in Europe for both CB05 and RACM2. The two mechanisms predict ozone concentrations above the current European ozone target value (120 $\mu g/m^3$ for 8h-maximum by EU Directive 2008/50/CE) there, as well as in the Strait of Gibraltar, Barcelona, Paris and Madrid. Because RACM2 overall predicts slightly more ozone than CB05, O_3 concentrations in some parts of the domain can exceed the European target value with RACM2 while they do not with CB05.

Significant differences of the ozone concentration between the two mechanisms are observed in remote areas far from urban regions. In Figure 2.1c, these differences appear clearly in eastern Europe, the coastline of northern Africa, Italian Peninsula, North Sea and Ionian Sea. Smaller differences are observed in other parts of the Mediterranean Sea and western Europe except Italy. Remote regions can be classified by their ozone characteristics in four categories.

1. High ozone concentration and high ozone difference (Italian Peninsula and Ionian Sea)
2. High ozone concentration and low ozone difference (Ligurian Sea and Sicily)
3. Low ozone concentration and high ozone difference (the coastline of northern Africa and North Sea)
4. Low ozone concentration and low ozone difference (most of western Europe)

Similar discrepancies in remote areas were observed in a comparison between CB05 and CBM-IV mechanisms [Luecken *et al.*, 2008]. These differences for the remote areas are discussed in detail in Section 2.4.2.

2.3 Comparison methodology

2.3.1 Categorization of volatile organic compounds

Our objective is to compare the two mechanisms in a systematic fashion in order to identify the causes of the most significant differences in ozone formation. To that end, we compare the two mechanisms first for the effect on O_3 of inorganic chemistry only. Next, we investigate the effect of organic chemistry on ozone formation. Since it is well established (e.g., Bowman *et al.*, 1995; Carter *et al.*, 1995; Carter, 1995; Martien *et al.*, 2003; Hakami *et al.*, 2004; Derwent *et al.*, 2007) that different classes of volatile organic compounds (VOC) have different reactivities with respect to ozone formation, it seems appropriate to investigate the treatment of ozone formation in both mechanisms by VOC classes. One possibility is to study how each model species (i.e., the carbon-bond species in CB05 and the surrogate molecules in RACM2) leads to ozone formation. Such an approach, however, does not lend itself to a straightforward comparison because there is no direct correspondence between the model species of the two mechanisms except for a few cases (e.g., formaldehyde and acetaldehyde). Another possibility is to study how each mechanism treats ozone formation for a class of VOC defined before processing into model species. This second approach offers the advantage of being consistent with experimental and theoretical investigations conducted on VOC reactivity. It also takes into account the processing of actual VOC classes into model species, which is a major component of a condensed chemical kinetic mechanism. Therefore, this second approach was selected here for our comparison of CB05 and RACM2.

Two distinct methods can be used to investigate the influence of CO or a VOC class on ozone formation: (1) CO or a VOC class can be removed from the simulation (i.e., its emissions, boundary conditions and initial conditions) and its effect can then be estimated by comparing the base simulation (with all species) and the sensitivity simulation (with all species except CO or the VOC class); (2) CO or the VOC class can be added to a simulation containing only inorganic species except CO (i.e., nitrogen and sulfur species, NO_y and SO_x) and its effect can be estimated by comparing the simulation with only NO_y and SO_x species and a simulation with these species plus CO or the VOC class studied. The first method analyzes the differences

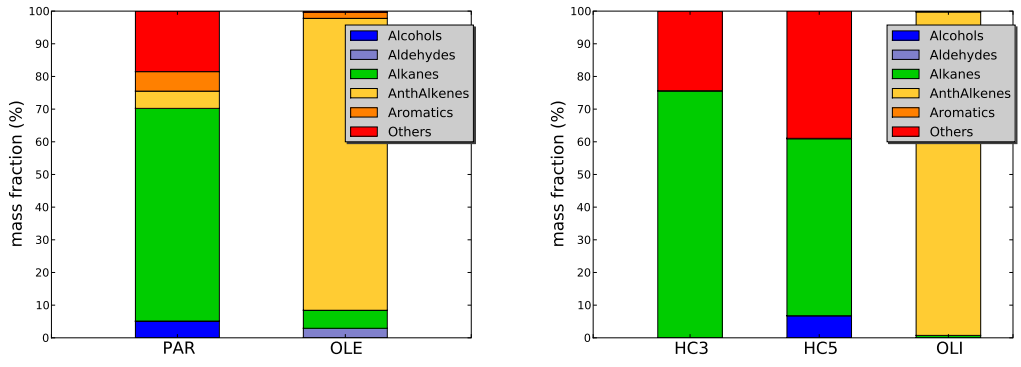

(a) CB05 (b) RACM2

Figure 2.2: Examples of distribution of some model species among VOC categories for the European emission inventory.

between the two mechanisms in a context similar to that used to define incremental reactivity, i.e., the contribution of CO or a VOC class to ozone formation is estimated in the presence of nitrogen oxides (NO_x) and other carbonaceous compounds. The second method focused on the differences between the two mechanisms when only the chemistry of CO or a VOC class takes place in the presence of NO_x. Because the relationship between ozone formation and carbonaceous emissions is highly non-linear, the two methods will give different results. Consequently, we applied both methods in this study (note that for a class such as aldehydes, removing emissions and other inputs does not lead to a complete removal of that class because aldehydes are produced during the oxidation of other classes of VOC).

CB05 and RACM2 have predefined speciation rules to convert molecular VOC species to model species. For example, the paraffinic carbon model species PAR in CB05 appears in all types of anthropogenic VOC emissions species: alkanes, alkenes, aldehydes, alcohols and aromatic compounds. In RACM2, the model species HC5, for example, is used for both alkanes and some alcohols (those with more than two carbons). Figure 2.2 shows some examples of such distributions of model species among the different VOC classes for the two mechanisms. When defining VOC classes, an issue arises for benzaldehyde, which consists of a benzene ring with an aldehyde substituent; we chose to include it in both aldehyde and aromatic compound categories.

For the first method, the reference simulation uses all emissions (hereafter AllEmis). The sensitivity simulations use the full emission inventory, but the emissions, boundary conditions and initial conditions of a carbonaceous category are removed: CO, aldehydes, alkanes, biogenic alkenes, aromatic compounds, anthropogenic alkenes, alcohols (these simulations are referred to hereafter as NoCO, NoAldehy, NoAlkane,NoBioAlkene, NoAromat, NoAnthAlkene and NoAlcohol, respectively). Similarly, for the second method, the reference simulation is referred to as NOySOx and emissions, boundary conditions and initial conditions of CO and each VOC class were added separately to the reference simulation, NOySOx in 7 distinct sets of simulations (these simulations are hereafter referred to as WithCO, WithAldehy, WithAlkane, WithBioAlkene, WithAromat, WithAnthAlkene and WithAlcohol, respectively).

2.3.2 Indicators for NO_x-VOC sensitivity

The ozone-precursor relationship can be understood in terms of NO_x-sensitive and VOC-sensitive (or NO_x-saturated) chemical regimes [Sillman, 1999] and it is useful to understand these chemical regimes in the modeling domain when analyzing differences between the mechanisms. To predict NO_x-VOC sensitivity for each location, one may compare differences between O_3 concentrations in a base model simulation and those in simulations with, for example, 35% reductions in anthropogenic VOC and in NO_x. Because the estimations of NO_x- and VOC-sensitivity at individual locations are often very uncertain [Sillman, 1999], two distinct methods were used here.

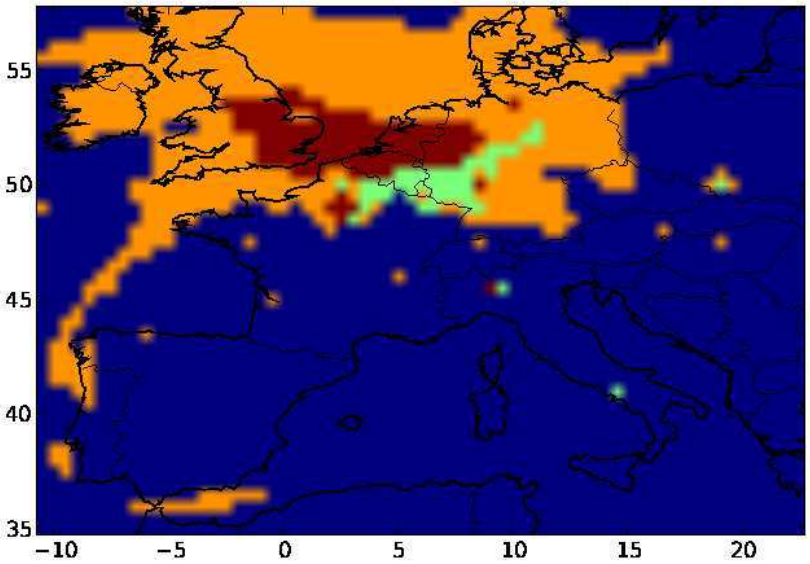

(a) Method of Sillman and He (2002) - Red: VOC-sensitive; Blue: NO_x-sensitive; Green: Mixed; Orange: insensitive, when the threshold is 2 ppb

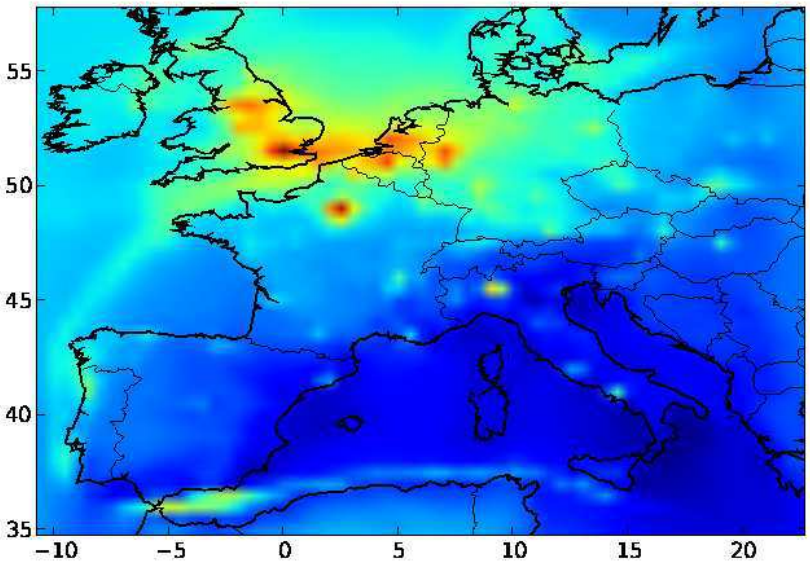

(b) Method of Junier et al. (2005) - Red and yellow: VOC-sensitive; Blue: NO_x-sensitive; Green: mixed or insensitive

Figure 2.3: NO_x-VOC sensitivity distributions over Europe in this study (15 July - 15 August 2001 simulation).

First, as done in Sillman et He [2002], locations are classified according to the following definitions:

1. NO_x-sensitive: O_3 in the scenario with reduced NO_x (Reduc-NO_x below) is lower than O_3 in both the base case (Base below) and in the scenario with reduced VOC (Reduc-VOC below) at the specified location by at least a few ppb (which is referred to as the threshold in the following).

2. VOC-sensitive: O_3 in the Reduc-VOC is lower than O_3 in both the Base and the Reduc-NO_x by at least the threshold.

3. Mixed: Both the Reduc-NO_x and the Reduc-VOC have O_3 lower than in the Base by at least the threshold, and their reciprocal difference is within the threshold.

4. NO_x-titration: O_3 in the Reduc-NO_x is larger than O_3 in the Base by at least the threshold, and difference between O_3 in the Reduc-VOC and O_3 in the Base is within the threshold.

All other locations are viewed as insensitive to NO_x and VOC in the context of the model domain. In this study, a monthly-averaged O_3 concentration was used at each location to estimate the overall chemical regime (this is an approximation because VOC- or NO_x-sensitivity may vary over time; it is nevertheless appropriate for our purpose here).

The second method is simpler than the first but also appropriate. The difference of the averaged ozone concentration between the Reduc-NO_x and the Reduc-VOC is estimated at each location. The positive value of the difference is regarded as VOC-sensitive chemistry and the negative value is regarded as NO_x-sensitive chemistry [Junier *et al.*, 2005; Sportisse, 2008]. Figure 2.3 displays the results of the two methods for NO_x-VOC sensitivity over the modeling domain.

The two methods give similar results about the locations that are NO_x-sensitive or VOC-sensitive for ozone formation. As expected, the VOC-sensitive regime appears mostly in polluted urban regions in northwestern Europe whereas the NO_x-sensitive regime dominates the southern parts of Europe where biogenic alkenes emissions are abundant [Curci *et al.*, 2009]. These results agree well with some previous studies. For example, Kuebler *et al.* [1996] showed that ozone production was limited by NO_x in Switzerland whereas Dommen *et al.* [2002] reported VOC-sensitive chemistry in Milan. Ozone formation in the Paris region has been estimated to be either VOC- or NO_x-sensitive [Honoré *et al.*, 2000; Menut *et al.*, 2000; Sillman *et al.*, 2003]; it is classified here as VOC-sensitive on average for Paris and with mixed sensitivity for Fontainebleau, where NO_x-sensitive would be expected but a NO_x plume from Paris can have an effect on the chemical regime [Tulet *et al.*, 2000].

The chemical regime in a location is determined by the concurrence of NO_x and VOCs emission rates and regional transport. In Figure 2.4, it appears that high NO_x emission rate in a given location leads to VOC-sensitive (star) chemical regime in that point and high VOCs emission rate causes NO_x-sensitive (circle) regime there. The results from the second sensitivity estimation method above were used to display the sensitivity in each location.

2.3.3 Selection of sites for analysis

Because ozone is both an urban and a regional pollutant, it is desirable to study its chemistry at both urban and non-urban receptors [e.g., Zhang *et al.*, 2005; Luecken *et al.*, 2008]. Therefore,

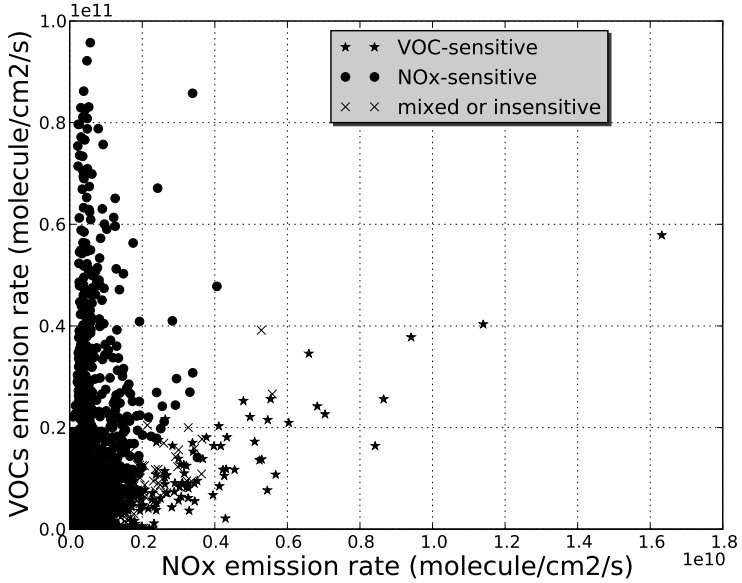

Figure 2.4: Sensitivity in each location determined by emission rates of ozone precursors. The emission rates are averaged values during the whole simulation period (July 15 to August 15). Each point represents a grid cell of the simulation domain; star, circle and cross correspond to the chemical regimes, defined in each grid cell as VOC-sensitive, NO_x-sensitive and mixed or insensitive, respectively (see text).

to highlight differences between the two mechanisms for O_3 formation at different locations and under different chemical regimes, we chose several locations (grid cells) including 8 cities and 4 remote areas. Based on the results of the NO_x-VOC sensitivity (see Figure 2.3), four urban locations were selected respectively in the NO_x-sensitive region and the VOC-sensitive region to investigate the influences related to the chemical regimes in addition to differences in emission levels. The four non-urban sites were taken to represent different ozone levels and discrepancies between the chemical mechanisms. For two non-urban sites, low ozone concentrations are simulated with the two mechanisms but the difference of the O_3 concentrations at one site was higher than that at the other. Similarly, at the two other non-urban sites where high ozone concentrations are simulated, the differences in ozone formation by the two mechanisms differed.

In Europe during this 2001 summer simulation, high biogenic emissions occur mostly in the Iberian Peninsula [Simpson *et al.*, 1999]. Accordingly, three receptors were selected as representatives of the biogenic emission region to focus on the characteristics of CB05 and RACM2 in the region where biogenic alkenes are abundantly emitted. Figure 2.5 illustrates the sites selected.

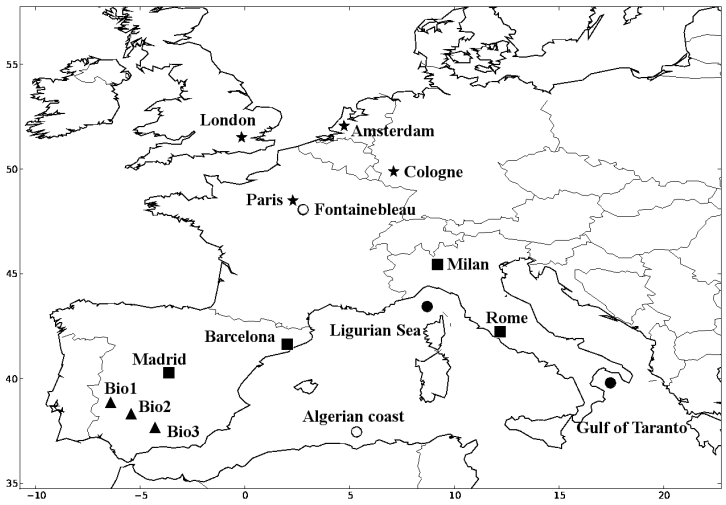

Figure 2.5: Locations of model grid cells used in the analysis. Stars and squares indicate NO_x-sensitive and VOC-sensitive urban areas, respectively; circles indicate non-urban areas (white circle: low ozone (< 65 ppb), black circle: high ozone (> 75 ppb) and triangles indicate locations with strong biogenic emissions.

2.4 Results

2.4.1 Ozone spatial distributions

Difference in ozone concentrations obtained between the two mechanisms is studied by investigating the relative contribution of inorganic versus organic chemistry. The major differences in the inorganic chemistry are the kinetics of NO oxidation by O_3 and HO_2. The kinetics of the first one is greater in CB05 than in RACM2, whereas the kinetics of the second one is greater in RACM2 than in CB05 (both by about 10% at 298 K). Consequently, inorganic chemistry is more conducive to O_3 formation in RACM2 than in CB05.

If one uses the RACM2 kinetics of these reactions in CB05, the mean fractional absolute difference in average ozone concentration over the whole domain is 5% between the two versions of CB05. It is 3% between CB05 and RACM2 when the same NO kinetics is used, with CB05 producing more ozone. Therefore, inorganic chemistry leads to a difference between the two mechanisms as significant as that due to organic chemistry. As discussed below, there are some compensating effects in the differences due to organic chemistry. Nevertheless, this result highlights the fact that both inorganic and organic chemistry contribute to differences between mechanisms.

2.4.1.1 Sensitivity methods

Following Section 2.3.1, two methods are used to investigate the influence of CO or a VOC class on ozone formation. In method 1, the reference simulation includes all species (their emissions, boundary conditions and initial conditions); in method 2, it includes only inorganic species. For each method, Figure 2.6 displays the differences between each emission sensitivity case and the corresponding reference case of the monthly average of daily 8h-maximum ozone

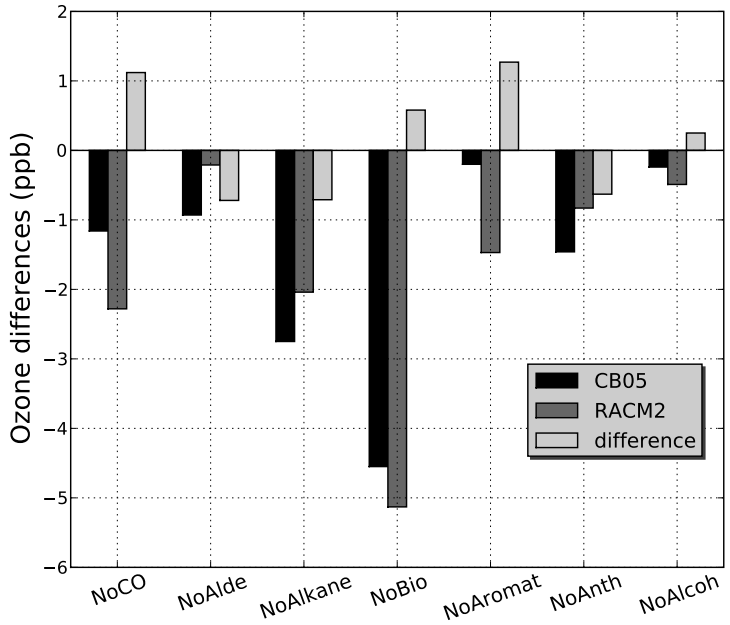

(a) Method 1

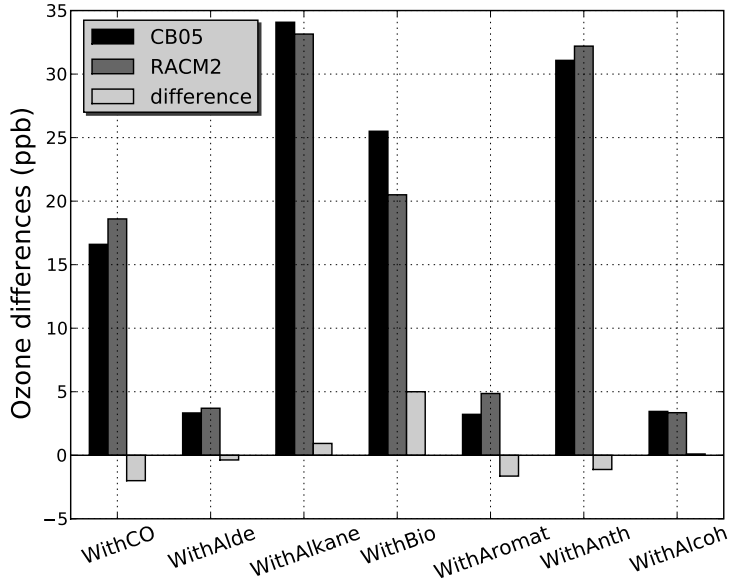

(b) Method 2

Figure 2.6: Differences of the monthly averaged daily maximum 8-h average ozone concentrations averaged over the entire domain (ppb) between the emission scenario case and the reference case and differences between CB05 and RACM2 results. The reference case is AllEmis for the first method and NOySOx for the second method.

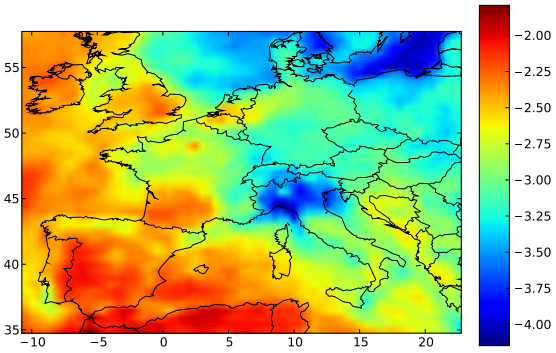

(a) WithCO case

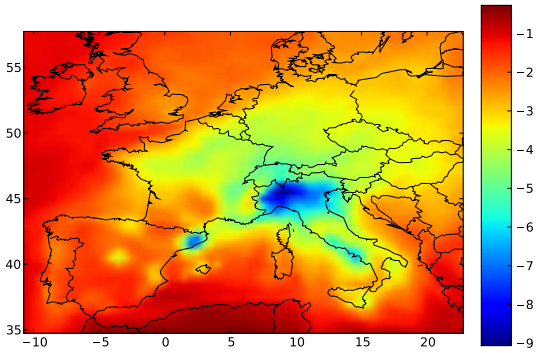

(b) WithAromat case

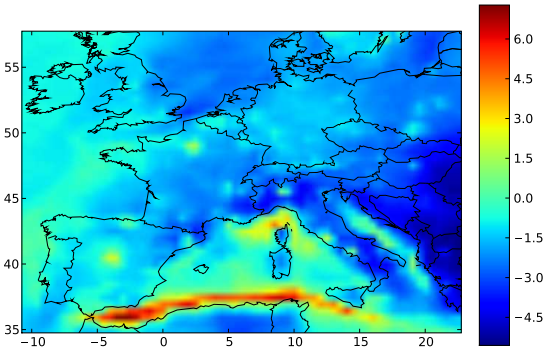

(c) NoCO case

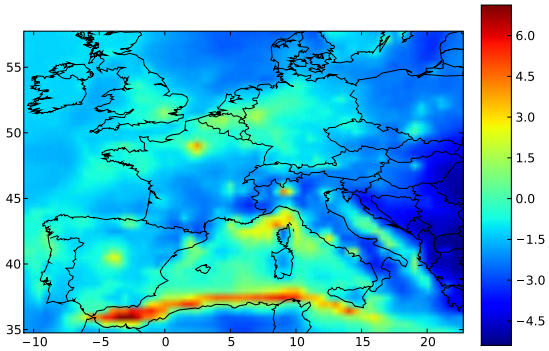

(d) NoAromat case

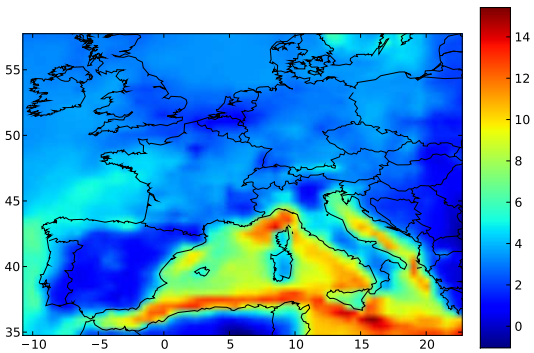

(e) WithBioAlkene case

Figure 2.7: Differences in monthly-averaged daily maximum 8-h average ozone concentration (ppb) between CB05 and RACM2 for five emission scenario cases: (a) CO, method 2; (b) aromatics, method 2; (c) CO, method 1; (d) aromatics, method 1; (e) biogenic alkenes, method 2.

concentrations averaged over the entire domain. Results are shown for CB05 and RACM2; the differences between the results obtained with the two mechanisms are also shown. The largest differences ($\sim$ 1 to 5 ppb) between the two mechanisms are obtained with both methods for carbon monoxide, aromatic compounds and biogenic alkenes (NoCO, NoAromat, WithCO, WithAromat and WithBioAlkene). In the case of the NoCO and NoAromat scenarios, CB05 predicts more ozone at the coastline of northern Africa, the Ligurian Sea, Paris and Madrid, but RACM2 predicts higher ozone concentrations in southern France, Switzerland, Italy and eastern Europe. RACM2 predicts greater ozone concentrations than CB05 over the whole domain in the WithCO and WithAromat cases. In the WithAromat case, the largest differences are obtained in northern Italy and Barcelona; in the WithCO case, they are obtained in northern Italy and the Baltic Sea. In the case of the WithBioAlkene, CB05 predicts greater ozone concentrations than RACM2 over the whole domain (see Figure 2.7). Overall, RACM2 has more reactive CO and aromatic VOC chemistry than CB05. On the other hand, the latter oxidizes alkane compounds and biogenic alkenes more effectively than the former. Results are mixed depending on the method for the other VOC classes. The reasons for these differences are discussed in Section 2.4.2.

2.4.1.2 Emission rates consideration

The analysis presented above addressed the effect of the chemical mechanism given the European emission inventory. Therefore, a VOC class with a large emission rate is more likely to lead to a significant difference between the two mechanisms than a VOC class with a small emission rate, everything else being equal. The differences discussed above are of interest because they are directly relevant to the results of an air quality simulation. However, it is also of interest to investigate whether the chemistry of a VOC class may differ significantly between the two mechanisms, even if the impact for the air quality simulation remains small because that VOC class has small emissions relative to other categories. To that end, we repeated the analysis presented above by normalizing the differences in ozone concentrations by the emission rate of the corresponding VOC class or CO. Thus, we define the normalized ozone differences in each emission sensitivity case as follows

$$\frac{[O_3]_{case} - [O_3]_{ref}}{MoleC_{case}/MoleC_{total}} \tag{2.2}$$

where $MoleC_{case}$ and $MoleC_{total}$ are the total emissions (in moles of C) for the emission scenario case and the reference case, respectively.

Figure 2.8 presents those normalized ozone differences for the two mechanisms and their differences. From this analysis, significant differences appear between CB05 and RACM2 for aldehydes, anthropogenic alkenes, aromatics and alkanes. Aldehydes show significant differences with both methods. The difference in the NoAldehy case is significant as CB05 predicts an effect that is 3.5 times greater than that of RACM2. This effect was limited in Figure 2.6 because the aldehyde class has a small emission rate (0.3% of total carbon atoms). The differences, which occur in the NoAldehy and WithAldehy cases are significant (2.4 ppb and 1.2 ppb for $[O_3]$, respectively), but the difference is more evident when the overall influence of aldehyde chemistry is maximized by the presence of other VOC classes.

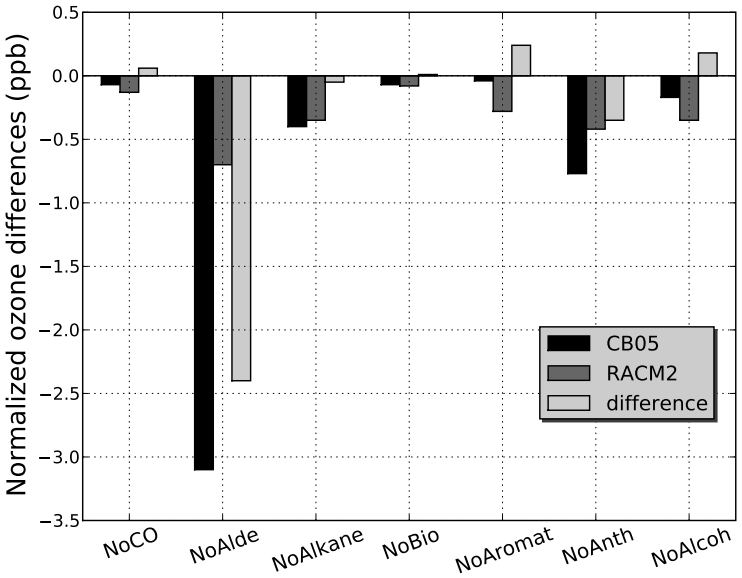

(a) Method 1

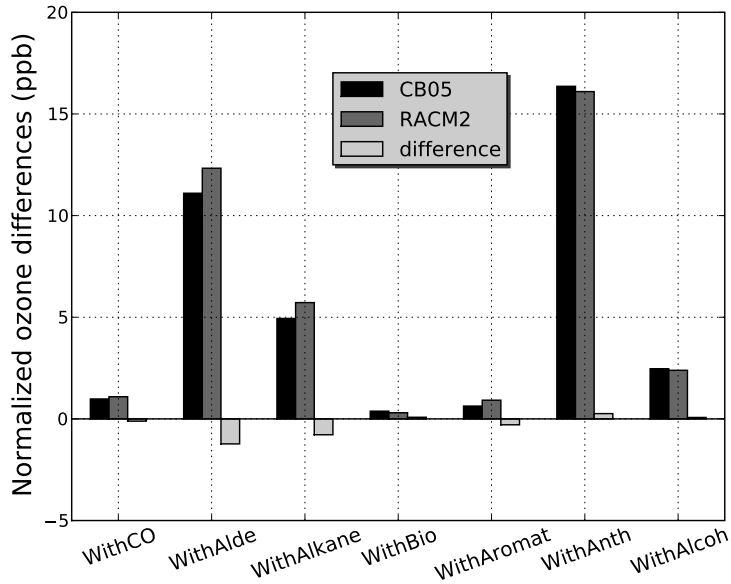

(b) Method 2

Figure 2.8: Differences of the monthly-averaged daily maximum 8-h average ozone concentrations averaged over the entire domain (ppb) between the emission scenario case and the reference case normalized by the corresponding emission rate, and differences between the CB05 and RACM2 results.

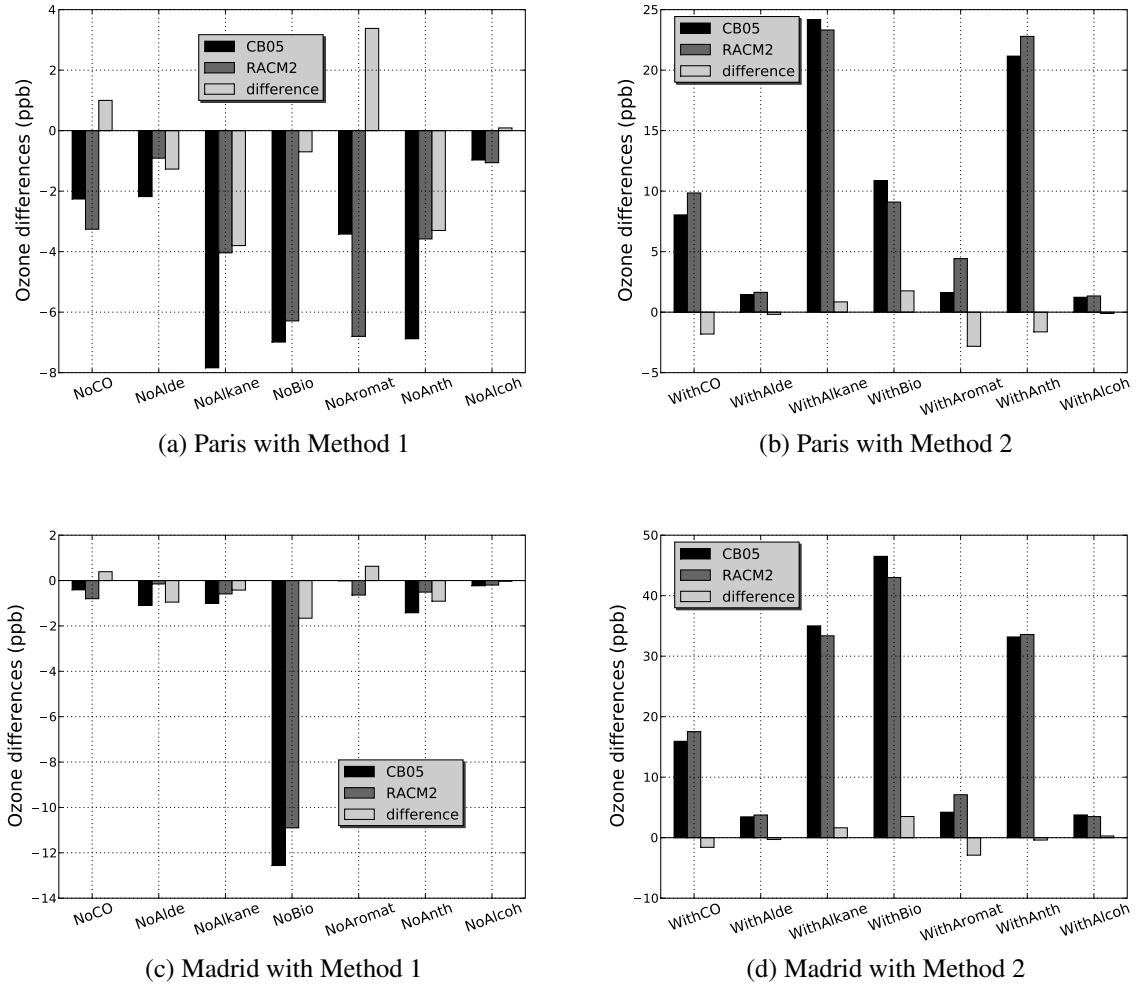

(a) Paris with Method 1

(b) Paris with Method 2

(c) Madrid with Method 1

(d) Madrid with Method 2

Figure 2.9: Different patterns of ozone differences in Paris and Madrid.

2.4.2 Local ozone distributions

2.4.2.1 NO_x- and VOC-sensitive regimes in urban areas

We discuss here the results for the eight selected urban areas (see Figure 2.5). The differences between CB05 and RACM2 in ozone concentrations simulated with only NO_y and SO_x emissions are about 10% in the urban areas considered here (9% for the monthly average 8-h maximum averaged over the whole domain). This non-negligible difference is due primarily to differences in the oxidation reactions of NO by O_3 and HO_2. This result highlights the fact that uncertainties in the modeling of gas-phase chemistry are not solely due to the condensed representation of VOC but also results from uncertainties in the kinetics of key inorganic reactions.

Differences of 8h-maximum ozone concentrations between the mechanisms occur for both methods 1 and 2 at all locations, ranging from 0.01 to 8.5 ppb. Figure 2.9 shows the different patterns in two cities representing VOC-sensitive and NO_x-sensitive chemistry, respectively: Paris and Madrid. From the Method 1 results in Paris, all categories of carbonaceous compounds contribute to ozone formation. In Madrid, the contribution of biogenic compounds to ozone formation is the most important and leads to a NO_x-sensitive chemistry in that location

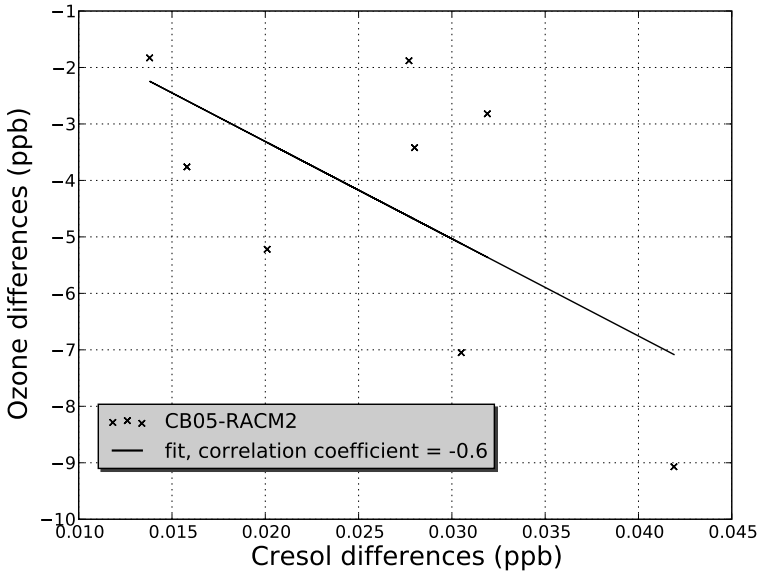

Figure 2.10: Relation between the differences in cresol concentrations and ozone concentrations obtained with CB05 and RACM2 from the results of the eight urban areas.

[Sillman, 1999].

With Method 2, for most cases the ozone amounts in RACM2 are higher than these in CB05; exceptions are alkanes and biogenic compounds. The most significant differences (1.5 to 8.5 ppb) occur in the WithCO and the WithAromatic cases. The kinetics of the oxidation of CO by OH is identical in CB05 and RACM2. However, as discussed above, the O_3 concentrations due to NO_x chemistry differ and, as a result, the OH concentrations differ, thereby affecting the CO oxidation rate and subsequently, O_3 formation. The O_3 concentration differences in the WithCO case range from 10% in the southern urban area (Madrid, Barcelona and Roma) to 18% in northern urban areas. The aromatic-OH adduct reacts with O_2 to either abstract an H atom to form a cresol (via the oxidation of toluene) or add O_2 to form a peroxyl radical that subsequently leads to ring opening and the formation of scission products. Therefore, the cresol yield is a key element to differentiate the relative importance of these two pathways in chemical mechanisms. The experimental cresol yield from the oxidation of toluene varies from $\leq 3\%$ to 38% under different conditions, e.g., presence of NO_x and H_2O_2 [Calvert *et al.*, 2002]. Because of the discrepancy of the experimental results, assumptions about the importance of ring-opening pathways for the toluene reactions with hydroxyl radical species differ among various mechanisms. RACM2 assumes that the majority of the reaction products are highly reactive species associated with ring-opening reactions (DCB2 and EPX). In contrast, CB05 has a high fraction of the ring-retaining products (CRES); therefore, aromatic oxidation products in RACM2 are more reactive than those in CB05 [Faraji *et al.*, 2008; Luecken *et al.*, 2008]. These different pathways are the main cause of differences in ozone formation in the WithAromat case. To illustrate the influence of aromatics on ozone formation, Figure 2.10 shows differences of monthly mean cresol concentration between the two mechanisms at the eight urban areas. The correlation coefficient between cresol concentrations and ozone concentrations implies that more cresol corresponds to less ozone formation.

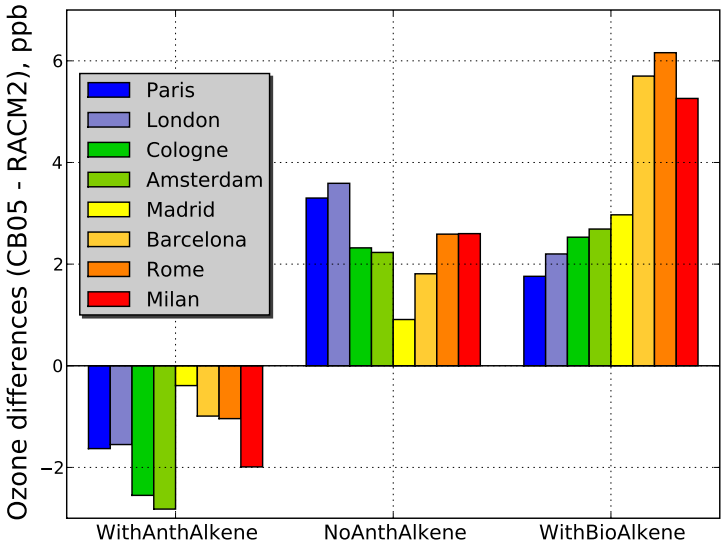

Figure 2.11: Ozone differences between the two mechanisms for all eight urban areas in three cases: WithAnthAlkene, NoAnthAlkene and WithBioAlkene

Figure 2.11 displays the ozone differences between the two mechanisms for the eight urban areas for the WithAnthAlkene, NoAnthAlkene and WithBioAlkene cases. Both WithAnthAlkene and NoAnthAlkene cases (anthropogenic alkenes) lead to significant differences in ozone concentration between the two mechanisms. These differences are greater in the VOC-sensitive cities than in the NO_x-sensitive cities for the two cases but it is opposite for the WithBioAlkene case. The treatment of anthropogenic alkenes differs significantly between the two mechanisms. For example, 1-butene is represented by 3 PAR + FORM in CB05 and by OLT in RACM2. Propene is represented by PAR + OLE in CBO5 and by OLT in RACM2. Ozone differences are greater in the four VOC-sensitive cities than in the others because O_3 concentrations are more sensitive to VOC emissions in the former; furthermore, total carbon emisssion rates of anthropogenic alkenes in these VOC-sensitive cities are higher than those in the four NO_x-sensitive cities.

In the WithBioAlkene case, the influence on ozone concentration is greater in CB05 than in RACM2 (see Figure 2.11). The difference between the two mechanisms varies from 1.8 ppb (Paris) to 6.2 ppb (Rome), and is explained by the different treatment of isoprene and monoterpenes. The kinetics for isoprene is identical in the two mechanisms but the primary isoprene products differ; CB05 includes one isoprene product (ISPD) but RACM2 includes methacrolein (MACR) and methyl vinyl ketone (MVK) as products. The rate constants for the reactions of ISPD and MACR with OH are identical at 298 K, however, the rate constant for MVK is lower than that for ISPD. Thus, the ozone formation for isoprene is greater in CB05 than in RACM2. Similarly, CB05 includes only one terpene species (TERP) whereas RACM2 has a more detailed monoterpene mechanism with two terpene species (API and LIM). The oxidation of TERP in CB05 leads to more ozone formation over Europe than the oxidation of API and LIM in RACM2. The rate constant for the reaction of TERP with OH radicals falls between the two rate constants for the reactions of API and LIM with OH; i.e.,

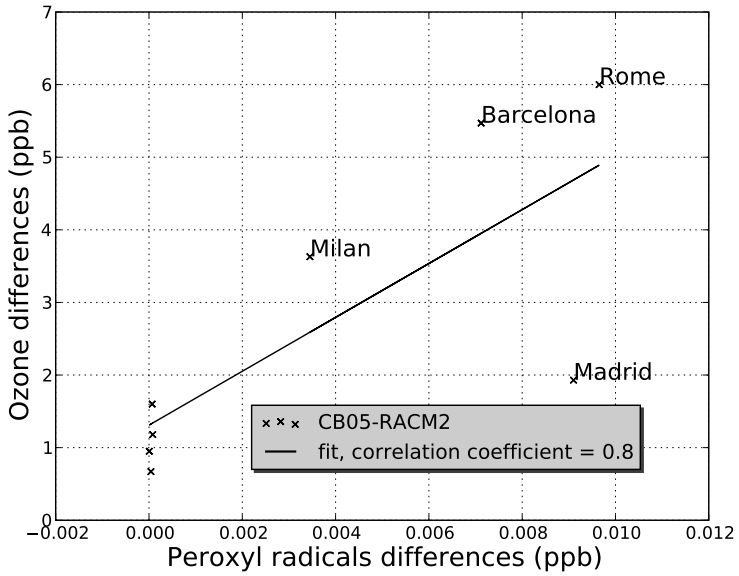

Figure 2.12: Relation between the differences in peroxyl radicals concentrations and ozone concentrations obtained with CB05 and RACM2 in the eight urban areas for the case With-BioAlkene.

$k_{API,OH} < k_{TERP,OH} < k_{LIM,OH}$. However, the formation of the hydroperoxyl radicals and nitrogen dioxide by the oxidation with OH differs and the amount is about 15% higher in CB05 than in RACM2. Thus, CB05 leads to about 10% more ozone formation than RACM2 in the WithBioAlkene case. Locations with highly reactive VOC, e.g., xylenes or isoprene are more likely to have NO_x-sensitive chemistry than locations with similar total VOC but lower reactivity [Sillman, 1999; Hakami *et al.*, 2004]. The enhancement of ozone is mainly attributed to the evident increase in the peroxyl radicals (HO_2+RO_2, RO_2 representing all organic peroxyl radicals) by biogenic emissions [Han *et al.*, 2005]. Figure 2.12 illustrates the differences of O_3 and peroxyl radicals in the eight cities selected. We find that the influence of biogenic emissions on ozone concentrations in the four cities (Madrid, Rome, Milan and Barcelona) classified NO_x-sensitive in Figure 2.3 is correlated with the peroxyl radicals. This result shows that those cities are NO_x-sensitive because of the large biogenic emissions.

Alkanes are not very reactive chemical compounds at the urban scale compared with alkenes and aromatic compounds [Calvert *et al.*, 2008]. However, their emissions can be significant, 47% of anthropogenic VOCs over Europe. Differences are small for Method 2 ($< 10\%$) but greater for Method 1 (about 50%). Similarly, aldehydes show significant differences for Method 1 and negligible differences for Method 2. The difference in aldehyde chemistry is explained in part by the fact that some aldehyde species are explicitly represented in RACM2 with species that have greater reactivity than the surrogate functional groups of CB05. Benzaldehyde, methacrolein and glyoxal contribute 20, 9 and 1% of total aldehyde emissions, respectively. Benzaldehyde is represented as BALD in RACM2, whereas it is aggregated with TOL in CB05. Methacrolein and glyoxal are explicitly represented in RACM2 as MACR and GLY, which have relatively high reactivities with OH, whereas these two species are implicitly aggregated in CB05 as OLE + ALDX and PAR + FORM, which have lower reactivities with

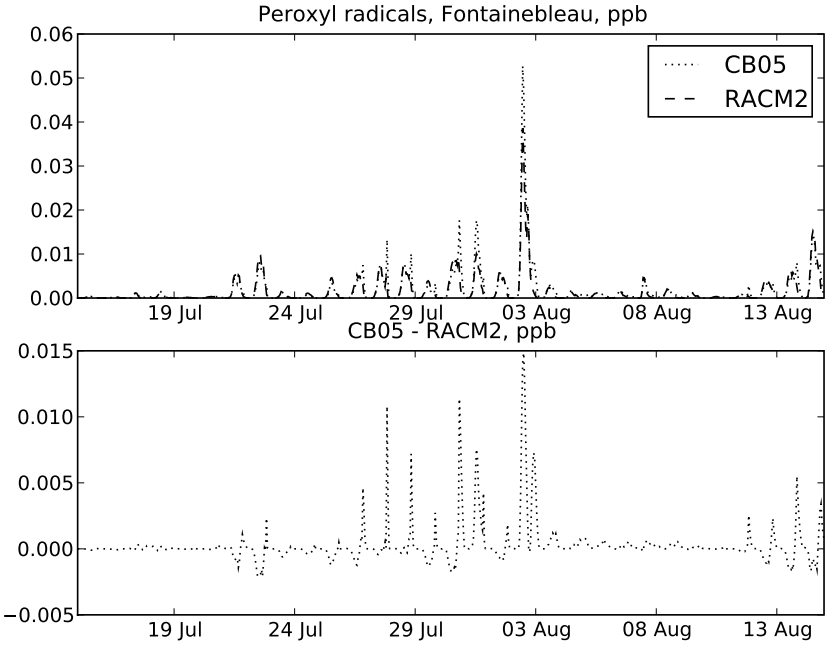

(a) Fontainebleau

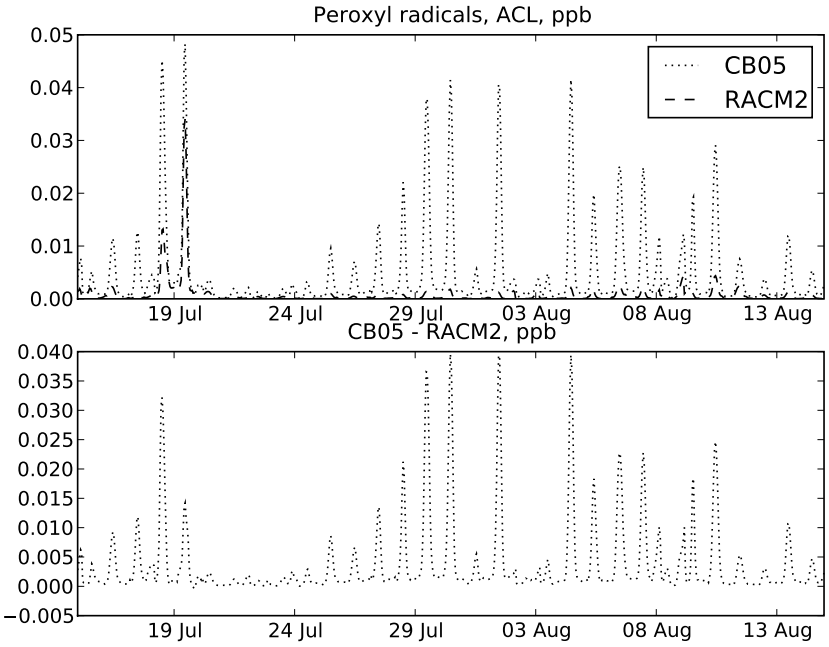

(b) Algerian coastal location

Figure 2.13: Temporal differences of peroxyl radicals between CB05 and RACM2 at Fontainebleau and ACL, WithBioAlkene case

OH.

2.4.2.2 Remote areas

We compare CB05 and RACM2 for the four remote locations indicated in Figure 2.3. Both Fontainebleau and the Algerian coastal location (ACL hereafter) show similar moderate ozone concentrations (61 to 65 ppb); however, the ozone difference between the two mechanisms is high at ACL but low at Fontainebleau. ACL clearly has NO_x-sensitive chemistry but the chemical regime at Fontainebleau is mixed-chemistry. This is due to the transport of NO_x emissions from Paris. For the WithBioAlkene case, the ozone concentration with CB05 is up to 12.5 ppb greater than that with RACM2 at ACL. As mentionned above, this difference due to the biogenic emissions can be explained by the enhancement of the peroxyl radicals in CB05 (average differences between the mechanisms of 2.8×10^{-4} ppb at Fontainebleau, 3.8×10^{-3} ppb at ACL, see Figure 2.13). At the other two locations, Gulf of Taranto and Ligurian Sea, where O_3 concentrations are rather high (> 75 ppb), RACM2 predicts more ozone than CB05 in the Gulf of Taranto but the two mechanisms predict the same ozone concentration in the Ligurian Sea. In the Ligurian Sea, CB05 leads to more ozone formation than RACM2 in the WithAlkane case (5.8 ppb) and WithBioAlkene case (12.2 ppb). On the contrary, RACM2 leads to more ozone formation than CB05 in the WithCO case (2.8 ppb), the WithAromat case (4.4 ppb), and the WithAnthAlkene case (1.8 ppb). These results show that the greater ozone formation from alkanes and biogenic alkenes in CB05 is compensated by the lower ozone formation from the other VOC. However, in the Gulf of Taranto, RACM2 leads to more ozone formation than CB05 and the ozone concentration in RACM2 from the AllEmis case is 4 ppb greater than that in CB05. CB05 leads to more ozone formation than RACM2 in the WithAlkane (2.9 ppb) and the WithBioAlkene (4.2 ppb) cases but RACM2 leads to more ozone formation in the WithCO (2 ppb), the WithAromat (2.8 ppb) and the WithAnthAlkene (0.9 ppb) cases. These results show that the oxidation of the biogenic emissions in the Gulf of Taranto is weaker than in the Ligurian Sea.

Finally, ACL and the Gulf of Taranto where large differences between the two mechanisms are observed, differ by the amount of ozone formation in the WithBioAlkene case (see Figure 2.14). When all emissions are considered, the O_3 concentration is greater with CB05 than with RACM2 (3.5 ppb) at ACL, but it is the opposite (4.4 ppb) at the Gulf of Taranto. There is greater ozone formation with CB05 than with RACM2 at ACL because of higher biogenic emissions (see above for the cause of greater reactivity of biogenic VOC with CB05).

2.4.2.3 Locations with high biogenic emissions

Small differences (0.03 to 1.86 ppb) between the two chemical mechanisms are obtained at the locations where the biogenic emission rates are high (see Figure 2.1c and 2.5). This is due to a strong NO_x-sensitive chemistry in that region. Despite these weak differences, some cases are of interest to analyze. The NoAromat case of Method 1 shows slightly increased O_3 concentration with regard to the AllEmis case only with the CB05 mechanism (0.06 to 0.18 ppb). As we mentioned before, the major product of the oxidation of aromatic chemical compounds in CB05 is cresol. Hence, fewer aromatic compounds cause lower amounts of cresols and allow other VOC to be oxidized by more OH resulting in more ozone formation. For Method 2, ozone concentrations with CB05 are higher than those with RACM2 in the WithAlkane and

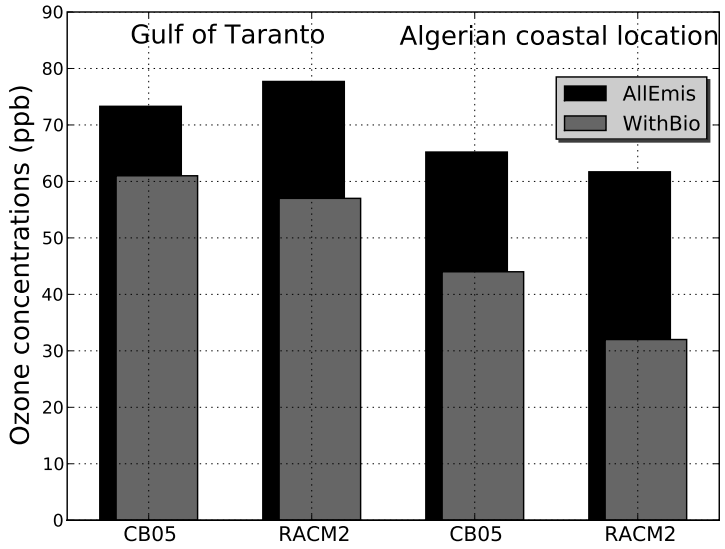

Figure 2.14: Ozone concentrations with WithBioAlkene and AllEmis cases at the Gulf of Taranto and ACL.

the WithBioAlkene cases, similar to what was obtained at the four NO_x-sensitive cities. Figure 2.13 displays differences of 8h-maximum ozone between the two mechanisms at one of these locations.

When only biogenic emissions are considered, i.e., without all anthropogenic VOC and NO_x, the modeled ozone concentrations remain near background levels in any area of the Iberian Peninsula, because the biogenic emission contribution to ozone formation requires interaction with anthropogenic emissions [Castell *et al.*, 2008]. This interaction differs between CB05 and RACM2 in the Iberian Peninsula. In the NoBioAlkene case, the decrease in ozone from the reference case is significantly greater in RACM2 than in CB05. The ozone difference between the two mechanisms does not seem significant in the WithBioAlkene case; although it is comparable in absolute concentration ($\sim$ 1 ppb) to that obtained in the NoBioAlkene case. However, the effect is reversed with RACM2 contributing more ozone when all emissions are considered and CB05 contributing more ozone when only biogenic emissions are considered (see Figure 2.15).

2.5 Conclusion

The comparison of the two chemical mechanisms was conducted by species categories including non-carbonaceous species (i.e., nitrogen and sulfur oxides), CO, alkanes, anthropogenic alkenes, aromatics, aldehydes, alcohols and biogenic VOC. Overall, the two mechanisms show similar ozone spatial patterns and domain-averaged concentrations (difference of only 3 ppb or 5%). This result is consistent with earlier comparisons conducted for other mechanisms where differences ranged from less than 1% to 8%. Significant differences, however, appear at specific locations and/or for specific chemical species categories.

Uncertainties in the kinetics of two key inorganic reactions, $NO + O_3 \longrightarrow NO_2 + O_2$ and

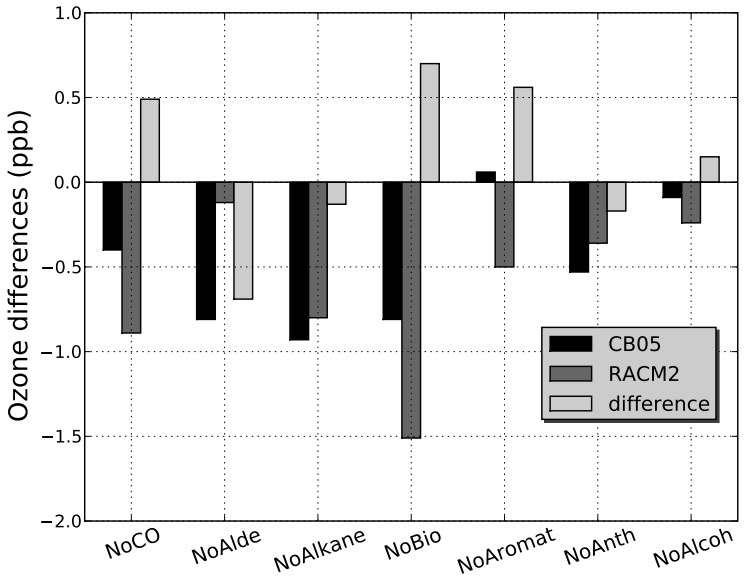

(a) Method 1

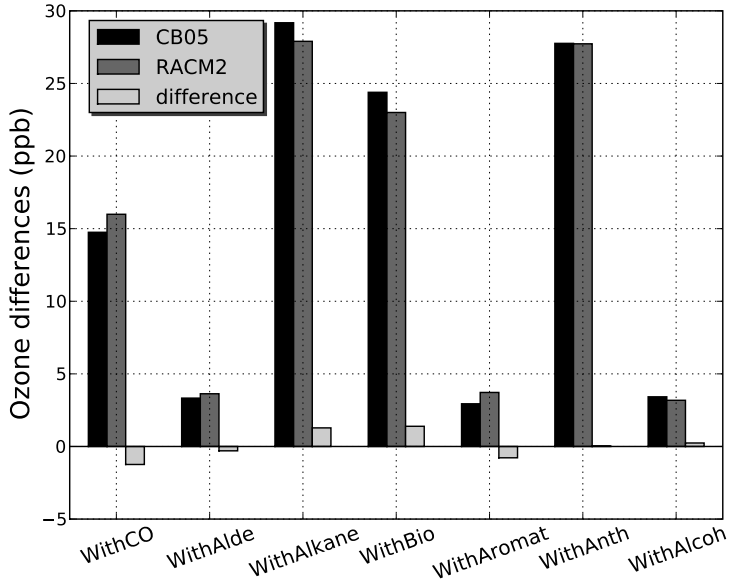

(b) Method 2

Figure 2.15: 8h-maximum ozone differences (ppb) between CB05 and RAMC2 at the Bio 1 location in the Iberian Peninsula.

$NO + HO_2 \longrightarrow NO_2 + OH$, lead to non-negligible differences in oxidant concentrations (mean fractional absolute difference of 5% over the whole domain). When analyzing ozone differences by categories of carbonaceous species (CO and VOC classes), the largest differences occur for CO and aromatics due in part to the large contributions of their emissions to the total inventory. When differences in ozone concentrations are normalized by the corresponding VOC emissions, significant differences appear also due to the chemistry of aldehydes, anthropogenic alkenes and alkanes. Differences in the treatment of biogenics have a significant effect in areas with large biogenic emissions.

Diagnostic analyses lead to the following conclusions. Although the CO chemical kinetics is identical in the two mechanisms, different OH concentrations due to uncertainties in nitrogen chemistry lead to significant differences in ozone formation from CO emissions. Differences in the contribution of aromatics to ozone formation are due mostly to the fact that aromatics oxidation in RACM2 leads to more ring-opening products than in CB05, which favors the formation of aromatic alcohols (e.g., cresol formation from toluene oxidation). The former products being more reactive, RACM2 aromatics chemistry leads to more ozone formation than CB05.

The differences in aldehyde and biogenics chemistry are due to the more detailed treatment in RACM2 where several surrogate molecules are used to characterize the products. The assumptions made in the two mechanisms lead to more reactivity of aldehydes in RACM2 but more reactivity of biogenics in CB05.

Differences in the chemistry of alkanes and anthropogenic alkenes result primarily from the fundamental representations of those VOC categories in the two mechanisms: lumped structure versus lumped molecules. Approximations are necessary in both approaches and they translate into differences in ozone formation. Those differences, however, are not larger than those obtained for other parts of the mechanisms, which suggests that the lumped representations have been optimized to the extent possible.

The results obtained in this comparison of two recent gas-phase chemical mechanisms for ozone formation are encouraging because (1) the differences are small on average and (2) the differences identified for specific chemical categories are due mostly to uncertainties in our knowledge of the chemistry (e.g., kinetics of NO oxidation reactions, relative importance of chemical pathways for aromatics oxidation). Differences in the approximations needed to condense the VOC chemistry (i.e., lumped structures or lumped molecules) do not contribute more to the overall uncertainties than those other factors. Therefore, future improvements in gas-phase chemical kinetic mechanisms will require experimental data to reduce current uncertainties. Those improvements are likely to benefit both lumped-structure and lumped-molecule mechanisms as both appear to be able to represent ozone chemistry satisfactorily.

Chapitre 3

Influence des mécanismes chimiques sur les concentrations de particules fines ($PM_{2.5}$)

Résumé

Nous étudions ici les différences de concentrations des composés minéraux et organiques des particules fines (de diamètre aérodynamique inférieur à 2,5 micromètres, $PM_{2.5}$) simulées avec le modèle de qualité de l'air (MQA) Polair3D/Polyphemus et deux mécanismes chimiques différents (CB05 et RACM2). Les développements dans RACM2 (par rapport à RACM) incluent un nouveau schéma du benzène, la séparation des isomères du xylène (XYO pour o-xylène et XYL pour m-, p-xylène) et des nouvelles photolyses pour le benzaldéhyde et le glyoxal. Dans le schéma du benzène, le phénol est spécifié de manière explicite comme un produit d'oxydation du benzène. Les développements dans CB05 (par rapport à CBM-IV) concernent la chimie du pentoxyde de diazote (N_2O_5). La concentration de N_2O_5 n'a pas un impact fort sur la formation d'ozone, mais elle est importante pour la formation du nitrate en phase particulaire par chimie hétérogène. CB05 comprend deux réactions de N_2O_5 en phase gazeuse avec l'eau : l'une est une réaction bimoléculaire et l'autre est une réaction trimoléculaire. Suite à une recommandation récente de l'IUPAC (International Union of Pure and Applied Chemistry), nous avons exclu la réaction trimoléculaire de CB05 et fixé une limite de $1{,}0\times10^{-22}$ cm^3 molecule^{-1} s^{-1} pour le taux de réaction bimoléculaire dans les deux mécanismes.

Le MQA Polair3D/Polyphemus utilise plusieurs modèles pour simuler la granulométrie et la composition chimique des particlues : le modèle SIREAM pour la granulométrie, le modèle ISORROPIA pour les espèces minérales et le modèle AEC pour les espèces organiques. SIREAM résout l'équation dynamique des particules qui tient compte des processus de nucléation, coagulation, condensation et évaporation. ISORROPIA est un modèle d'équilibre thermodynamique des espèces minérales (sulfate, nitrate, ammonium, sodium, chlore, etc.). AEC est un modèle d'équilibre thermodynamique qui calcule la composition chimique organique des particules ; il distingue les espèces organiques hydrophobes et hydrophiles. Le modèle AEC a été modifié (MAEC) afin de prendre en compte la formation des aérosols organiques secondaires (AOS) due à l'oxydation de l'isoprène, l'oligomérisation et l'influence de composés organiques semi-volatils émis par le trafic routier.

Les mécanismes de chimie gazeuse CB05 et RACM2 ont été modifiés ici pour inclure les précurseurs gazeux des aérosols organiques. La formation des AOS due à l'oxydation du benzène est prise en compte ; cette formation a lieu par oxydation du phénol qui est un produit d'oxydation du benzène. Dans RACM2, l'oxydation du phénol est maintenant modélisée et donc utilisée pour la formation d'AOS phénolique. Le benzène et le phénol ne sont pas explicitement représentés dans CB05, cependant la formation d'AOS phénolique dans CB05 est impliquée par oxydation du crésol. De plus, les deux espèces suppléantes (XYO et XYL) du xylène sont incluses pour la formation des AOS aromatiques. CB05 n'incluant pas d'espèce alcane de faible volatilité, une espèce supplémentaire a été ajoutée pour prendre en compte l'effet des alcanes sur la formation des AOS. L'espèce ajoutée est HC8 de RACM2. MAEC utilise deux précurseurs biogéniques gazeux des AOS (α-pinène API et limonène LIM). Ces précurseurs existent dans RACM2 et ont été ajoutés dans CB05 qui ne comprenait qu'un seul précurseur biogénique gazeux.

Une approche harmonisée a été utilisée lors de la modification des deux mécanismes pour gérer la formation des AOS afin que cette étude cible seulement l'effet du mécanisme de la chimie en phase gazeuse sur la formation des aérosols. En général, le traitement de la formation des AOS dans les MQAs utilise des approches simples, où les composés organiques semi-volatils (COSV) qui peuvent se condenser pour former des AOS sont formés à la première étape d'oxydation des précurseurs. Cependant, pour prendre en compte la formation des COSV par oxydation des composés aromatiques sous différents régimes de NO_x, il a été nécessaire de former des COSV à des étapes d'oxydation ultérieure.

Polyphemus version 1.5 et son MQA Polair3D ont été utilisés pour cette étude. Le domaine du modèle, les niveaux verticaux, la période et les données d'entrée (météorologie, émissions, vitesses de dépôts, etc.) sont identiques à ceux des simulations du chapitre 2 pour l'ozone. En particulier, deux tiers des émissions de monoterpènes ont été allouées à API et un tiers à LIM pour la formation des AOS biogéniques dans CB05 et dans RACM2.

Les différences majeures dans la chimie minérale entre les deux mécanismes sont les cinétiques de l'oxydation de NO par O_3 et HO_2 (voir chapitre 2) qui peuvent modifier les concentrations des oxydants (O_3, OH et NO_3).

La concentration moyenne de sulfate est plus grande dans RACM2 que dans CB05 (15%). L'oxydation du dioxyde de soufre (SO_2) par les radicaux hydroxyles (OH) est le chemin unique pour la formation du sulfate dans la phase gazeuse. L'oxydation de SO_2 avec OH produit l'acide sulfurique qui va se condenser pour former du sulfate en phase particulaire. La différence de concentration de sulfate est due à la différence de concentration de OH (24%). De plus, la cinétique de l'oxydation de SO_2 est plus rapide dans RACM2 que dans CB05 (5%). Le sulfate est formé aussi en phase aqueuse : le SO_2 dissous peut être oxidé par O_3 et/ou le peroxyde d'hydrogène (H_2O_2).

RACM2 produit 11% de plus de nitrate que CB05 en moyenne sur tout le domaine. Les deux mécanismes ne présentent pas de différence importante dans les concentrations de NO_2 (1%). Bien que la cinétique de l'oxydation de NO_2 par OH soit légèrement différente entre les deux mécanismes (3%), l'effet de la cinétique sur la concentration de l'acide nitrique (HNO_3) est faible. En fait, le facteur majeur pour la différence de la formation de HNO_3 est la concentration de l'oxydant OH, comme pour le sulfate.

La formation de nitrate d'ammonium en Europe est principalement limitée par la concentration de HNO_3. Parce que la concentration de HNO_3 est en moyenne plus élevée dans RACM2 que dans CB05, la formation de nitrate d'ammonium est renforcée dans RACM2. La com-

binaison de concentrations plus élévées de sulfate et de HNO_3 dans RACM2 conduit à des concentrations d'ammonium également plus élévées (10%).

Les moyennes mensuelles de concentration des AOS ne sont pas très différentes entre les deux mécanismes. La différence est de 2% en moyenne sur le domaine et la concentration moyenne des AOS dans CB05 est supérieure à celle dans RACM2 de 0,04 $\mu g/m^3$. Localement, le maximum des différences de concentrations entre les deux mécanismes est de 0,6 $\mu g/m^3$ pour des endroits où les concentrations calculées avec CB05 sont plus élevées et de 0,8 $\mu g/m^3$ pour des endroits où les concentrations calculées avec RACM2 sont plus élevées.

CB05 et RACM2 ont les mêmes précurseurs gazeux biogéniques (émissions, conditions initiales, conditions aux limites et cinétiques) pour les monoterpènes. Les concentrations des oxydants (OH, O_3 et NO_3) sont donc les seules différences entre les deux mécanismes pour la formation des monotèrpenes en phase particulaire. RACM2 produit plus d'oxydants que CB05 en moyenne : OH (+24%) et O_3 (+3%). Donc RACM2 est plus favorable à la formation de COSV de monoterpènes hydrophiles (acides monocarboxyliques, BiA1D : 5% et acides dicarboxyliques, BiA2D : 7%). Par contre, la réaction de API avec NO_3 produit un COSV hydrophobe, BiBmP. La concentration de BiBmP est plus grande dans CB05 que dans RACM2 (8%), car la concentration de NO_3 est plus élevée dans CB05 (17%).

La contribution de l'isoprène à la formation des AOS est importante dans les deux mécanismes (environ 25% des AOS sont formés à partir de l'isoprène en moyenne). La cinétique de l'oxydation de l'isoprène avec OH est légèrement plus élevée dans RACM2 que dans CB05 (1%). RACM2 est plus favorable à la formation de COSV d'isoprène (BiISO1 : 6% et BiISO2 : 7%). La différence des concentrations de deux COSV d'isoprène s'explique par les différences de concentrations d'OH entre les deux mécanismes.

La production d'AOS anthropiques est plus importante avec CB05 qu'avec RACM2. Pour les composés aromatiques, les différences dans les produits formés (produits de scission ou produits retenant le cycle aromatique, e.g., crésol) sont la cause principale des différences dans la formation des AOS aromatiques. La concentration du crésol dans RACM2 n'est que 20% de celle obtenue dans CB05. La concentration plus élevée de crésol dans CB05 conduit à des concentrations plus élevées des deux COSV hydrophobes (AnBlP : 9% et AnBmP : 40%) dans CB05. Si la formation des COSV par oxydation du crésol est retirée des deux mécanismes, les différences des concentrations de AnBlP et AnBmP sont beaucoup plus faibles (AnBlP : 3% et AnBmP : 0,3%). Par ailleurs, la concentration moyenne de toluène sur tout le domaine est plus importante avec CB05 qu'avec RACM2 (16%). Lorsque les émissions de COV sont allouées aux espèces du modèle, chaque mécanisme utilise des méthodes différentes pour l'agrégation des COV. L'espèce du modèle, qui représente le toluène, a donc un taux d'émission différent selon le mécanisme (différence de 10%).

Un autre AOS anthropique, PAMGLY, est formé à partir du méthyl-glyoxal (MGLY) en phase aqueuse par oligomérisation. La concentration de PAMGLY ne dépend que de la concentration de MGLY. En effet, le coefficient de la répartition gaz/particule est supposé constant. Comme RACM2 forme plus de MGLY que CB05 (11%), la concentration de PAMGLY dans RACM2 est plus élevée que dans CB05 (20%). Mais les concentrations de PAMGLY sont faibles par rapport à celles des autres AOS anthropiques.

Les concentrations de $PM_{2.5}$ avec les deux mécanismes sont similaires (seulement 6% de différence en moyenne et 15% au maximum). Les différences peuvent être plus élevées pour des composés spécifiques (nitrates, AnBmP et BiBmP). Par ailleurs, la plus grande différence, qui est obtenue pour les AOS anthropiques (oxydation de composés aromatiques), pourrait

être partiellement résolue par la mise à jour de CB05 avec CB05-TU, un mécanisme chimique dans lequel le mécanisme d'oxydation du toluène a été récemment amélioré. La concentration de crésol est plus faible avec CB05-TU qu'avec CB05 d'environ 70%. Ainsi, l'écart dans la formation des AOS aromatiques entre CB05 et RACM2 serait significativement réduit avec CB05-TU.

Les effets d'un mécanisme chimique en phase gazeuse sur les concentrations de SOA peuvent être classés en trois catégories principales : (1) les effets directs qui résultent de la conception du mécanisme et qui conduisent à des rendements différents des précurseurs des AOS (e.g., émissions différentes des précurseurs en raison de l'agrégation des différentes espèces moléculaires des COV en espèces du modèle, cinétiques d'oxydation différentes des COV, coefficients stoechiométriques différents des produits d'oxydation des COV comme les différents rendements du crésol dans RACM2 et CB05), (2) les effets indirects primaires dus aux différentes concentrations des oxydants (OH, O_3 et NO_3) qui affectent le taux d'oxydation des COV et (3) les effets indirects secondaires dus aux interactions entre les composés en phase particulaire (e.g., une augmentation d'un composé d'AOS conduit à une plus grande masse de particules organiques disponibles pour l'absorption supplémentaire des autres AOS). L'amélioration des mécanismes de la chimie de la phase gazeuse permettra de réduire les incertitudes liées aux deux premières catégories de façon directe. L'incertitude liée à la dernière catégorie dépend aussi du modèle d'aérosols, ce qui est étudié dans le chapitre 4

Ce chapitre est constitué de
Kim, Y., Sartelet, K. et Seigneur, C. (2011). **Formation of secondary aerosols over Europe : comparison of two gas-phase chemical mechanisms**, *Atmos. Chem. Phys.*, 11 :583-598.

Sommaire

3.1 Introduction

The contribution of secondary aerosols formed from atmospheric gas-phase species to the total amount of particulate matter (PM) is important in many urban and remote areas [Seinfeld et Pandis, 1998; Finlayson-Pitts et Pitts, Jr., 2000]. In particular, secondary aerosols dominate atmospheric PM in Europe at many monitoring sites [Putaud *et al.*, 2010]. Secondary aerosols consist of inorganic and organic components. The formation of secondary aerosols is due to various physical processes (nucleation, condensation and evaporation) and chemical processes (photochemical gas-phase oxidation leading to the formation of semi-volatile products that may condense onto particles, aqueous-phase oxidation and particulate-phase processes).

Hence the gas-phase chemical mechanisms in air quality models (AQMs) play an important role in modeling aerosol concentrations. Different gas-phase chemical kinetic mechanisms have been developed to represent atmospheric chemistry, ranging from simple (less than ten species) to complex (several thousand species). Condensed mechanisms with 50 to 100 species (e.g., SAPRC [Carter, 2000, 2010], RACM [Stockwell *et al.*, 1997; Goliff et Stockwell, 2008] and carbon-bond mechanisms [Gery *et al.*, 1989; Yarwood *et al.*, 2005]) are typically used in three-dimensional (3-D) AQMs to simulate the evolution of ozone and PM. Condensed mechanisms are classified as lumped structure mechanisms (carbon-bond mechanisms: CB05 and CBM-IV) and lumped species mechanisms (e.g., SAPRC and RACM mechanisms).

Several studies have been carried out to understand the impact of the gas-phase chemical mechanism on the formation of secondary aerosols. Sarwar *et al.* [2008] compared CB05 and CBM-IV for the formation of sulfate, nitrate and secondary organic aerosol (SOA) using the Community Multiscale Air Quality model (CMAQ). Luecken [2008] compared the impact of CB05, CBM-IV and SAPRC99 on $PM_{2.5}$ (particles less than 2.5 μm in aerodynamic diameter) for regulatory applications in the United States. Pan *et al.* [2008] compared CBM-Z, CB05 and SAPRC99 for the formation of inorganic PM using the Weather Research and Forecasting model coupled with Chemistry (WRF/Chem) and the Model of Aerosol Dynamics, Reaction, Ionization, and Dissolution 1 (MADRID 1).

This study focuses on differences in $PM_{2.5}$ concentrations over Europe simulated with two recent chemical mechanisms, a carbon-bond mechanism, CB05, and a lumped species mechanism, RACM2. The gas-phase mechanisms were incorporated within Polair3D, the 3-D AQM of the Polyphemus air-quality platform [Kim *et al.*, 2009]. First, a brief description of the model used in this study is given. Coupling between the aerosol model and the chemical mechanisms is then discussed. Next, the setup of the simulations is described and simulation results are compared to observed data. To analyze the impact of the gas-phase chemical mechanism on PM concentrations, the chemical composition of $PM_{2.5}$ over Europe is presented in the first part of the analysis. Then, mean concentrations of inorganic and organic $PM_{2.5}$ simulated with CB05 and RACM2 are compared over the whole domain for each chemical component. Next, comparisons of the spatial distributions of aerosols are presented. The results are discussed in a diagnostic manner to identify the main causes of the discrepancies.

3.2 Model descriptions

The chemistry transport model Polair3D [Sartelet *et al.*, 2007] of the air-quality platform Polyphemus version 1.6 [Mallet *et al.*, 2007] is used in this study (`http://cerea.enpc.`

`fr/polyphemus`). PM is modeled with SIREAM (SIze REsolved Aerosol Model). SIREAM segregates the particle size distribution into sections and simulates nucleation, coagulation and condensation/evaporation processes [Debry *et al.*, 2007a]. SIREAM is coupled to the thermodynamic model ISORROPIA for inorganic species [Nenes *et al.*, 1998].

3.2.1 SOA module

The SOA Modified AER/EPRI/Caltech module (MAEC) calculates the secondary organic components of particles [Debry *et al.*, 2007b]. MAEC is based on the AEC model of Pun *et al.* [2002, 2006]. Precursors of SOA in the model include anthropogenic compounds (aromatics, long-chain alkanes and long-chain alkenes) and biogenic compounds (isoprene, monoterpenes, and terpenoids). This model includes an explicit treatment of hydrophilic SOA species. As described by Pun *et al.* [2002], condensable oxidation products of VOC are grouped into two categories: hydrophobic compounds, which can be absorbed into organic particles and hydrophilic compounds, which can be absorbed into aqueous particles (typically inorganic particles containing sulfate, ammonium and possibly nitrate). When the relative humidity is very low and no aqueous particles are present, hydrophilic compounds may be absorbed into organic particles. Those condensable oxidation products are represented by a limited number of surrogate SOA species, which are selected to represent the ensemble of possible SOA species. Those surrogate SOA species are selected based on the SOA molecular constituents identified in smog chamber experiments for monoterpene precursors and their physico-chemical properties such as their octanol/water partitioning coefficient (to determine whether they are hydrophobic or hydrophilic), their saturation vapor pressure (for both hydrophobic and hydrophilic SOA species) and their dissociative properties in aqueous solutions (for hydrophilic SOA species) (see Pun *et al.* [2006] for details on the method for selecting SOA surrogates). Because less information on the molecular constituents of SOA is available for products of anthropogenic precursors, the surrogate SOA species were selected based on SOA molecular species derived from a theoretical chemical mechanism of the precursor oxidation (e.g., Griffin *et al.* [2002]).

Table 3.1 summarizes the surrogate SOA species, their precursors, and their physico-chemical properties used in the model. For isoprene, the representation of Zhang *et al.* [2007] was used. Absorption of SOA into organic particles follows Raoult's law and depends on the average molecular weight of the organic particulate mixture, the saturation vapor pressure of the condensing SOA surrogate and its activity coefficient in the particle. Absorption of hydrophilic SOA into aqueous particles follows Henry's law and depends on the liquid water content of the particle, its pH (for mono- and dicarboxylic acids, i.e., BiA1D and BiA2D, respectively) and the activity coefficients of the dissolved species. Activity coefficients of organic compounds are calculated for both the organic phase and the aqueous phase using UNIFAC (see Pun *et al.* [2002] for details regarding the computational implementation of the gas/particle partitioning and activity calculations).

Oligomerization is represented according to the pH-dependent parametrization of Pun et Seigneur [2007], which applies to aqueous-phase oxo-SOA (i.e., BiA0D). In addition, it is assumed that glyoxal and methylglyoxal can oligomerize and thereby contribute to SOA formation; following Pun et Seigneur [2007], empirical gas/particle partitioning coefficients were used to that end (9.1×10^{-6} (µg / µg water) / (µg / m^3 air) for glyoxal and 5.6×10^{-12} (µg / µg water) / (µg / m^3 air) for methylglyoxal).

A major difference with previous work is the NO_x-dependency for SOA formation from

Table 3.1: Surrogate SOA compounds, their corresponding precursors and their physico-chemical properties.

Precursors	Surrogate SOA species[a]	Molecular weight (g/mole)	Saturation vapor pressure (Pa)	Henry's law constant[b] ((μg/μg water) / (μg/m^3 air))	Enthalpy of vaporization (kJ/mole)
Anthropogenic compounds (aromatics, long-chain alkanes and alkenes)	AnBmP	152	4.0×10^{-4}	NA	88
	AnBlP	167	2.7×10^{-7}	NA	88
	AnClP	167	2.7×10^{-7}	NA	88
Biogenic compounds (monoterpenes and terpenoids)	BiA0D	168	3.6×10^{-2}	4.82×10^{-5}	88
	BiA1D	170	2.9×10^{-5}	2.73×10^{-3}	88
	BiA2D	186	1.9×10^{-5}	6.25×10^{-3}	109
	BiBmP	236	4.0×10^{-5}	NA	175

(a) The SOA surrogate nomenclature is as follows. First two letters: An = anthropogenic, Bi = biogenic; third letter: A = hydrophilic, B: hydrophobic, C: hydrophobic formed under low-NO_x conditions (see text); last two characters: 2D = twice dissociative, 1D = once dissociative, 0D = non-dissociative for hydrophilic compounds; lP = low saturation vapor pressure, mP = moderate saturation vapor pressure for hydrophobic compounds.
(b) NA: not applicable for hydrophobic compounds.

aromatic compounds. Ng *et al.* [2007b] showed that the SOA yields from aromatic oxidation were greater under low-NO_x conditions than under high-NO_x conditions. Accordingly, different yields are used for SOA formation under those different regimes with two surrogates being used for the high-NO_x regimes (AnBmP and AnBlP) and one surrogate being used for the low-NO_x regime (AnClP). To properly account for different yields for different NO_x regimes, SOA formation is not treated as a product of the first oxidation step of the VOC precursor, but instead it is treated in later oxidation steps as discussed in Section 3.2.2.

3.2.2 Chemical kinetic mechanisms

RACM2 [Goliff et Stockwell, 2008, 2010] is a recent mechanism developed via various improvements in RACM [Stockwell *et al.*, 1997]. Recent developments in RACM2 related to aerosol formation concern the benzene scheme, separation of xylene isomers (XYO for o-xylene and XYL for m- and p-xylene) and glyoxal photolysis. For the benzene scheme, phenol is now explicitly speciated as a product of benzene oxidation [Goliff et Stockwell, 2010]. This speciation of phenol is important because the oxidation of phenol leads to the formation of aromatic compounds, which are SOA precursors [Pun et Seigneur, 2007].

CB05 [Yarwood *et al.*, 2005] is an updated version of CBM-IV [Gery *et al.*, 1989]. In CB05, most organic compounds are divided into smaller species elements based on the bond types of their carbon atoms.

Kim *et al.* [2009] studied the impact of using either CB05 or RACM2 on the chemistry of ozone formation over Europe. This work focuses on aerosol formation. To couple the chemical

kinetic mechanisms with the aerosol module MAEC, gas-phase organic precursors of SOA in CB05 and RACM2 were modified or added as described in Section 3.2.3.

Furthermore, the dinitrogen pentoxide (N_2O_5) chemistry in CB05 was modified. The concentration of N_2O_5 does not strongly impact ozone formation chemistry, but it is important for the formation of particulate nitrate via heterogeneous chemistry [Jacob, 2000]. CB05 involves two gas-phase reactions of N_2O_5 with water; one is a bimolecular reaction and the other is a termolecular reaction. Following the recent recommendation of IUPAC (International Union of Pure and Applied Chemistry), we excluded the termolecular reaction from CB05 and set an upper limit of 1.0×10^{-22} cm^3 molecule^{-1} s^{-1} for the bimolecular reaction rate coefficient in the two mechanisms (`www.iupac-kinetic.ch.cam.ac.uk`).

3.2.3 SOA formation in CB05 and RACM2

As organic gases are oxidized in the gas phase by hydroxyl radicals (OH), ozone (O_3) and nitrate radicals (NO_3), their volatility evolves. Their volatility may decrease by the addition of polar functional groups (such as hydroxyl, hydroperoxyl, nitrate and acid groups). On the other hand, oxidation products may have higher volatility than the parent organic gases due to the cleavage of carbon-carbon bonds. Products of low volatility may condense on the available particles to establish equilibrium between the gas and particle phases. There are four types of gas-phase organic precursors treated in MAEC: aromatics, long-chain alkanes, long-chain anthropogenic alkenes and biogenic alkenes. These precursors are consistent with the RACM2 species because MAEC was originally developed in conjuction with RACM [Debry *et al.*, 2007b]. However, some of these precursors are not available in CB05 and it is necessary to add them to make CB05 compatible with MAEC. These additions are made in such a way that they do not affect CB05 for oxidant formation. Table 3.2 summarizes the gas-phase organic precursors for CB05 and RACM2. The gas-phase organic precursors are oxidized to form Semi-Volatile Organic Compound (SVOC), which may condense onto particles.

For aromatic precursors, RACM2 includes two surrogates (XYO, XYL) for xylenes, whereas CB05 includes only one surrogate (XYL) for all xylene isomers. Phenol is explicitly modeled in RACM2 with the PHEN surrogate species. The two mechanisms have the same precursors for toluene and cresols. RACM2 represents long-chain alkane precursors with the HC8 surrogate species, which represents alkanes with an OH rate constant greater than 6.8×10^{-12} cm^3 molecule^{-1} s^{-1}. CB05 does not explicitly include any alkane surrogate to form SOA because alkane species are decomposed into PAR elements, which is the single carbon-bond

Table 3.2: Gas-phase organic precursors in the two mechanisms.

Precursor type	RACM2	CB05
Aromatics	TOL, XYL, XYO, CSL, PHEN	TOL, XYL, CRES
Alkanes	HC8	HC8*
Anthropogenic alkenes	OLT, OLI	OLE, IOLE
Biogenic alkenes	API, LIM, ISO	API*, LIM*, ISOP

*: added surrogates

surrogate. Therefore, it is necessary to add a supplementary species to take into account the effect of alkanes on SOA formation in CB05. Here, we add the HC8 surrogate of RACM2 to the CB05 mechanism. The two mechanisms have the same anthropogenic alkene precursors, but biogenic alkene precursors differ. Monoterpenes are represented with two species, API (α-pinenes and other cyclic terpenes with one double bond) and LIM (d-limonene and other cyclic diene-terpenes), in RACM2 but only one species, TERP, in CB05. Because MAEC was developed originally using surrogate species of RACM [Debry *et al.*, 2007b], biogenic SOA are formed from the two species API and LIM. To have a similar treatment of SOA formation by monoterpenes in CB05, API and LIM are added to CB05 for biogenic SOA formation, in parallel to TERP, which is used solely for the gas-phase chemistry.

Tables 3.3a and 3.3b present the toluene and xylene oxidation chemistry, respectively, for SVOC formation in CB05 and RACM2. For toluene and xylene, we differentiate the oxidation under low-NO_x and high-NO_x conditions. Under low-NO_x conditions, SVOC are formed from the oxidation of peroxy radicals formed from toluene or xylenes by HO_2, methyl-peroxy radical or higher peroxy radical surrogates (carbon number ≥ 2), whereas under high-NO_x conditions, SVOC are formed from the oxidation of those toluene or xylene peroxy radicals with NO and NO_3. New reactions to model the formation of SVOC by the oxidation of toluene and xylene peroxy radicals are added to both CB05 and RACM2. In these reactions, the oxidants are also added as product of the reactions, so that oxidant formation is not affected by SVOC formation.

The SVOC formation chemistry for other aromatic precursors (cresol and phenol) is similar between CB05 and RACM2 even though only RACM2 explicitly includes phenol. We assume that the yield of SVOC from phenol is analogous to the yield of SVOC from cresol [Pun et Seigneur, 2007]. Table 3.3c presents the cresol and phenol oxidation chemistry.

Table 3.3a: Toluene oxidation chemistry for SVOC formation.

RACM2	CB05
TOL + HO $\rightarrow$ 0.25 TOLPAEC* + other products	TOL + OH $\rightarrow$ 0.25 TOLPAEC* + other products
TOLPAEC + HO2 $\rightarrow$ 0.78 AnClP + HO2** †	TOLPAEC + HO2 $\rightarrow$ 0.78 AnClP + HO2** †
TOLPAEC + MO2 $\rightarrow$ 0.78 AnClP + MO2** †	TOLPAEC + MEO2 $\rightarrow$ 0.78 AnClP + MEO2** †
TOLPAEC + ACO3 $\rightarrow$ 0.78 AnClP + ACO3** †	TOLPAEC + C2O3 $\rightarrow$ 0.78 AnClP + C2O3** †
TOLPAEC + NO $\rightarrow$ 0.053 AnBlP + 0.336 AnBmP + NO** †	TOLPAEC + NO $\rightarrow$ 0.053 AnBlP + 0.336 AnBmP + NO** †
TOLPAEC + NO3 $\rightarrow$ 0.053 AnBlP + 0.336 AnBmP + NO3** †	TOLPAEC + NO3 $\rightarrow$ 0.053 AnBlP + 0.336 AnBmP + NO3** †

*: new peroxy radical formed from toluene, **: oxidant species added as a product to retain the original gas-phase mechanism, †: new reactions added to both RACM2 and CB05 mechanisms for the SVOC formation.

Table 3.3b: Xylenes oxidation chemistry for SVOC formation.

RACM2	CB05
XYL + HO → 0.274 XYLPAEC* + other products	XYL + OH → 0.274 XYLPAEC* + other products
XYLPAEC + HO2 → 0.71 AnClP + HO2** †	XYLPAEC + HO2 → 0.71 AnClP + HO2** †
XYLPAEC + MO2 → 0.71 AnClP + MO2** †	XYLPAEC + MEO2 → 0.71 AnClP + MEO2** †
XYLPAEC + ACO3 → 0.71 AnClP + ACO3** †	XYLPAEC + C2O3 → 0.71 AnClP + C2O3** †
XYLPAEC + NO → 0.023 AnBlP + 0.32 AnBmP + NO** †	XYLPAEC + NO → 0.023 AnBlP + 0.32 AnBmP + NO** †
XYLPAEC + NO3 → 0.023 AnBlP + 0.32 AnBmP + NO3** †	XYLPAEC + NO3 → 0.023 AnBlP + 0.32 AnBmP + NO3** †
XYO + HO → 0.274 XYOPAEC* + other products	
XYOPAEC + HO2 → 0.71 AnClP + HO2** †	
XYOPAEC + MO2 → 0.71 AnClP + MO2** †	
XYOPAEC + ACO3 → 0.71 AnClP + ACO3** †	
XYOPAEC + NO → 0.023 AnBlP + 0.32 AnBmP + NO** †	
XYOPAEC + NO3 → 0.023 AnBlP + 0.32 AnBmP + NO3** †	

*: new peroxy radicals formed from xylenes. **, †: see Table 3.3a.

For long-chain alkanes and anthropogenic alkenes, the two mechanisms have the same oxidation chemistry. Table 3.3d presents the long-chain alkane and anthropogenic alkene oxidation chemistry.

The oxidation chemistry of biogenic alkenes (monoterpenes and isoprene) is presented in Table 3.3e. As mentioned above, the monoterpene surrogates API and LIM of RACM2 were added to CB05, as well as the reactions in which they are involved for the SVOC formation. In these reactions, the oxidants are also added as products of the reactions, so that the original gas-phase mechanism is not affected by SVOC formation.

Table 3.3c: Cresol and phenol oxidation chemistry for SVOC formation.

RACM2	CB05
CSL* + HO → 0.014 AnBlP + 0.09 AnBmP + other products	CRES* + OH → 0.014 AnBlP + 0.09 AnBmP + other products
CSL + NO3 → 0.04 AnBlP + 0.12 AnBmP + other products	CRES + NO3 → 0.04 AnBlP + 0.12 AnBmP + other products
PHEN + HO → 0.014 AnBlP + 0.09 AnBmP + other products	
PHEN + NO3 → 0.04 AnBlP + 0.12 AnBmP + other products	

*: CSL (cresol and other hydroxy substituted aromatics except phenols), CRES (cresol and higher molecular weight phenols)

Table 3.3d: Long-chain alkane and anthropogenic alkene oxidation chemistry for SVOC formation.

RACM2	CB05
HC8* + HO → 0.048 AnBlP + other products	HC8*** + OH → 0.048 AnBlP + OH** †
OLT* + HO → 0.0016 AnBlP + other products	OLE* + OH → 0.0016 AnBlP + other products
OLT + O3 → 0.0016 AnBlP + other products	OLE + O3 → 0.0016 AnBlP + other products
OLT + NO3 → 0.0016 AnBlP + other products	OLE + NO3 → 0.0016 AnBlP + other products
OLI* + HO → 0.003 AnBlP + other products	IOLE* + OH → 0.003 AnBlP + other products
OLI + O3 → 0.003 AnBlP + other products	IOLE + O3 → 0.003 AnBlP + other products
OLI + NO3 → 0.003 AnBlP + other products	IOLE + NO3 → 0.003 AnBlP + other products

*: HC8 (surrogate for long-chain alkanes), OLT and OLE (surrogate for terminal alkenes), OLI and IOLE (surrogate for internal alkenes). **, †: see Table 3.3a. ***: new species added to the CB05 mechanism for the SVOC formation.

3.3 Description of the simulations

3.3.1 Modeling domain and setup

The modeling domain covers western and part of eastern Europe with a horizontal resolution of $0.5^\circ \times 0.5^\circ$. Detailed descriptions of the modeling domain and setup are found in Kim *et al.* [2009] and Sartelet *et al.* [2007]. The simulations are carried out for one month from 15 July to 15 August 2001. Meteorological inputs are obtained from a reanalysis provided by the European Centre for Medium-Range Weather Forecasts (ECMWF). Anthropogenic emissions of gases and PM were generated with the European Monitoring and Evaluation Programme (EMEP) inventory for 2001. NMHC (non-methane hydrocarbons) are disaggregated

Table 3.3e: Biogenic alkene oxidation chemistry for SVOC formation.

RACM2	CB05
API* + HO → 0.164 BiA0D + 0.117 BiA1D + 0.076 BiA2D + other products	API*** + OH → 0.164 BiA0D + 0.117 BiA1D + 0.076 BiA2D + OH** †
API + NO3 → 0.8 BiBmP + other products	API + NO3 → 0.8 BiBmP + NO3** †
API + O3 → 0.127 BiA0D + 0.142 BiA1D + 0.044 BiA2D + other products	API + O3 → 0.127 BiA0D + 0.142 BiA1D + 0.044 BiA2D + O3** †
LIM* + HO → 0.407 BiA0D + 0.173 BiA1D + 0.003 BiA2D + 0.024 BiBmP + other products	LIM*** + OH → 0.407 BiA0D + 0.173 BiA1D + 0.003 BiA2D + 0.024 BiBmP + OH** †
LIM + NO3 → 0.309 BiA0D + 0.02 BiA1D + other products	LIM + NO3 → 0.309 BiA0D + 0.02 BiA1D + NO3** †
LIM + O3 → 0.197 BiA0D + 0.094 BiA1D + other products	LIM + O3 → 0.197 BiA0D + 0.094 BiA1D + O3** †
ISO + HO → 0.232 BiISO1 + 0.0288 BiISO2 + other products	ISOP + OH → 0.232 BiISO1 + 0.0288 BiISO2 + other products

*: API (surrogate for alpha-pinene and other cyclic terpenes with one double bond), LIM (surrogate for d-limonene and other cyclic diene-terpenes). **, †: see Table 3.3a. ***: see Table 3.3d.

into molecular species following Passant [2002]. The re-aggregation into model species is done following Carter's speciation database for both CB05 and RACM2 [Carter, 2008]. As mentioned in Section 3.2.3, HC8, API and LIM were added to CB05 as model species for SVOC formation. Therefore, the speciation database of RACM2 is used to generate the emissions of HC8, API and LIM in CB05. For anthropogenic PM, the EMEP inventory provides yearly emissions of $PM_{2.5}$ and PM_{coarse}. These raw data are temporally, chemically and granulometrically distributed. PM_{coarse} is totally attributed to mineral dust and $PM_{2.5}$ is speciated into black carbon (20%), mineral dust (35%) and primary organic aerosol (POA, 45%). Gas-phase biogenic emissions are computed as in Simpson *et al.* [1999]. Two-thirds of monoterpene emissions are allocated to API and one-third to LIM in RACM2. In CB05, all monoterpenes are allocated to model species TERP for the original gas-phase mechanism whereas the allocation using API and LIM is also used for SVOC formation. Sea-salt emissions are included in fine and coarse particles. The parametrization of Monahan *et al.* [1986] for indirect generation by bubbles is used. This parametrization is valid for diameters larger than 1.6 µm. The rate of sea-salt generation is assumed to be zero for diameters lower than 1.6 µm. The distribution of sea-salt emission between the different particulate sections is done by integrating the dry rate of sea-salt generation for mass between the section bounds. By assuming that the wet radius at 80% humidity is about 2 times the dry radius of particles [Gerber, 1985], 76% of sea-salt are emitted in our last section (2.5119 to 10 µm) and 28% in the section (0.6310 to 2.5119 µm). Following Seinfeld et Pandis [1998], sea-salt emissions are assumed to be made of 30.61%

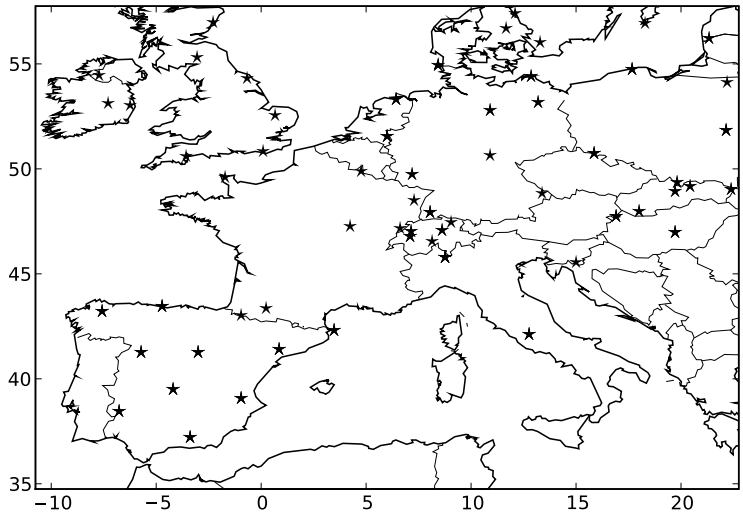

Figure 3.1: Locations of the EMEP observation stations for PM.

sodium, 55.04% chloride and 7.68% sulfate. For gaseous boundary conditions, daily means are extracted from outputs of the global chemistry-transport model MOZART2 run over a typical year [Horowitz *et al.*, 2003]. For PM boundary conditions, daily means are based on outputs of the Goddard Chemistry Aerosol Radiation and Transport (GOCART) model for sulfate, dust, black carbon, organic carbon and sea salt [Chin *et al.*, 2000].

3.3.2 Comparisons to observations

We compared the results obtained by the simulations to observed data provided by the EMEP database. For O_3, comparisons to data can be found in Kim *et al.* [2009]. The EMEP database also provides observed data of PM_{10}, $PM_{2.5}$ and inorganic particulate species (sulfate, nitrate and ammonium) for the year 2001. The observations are given only as 24-hour averages (hourly observations are not available for 2001). Figure 3.1 displays the locations of the observation stations. Details on the measurement are available at `http://www.emep.int`.

To evaluate PM modeling, Boylan et Russell [2006] suggested to use the mean fractional bias (MFB) and the mean fractional error (MFE) defined, respectively, by

$$\mathrm{MFB} = \frac{1}{n}\sum_{i=1}^{n}\frac{c_\mathrm{i} - o_\mathrm{i}}{(c_\mathrm{i} + o_\mathrm{i})/2} \tag{3.1}$$

$$\mathrm{MFE} = \frac{1}{n}\sum_{i=1}^{n}\frac{\mid c_\mathrm{i} - o_\mathrm{i} \mid}{(c_\mathrm{i} + o_\mathrm{i})/2} \tag{3.2}$$

They proposed model performance goals (the level of accuracy that is considered to be close to the best a model can be expected to achieve) and criteria (the level of accuracy that is considered

to be acceptable for modeling applications) using the MFB and the MFE. For major components of PM, the model performance goal is met when both the MFB and the MFE are less than or equal to $\pm$ 30% and + 50%, respectively, and the model performance criterion is met when the MFB and the MFE are less than or equal to $\pm$ 60% and + 75%, respectively. Table 3.4 summarizes the statistics obtained in the comparisons of modeled concentrations to observed data from the EMEP database. The nitrate results show the largest bias and error for both CB05 and RACM2.

The model performance goal for PM_{10} values obtained by the simulation using RACM2 is met at 17 stations among 26 stations and the model performance criterion is not met at only 6 stations. Similarly, the model performance goal for PM_{10} values obtained by the simulation using CB05 is met at 16 stations among 26 stations. The model performance criterion is mostly not met at the stations located in Spain, where the model underpredicts for both CB05 and RACM2.

Better results were obtained for $PM_{2.5}$ than for PM_{10}. The model performance goal, for both CB05 and RACM2, is met at 11 stations among 17 stations and the model performance criterion is met at all stations. Again, lower performance is obtained at the stations in Spain.

For sulfate, 24 stations and 30 stations among 54 stations meet the model performance goal for CB05 and RACM2, respectively. Only 9 stations for CB05 and 7 stations for RACM2 are out of the model performance criterion. For ammonium, better model performance is obtained than for sulfate. Six among 9 stations meet the model performance goal for both CB05 and RACM2. For nitrate, the goal is met at only 4 stations out of 14 stations for both CB05 and RACM2. However, the model performance criterion is not met at only 3 stations with CB05 and 6 stations with RACM2.

When averaged over all stations (see Table 3.4), the performance goal is met for all species

Table 3.4: Comparison of modeled concentrations to observations from the EMEP database ($\mu g/m^3$).

	Stations	Observation* †	Chemical mechanism	Modeled data* †	MFB*	MFE*
PM_{10}	26	18.9	CB05	14.0	-27%	41%
			RACM2	14.8	-22%	40%
$PM_{2.5}$	17	13.6	CB05	12.7	-12%	39%
			RACM2	13.5	-7%	39%
Sulfate	54	2.9	CB05	2.5	-0.1%	45%
			RACM2	2.8	1%	45%
Nitrate	14	1.6	CB05	2.4	0%	73%
			RACM2	2.7	11%	72%
Ammonium	9	1.6	CB05	1.8	10%	43%
			RACM2	2.0	19%	45%

*: mean values over all stations, †: monthly-mean concentrations

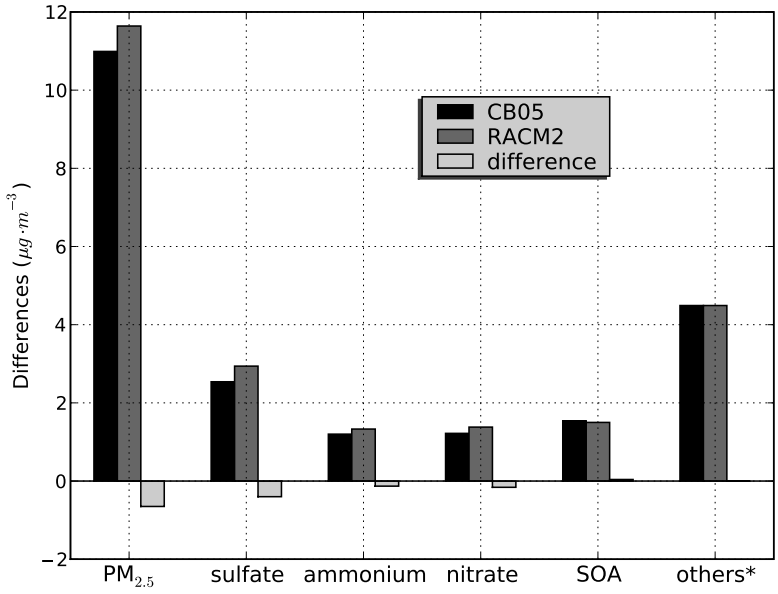

Figure 3.2: Domain-averaged differences of the concentrations of $PM_{2.5}$ and $PM_{2.5}$ chemical components between the two mechanisms, CB05 and RACM2. *: mineral dust, black carbon, sea salts and primary organic aerosol.

except nitrate, for which the performance criterion is met. These results are consistent with PM model performance obtained in previous studies [Zhang *et al.*, 2006; Bailey *et al.*, 2007; Russell, 2008] and are, therefore, considered to be satisfactory.

3.4 Results

The averaged concentration of $PM_{2.5}$ over the domain is slightly higher with RACM2 than with CB05 (difference < 1 µg/m^3, 6%). Figure 3.2 displays domain-averaged differences of the concentrations of $PM_{2.5}$ and $PM_{2.5}$ chemical components between the two mechanisms. The concentration of inorganic $PM_{2.5}$ is higher for RACM2 than for CB05 (+16% of sulfate, +10% of ammonium and +11% of nitrate), whereas the concentration of SOA is slightly higher for CB05 than for RACM2 (+2%). The concentrations of mineral dust and POA remain unchanged when using CB05 or RACM2. Before studying the impact of using CB05 or RACM2 on particulate chemical components, we discuss the $PM_{2.5}$ chemical composition over Europe.

3.4.1 $PM_{2.5}$ chemical composition

Accurate measurements of aerosol chemical composition remain challenging. Inorganic species may be accurately measured with an uncertainty of about $\pm$ 10% for major species [Putaud *et al.*, 2000], except in case where significant artifacts occur for nitrate and ammonium (e.g., under warm conditions) [Hering et Cass, 1999; Keck et Wittmaack, 2005]. However, mea-

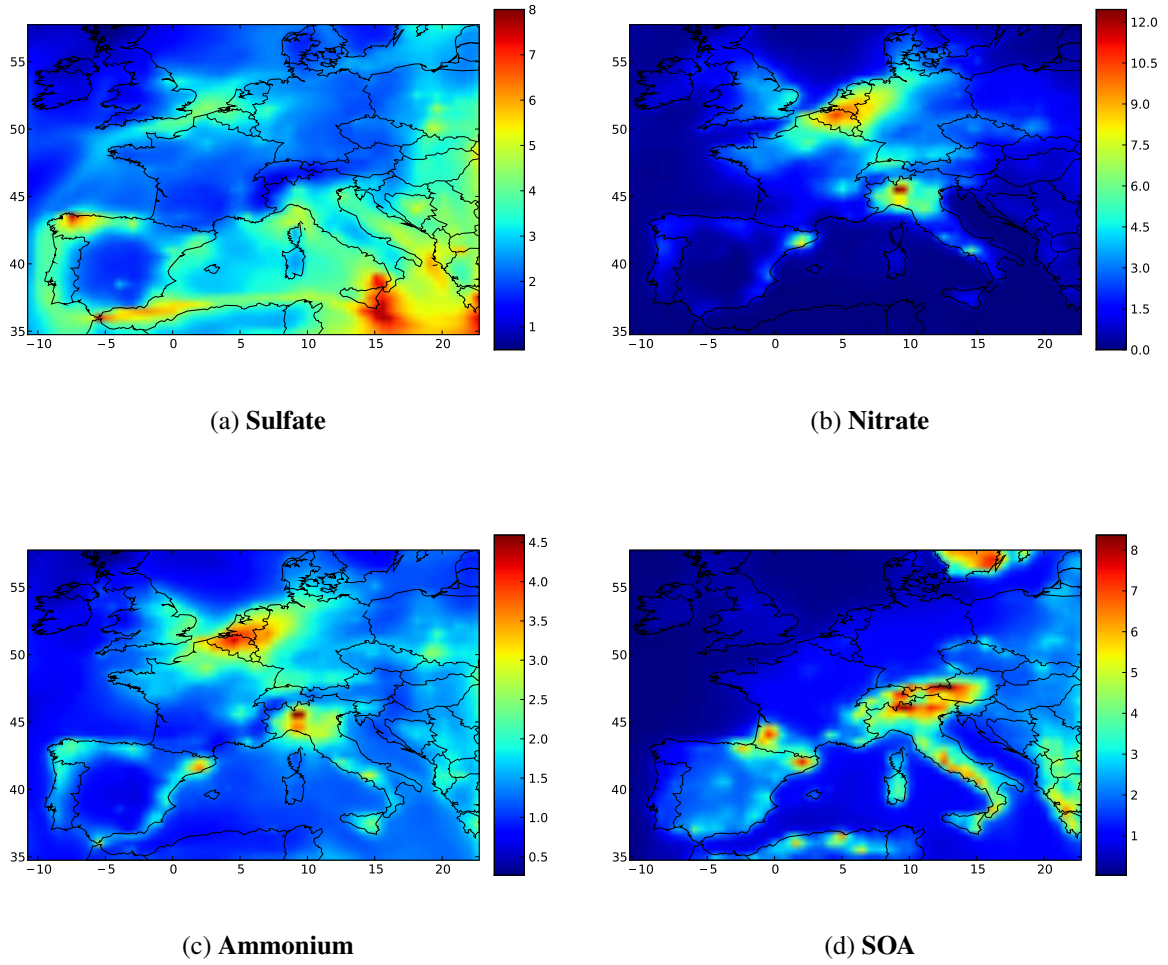

(a) **Sulfate** (b) **Nitrate**

(c) **Ammonium** (d) **SOA**

Figure 3.3: Contributions ($\mu g/m^3$) of secondary chemical components to $PM_{2.5}$ over Europe: (a) sulfate, (b) nitrate, (c) ammonium, (d) SOA.

surements of organic carbon and black carbon concentrations in particles may vary from an instrumental method to another. As a result, the uncertainties in black carbon may be on the order of a factor of two and those in organic carbon can be about 20% [Chow *et al.*, 2001].

In our study, $PM_{2.5}$ is composed on average of sulfate (25%), mineral dust (17%), nitrate (12%), SOA (13%), ammonium (11%), chloride (10%), sodium (7%), black carbon (2%) and POA (3%). Figure 3.3 presents the contributions of secondary chemical components to $PM_{2.5}$ over Europe using RACM2. Results obtained using CB05 are not significantly different.

Sulfate is a dominant component of $PM_{2.5}$ in marine regions. This is partly due to direct emissions of sea-salt and to the oxidation of SO_2 from ship emissions. Nitrate and ammonium are mostly formed over land in northern Europe, where emissions of NH_3 and NO_x are the largest. Ammonium is also formed over marine regions because it neutralizes particulate sulfate. Anthropogenic organic aerosols are mostly formed in large urban regions, whereas biogenic organic aerosols are formed where emissions of monoterpenes are high (northern Africa,

Austria, southwestern France and Sweden) or where emissions of isoprene are high (Spain, Italy and eastern Europe).

3.4.2 $PM_{2.5}$ differences by species

Differences in PM concentrations between CB05 and RACM2 are mostly due to differences in oxidant concentrations. Differences in concentrations of OH and NO_3 between CB05 and RACM2 are partly due to differences in the organic chemistry formulation but also to different kinetics of oxidation of NO [Kim *et al.*, 2009]. The kinetics of oxidation of NO + $O_3 \rightarrow NO_2$ is higher in CB05 than in RACM2, whereas the kinetics of oxidation of NO + $HO_2 \rightarrow NO_2$ + OH is higher in RACM2 than in CB05. Over the entire domain, OH and O_3 concentrations are on average higher with RACM2 (OH: 24% and O_3: 3%) but the average NO_3 concentration is higher with CB05 (17%).

3.4.2.1 Inorganic aerosols

The mean concentration of sulfate is higher in RACM2 than in CB05 (16%). Sulfate is formed in both the gas phase and the aqueous phase. In the gas phase, the oxidation of SO_2 by the hydroxyl radical (OH) produces sulfuric acid, which condenses to form sulfate. Because the mean concentration of OH is 24% higher in RACM2, and the kinetics of the oxidation of SO_2 is greater in RACM2 than in CB05 by 5%, the concentration of sulfate is higher in RACM2. In the aqueous phase, it is not easy to diagnose whether RACM2 or CB05 would produce more sulfate. The oxidation of SO_2 by ozone and/or hydrogen peroxide (H_2O_2) produces sulfate. O_3 is higher on average in RACM2 than CB05 (3%), whereas H_2O_2 is higher in CB05 than in RACM2 (13%). The modeling results show that gas-phase SO_2 oxidation dominates sulfate formation here.

The nitrate concentration over the entire domain is 11% higher with RACM2 than CB05. Differences in nitrate concentrations are due to differences in HNO_3 concentrations, which may condense to form nitrate. HNO_3 is produced in the gas phase, the aqueous phase, as well as heterogeneously on particle and droplet surfaces. The following gas-phase reaction is the dominant daytime source:

$$NO_2 + OH \rightarrow HNO_3 \tag{3.3}$$

and the main nighttime sources are the NO_3 and N_2O_5 heterogeneous reactions:

$$NO_3 + NO_2 \rightarrow N_2O_5 \tag{3.4}$$

$$N_2O_5 + H_2O \rightarrow 2HNO_3 \tag{3.5}$$

$$NO_3 + H_2O \rightarrow HNO_3 + OH \tag{3.6}$$

Differences in the production of HNO_3 from the oxidation of NO_2 by OH are mostly due to differences in OH concentrations, because the concentration of NO_2 is similar in RACM2 and CB05 (average difference 1%). The difference in the kinetics of the oxidation of NO_2 by OH between the two mechanisms is small (3%). The formation of HNO_3 by heterogeneous reactions is higher with CB05 because of the higher concentration of NO_3 (17%). However, the contribution of the heterogeneous reactions to the formation of HNO_3 is not significant (3% only) compared to the gas-phase formation in this study.

Ammonium is produced by the condensation of NH_3 on particles, mostly via neutralization of sulfate and formation of ammonium nitrate. As shown in Sartelet *et al.* [2007], ammonium nitrate formation over Europe is limited by the formation of HNO_3. Because the HNO_3 concentration is higher on average in RACM2 than in CB05, the ammonium nitrate formation is enhanced in RACM2. The combination of higher sulfate and HNO_3 concentrations leads to higher ammonium concentrations with RACM2 (+10%).

3.4.2.2 Secondary organic aerosols

Monthly-mean concentrations of SOA are not considerably different between the two mechanisms. The mean difference is 2% over the entire domain and the average value of the concentration of SOA in CB05 is higher than in RACM2 by only 0.04 $\mu g/m^3$. The maximum of the local differences between the two mechanisms is 0.6 $\mu g/m^3$ at locations where SOA concentrations predicted by CB05 are higher and 0.8 $\mu g/m^3$ at locations where SOA concentrations predicted by RACM2 are higher.

CB05 and RACM2 have the same emissions and photochemical reaction rates of gaseous biogenic VOC for monoterpenes (see Section 3.2.3). Therefore, differences in the particulate phase for monoterpenes come from differences in the concentrations of oxidants (OH, O_3 and NO_3). RACM2 produces more OH (24%) and O_3 (3%) than CB05 whereas CB05 produces more NO_3 (17%) than RACM2. Because the formation of the hydrophilic monoterpene SVOC depends on OH and O_3, their concentration is mostly higher in RACM2 than in CB05 (BiA1D: 5% and BiA2D: 7%). The concentration of BiA0D is higher in CB05 than in RACM2. The reaction of LIM with NO_3 is the main reaction for the formation of BiA0D at nighttime. The higher concentration of NO_3 in CB05 leads to the higher concentration of BiA0D in CB05. However, the concentration of BiAOD is very low compared to those of BiA1D and BiA2D. The reaction of API with NO_3 produces a hydrophobic monoterpene SVOC: BiBmP. The concentration of BiBmP is higher in CB05 than in RACM2 (8%), because of the higher NO_3 concentration in CB05.

The contribution of isoprene to the formation of SOA is important in both mechanisms (about 25% of the monthly-mean concentration of SOA). The kinetics of the isoprene oxidation by OH is almost the same in RACM2 and in CB05 (1% difference). Therefore, the difference in OH concentrations is the main cause of the difference in isoprene SOA concentrations in the particulate phase. RACM2 is more conducive to the formation of isoprene SVOC than CB05 (differences for BiISO1: 6% and BiISO2: 7%) because of higher concentration of OH (24%).

The production of anthropogenic SVOC is more important with CB05 than with RACM2, although OH concentration is lower in CB05. The difference between CB05 and RACM2 originates from the modeling of the reaction of aromatic-OH adducts with O_2 in the gas phase. Aromatic-OH adducts react with O_2 to either abstract an H atom to form ring-retaining products (cresol; via the oxidation of toluene) or add O_2 to form a peroxyl radical that subsequently leads to ring opening and the formation of scission products. RACM2 assumes that the majority of this reaction leads to ring-opening products (dicarbonyls and epoxide). In contrast, CB05 has a high fraction of ring-retaining products (cresol). Figure 3.4 presents the differences of monthly-mean concentrations of cresol between CB05 and RACM2 at each grid point. The mean concentration of cresol in RACM2 is only 20% of that in CB05. Higher concentration of cresol in CB05 results in higher concentrations of the two hydrophobic SVOC (AnBlP: 9% and AnBmP: 40%) in CB05 than in RACM2. If the formation of these SVOC by cresol oxidation

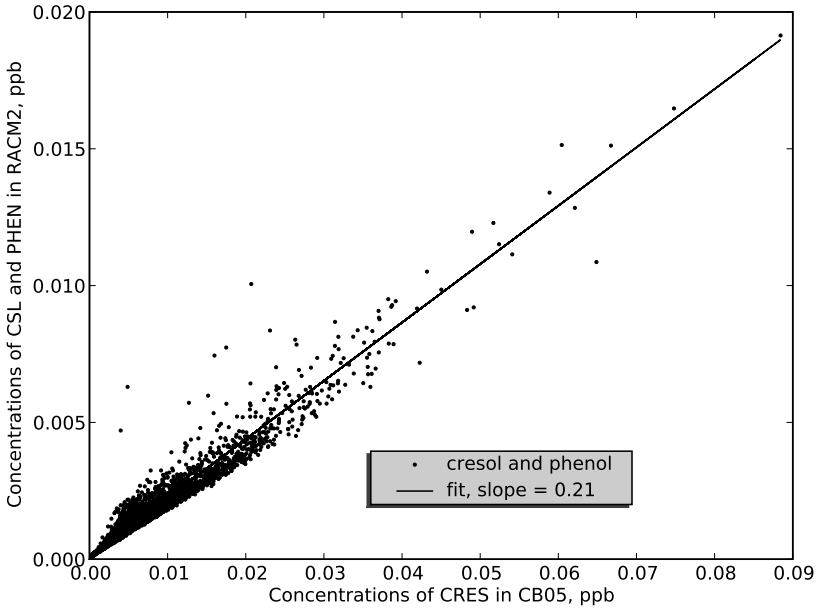

Figure 3.4: Relation of concentrations of cresol between CB05 and RACM2 at each location. The concentration of phenol that is specified only in RACM2 is added to the concentration of cresol for RACM2.

is removed from the two mechanisms, the differences in AnBlP and AnBmP concentrations become much lower (AnBlP: 3% and AnBmP: 0.3%).

The mean concentration of toluene is higher with CB05 than with RACM2 (16%), because the emission rate of TOL (model species for toluene) is higher in CB05 (10%). When volatile organic compound (VOC) emissions are allocated to model species, each mechanism uses different methods for the VOC aggregation, leading to different emission rates (e.g., benzaldehydes are explicitly represented by BALD model species in RACM2, however, they are represented by TOL in CB05).

PAMGLY, another anthropogenic aerosol is formed from methylglyoxal (MGLY) in the aqueous phase by oligomerization. PAMGLY concentration depends only on MGLY concentration because the coefficient of gas/particle partition for methylglyoxal is assumed to already include the effect of oligomerization [Debry *et al.*, 2007b]. Because the kinetics of the oxidation of MGLY by OH is higher in CB05 than in RACM2 at 298 K (13%), the concentration of MGLY is higher in RACM2 than in CB05 (11%). Therefore, the concentration of PAMGLY in RACM2 is higher than in CB05 (20%). Similarly, PAGLY is formed from glyoxal (GLY) by oligomerization. GLY is only included in RACM2. The concentrations of PAMGLY and PAGLY are low compared with other anthropogenic aerosols and they have, therefore, little influence on SOA total concentrations.

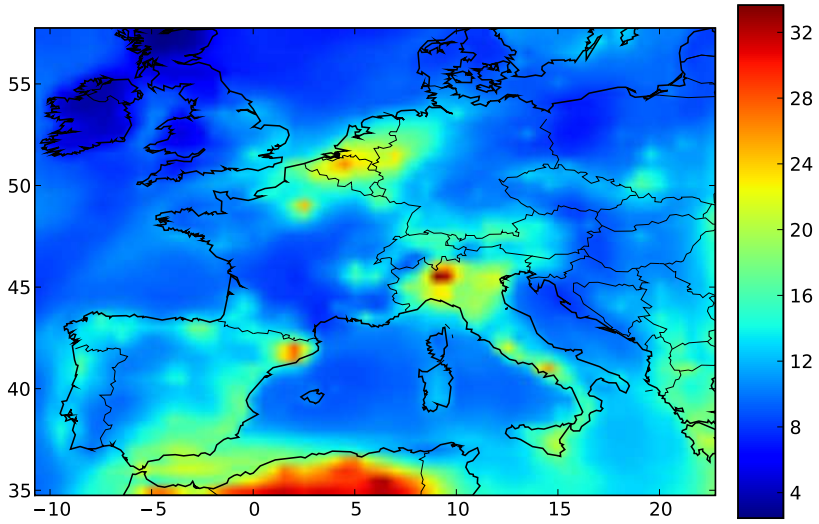

(a) **$PM_{2.5}$ with RACM2**

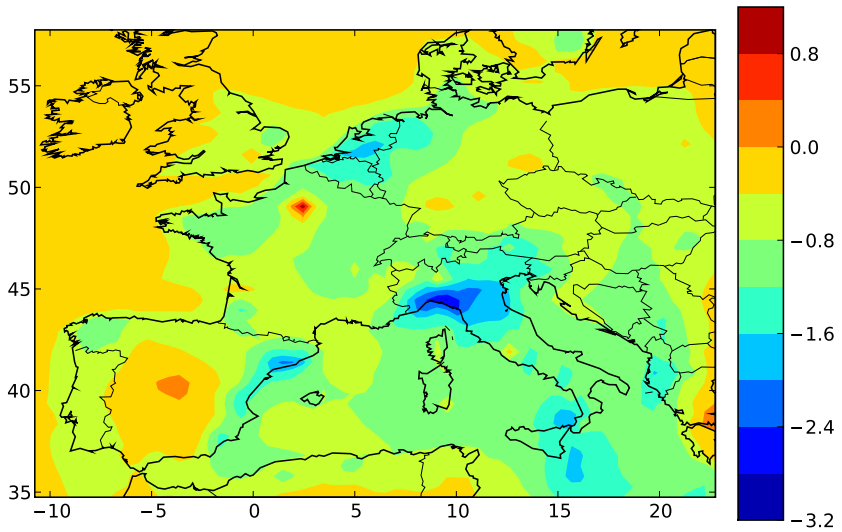

(b) **CB05 - RACM2**

Figure 3.5: Modeled $PM_{2.5}$ concentrations ($\mu g/m^3$) over Europe with (a) RACM2 and (b) the corresponding differences between the two mechanisms (CB05 - RACM2).

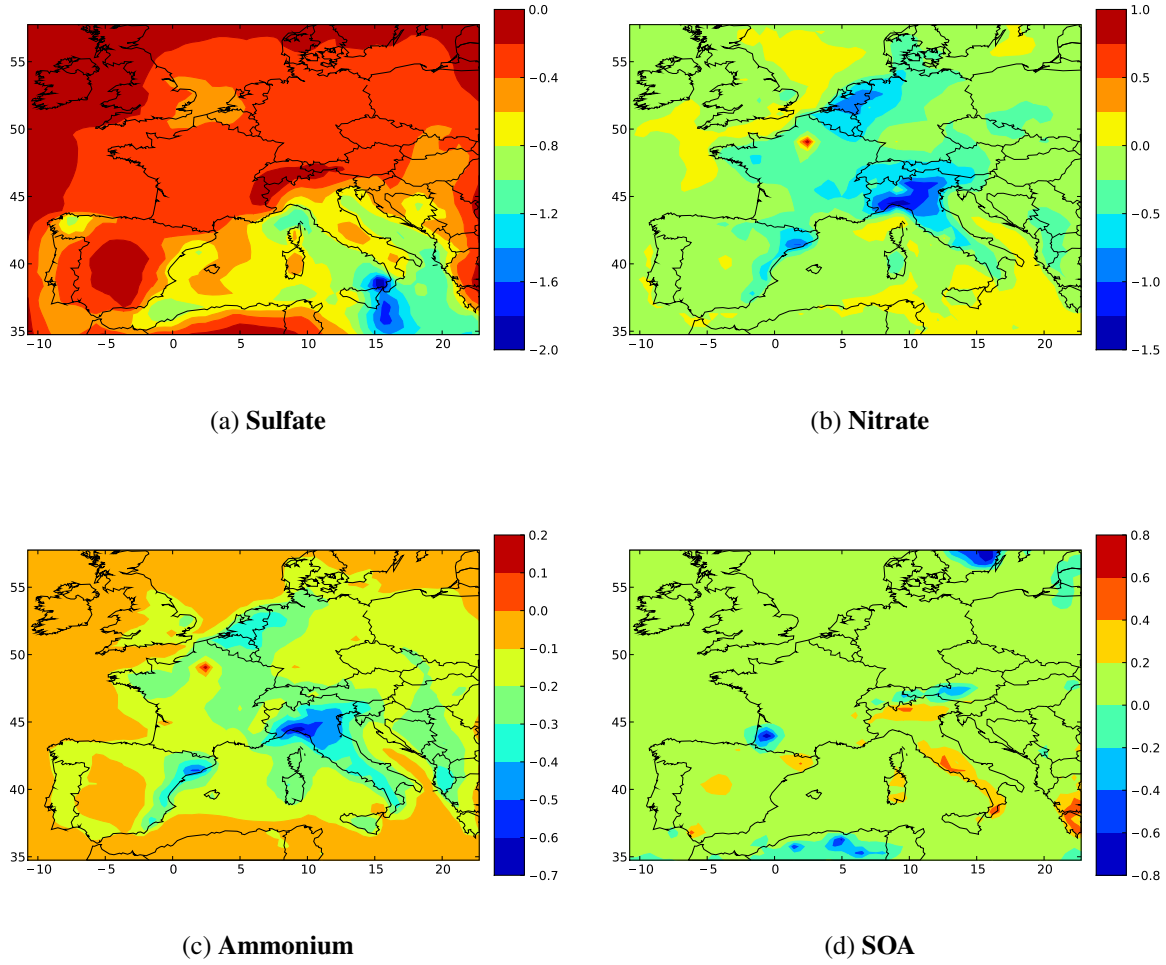

(a) **Sulfate** (b) **Nitrate**

(c) **Ammonium** (d) **SOA**

Figure 3.6: Differences (CB05 - RACM2, µg/m^3) of $PM_{2.5}$ chemical components over Europe: (a) sulfate, (b) nitrate, (c) ammonium, (d) SOA.

3.4.3 $PM_{2.5}$ spatial distributions

Figure 3.5 presents the modeled $PM_{2.5}$ concentrations over Europe for RACM2 and the differences between CB05 and RACM2. For the two chemical mechanisms, high concentrations of $PM_{2.5}$ are simulated over large urban areas (e.g. Antwerp, Barcelona, Cologne, Milan and Paris) and over northern Africa (due to mineral dust) by both CB05 and RACM2 ($>$ 20 µg/m^3). RACM2 overall predicts more $PM_{2.5}$ than CB05 except in cities such as Paris and Madrid where the formation of nitrate, ammonium and SOA with CB05 is higher than with RACM2. The differences are large over northern Italy, part of the Mediterranean Sea and Barcelona in Spain ($>$ 1.5 µg/m^3).

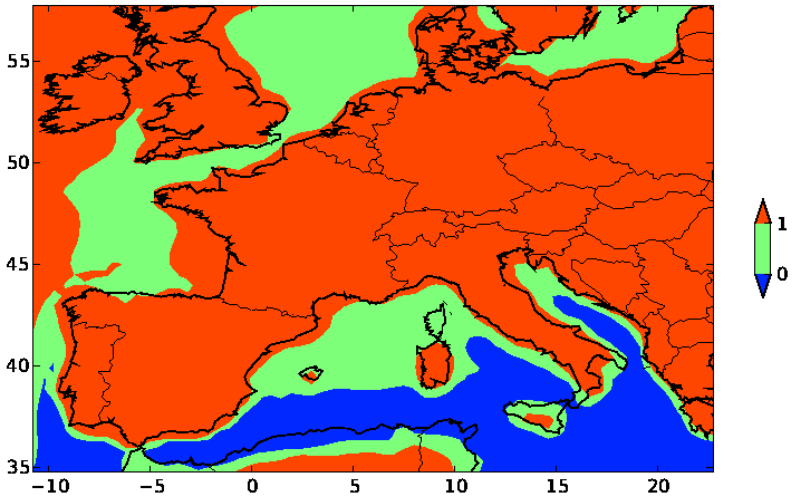

Figure 3.7: Monthly-mean gas ratio (GR) in summer 2001 over Europe. GR < 0: acidic sulfate aerosol (blue), $0 <$ GR < 1: nitrate formation limited by ammonia (green), GR > 1: nitrate formation limited by HNO_3 (orange).

3.4.3.1 Inorganic aerosols

Figure 3.6 presents the differences of the secondary $PM_{2.5}$ chemical components between CB05 and RACM2. Monthly-mean concentrations of sulfate are higher with RACM2 than CB05. The difference is particularly high over the Mediterranean Sea and northwestern Spain. The differences are due to the oxidation of SO_2 by OH in the gas-phase as explained in Section 3.4.2.1. In these regions, high SO_2 emissions from marine traffic combine with high OH concentrations. OH concentrations are higher in RACM2 than in CB05, for example, the monthly-mean concentration of OH is about 50% and 25% higher in RACM2 than CB05 over the Adriatic Sea and northwestern Spain, respectively.

For nitrate, differences of monthly-mean concentrations are large in Paris, Barcelona, the Netherlands and northern Italy. In Paris, a higher concentration of nitrate is obtained with CB05. However, in Barcelona, northern Italy and the Netherlands, higher concentrations of nitrate are obtained with RACM2.

The formation of nitrate is limited by one of the two following precursors: ammonia or HNO_3. To diagnose the limiting precursor for the formation of nitrate, the following "Gas Ratio" indicator (GR) may be used :

$$\mathrm{GR} = \frac{[\mathrm{NH}_3^T] - 2[\mathrm{SO}_4^{2-}]}{[\mathrm{HNO}_3^T]}, \tag{3.7}$$

where NH_3^T (total ammonia) is the sum of ammonium and ammonia and HNO_3^T (total

HNO_3) is the sum of nitrate and HNO_3 [Ansari et Pandis, 1998; Park *et al.*, 2004]. Figure 3.7 shows the simulated monthly-mean GR over Europe. As discussed by Sartelet *et al.* [2007], over continental Europe, nitrate formation is limited by the formation of HNO_3 (GR > 1). Ammonia limits nitrate formation over the English Channel, the North Sea and part of the Mediterranean Sea ($0 <$ GR < 1). Negative GR values, which indicate an acidic sulfate aerosol, are limited to the southern Mediterranean Sea where there is high marine traffic and, therefore, high SO_2 emissions.

In Paris, Barcelona, northern Italy and the Netherlands, the nitrate concentration varies with the HNO_3 concentration (GR > 1). As the total HNO_3 concentration is higher with CB05 than RACM2 over Paris, the nitrate concentration is higher with CB05. However, over the rest of continental Europe, and specially over Barcelona, northern Italy and the Netherlands where the nitrate concentration is high, the nitrate concentration is lower with CB05 than RACM2 because the total HNO_3 concentration is lower. Over the North Sea, the Atlantic Ocean and the English Channel, the nitrate concentrations are low but higher with CB05 than RACM2. These higher concentrations of nitrate with CB05 are linked to higher concentrations of free ammonia under ammonia-limited condition ($0 <$ GR < 1), which are itself due to lower concentrations of sulfate with CB05.

Over continental Europe, because GR > 1, differences of ammonium monthly-mean concentration follow the same pattern as nitrate concentration (e.g., high differences in Paris, Barcelona, the Netherlands and northern Italy).

3.4.3.2 Secondary organic aerosols

The regions where high differences of SOA concentrations between CB05 and RACM2 are obtained, are well correlated with the regions where high SOA concentrations are obtained. Higher SOA concentrations are predicted by CB05 over most of Europe except Sweden, northern Africa, southwestern France and Austria. SOA concentrations are particularly higher with CB05 over parts of Italy, Spain and Greece.

The higher SOA concentrations with RACM2 over Sweden, northern Africa, southwestern France and Austria are due to higher SOA concentrations formed from monoterpene SVOC (BiA0D, BiA1D, BiA2D and BiBmP). In these regions, the concentrations of these SOA are high and as the concentrations increase, the differences of the concentrations also increase. The formation of the hydrophilic monoterpene SVOC (BiA0D and BiA1D) depends on the concentrations of OH and O_3. The concentration of the hydrophobic monoterpene SVOC (BiBmP) depends on the concentration of NO_3. In these regions, the concentrations of OH, O_3 and NO_3 tend to be higher with RACM2 than CB05. Therefore, the concentration of SOA is higher with RACM2 than CB05.

The concentrations of SOA formed from the anthropogenic SVOC are higher in CB05 than in RACM2 over the whole Europe because the concentration of the anthropogenic precursors are higher with CB05 than RACM2.

The higher SOA concentrations with CB05 in Italy, Spain and Greece are due to higher concentrations of SOA formed from the monoterpene SVOC (BiBmP) and the isoprene SVOC (BiISO1 and BiISO2). The differences of SOA formed from monoterpenes SVOC (BiBmP) are higher with CB05 because NO_3 concentrations are higher.

Differences of SOA concentrations formed from the two isoprene SVOC show different patterns. Figure 3.8 presents the differences of SOA formed from the isoprene SVOC (BiISO1

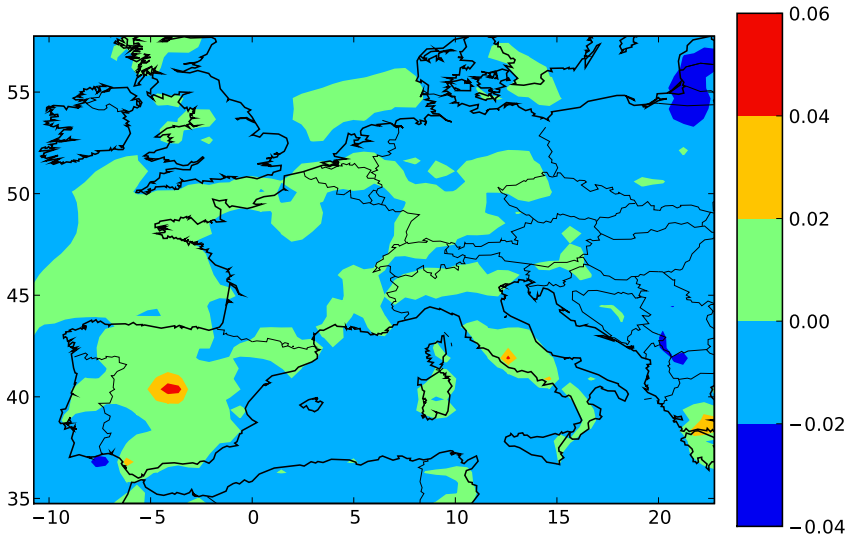

(a) **BiISO1**

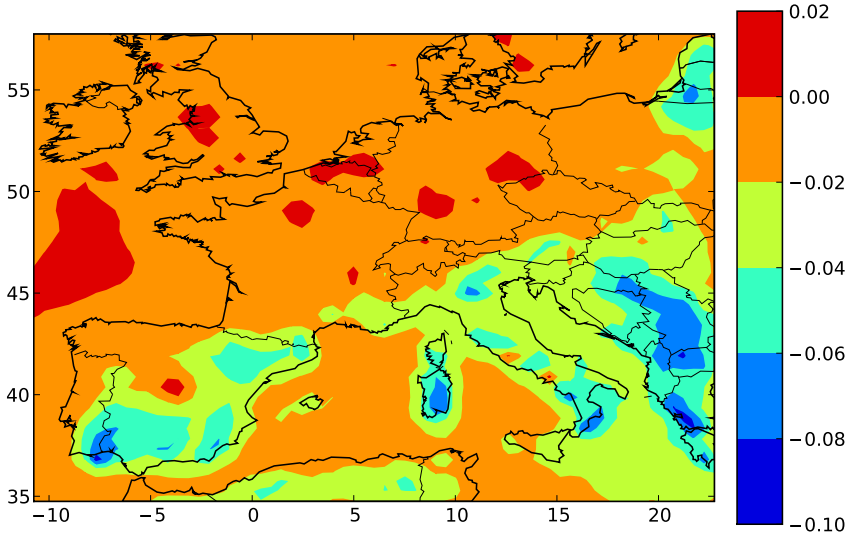

(b) **BiISO2**

Figure 3.8: Differences (CB05 - RACM2, µg/m^3) of SOA formed from (a) BiISO1 and (b) BiISO2 over Europe.

and BiISO2) between CB05 and RACM2. In Italy, Greece and Spain, the concentrations of SOA formed from BiISO1 are higher with CB05. However, in the same regions, the concentrations of SOA formed from BiISO2 are higher with RACM2. BiISO1 and BiISO2 have the same dependence on oxidant concentration. Differences are due to differences in gas/particle phase partitioning. The partitioning depends on the concentration of primary and secondary organics of PM, as follows Pankow [1994a, b]

$$[\mathrm{A}] \simeq \mathrm{K}[\mathrm{G}][\mathrm{OM}] \tag{3.8}$$

where K is the phase partitioning coefficient ($m^3/\mu g$), [OM] is the total organic mass (primary and secondary) ($\mu g/m^3$), [A] is the concentration of the organic species in the particulate phase ($\mu g/m^3$) and [G] is the concentration of the organic species in the gas phase ($\mu g/m^3$). In Italy, Greece and Spain, the organic mass ([OM]) is higher with CB05 (see Figure 3.6) because of higher BiBmP concentrations, which are due to higher NO_3 concentrations. However, gaseous SVOC (BiISO1 and BiISO2) are lower with CB05 because of lower OH concentrations. The compensating negative differences of [G] and positive differences of [OM] lead to variable differences in particulate concentrations, [A] that tend to be positive when the partitioning coefficient K is low (case of BiISO1) and negative when it is high (case of BiISO2).

3.5 Conclusions

The impact of two chemical mechanisms, CB05 and RACM2, on the formation of secondary inorganic and organic aerosols was studied using the air quality model, Polair3D of the Polyphemus modeling platform. The monthly-mean concentration of $PM_{2.5}$ over the domain is higher with RACM2 than CB05 by 6%. This difference is due to inorganic aerosols (sulfate, ammonium and nitrate) and organic aerosols (biogenic and anthropogenic).

Differences in inorganic aerosols result primarily from differences in OH concentrations. The monthly-mean difference for sulfate is 16% and the maximum local difference is 29%. For nitrate, the difference of monthly-mean concentrations is 11% and the maximum local difference is 51%. For ammonium, the difference of monthly-mean concentrations is 10% and the maximum local difference is 23%. Nitrate formation is limited by the formation of HNO_3 over continental Europe. However, ammonia limits nitrate formation over the English Channel, the North Sea and part of the Mediterranean Sea. In other words, differences in the concentrations of nitrate are mostly due to differences in the concentrations of HNO_3 where the concentrations of ammonia are high, whereas differences in the concentrations of ammonia, which are due to differences in the concentrations of sulfate, result in differences in the formation of nitrate where the concentration of HNO_3 is high relative to ammonia.

Differences in organic aerosols result also mostly from differences in oxidant concentrations (OH, O_3 and NO_3). The difference in monthly-mean concentrations of anthropogenic SOA is 22%. Most of that difference is due to aromatic SOA. Differences in the contribution of aromatics to anthropogenic aerosol formation are due to the fact that aromatics oxidation in CB05 leads to more cresol formation from toluene oxidation. The concentration of SOA formed by the cresol oxidation is very different between CB05 and RACM2. The maximum local differences are 40% for aerosol formed from AnBlP and 115% for aerosol formed from AnBmP.

The difference in monthly-mean concentrations of biogenic SOA is 1%, which is the compensating difference of higher concentrations of BiBmP with CB05 (+12%) and lower concentrations of the other biogenic SOA (-4%). Differences in the biogenic aerosol formation are partly due to differences in oxidant concentrations and partly to the total organic mass, which influences the formation of biogenic aerosol by gas-particle partitioning coefficients. The maximum local differences of aerosol formed from monoterpene SVOC are 12% (BiA0D), 52% (BiA1D), 45% (BiA2D) and 91% (BiBmP). For the aerosol formed from isoprene SVOC, the maximum local differences are 21% (BiISO1) and 16% (BiISO2).

The results obtained in this comparison of CB05 and RACM2 on the formation of secondary aerosols show that the predictions of $PM_{2.5}$ with the mechanisms are very similar (only 6% difference and 15% maximum local difference). Differences may be higher for specific compounds (nitrate, AnBmP and BiBmP). Besides, the highest difference, which is obtained for anthropogenic aerosols (aromatics oxidation), could be partly solved by updating CB05 with CB05-TU, a chemical mechanism in which the toluene oxidation mechanism was recently improved [Whitten *et al.*, 2010]. The concentration of cresol is lower with CB05-TU than with CB05 by about 70%. Thus, the discrepancy in aromatics SOA formation between CB05 and RACM2 would be significantly reduced with CB05-TU.

The effects of a gas-phase chemical kinetic mechanism for ozone formation on SOA concentrations can be classified into three main categories: (1) direct effects that result from the design of the mechanism leading to different yields of SOA precursors (e.g., different precursor emissions due to different aggregation of molecular VOC species into VOC surrogate model species, different kinetics of VOC oxidation, different stoichiometric coefficients for VOC oxidation products such as different cresol yields in RACM2 and CB05), (2) primary indirect effects due to different concentrations of the oxidant species (OH, O_3 and NO_3), which affect the rate of oxidation of VOC species and (3) secondary indirect effects due to interactions among SOA species (e.g., an increase in one SOA species leads to greater organic particulate mass available for additional absorption of other SOA species).

Here, a harmonized approach was used when modifying the two mechanisms to handle SOA formation. Early treatment of SOA formation in air quality models used simple approaches where SOA formation was treated at the first oxidation step of the precursor species and only a few mechanisms have treated SOA formation at later oxidation steps (e.g. Griffin *et al.* [2002]). We have attempted to reflect the current understanding of SOA formation by accounting for the NO_x-regime dependence of SOA formation from aromatic compounds and treating SOA formation at later oxidation steps. Accordingly, the future development of mechanisms for SOA formation will require chemical mechanisms that can account for the various gas-phase reaction steps that are important for SOA formation.

Chapitre 4

Influence des modules d'aérosols et des mécanismes chimiques sur les concentrations de particules fines ($PM_{2.5}$)

Résumé

La modélisation de qualité de l'air nécessite un système complexe, qui comprend des algorithmes pour simuler les processus de transport, un mécanisme chimique en phase gazeuse pour représenter la formation des gaz tel que l'ozone et un module d'aérosols pour représenter l'évolution de la composition chimique de la matière particulaire (PM) et sa distribution en taille. L'objectif de ce travail est d'évaluer les différences de concentration des particules fines (de diamètre aérodynamique inférieur à 2,5 micromètres, $PM_{2.5}$) qui résultent de l'utilisation de différents mécanismes chimiques et de différents modules d'aérosols dans un modèle de qualité de l'air (MQA).

Le MQA utilisé dans ce travail est le modèle de chimie-transport eulérien tridimensionnel, Polair3D de la plate-forme Polyphemus. Le domaine du modèle, les niveaux verticaux, la période de simulation et les données d'entrée (données météorologiques, émissions, taux de dépôts, etc.) sont identiques à ceux des simulations des chapitres précédents. Deux mécanismes en phase gazeuse, CB05 ou RACM2 sont utilisés. Pour l'évaluation de la composition chimique des particules minérales par condensation/évaporation, le module thermodynamique ISORROPIA est utilisé. Pour la formation des aérosols organiques secondaires (AOS), deux modules distincts sont comparés : le module SORGAM (Secondary ORGanic Aerosol Model) et le module AEC (AER/EPRI/Caltech).

SORGAM utilise une formulation standard pour la formation d'AOS par l'absorption hydrophobe d'AOS par les particules organiques, tandis qu'AEC représente de façon plus détaillée les processus physico-chimiques influençant la formation d'AOS. En particulier, AEC différencie les AOS hydrophiles et hydrophobes et la non-idealité des composés organiques mélangés dans les particules est représentée par des coefficients d'activité. Dans SORGAM, les COSV (composés organiques semi-volatils) qui peuvent se condenser pour former des AOS sont systématiquement produits à la première étape d'oxydation (e.g., oxydation des COV avec le radical hydroxyle, l'ozone, ou le radical nitrate) alors qu'ils peuvent être produits lors d'étapes d'oxydation ultérieures dans AEC (e.g., oxydation des radicaux péroxyles avec d'autre

radicaux péroxyles, le monoxyde d'azote ou le radical nitrate). Cela permet de faire la distinction entre les niveaux de NO_x (régimes haut-NO_x et bas-NO_x) pour la formation d'AOS. Par ailleurs, AEC comprend plus de précurseurs biogéniques d'AOS (isoprène et sesquiterpènes en plus des monoterpènes) que SORGAM, et il traite des processus d'oligomérisation qui dépendent du pH.

L'influence du module d'aérosol sur les concentrations de particules, et plus particulièrement des $PM_{2.5}$, est étudiée. Les concentrations de $PM_{2.5}$ sont simulées avec Polair3D/Polyphemus sur l'Europe en utilisant successivement AEC et SORGAM. La concentration des espèces minérales des $PM_{2.5}$ sont pratiquement identiques dans les deux simulations. Les différences des concentrations de $PM_{2.5}$ sont donc principalement dues aux composés organiques. Plus de $PM_{2.5}$ est formé avec AEC qu'avec SORGAM. Les différences sont de l'ordre de 6-7 $\mu g/m^3$ dans les régions du nord de l'Italie, sud de la France, nord de l'Espagne et l'Afrique du Nord et elles sont de l'ordre de 3-6 $\mu g/m^3$ dans le sud de la Suède.

Parce que SORGAM et AEC représentent deux extrémités d'un spectre de modèles d'AOS, il est particulièrement intéressant d'étudier les différences structurelles qui distinguent SORGAM d'AEC, et lesquelles contribuent le plus aux différences des concentrations d'AOS simulées : le nombre de précurseurs d'AOS, le traitement des régimes de haut-NO_x et bas-NO_x, des AOS hydrophiles, de la non-idéalité du mélange ou de l'oligomérisation. À cette fin, nous avons fait une série de simulations avec SORGAM et AEC en modifiant ces modules d'AOS "pas à pas" pour comprendre quelles sont les différences structurelles qui contribuent le plus aux différences de concentrations. L'influence de l'enthalpie de vaporisation sur les concentrations d'AOS a également été étudiée.

Nous avons remplacé les enthalpies de vaporisation dans SORGAM par les valeurs d'AEC, plus faibles et qui reflètent mieux les valeurs les plus récentes. Ces nouvelles enthalpies de vaporisation ont un faible effet en moyenne (4%), mais peuvent avoir un effet important localement avec une diminution des concentrations d'AOS dans les endroits où les températures sont basses et une augmentation dans les endroits où les températures sont élevées.

SORGAM fait l'hypothèse que la formation des AOS aromatiques a lieu uniquement quand les concentrations de NO_x sont élevées (régime haut-NO_x). Nous avons examiné deux méthodes différentes pour traiter explicitement le régime bas-NO_x dans SORGAM : une méthode consiste à remplacer les taux de formation des AOS en régime haut-NO_x par des taux correspondant au régime bas-NO_x (ces derniers étant généralement plus élevés que les premiers) et l'autre méthode consiste à implémenter la formation des AOS pour les deux régimes à la fois : Dans cette dernière méthode, la formation d'AOS a alors lieu à des étapes d'oxydation secondaires et les taux de formation des AOS différent selon les voies d'oxydation : taux du régime haut-NO_x pour les réactions avec les espèces azotées ; taux du régime bas-NO_x pour les réactions avec les radicaux péroxyles. Les concentrations d'AOS augmentent avec les deux méthodes (122% pour la première méthode et 32% pour la deuxième méthode). Il apparaît essentiel de développer des mécanismes chimiques en phase gazeuse qui peuvent explicitement prendre en compte des rendements différents d'oxydation selon les niveaux de NO_x.

La formation d'AOS à partir de l'isoprène n'est pas traitée dans SORGAM. Elle a été ajoutée selon le même formalisme que pour les autres AOS de SORGAM. Le traitement de l'isoprène et de ses AOS (hydrophobes dans SORGAM et principalement hydrophiles dans AEC) a un effet significatif sur les concentrations d'AOS : 0,15 $\mu g/m^3$ d'isoprène en phase particulaire est formé avec SORGAM, tandis que 0,34 $\mu g/m^3$ est formé avec AEC. L'affinité des COSV de l'isoprène avec l'eau conduit à plus d'AOS de l'isoprène dans des conditions humides. Pour

prendre en compte l'hydrophilie des AOS de l'isoprène, une paramétrisation simple a été incorporée dans SORGAM. Cette paramétrisation suppose une augmentation linéaire de la formation d'AOS de l'isoprène avec l'humidité relative. Son utilisation conduit à une augmentation des concentrations d'AOS dans les endroits où la formation d'AOS de l'isoprène est importante, e.g., près de la mer Méditerranée.

Le traitement des coefficients d'activité en phase particulaire a un effet faible en moyenne (9%) ; cependant, l'effet peut être important localement. Par ailleurs, les valeurs des coefficients d'activité peuvent différer de manière significative entre leurs valeurs implicites dans SORGAM et leurs valeurs calculées dans AEC car les coefficients d'activité d'un composé d'AOS peuvent différer considérablement entre les valeurs en chambre atmosphérique avec seulement un précurseur et en atmosphére réelle où une myriade d'espèces organiques primaires interagissent avec des sels minéraux et l'eau.

Le traitement de l'oligomérisation représente un effet important dans AEC (60% d'AOS). L'influence de l'oligomérisation sur la formation d'AOS est importante dans les régions où il y a d'importantes émissions de monoterpènes, qui sont des précurseurs d'espèces d'AOS de type aldéhyde qui peuvent être oligomérisés dans AEC.

Ensuite, la sensibilité conjointe des concentrations de particules aux différents traitements de la chimie en phase gazeuse et de la formation d'AOS est étudiée. Quatre combinaisons possibles de modules de chimie et d'aérosols ont été étudiées (RACM2-AEC, RACM2-SORGAM, CB05-AEC et CB05-SORGAM) pour la formation de $PM_{2.5}$. Les concentrations de $PM_{2.5}$ avec RACM2 sont légèrement plus élevées qu'avec CB05 (6% pour SORGAM et 3% pour AEC en moyenne). Ces faibles différences de $PM_{2.5}$ s'expliquent par des compensations des différences de divers composés chimiques des $PM_{2.5}$ (minéraux et organiques).

Les incertitudes dues à la chimie en phase gazeuse et au module d'aérosols ne sont pas additives et des non-linéarités fortes se produisent sur les concentrations de particules. Dans cette étude, modifier le mécanisme chimique en phase gazeuse peut conduire à la formation de plus d'aérosols minéraux secondaires mais à moins d'aérosols organiques secondaires à cause d'interactions complexes entre le mécanisme de chimie en phase gazeuse et les processus de formation d'aérosols secondaires.

Les concentrations des aérosols minéraux secondaires sont plus élévées avec RACM2 qu'avec CB05 (14%), tandis que les concentrations des AOS sont plus élevées avec CB05 qu'avec RACM2 (3% pour SORGAM et 20% pour AEC). Les différences entre RACM2 et CB05 sont plus élevées si on utilise AEC que SORGAM car les concentrations en AOS aromatiques sont plus élévées dans AEC que dans SORGAM. Ces différences de concentrations d'AOS entre les deux mécanismes chimiques avec AEC (RACM2-AEC et CB05-AEC) sont dues au fait qu'AEC prend en compte explicitement l'influence du régime de NO_x en phase gazeuse sur la formation des AOS aromatiques.

Ces résultats soulignent l'importance de plusieurs éléments pour la simulation des AOS : une liste de précurseurs complète, l'oligomérisation de certains AOS et l'effet des régimes haut-NO_x et bas-NO_x. Ce dernier élément implique qu'il est essentiel de développer des mécanismes chimiques de la phase gazeuse qui tiennent compte de la formation des AOS non seulement dans la première étape d'oxydation des COV mais plutôt à toutes les étapes d'oxydation pertinentes pour la formation des AOS.

Ce chapitre est constitué de
Kim, Y., Couvidat, F., Sartelet, K. et Seigneur, C. (2011). **Comparison of different gas-phase mechanisms and aerosol modules for simulating particulate matter formation**. *J. Air & Waste Manage. Assoc.*, 61 :1-9.

Sommaire

4.1 Introduction

Modeling air quality requires a complex system, which includes algorithms to simulate transport processes, a chemical kinetic mechanism, and an aerosol module. Various gas-phase mechanisms are currently available to simulate ozone formation and several aerosol modules are also available to simulate the evolution of particulate matter (PM) chemical composition and size distribution. A few studies have been conducted to investigate the effect of the gasphase chemical kinetic mechanism [Luecken, 2008; Sarwar *et al.*, 2008] or the effect of the aerosol module [Pun *et al.*, 2003; Morris *et al.*, 2006; Bailey *et al.*, 2007] on secondary PM formation. The objective of this work is to evaluate the differences in fine (aerodynamic diameter $\leq 2.5\mu$m) PM ($PM_{2.5}$) concentrations that result from the use of two different chemical mechanisms and $PM_{2.5}$ modules, with a special emphasis on identifying the major sources of uncertainties for secondary organic aerosol (SOA) formation. First, the models used in this study are briefly described and model performance evaluation against observations from routine monitoring networks is summarized. Then, $PM_{2.5}$ concentrations simulated using two different gas-phase chemical mechanisms and two secondary organic aerosol modules are compared. In particular, we investigate whether the uncertainties associated with those two distinct types of modules (gas-phase chemistry and secondary aerosol formation) are additive or whether their combination is nonlinear.

4.2 Description of the models

The air quality model used in this work is the threedimensional (3D) Eulerian chemical-transport model POLAIR3D of the Polyphemus modeling platform [Sartelet *et al.*, 2007; Mallet *et al.*, 2007].

Two recent gas-phase mechanisms are used in the following simulations: the Carbon-Bond 05 mechanism (CB05) [Sarwar *et al.*, 2008] and the Regional Atmospheric Chemistry Mechanism version 2 (RACM2) [Goliff et Stockwell, 2008]. The former is based on the carbon-bond formulation to represent organic chemistry, whereas the latter uses a surrogate molecule representation. Some differences also exist in the selection and kinetics of some inorganic reactions, as discussed by Kim *et al.* [2009]. For $PM_{2.5}$ formation, the ISORROPIA module [Nenes *et al.*, 1999], version 1.7, is used for inorganic species. For SOA formation, two distinct modules are used: the SORGAM module [Schell *et al.*, 2001], which uses the two-compound Odum approach [Odum *et al.*, 1996], and the AEC module [Pun *et al.*, 2006; Debry *et al.*, 2007b], which simulates both hydrophilic and hydrophobic organic aerosols. The two-compound Odum approach consists in using two surrogate SOA compounds to represent SOA formation from a given precursor and the first step of oxidation (e.g., oxidation by the hydroxyl radical, ozone, or the nitrate radical). The stoichiometric coefficient and gas/particle partitioning coefficient of each surrogate SOA compound are estimated by fitting this empirical model to smog chamber data [Odum *et al.*, 1996]. The treatment of gas/particle partitioning assumes that the SOA compounds absorb into a hydrophobic organic particle. This two-compound Odum approach is currently used in many air quality models such as the Community Multiscale Air Quality (CMAQ) model [Carlton *et al.*, 2010], the Comprehensive Air quality Model with extensions (CAMx) [Gaydos *et al.*, 2007], the Weather Research & Forecast model with Chemistry (WRF/Chem) [Zhang *et al.*, 2010c], the European Monitoring and Evaluation Programme (EMEP) model

Table 4.1: Major characteristics of the SORGAM and AEC SOA modules.

Characteristics	SORGAM	AEC
Precursors	Aromatics, long-chain alkanes, long-chain alkenes, monoterpenes	Aromatics, long-chain alkanes, long-chain alkenes, isoprene, monoterpenes, sesquiterpenes
SOA species	Two surrogates per precursor and oxidation pathway	Surrogate molecular species selected according to physicochemical properties
Gas/particle partitioning	Absorption into an hydrophobic organic phase	Absorption of hydrophobic SOA into an organic phase and absorption of hydrophilic SOA into an aqueous phase
Non-ideality of the particulate phase	Assumed constant and identical to that implicitly assumed in the gas/particle partitioning from the smog chamber experiments	Calculated via activity coefficients
Gas-phase chemistry	SOA yields for the first oxidation step with high-NO_x conditions	SOA yields from various oxidation steps with both high-NO_x and low-NO_x pathways
Particulate-phase chemistry	None	Oligomerization as a function of pH

[Simpson *et al.*, 2007], the European Air pollution and Dispersion (EURAD) model [Schell *et al.*, 2001], and POLAIR3D/Polyphemus [Sartelet *et al.*, 2007]. The AEC hydrophobic/hydrophilic SOA approach is used in several models such as CMAQ [Zhang *et al.*, 2004], WRF/Chem [Zhang *et al.*, 2010c], POLAIR3D/Polyphemus [Debry *et al.*, 2007b], and CHIMERE [Bessagnet *et al.*, 2008]. Thus, as for the gas-phase chemistry, two operational formulations for SOA formation are considered. SORGAM represents a standard SOA formulation with hydrophobic absorption of SOA into organic particles, whereas AEC includes a more complete set of physicochemical processes for SOA formation. In particular, AEC treats hydrophilic SOA in addition to hydrophobic SOA and it accounts for the variable nonideality of particles via the calculation of activity coefficients; in addition, the AEC version used here distinguishes between high-NO_x and low-NO_x regimes for SOA yields, it includes more SOA precursors (isoprene and sesquiterpenes) than SORGAM, and it treats pH-dependent oligomerization processes. Table 4.1 summarizes the main characteristics of these two SOA modules.

Kim *et al.* [2009] presented a detailed discussion of the results of an application of the air quality model with CB05 and RACM2 to Europe for the period 15 July to 15 August 2001. Model performance evaluation for hourly ozone (O_3) concentrations shows mean normalized error and bias of 23% and 9% for RACM2 and 21% and 4% for CB05, normalized mean error and bias of 43% and 30% for RACM2 and 39% and 25% for CB05, and mean fractional error and bias of 22% and 5% for RACM2 and 21% and 0% for CB05 (a threshold of 60 ppb was used for the observed hourly O_3 concentrations). This model performance is satisfactory compared to guidelines of mean normalized error and bias less than or equal to 35% and 15%, respectively [Russell et Dennis, 2000]. Average differences in O_3 concentrations between CB05 and

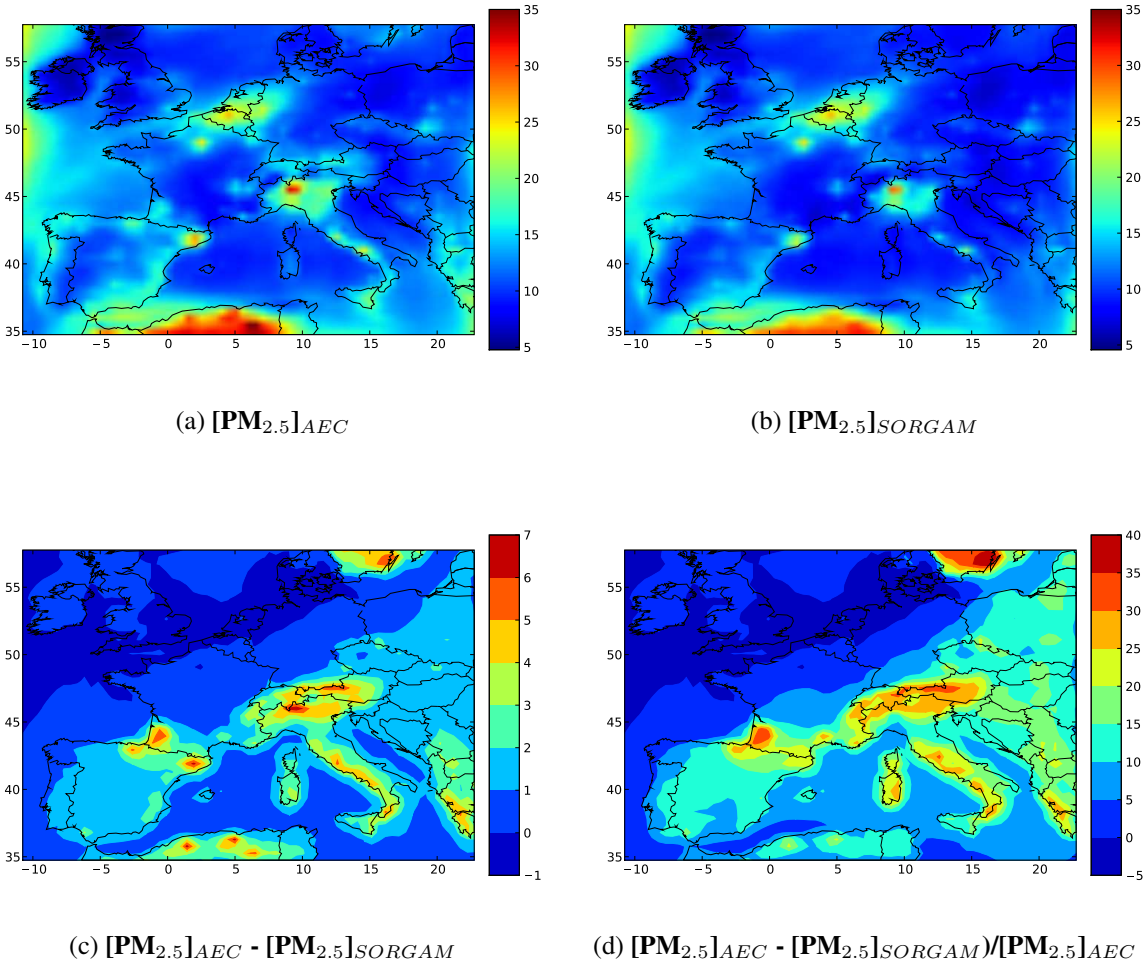

(a) **[PM**$_{2.5}$**]**$_{AEC}$

(b) **[PM**$_{2.5}$**]**$_{SORGAM}$

(c) **[PM**$_{2.5}$**]**$_{AEC}$ **- [PM**$_{2.5}$**]**$_{SORGAM}$

(d) **[PM**$_{2.5}$**]**$_{AEC}$ **- [PM**$_{2.5}$**]**$_{SORGAM}$**)/[PM**$_{2.5}$**]**$_{AEC}$

Figure 4.1: $PM_{2.5}$ concentrations (µg/m^3) over Europe simulated with AEC and SORGAM for SOA formation and RACM2 for gas-phase chemistry. Results are averaged over the 1-month simulation of 15 July to 15 August 2001: (a) $[PM_{2.5}]_{AEC}$ (top left); (b) $[PM_{2.5}]_{SORGAM}$ (top right); (c) $[PM_{2.5}]_{AEC}$ - $[PM_{2.5}]_{SORGAM}$ (bottom left); (d) ($[PM_{2.5}]_{AEC}$ - $[PM_{2.5}]_{SORGAM}$)/$[PM_{2.5}]_{AEC}$ (bottom right)

RACM2 are on the order of 3 ppb, that is, about 5%. Maximum differences are 6 ppb (9%). It was concluded that both inorganic and organic chemistry contributed to differences between the mechanisms. Formation of inorganic PM is identical in those two simulations and differences are due solely to the SOA formation modules. When using RACM2, the $PM_{2.5}$ mean fractional error and bias are 41% and -4% with AEC and 45% and -16% for SORGAM, respectively; the normalized mean error and bias are 38% and 2% with AEC and 40% and -8% for SORGAM, respectively. When using CB05, the $PM_{2.5}$ mean fractional error and bias are 37% and -4% with AEC and 47% and -22% for SORGAM, respectively; the normalized mean error and bias are 36% and 1% with AEC and 44% and -15% for SORGAM, respectively. These values are within the performance goals recommended by Boylan et Russell [2006]. Model performance

is comparable for the inorganic components and the differences in model performance are due to the particulate organic fraction (no particulate organic carbon measurements are available from the EMEP monitoring network for the period considered here). Therefore, model performance is satisfactory for $PM_{2.5}$ with both gas-phase chemical mechanisms and both SOA modules and commensurate with those of other models for atmospheric PM [Russell, 2008].

4.3 Sensitivity of PM concentrations to the aerosol module

The sensitivity of PM concentrations is first investigated with respect to the aerosol module. The molecule-based formulation of RACM2 is more conducive to detailed interactions between gas-phase chemistry and SOA formation than the carbon-bond formulation of CB05; therefore, RACM2 is used here for the gas-phase chemistry.

Figure 4.1 presents the $PM_{2.5}$ concentrations simulated with AEC and SORGAM over Europe, as well as the differences between the two model simulations. Overall, more $PM_{2.5}$ is formed with AEC than with SORGAM. This result is due to the fact that more SOA formation processes are included in AEC (see Table 4.1). Differences are significant; they reach 6-7 $\mu g/m^3$ in parts of northern Italy, southwestern France, northern Spain, and North Africa and are in the range of 3-6 $\mu g/m^3$ in southern Sweden (the European regulation is 20 $\mu g/m^3$ for annual concentrations). Relative differences follow a similar spatial pattern with differences up to 40% (with respect to the AEC simulation) in southern Sweden, southwestern France, and Austria. These results highlight that uncertainties in PM formation greatly exceed those in ozone gas-phase chemistry, which is consistent with earlier findings [Pun *et al.*, 2003; Bailey *et al.*, 2007].

Table 4.2: Characteristics of SOA modules used in the sensitivity simulations.

SOA module	Precursors	NO_x regime	Hydrophobic and hydrophilic absorption	Activity coefficients	Oligomerization	Enthapies of vaporization
SORGAM	Anthropogenics, monoterpenes	High-NO_x only	Hydrophobic only	Implicit and constant	None	156 kJ/mol [Schell *et al.*, 2001]
SORGAM-ΔH	Anthropogenics, monoterpenes	High-NO_x only	Hydrophobic only	Implicit and constant	None	88 kJ/mol [Pun *et al.*, 2006]
SORGAM-NO_x	Anthropogenics, monoterpenes	High- and low-NO_x	Hydrophobic only	Implicit and constant	None	88 kJ/mol [Pun *et al.*, 2006]
SORGAM-bio	Anthropogenics, all terpenes	High- and low-NO_x	Hydrophobic only	Implicit and constant	None	42-175 kJ/mol[a]
Super-SORGAM	Anthropogenics, all terpenes	High- and low-NO_x	Hydrophobic, parametrization for hydrophilic isoprene SOA	Implicit and constant	None	42-175 kJ/mol[a]
Mini-AEC	Anthropogenics, all terpenes	High- and low-NO_x	Hydrophobic and hydrophilic	Constant (unity)	None	25-175 kJ/mol[b]
AEC-no-oligo	Anthropogenics, all terpenes	High- and low-NO_x	Hydrophobic and hydrophilic	Calculated and variable	None	25-175 kJ/mol[b]
AEC	Anthropogenics, all terpenes	High- and low-NO_x	Hydrophobic and hydrophilic	Calculated and variable	Parametrization for aldehyde SOA	25-175 kJ/mol[b]

Notes: [a]42 kJ/mol for isoprene SOA [Zhang *et al.*, 2007], 88 kJ/mol for anthropogenic and monoterpene SOA [Pun *et al.*, 2006], 175 kJ/mol for sesquiterpene SOA [Pun *et al.*, 2006].
[b]25 kJ/mol for glyoxal [Debry *et al.*, 2007b], 38 kJ/mol for methylglyoxal [Debry *et al.*, 2007b], 42 kJ/mol for isoprene SOA [Zhang *et al.*, 2007], 88 kJ/mol for biogenic hydrophilic aldehyde and monocarboxylic SOA and for anthropogenic SOA [Pun *et al.*, 2006], 109 kJ/mol for biogenic dicarboxylic acids [Pun *et al.*, 2006], 175 kJ/mol for biogenic hydrophobic SOA [Pun *et al.*, 2006].

Because SORGAM and AEC represent two ends of a spectrum of SOA models, it is of particular interest to investigate which of the structural differences that distinguish SORGAM from AEC contribute the most to the differences in simulated SOA concentrations: number of SOA precursors, treatment of high- versus low-NO_x regimes, treatment of hydrophilic SOA, treatment of the variability of activity coefficients, or treatment of oligomerization. To that end, we conducted a series of simulations with SORGAM and AEC that involve modifications to the SOA modules to represent these various structural modifications. In addition to these structural changes, the influence of the enthalpies of vaporization on SOA concentrations was also investigated. Table 4.2 presents the characteristics of the SOA modules used in those sensitivity simulations.

Figures 4.2 and 4.3 present the SOA concentrations averaged over the 1-month simulation period for each of the eight simulations. Differences between a model simulation and the simulation of the nearest model in terms of formulation are also presented. Overall, SOA concentrations increase as the SOA module evolves from SORGAM (the simplest mechanistic representation of SOA formation) to AEC (the most complete representation of SOA formation processes). The results are discussed in detail below.

The values of the enthalpies of vaporization for the equilibrium calculations of SOA have been shown to have some effects on average SOA concentrations [Zhang *et al.*, 2007] as well as on their diurnal patterns [Pun et Seigneur, 2008]. Accordingly, we replaced the original enthalpies of vaporization of SORGAM (156 kJ/mol for all SOA) by a value of 88 kJ/mol, which better reflects the more recent values used in AEC, as shown in Table 4.2 (SORGAM-ΔH). The difference in SOA concentrations averaged over the entire domain is low (0.01 $\mu g/m^3$) because there are both positive and negative differences in various parts of the domain depending on temperature. In areas with the lower temperatures (the Alps, the Pyrenean Mountains, and Sweden), the decrease in the enthalpies of vaporization leads to a decrease in SOA concentrations by as much as 0.5 $\mu g/m^3$ because the experimental data used in the SOA model were obtained at greater temperatures than those modeled in those areas and the temperature correction, which leads to greater SOA concentrations as the temperature decreases, is less for a smaller value of the enthalpy of vaporization. For the other areas where the temperatures are higher, the opposite effect is obtained. The lower enthalpy of vaporization used in SORGAM-ΔH leads to less displacement of the gas/particle equilibrium toward the gas phase and the SOA concentrations are consequently greater than in SORGAM by up to 0.2 $\mu g/m^3$.

Adding some representation of the NO_x regime for SOA formation (SORGAM-NO_x) has some effects because SOA formation is more important for aromatics and monoterpenes (which are major SOA precursors in SORGAM) under low-NO_x conditions than under high-NO_x conditions according to the smog chamber results of Ng *et al.* [2007a, b]. Here the stoichiometric coefficients and partitioning coefficients of Ng *et al.* [2007a, b] were used for the low-NO_x regime. Because most SOA formation at the regional scale occurs under low-NO_x conditions, SOA yields increase when one allows the mechanism to treat both high- and low-NO_x regimes. The effect depends, however, on how the low-NO_x versus high-NO_x regimes are implemented in the gasphase chemical kinetic mechanism. On one hand, if one simply uses the low-NO_x regime SOA yields in the first oxidation step of the precursor species (for both aromatics and monoterpenes), thereby neglecting the occurrence of the high-NO_x regime for SOA formation, the differences in SOA concentrations are significant: they reach 2 $\mu g/m^3$ in northern Italy and are about 0.35 $\mu g/m^3$ on average over the entire domain (not shown). On the other hand, if one implements the high-NO_x and low-NO_x SOA yields in later oxidation steps corresponding

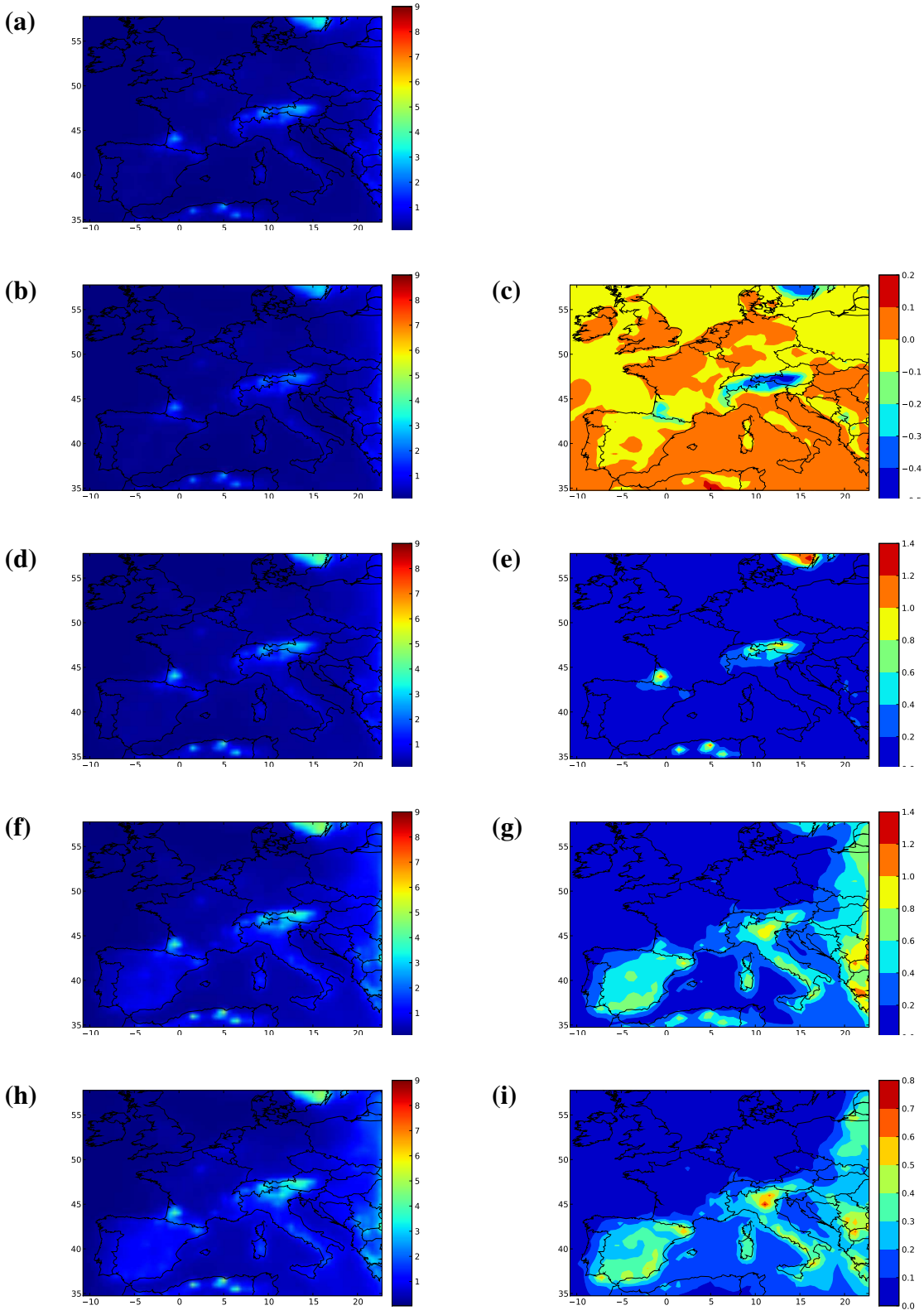

Figure 4.2: Simulations of $PM_{2.5}$ SOA ($\mu g/m^3$) over Europe with RACM2 for gas-phase chemistry and distinct SORGAM modules for SOA formation: (a) SORGAM (first row); (b) SORGAM-ΔH (second row left); (c) [SORGAM-Δ - SORGAM] (second row right); (d) SORGAM-NO_x (third row left); (e) [SORGAM-NO_x - SORGAM-ΔH] (third row right); (f) SORGAM-bio (fourth row left); (g) [SORGAM-bio - SORGAM-NO_x] (fourth row right); (h) Super-SORGAM (fifth row left); (i) [Super-SORGAM - SORGAM-bio] (fifth row right).

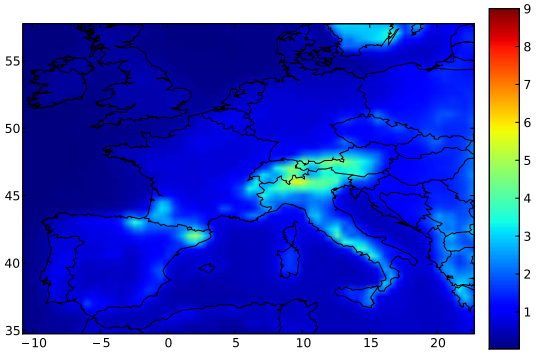

(a) **Mini-AEC**

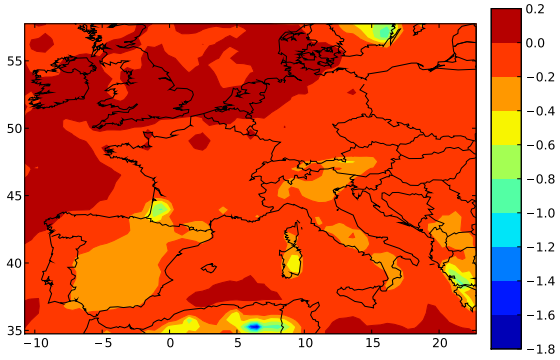

(b) **Mini-AEC - AEC-no-oligo**

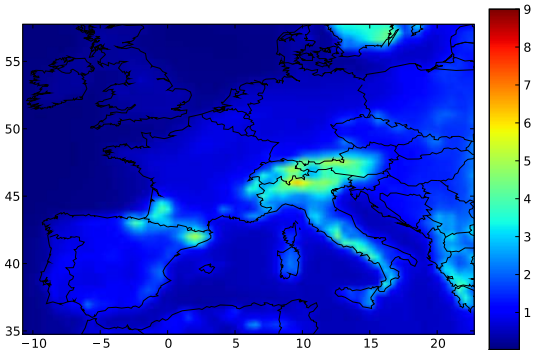

(c) **AEC-no-oligo**

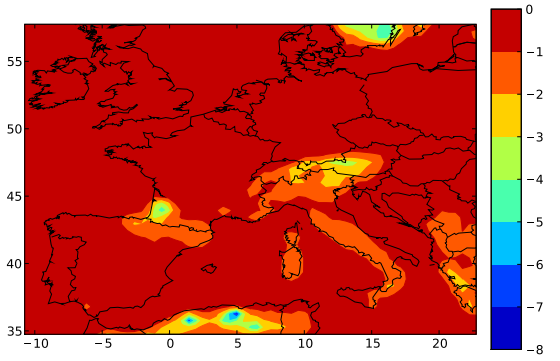

(d) **AEC-no-oligo - AEC**

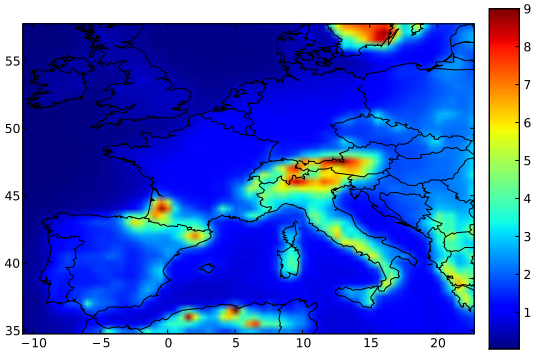

(e) **AEC**

Figure 4.3: Simulations of $PM_{2.5}$ SOA ($\mu g/m^3$) over Europe with RACM2 for gas-phase chemistry and distinct AEC modules for SOA formation: (a) Mini-AEC (first row left); (b) [Mini-AEC - AEC-no-oligo] (first row right); (c) AEC-no-oligo (second row left); (d) [AEC-no-oligo - AEC] (second row right); and (e) AEC (third row).

to reactions of precursor oxidation products with nitrogenous species and peroxyl radicals, respectively, but for aromatics only (because of insufficient information for monoterpenes), the differences are smaller, because the overall SOA yields include a combination of all oxidation routes and the low-NO_x regime is not treated for monoterpenes. Then, as shown in Figure 4.2, the differences in SOA concentrations reach 1.4 $\mu g/m^3$ in Sweden, southwestern France, and North Africa and approach 1 $\mu g/m^3$ in northern Italy; they are, however, only 0.08 $\mu g/m^3$ on average. These two results underscore the importance of treating the effect of the NO_x regime with sufficient detail in the gas-phase mechanism and further work is needed to develop gas-phase chemical kinetic mechanisms that can better integrate the dependency of SOA yields on NO_x regimes.

Adding isoprene and sesquiterpenes as precursors of SOA also increases the SOA concentrations (SORGAM-bio). The effect of NO_x regimes is also included in this simulation. However, SOA formation from sesquiterpenes is assumed to be lower under low-NO_x conditions than under high-NO_x conditions following Ng *et al.* [2007a]. For isoprene, no NO_x dependency is considered here, following Zhang *et al.* [2007]. The enthalpy of vaporization used by Zhang *et al.* [2007] was used for isoprene SOA; this value is in good agreement with the more recent experimental values of Kleindienst *et al.* [2009]. The enthalpy of vaporization used by Pun *et al.* [2006] was used for sesquiterpene SOA. Most of the increase in SOA concentrations is due to isoprene oxidation rather than sesquiterpene oxidation [Debry *et al.*, 2007b]. The largest increases occur in the lower latitudes where temperature and solar radiation are greater and, therefore, where isoprene emissions are higher. The SOA concentration increase reaches 1.4 $\mu g/m^3$ in the eastern part of the domain and is 0.25 $\mu g/m^3$ on average over the entire domain.

SOA formed from isoprene oxidation are believed to be hydrophilic and, therefore, may absorb into aqueous particles rather than into hydrophobic organic particles [Pun, 2008]. The affinity of those SOA compounds for aqueous particles is significantly larger than for organic particles, which could lead to greater SOA formation under humid conditions; for example, Pun [2008] calculated that SOA concentrations due to isoprene oxidation could be up to 5 times greater under humid conditions than under dry conditions. To account for this process, a simple parameterization is incorporated in the version of SORGAM, which already includes NO_x regimes and all terpene precursors. This parameterization accounts for a linear increase in isoprene SOA formation as a function of relative humidity (RH) (Super-SORGAM): K_i(RH) = K_i(RH = 0) (1 + 4 RH), where K_i, i = 1, 2, are the partitioning constants of the two isoprene SOA species and RH is expressed as a fraction (i.e., RH = 1 at 100% relative humidity). This parameterization leads to about 5 times more isoprene formation at 100% relative humidity than at 0% relative humidity, following the simulation results of Pun [2008]. The result shows an increase in SOA concentrations in regions where SOA formation from isoprene is significant, that is, mostly near the Mediterranean Sea. They reach 0.5-0.8 $\mu g/m^3$ in northern Italy and northern Spain, where SOA concentrations are in the 2-3 $\mu g/m^3$ range. They are less than 0.1 $\mu g/m^3$ in northern Europe, where SORGAM-NO_x SOA concentrations are mostly less than 2 $\mu g/m^3$.

AEC was simplified to obtain a version that closely resembles the formulation of Super-SORGAM, hereafter referred to as Mini-AEC. In that version, the activity coefficients are set to one (i.e., assuming ideal solutions) and oligomerization of SOA in the particulate phase is not simulated. The effect of activity coefficients set to one (ideal organic and aqueous solutions) for particulate SOA leads to a decrease in SOA concentrations of about 10% on average (0.08

$\mu g/m^3$). This relatively small effect, for example, compared to the difference reported by Pun [2008] is due in part to compensating effects for hydrophobic particles and aqueous particles. In some areas, the effect can be significant with the largest differences (> 0.5 $\mu g/m^3$) occurring in southern Sweden, southwestern France, Corsica, and North Africa.

The two other versions of AEC used here include one where only oligomerization [Pun et Seigneur, 2007] is not taken into account but the activity coefficients are calculated (referred to as AEC-no-oligo), and the base AEC configuration where all processes are simulated (see Table 4.1).

Neglecting oligomerization has a significant effect with an average decrease of 0.57 $\mu g/m^3$ in SOA concentrations over the entire domain. The largest decrease occurs in North Africa (up to 8 $\mu g/m^3$). Decreases in southwestern France and Austria are up to 5 $\mu g/m^3$. Significant increases are also obtained over southern Sweden. These regions have significant emissions of monoterpenes, which are precursors of the aldehyde SOA surrogate species that is subject to oligomerization in AEC.

4.4 Joint sensitivity of PM concentrations to the gas-phase chemistry and aerosol module

The joint sensitivity of PM concentrations to different treatments of both gas-phase chemistry and SOA formation is investigated. In particular, we evaluate whether the effects of gas-phase chemistry and SOA formation are simply additive or whether synergistic or antagonistic effects are significant. Figure 4.4 presents the differences in $PM_{2.5}$ concentrations averaged over the 1-month simulation obtained with the four possible combinations of gasphase chemistry (RACM2 and CB05) and SOA modules (SORGAM and AEC).

The effect of the gas-phase chemical mechanism differs depending on which aerosol module is used. With both aerosol modules, the average $PM_{2.5}$ concentration is greater with RACM2 than with CB05: when SORGAM is used, the difference in $PM_{2.5}$ concentrations is 6% on average; it is 3% on average when AEC is used. These differences are commensurate with the 5% difference obtained for ozone concentrations between CB05 and RACM2 [Kim *et al.*, 2009]; however, the $PM_{2.5}$ differences result from compensating differences in inorganic and organic $PM_{2.5}$ concentrations. Secondary inorganic aerosol concentrations are greater on average with RACM2 than with CB05 by about 14%. On the other hand, SOA concentrations are greater with CB05 than with RACM2. The difference is only 3% with SORGAM, but it is 20% on average with AEC. This larger difference obtained with AEC is due in part to the fact that AEC takes into account the influence of the NO_x regime on SOA formation explicitly. At low NO_x concentrations, the formation of organic peroxide SOA is favored, whereas at high NO_x concentrations, the formation of other condensable products such as organic nitrates is favored. Because the SOA yields differ for those distinct SOA species, the gas-phase chemical mechanism has a strong influence on the SOA formation rate, particularly in the transition regime between high-NO_x and low-NO_x regimes (i.e., as the air mass is transported, for example, from an urban area to a remote location). CB05 switches more rapidly from a high-NO_x regime to a low-NO_x regime than RACM2, as documented by a map of HO_2/NO concentration ratios (not shown), which are greater with CB05 than with RACM2. As a result, CB05 is more conducive to SOA formation than RACM2.

This result demonstrates that the formation of SOA is very closely tied to the gas-phase

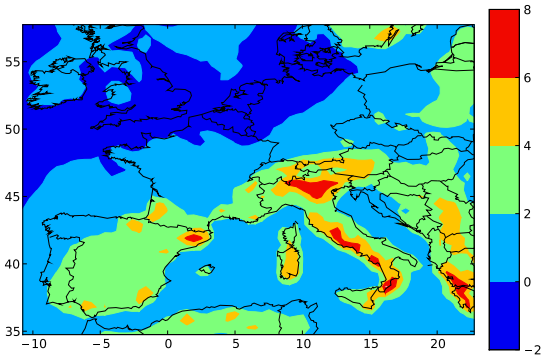

(a) **[PM**$_{2.5}$**]**$_{CB05,AEC}$ **- [PM**$_{2.5}$**]**$_{CB05,SORGAM}$

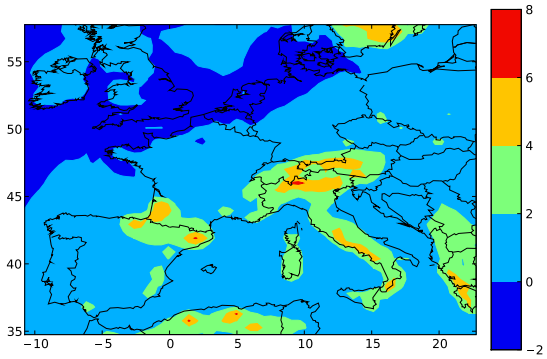

(b) **[PM**$_{2.5}$**]**$_{RACM2,AEC}$ **- [PM**$_{2.5}$**]**$_{RACM2,SORGAM}$

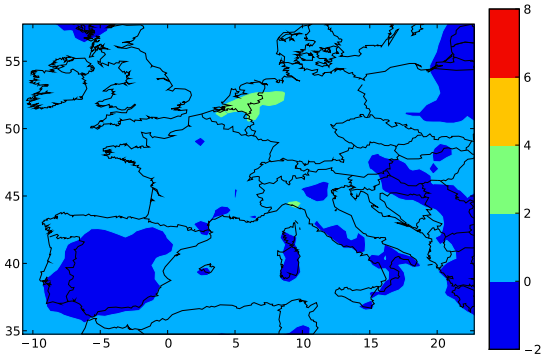

(c) **[PM**$_{2.5}$**]**$_{RACM2,AEC}$ **- [PM**$_{2.5}$**]**$_{CB05,AEC}$

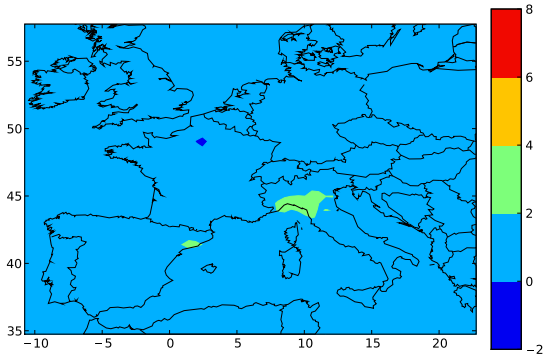

(d) **[PM**$_{2.5}$**]**$_{RACM2,SORGAM}$ **- [PM**$_{2.5}$**]**$_{CB05,SORGAM}$

Figure 4.4: Differences in $PM_{2.5}$ concentrations ($\mu g/m^3$) over Europe simulated with RACM2 and CB05 for gas-phase chemistry and with AEC and SORGAM for SOA formation. Results are averaged over the one-month simulation of 15 July to 15 August 2001: (a) $[PM_{2.5}]_{CB05,AEC}$ - $[PM_{2.5}]_{CB05,SORGAM}$ (top left); (b) $[PM_{2.5}]_{RACM2,AEC}$ - $[PM_{2.5}]_{RACM2,SORGAM}$ (top right); (c) $[PM_{2.5}]_{RACM2,AEC}$ - $[PM_{2.5}]_{CB05,AEC}$ (bottom left); (d) $[PM_{2.5}]_{RACM2,SORGAM}$ - $[PM_{2.5}]_{CB05,SORGAM}$ (bottom right).

chemical kinetic mechanism because the types of SOA formed and, therefore, the SOA yields differ in low-NO_x versus high-NO_x regimes. Consequently, uncertainties in the gas-phase chemistry and the aerosol module should not be treated separately but jointly.

4.5 Conclusion

The gas-phase chemical mechanism and aerosol module used in air quality models are shown to influence the simulated ozone and PM concentrations. Differences in SOA formation resulting from the use of different modules are more significant than those due to gas-phase chemistry

and can be up to about 65%. The major sources of those differences include the following: the list of VOC included as VOC precursors (+66%, particularly isoprene, +44%), the explicit treatment of high-NO_x and low-NO_x regimes in the gas-phase chemistry leading to SOA (+32% to +122% depending on the implementation within the gas-phase chemical mechanism), and the treatment of oligomerization (+60%). Further work is needed to develop gas-phase chemical kinetic mechanisms that can explicitly account for different SOA yields depending on the oxidation pathways for high-NO_x (e.g., organonitrate formation) and low-NO_x (e.g., peroxide formation) regimes.

The enthalpies of vaporization have a small effect on average (4%) but may have an important effect locally with lower values leading to less SOA in regions with low temperature and more SOA in regions with high temperature.

The treatment of activity coefficients in the particulate phase has a small effect on average (+9%); however, the effect can be significant in some areas. Furthermore, the values of the activity coefficients may differ significantly between their implicit value in SORGAM and their calculated values in AEC because the activity coefficients of an SOA compound may differ significantly between their values in a smog chamber experiment with only one precursor and ammonium sulfate seed particles under dry conditions and the atmosphere where a myriad of SOA and POA species interact with inorganic salts and water.

The treatment of isoprene SOA (hydrophobic in SORGAM and hydrophilic in AEC) has a significant effect on SOA concentrations: 0.15 $\mu g/m^3$ of isoprene SOA is formed with SORGAM, whereas 0.34 $\mu g/m^3$ is formed with AEC. This result is consistent with that obtained by Pun [2008], who found a large increase in SOA concentration when hydrophilic SOA condensed in an aqueous phase. However, the two models differ because AEC includes interactions among SOA and inorganic salts in the aqueous phase, whereas the model of Pun [2008] only considered SOA in the aqueous phase. Further investigations appear warranted to better characterize the effect of an atmospheric aqueous particulate phase on isoprene SOA. Aqueous-phase formation of SOA species was not considered here; it could be a significant factor [Pun *et al.*, 2000; Lim *et al.*, 2005; Carlton *et al.*, 2008; Ervens *et al.*, 2008; El Haddad *et al.*, 2009; Deguillaume *et al.*, 2009] and should be investigated in future work.

The uncertainties due to the gas-phase chemistry and to the aerosol module are not additive and some strong nonlinearities occur for PM concentrations. In this study, one gas-phase chemical mechanism led to greater secondary inorganic aerosol formation, but to less secondary organic aerosol formation due to the intricate interactions between the gas-phase mechanism and secondary aerosol formation processes. These results have implications for air quality modeling in general, as they highlight which processes appear to be the most important for SOA modeling and the uncertainties associated with neglecting or parameterizing those processes.

Chapitre 5

Modélisation de la distribution verticale des PM_{10} : Évaluation météorologique

Résumé

La dispersion verticale des polluants atmosphériques dans la couche limite atmosphérique (CLA) est principalement dominée par la turbulence, en dehors des zones de convection forte. Un schéma de fermeture est nécessaire pour décrire les flux turbulents dans la CLA. Nous avons évalué quatre paramétrisations des flux turbulents verticaux qui sont actuellement opérationnelles dans le modèle météorologique WRF (Weather Research and Forecast).

YSU (the Yonsei University) est une paramétrisation obtenue à partir d'une paramétrisation appelée MRF (Medium-Range Forecast). Le schéma de fermeture est non-local et YSU utilise un terme de "*contre-gradient*". ACM2 est la nouvelle version d'ACM (Asymmetric Convective Model). ACM2 utilise aussi un schéma de fermeture non-local. Dans ACM2, la non-localité est représentée en utilisant un terme qui définit le flux de masse entre toute paire de couches du modèle, même si elles ne sont pas adjacentes. Les deux autres paramétrisations MYJ (Mellor-Yamada-Janjic) et MYNN (Mellor-Yamada-Nakanishi et Niino) utilisent des schémas de fermeture locaux. MYJ et MYNN déterminent la diffusion turbulente par l'énergie cinétique turbulente calculée pronostiquement. La principale différence entre MYJ et MYNN est la méthode utilisée pour déterminer les paramètres inconnus : MYJ utilise des observations alors que MYNN utilise des résultats de simulations à grande échelle.

Le modèle météorologique WRF est utilisé pour calculer les champs météorologiques sur trois domaines emboîtés bi-directionnellement : le plus grand domaine de résolution 0,5 ° × 0,5 ° couvre l'Europe, le deuxième domaine de résolution 0,125 ° × 0,125 couvre la France et le plus petit domaine de résolution 0,03125 ° × 0,03125 ° couvre l'Île de France. Il y a 28 niveaux verticaux raffinés près du sol et la pression au sommet du modèle est de 100 hPa. La période simulée correspond aux trois semaines du 6 au 27 mai 2005, et les résultats simulés sont sauvegardés toutes les 30 minutes pour les simulations sur le plus petit domaine.

Les données météorologiques obtenues avec les quatre paramétrisations sont comparées aux observations à différentes stations météorologiques en Île de France. La température est relativement bien modélisée par toutes les paramétrisations et les performances de MYNN sont légèrement meilleures que les autres. Cependant, les températures sont sous-estimées, particulièrement pendant la journée, et les sous-estimations ont tendance à augmenter avec l'altitude.

Des erreurs significatives sont constatées pour la vitesse du vent. L'erreur moyenne fractionnelle (EMF) et le biais moyen fractionnel (BMF) avec MYJ pour la vitesse à 10 mètres atteignent 76% et 73%, respectivement. De meilleurs performances sont obtenues avec les paramétrisations YSU et MYNN ; cependant la vitesse du vent reste surestimée, surtout près du sol (BMF : 66% pour YSU et 61% pour MYNN). La surestimation diminue avec l'altitude. Pour l'humidité, les valeurs modélisées sont en bon accord avec les valeurs observées pour les quatre paramétrisations, bien que l'humidité relative tend à être surestimée (BMF : 12% pour YSU, 21% pour ACM2). YSU et MYNN ont les meilleures performances pour l'humidité relative au sol et pour les profils de radiosondes d'humidité spécifique.

Les hauteurs de la CLA diagnostiquées à partir de différents schémas présentent des différences importantes. D'une part, les hauteurs de la CLA simulées sont comparées à celles mesurées par radiosonde à 0000 et 1200 UTC à Trappes. À 1200 UTC, les hauteurs obtenues avec les différentes paramétrisations sont sous-estimées : le BMF varie de -13% pour MYJ à -41% pour MYNN. En revanche, à 0000 UTC, les hauteurs obtenues par YSU et MYJ sont surestimées et celles obtenues par ACM2 et MYNN sont sous-estimées. La différence maximale entre les quatre hauteurs moyennes simulées par les différentes paramétrisations est de 20% (180 m) à 1200 UTC et de 335% (500 m) à 0000 UTC. D'autre part, les hauteurs de la CLA simulées sont également comparées à des hauteurs de la CLA estimées à partir de profils lidar. Les mesures lidar ont été effectuées à partir d'un véhicule mobile de la banlieue de Paris (Palaiseau) au centre de Paris (Les Halles) les 24 et 25 mai, pendant la nuit ou au lever du jour. Toutes les paramétrisations sous-estiment les hauteurs de la CLA le 24 mai, sauf YSU au centre de Paris où les hauteurs modélisées sont surestimées (750 m contre 486 m pour la mesure). Cette surestimation est due à une température potentielle simulée au sol qui est aussi élevée que celle à 750 m d'altitude, provoquant une instabilité dans la CLA. Pour le 25 mai, toutes les paramétrisations sous-estiment largement les hauteurs de la CLA. La moyenne des hauteurs modélisées est inférieure à 100 m sauf pour YSU (130 m) tandis que la hauteur moyenne observée par le lidar est d'environ 390 m.

La différence de température entre la zone urbaine et les environs ruraux est d'environ 8 à 12 °C pour les villes d'un million d'habitants ou plus. Cette différence est principalement due à un dégagement de chaleur anthropique par le chauffage, le transport, l'éclairage, les activités industrielles, etc. L'inclusion du dégagement de chaleur anthropique dans le modèle météorologique affecte la température de surface et par conséquent, le bilan thermique et la température de l'air. Ces augmentations de température affectent le développement de la CLA dans les régions urbanisées.

Pour considérer l'effet de l'urbanisation, le modèle de canopée urbaine de WRF, appelé UCM (Urban Canopy Model), est utilisé dans cette étude. Le dégagement de chaleur anthropique en Île de France est calculé approximativement à partir de données bibliographiques. Pour considérer les changements récents de l'occupation des sols, la base de données "*Corine*" gérée par l'Agence Européenne pour l'Environnement (AEE) est utilisée.

L'utilisation d'UCM et de "*Corine*" (UCM-Corine) rend les données météorologiques obtenues avec WRF plus réaliste, en particulier pour la vitesse du vent, l'humidité relative et la hauteur de la CLA qui sont significativement améliorées en utilisant UCM-Corine. En particulier, UCM-Corine augmente la hauteur de la CLA sur la surface urbanisée. Cette augmentation est plus importante pendant la nuit que pendant la journée. Pour la comparaison aux données de hauteurs de la CLA obtenues à partir des radiosondes, l'utilisation d'UCM-Corine entraîne une augmentation de la hauteur de la CLA de 8% avec YSU et de 5% avec MYNN à 1200 UTC,

de 15% avec YSU et de 200% avec MYNN à 0000 UTC. Les différences entre les simulations sans/avec UCM-Corine pour la hauteur moyenne de la CLA du 6 au 27 mai en Île de France sont importantes jusqu'à 30 km de Paris. Par ailleurs, la mise à jour de la base de donnée d'occupation des sols avec des données récentes influence de manière significative les hauteurs de la CLA, surtout entre 10 km et 30 km de Paris.

L'influence de l'utilisation d'UCM-Corine sur les variables météorologiques modélisées est supérieure à celle des différentes paramétrisations de la CLA à la surface, tandis que cette dernière est plus grande pour les températures des couches supérieures de la CLA (au-dessus de 40 mètres) et pour les hauteurs de la CLA estimées par profil de radiosonde à Trappes. Pour les hauteurs de la CLA par lidar, l'influence du choix de la paramétrisation de CLA est plus importante que celle de UCM-Corine dans la banlieue de Paris, tandis que cette dernière est plus importante au centre de Paris.

Ces résultats démontrent l'importance des flux de chaleur anthropique et d'une base de données d'occupation des sols précise pour obtenir une représentation satisfaisante de la météorologie urbaine.

Ce chapitre est constitué de
Kim, Y. et Sartelet, K. (2011). **Evaluation of the modeling of the PM_{10} vertical distribution over Greater Paris : Part I - Meteorological evaluation**. soumis à *Tellus B*.

Sommaire

5.1 Introduction

The vertical dispersion of atmospheric pollutants in the planetary boundary layer (PBL) is mostly governed by motions caused by turbulence. For the vertical dispersion, the temperature stratification plays an important role in defining the atmospheric stability, the intensity of thermal turbulence and the depth of the boundary layer. They regulate the upward dispersion of pollutants and the rate of replacement of cleaner air from above [Oke, 1987].

Many experimental campaigns have been dedicated to understand the atmospheric motion and the vertical structure of the atmosphere in North America [Stull *et al.*, 1997; Fast *et al.*, 2000; Doran *et al.*, 2002] and in Europe [Rotach, 1995; Ulden et Wieringa, 1996; Argentini *et al.*, 1999; Dupont *et al.*, 1999]. Numerical experiments have also been carried out to depict the vertical atmospheric motion and to evaluate numerical parameterizations for boundary layer modeling [Pleim et Chang, 1992; Holtslag *et al.*, 1995; Hong et Pan, 1996; Hong *et al.*, 2006; Pleim, 2007; Srinivas *et al.*, 2007; Borge *et al.*, 2008; Nakanishi et Niino, 2009; Olson et Brown, 2009; Hu *et al.*, 2010; Kim *et al.*, 2010a].

The temperature difference between urban area and surrounding rural area is thought to be 2 to 3°C for cities with a population of about 1000 inhabitants and it increases around 8 to 12°C for cities of a million or more inhabitants [Stull, 1988]. The difference is mostly due to anthropogenic heat release by space heating, manufacturing, transportation, lighting, etc. [Oke, 1987; Stull, 1988]. Including the anthropogenic heat release in the meteorological model affects the surface temperature and then the temperature in the upper air. The temperature changes then affect the development of PBL in urbanized regions [Lin *et al.*, 2008]. The diurnal evolution of anthropogenic heat release in cities in the United States and in France is different. The effect of the anthropogenic heat release has been studied by Dupont *et al.* [2004]; Sailor et Lu [2004]; Fan et Sailor [2005] over U.S. and by Sarrat *et al.* [2006]; Pigeon *et al.* [2007]; Sarkar et De Ridder [2011] over France.

This study focuses on the comparison of modeled meteorological data in the PBL to observation data over Paris and its suburbs. First, we present modeling of meteorological conditions. The settings of the model (the Weather Research and Forecast, WRF) used here are described. Because the parameterization of the vertical dispersion of pollutants is one of the largest uncertainties in air quality modeling [Roustan *et al.*, 2010b], four PBL schemes are used in this study. Simulation results are compared to meteorological measurements. A sensitivity study of meteorological data to the PBL schemes is performed, as well as to urban canopy models and land-use data.

5.2 The Weather Research and Forecast model (WRF)

The meteorological inputs are crucial to correctly simulate the vertical dispersion of PM in air quality models. In particular, accurate modeling of the boundary layer, where vertical mixing is strong, is needed. WRF version 3.3 with the Advanced Research WRF (ARW) dynamics solver is used to obtain meteorological inputs [Skamarock *et al.*, 2008].

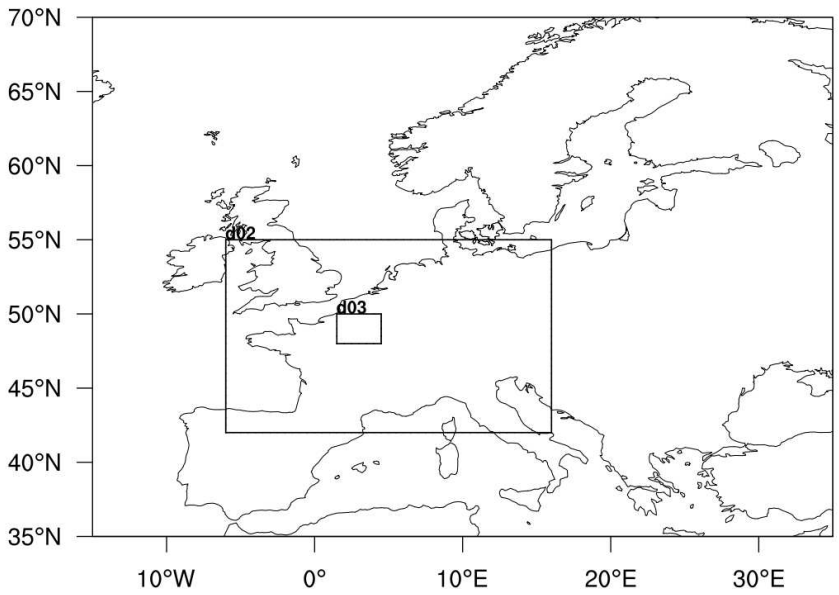

Figure 5.1: Modeling domains for WRF simulations.

5.2.1 Simulation settings

The regular latitude-longitude map projection is used for three simulation domains with two-way nesting. Horizontal grid spacing of the coarse domain is 0.5° and those of the two nested domains are 0.125° and 0.03125°. The largest 0.5° domain covers Europe and the smallest domain covers Paris and its suburbs (hereafter Greater Paris), as shown in Figure 5.1. The U.S. Geological Survey (USGS) Global Land Cover Characteristics (GLCC) database is used (10-arcminute, 2-arcminute and 30-arcsecond land-use data for the three domains, respectively). There are 28 vertical levels refined near the surface and the pressure at the model top is 100 hPa. The physical parameterizations used include the Kessler microphysics scheme [Kessler, 1969], the RRTM longwave radiation scheme [Mlawer *et al.*, 1997], the Goddard shortwave scheme [Chou et Suarez, 1994], the Grell-Devenyi ensemble cumulus parameterization scheme [Grell et Devenyi, 2002] and the Noah land surface model [Chen et Dudhia, 2001]. The National Centers for Environmental Prediction (NCEP) final (FNL) operational model global tropospheric analyses are used for initial and boundary conditions. The NCEP FNL analyses are available on a $1.0^\circ \times 1.0^\circ$ grid every six hours. The 3-dimensional analysis nudging method of the NCEP analyses is used in WRF. The simulations are carried out for three weeks from 6 May to 27 May 2005, and simulated results are saved every 30 minutes for the finer grid simulations.

5.2.2 Planetary boundary layer schemes

The PBL is defined as the part of the troposphere that is directly influenced by the presence of the Earth's surface. The surface warms up and cools down in response to solar radiation and

it forces meteorological changes in the boundary layer via processes, such as turbulence, convection, etc. In general, a parameterization is used to depict the turbulence in the PBL because the set of equations for turbulence is very complex and the number of unknowns in the set of equations is larger than the number of equations [Stull, 1988]. We evaluate, here, four PBL schemes which are currently operational in WRF. Brief descriptions of these schemes are given below.

The Yonsei University (YSU) scheme [Hong *et al.*, 2006] is a revised Medium-Range Forecast (MRF) scheme [Hong et Pan, 1996]. The YSU scheme is a nonlocal closure scheme, where an unknown quantity at one point is parameterized by values of known quantities at many points [Stull, 1988]. In the YSU and MRF schemes, a counter-gradient term is incorporated to apply the nonlocal closure. This term is a correction of the local gradient of heat and water vapor. It incorporates the contribution of the large-scale eddies to the total flux in the PBL under unstable conditions [Hong et Pan, 1996].

The second scheme, ACM2 is the new version of the Asymmetric Convective Model (ACM) scheme [Pleim, 2007]. The ACM2 scheme is also a nonlocal closure scheme. In the ACM schemes, the nonlocality is represented by using a transilient term that defines the mass flux between any pair of model layers even if they are not adjacent [Pleim et Chang, 1992]. The ACM2 scheme adds an eddy diffusion component to the transilient term of the original ACM scheme.

The Mellor-Yamada-Janjic (MYJ) scheme [Janjic, 2001] is a local closure scheme, where an unknown quantity at any point is parameterized by values and/or gradients of known quantities at the same point [Stull, 1988]. The MYJ scheme determines eddy diffusivities from prognostically calculated turbulent kinetic energy (TKE) [Hu *et al.*, 2010]. The Mellor-Yamada-Nakanishi and Niino (MYNN) level 2.5 scheme [Nakanishi et Niino, 2004] is also a TKE-based scheme. The MYNN scheme and the MYJ scheme are developed to improve performances of its original Mellor-Yamada model [Mellor et Yamada, 1974]. Major differences between the two schemes are formulations of mixing length scale and method to determine unknown parameters. The MYJ scheme uses observations to determine unknown parameters while the MYNN scheme uses large-eddy simulation (LES) results. Olson et Brown [2009] highlighted the differences between the MYJ and the MYNN schemes. The MYNN scheme has larger TKE and mixing length, which lead to slightly larger mixed-layer depths in the MYNN scheme than in the MYJ scheme.

5.2.3 Urban surface models

To consider the effect of urbanization, WRF includes three urban surface models: the Urban Canopy Model (UCM) [Kusaka *et al.*, 2001], the Building Environment Parameterization (BEP) [Martilli *et al.*, 2002] and the Building Energy Model (BEM) [Salamanca *et al.*, 2010]. UCM is a simple single-layer model, while BEP and BEM are multi-layer models. Urban models are used to represent the influence of urbanization on the surface temperature. Kusaka *et al.* [2001] showed that the diurnal variations of surface temperatures from UCM are close to those from the multi-layer models. In addition, UCM explicitly includes the anthropogenic heat release in the total heat flux. It is not explicitly represented in the multi-layer models. Therefore UCM is used for this study.

Geometric (building height, building width, road width, etc.) and thermal parameters (an-

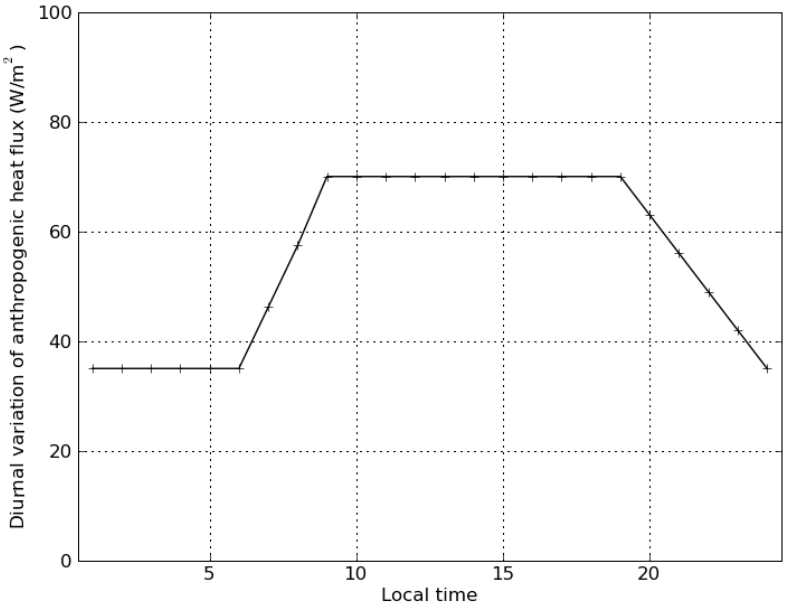

Figure 5.2: Diurnal variation of anthropogenic heat flux for Paris in May.

thropogenic heat, thermal conductivities, heat capacity, etc.) for UCM have a significant effect on the transfer of energy and momentum between the urban surface and the atmosphere. The parameters used in this study are summarized in Table 5.1. A reference width of 15 m corresponding to the sum of the building and road widths is taken. The ratio of the building to the road width was estimated using Google maps (`http://maps.google.fr/`). The ratio of the building to the road width is taken as 0.25 (3.75 m) and 0.50 (7.5 m) for the suburbs of Paris and for Paris center, respectively. Other parameters are based on Kusaka *et al.* [2001].

The anthropogenic heat release (hereafter AH) in Paris is calculated by the method of Sarkar et De Ridder [2011]. The annual mean AH in Paris is 59.6 W m^{-2} based on Makar *et al.* [2006] (see also `http://www.iiasa.ac.at/Research/TNT/WEB/heat/`). Monthly AH are assumed to follow the evolution of monthly mean AH in Toulouse in southern France [Pigeon *et al.*, 2007]. The diurnal variation of AH for Paris is based on the diurnal variation for Marseille in France [Demuzere *et al.*, 2008]. Figure 5.2 presents the diurnal variation of AH for Paris in May.

The USGS land-use data are commonly used in WRF. However, this database was created in 1993 and the land-use changes between 1993 and 2005 are important over Greater Paris according to the database of the European Environment Agency (EEA). Therefore, the recent Corine land-use map of EEA is used instead of USGS. In order to use the Corine land-use data in the WRF simulations, the land-use categories of the Corine land-use data were converted to the categories of the USGS data following Pineda *et al.* [2004]. The geographical coordinate system of the Corine land-use data, European Terrestrial Reference System 1989 (ETRS89) - Lambert Azimuthal Equal Area (LAEA) is not directly usable in WRF. Thus the reprojection of the coordinate system to World Geodetic System 1984 (WGS84) was carried out following Arnold *et al.* [2010]. The Corine land cover 2006 raster data (version 13) with a resolution

Table 5.1: Geometric and thermal parameters for the urban canopy model.

Parameter	Value
Building height	12 m
Roof width	3.25 m
Road width	11.25 m
Urban area ratio for a grid	0.95
Vegetation area ratio for a grid	0.05
Anthropogenic heat	70 W m^{-2}
Diurnal profile of anthropogenic heat	see Figure 5.2
Surface albedo of roof, road and wall	0.20
Surface emissivity of roof, road and wall	0.97
Volumetric heat capacity of roof, road and wall	2.01×10^6 J m^{-3} K^{-1}
Thermal conductivity of roof, road and wall	2.28 W m^{-1} K^{-1}

of 250 m, which are freely available at `http://www.eea.europa.eu/data-and-maps/data/corine-land-cover-2006-raster`, were used for this study.

5.3 Measurements

We compared the results obtained using the four PBL schemes to meteorological measurements provided by various observatories. Figure 5.3 presents the locations of the measurement stations. A French national atmospheric observatory, Site Instrumental de Recherche par Télédétection Atmosphérique (SIRTA) provides measurements of wind speed/direction, temperature, pressure, relative humidity and precipitation rate at a ground station located in Palaiseau, 20 km south west of Paris, in a semi-urban environment [Haeffelin *et al.*, 2005]. SIRTA also provides radiosonde profiles of pressure, temperature, potential/virtual potential temperature, relative/specific humidity, wind speed/direction and PBL height performed at 0000 and 1200 UTC at Trappes. The PBL heights at Trappes are retrieved using radiosonde profiles of the virtual potential temperature. The convective boundary layer height is taken as the height where the virtual potential temperature begins to increase. The stable boundary layer height is taken as the height where the first important variation in the vertical gradient of the virtual potential temperature occurs [Dupont *et al.*, 1999]. The station in Trappes is 15 km west away from the SIRTA site in Palaiseau and it is in a urban environment. Details on the measurements are available at `http://sirta.ipsl.polytechnique.fr`. The Commissariat à l'Energie Atomique (CEA) operates an observation mast of 100 meters high in Saclay. Hourly measurements are carried out for wind speed/direction, relative humidity, pressure, precipitation rate, solar radiation and temperature at various heights. The mast is located in a rural environment. The French national meteorological service organization, Météo-France operates an observation deck on the Eiffel Tower in Paris. Hourly measurements are carried out at a height of 319

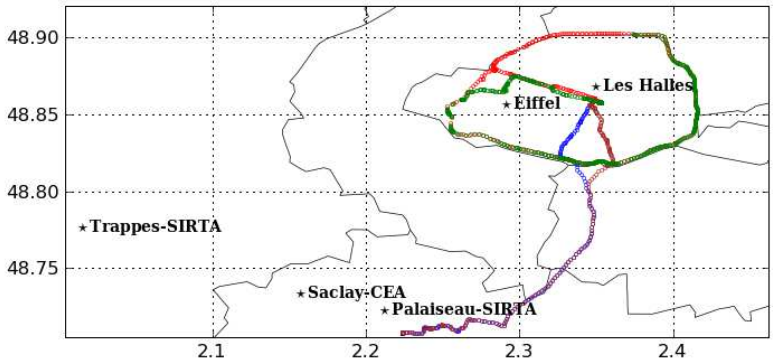

Figure 5.3: Locations of meteorological observation stations and route taken for the measurements of the GBML. Blue and brown marks show the route for the measurements from the suburbs of Paris to Paris center for 24 May and 25 May, respectively. Red ones are for the measurements on the beltway of Paris before rush-hour and green ones are for the measurements on the beltway during rush-hour.

m. The comparison is performed for the period from 6 May to 27 May 2005.

Lidar data are also used to estimate the PBL height. A ground-based mobile lidar (GBML) was used during the air quality observation campaign, LIdar pour la Surveillance de l'AIR (LISAIR) for Greater Paris from 24 May to 27 May 2005 [Raut et Chazette, 2009]. Observations of the aerosol extinction coefficients profiles by the GBML were performed to retrieve the multiple boundary layers in the free troposphere and in turn the vertical distribution of PM (see Part II, Kim et Sartelet, 2011b). The PBL height is obtained from the vertical derivative of the aerosol extinction coefficients profile following Raut [2008]. The PBL height is the altitudes where the derivative is minimum. Two kinds of observations were performed with the GBML: the PM gradients between the suburbs of Paris and Paris center were observed, and observations along the main roads (from Les Halles to the Arc de Triomphe through the Avenue des Champs-Élysées) and the beltway of Paris were carried out. Routes followed by the automobile embarking the lidar are presented in Figure 5.3. Details on the GBML measurements can be found in Raut et Chazette [2009].

Table 5.2: Definitions of the statistical indicators.

Indicators	Definitions
Root mean square error (RMSE)	$\sqrt{\frac{1}{n}\sum_{i=1}^{n}(c_i - o_i)^2}$
Mean fractional bias (MFB) and mean fractional error (MFE)	$\frac{1}{n}\sum_{i=1}^{n}\frac{c_i - o_i}{(c_i + o_i)/2}$ and $\frac{1}{n}\sum_{i=1}^{n}\frac{\mid c_i - o_i \mid}{(c_i + o_i)/2}$
Normalized mean bias (NMB) and normalized mean error (NME)	$\frac{\sum_{i=1}^{n}(c_i - o_i)}{\sum_{i=1}^{n} o_i}$ and $\frac{\sum_{i=1}^{n}(\mid c_i - o_i \mid)}{\sum_{i=1}^{n} o_i}$
Mean normalized bias (MNB) and mean normalized gross error (MNGE)	$\frac{1}{n}\sum_{i=1}^{n}\frac{c_i - o_i}{o_i}$ and $\frac{1}{n}\sum_{i=1}^{n}\frac{\mid c_i - o_i \mid}{o_i}$
Correlation coefficient	$\frac{\sum_{i=1}^{n}(c_i - \overline{c})(o_i - \overline{o})}{\sqrt{\sum_{i=1}^{n}(c_i - \overline{c})^2}\sqrt{\sum_{i=1}^{n}(o_i - \overline{o})^2}}$ with $\overline{o} = \frac{1}{n}\sum_{i=1}^{n} o_i$ and $\overline{c} = \frac{1}{n}\sum_{i=1}^{n} c_i$

c_i: modeled values, o_i: observed values, n: number of data.

5.4 Comparisons to measurements: sensitivity to the PBL schemes

The fine-grid simulation results for Greater Paris are used for the comparisons to measurements. The statistical indicators used in this study are the root mean square error (RMSE), the mean fractional bias and error (MFB and MFE), the normalized mean bias and error (NMB and NME) and the correlation coefficient. They are defined in Table 5.2. Statistical indicators for the comparison to measurements are given in Tables 5.3a-5.3d for the four different simulations done with the different PBL schemes.

Table 5.3a: Comparison of modeled values with the YSU PBL scheme to observations.

Variables*	Observed mean	Modeled mean	RMSE†	MFB†	MFE†	NMB†	NME†	Correlation†
T2 at Palaiseau	13.7 °C	12.7 °C	2.82 °C	**-0.06**	0.20	**-0.05**	0.19	0.80
T40 at Saclay	12.5 °C	10.9 °C	2.92 °C	**-0.15**	0.21	**-0.13**	0.19	0.83
T100 at Saclay	12.1 °C	10.4 °C	2.93 °C	-0.17	0.23	-0.14	0.20	0.84
T319 at Eiffel	13.0 °C	9.8 °C	4.23 °C	-0.32	0.35	-0.25	0.27	0.87
PT_{12h} at Trappes	296.4 K	294.4 K	2.41 K	**-0.01**	**0.01**	**-0.01**	**0.01**	**0.99**
PT_{00h} at Trappes	295.8 K	293.5 K	2.63 K	**-0.01**	**0.01**	**-0.01**	**0.01**	**0.99**
WS10 at Palaiseau	2.31 m/s	4.11 m/s	2.23 m/s	0.66	0.71	1.08	1.16	0.34
WS58 at Saclay	4.72 m/s	6.12 m/s	2.03 m/s	0.29	0.35	0.29	**0.35**	**0.66**
WS110 at Saclay	5.91 m/s	6.87 m/s	**1.93 m/s**	**0.19**	**0.28**	**0.16**	**0.25**	**0.67**
WS319 at Eiffel	6.38 m/s	7.56 m/s	**2.72 m/s**	**0.18**	**0.31**	**0.18**	**0.34**	**0.64**
WS_{12h} at Trappes	11.43 m/s	11.19 m/s	**2.44 m/s**	**0.07**	**0.25**	**0.05**	**0.24**	0.69
WS_{00h} at Trappes	12.17 m/s	11.68 m/s	**2.54 m/s**	**0.00**	**0.23**	**0.04**	**0.23**	0.81
RH at Palaiseau	0.65	0.71	**0.14**	**0.12**	**0.20**	**0.11**	**0.19**	0.68
SH_{12h} at Trappes	2.59 g/kg	2.74 g/kg	0.84 g/kg	0.09	**0.34**	0.06	0.26	**0.94**
SH_{00h} at Trappes	2.57 g/kg	2.51 g/kg	0.73 g/kg	0.05	0.30	**0.00**	0.22	0.93
$PBLH_{12h}$ at Trappes	1227 m	963 m	418 m	-0.25	0.34	-0.21	0.28	0.71
$PBLH_{00h}$ at Trappes	322 m	652 m	446 m	0.60	0.64	1.02	1.09	0.31
PBLH by lidar								
Palaiseau-Paris (24 May)	425 m	480 m	170 m	**0.06**	0.31	**0.13**	0.33	0.26
Palaiseau-Paris (25 May)	390 m	127 m	**267 m**	**-1.01**	**1.01**	**-0.67**	**0.67**	0.40
Paris before rush-hour	445 m	83 m	**363 m**	**-1.38**	**1.38**	**-0.81**	**0.81**	**0.48**
Paris during rush-hour	376 m	111 m	271 m	-1.09	1.09	-0.71	0.71	-0.60

*: Tx: x-m temperature, PT: potential temperature, WSx: x-m wind speed, RH: relative humidity, SH: specific humidity, PBLH: planetary boundary layer height, tiny letters $_{00h}$ and $_{12h}$ mean radiosonde profiles at 0000 and 1200 UTC at Trappes, respectively.
†: see Tabel 5.2.
Values with boldface indicate best performance among the PBL schemes.

Table 5.3b: Comparison of modeled values with the ACM2 PBL scheme to observations.

Variables*	Observed mean	Modeled mean	RMSE†	MFB†	MFE†	NMB†	NME†	Correlation†
T2 at Palaiseau	13.7 °C	11.9 °C	2.91 °C	-0.11	0.20	-0.11	0.18	0.84
T40 at Saclay	12.5 °C	10.3 °C	3.10 °C	-0.20	0.23	-0.18	0.20	0.86
T100 at Saclay	12.1 °C	10.0 °C	2.96 °C	-0.19	0.23	-0.17	0.20	0.87
T319 at Eiffel	13.0 °C	9.8 °C	4.22 °C	-0.29	0.32	-0.25	0.27	0.88
PT_{12h} at Trappes	296.4 K	294.3 K	2.58 K	**-0.01**	**0.01**	**-0.01**	**0.01**	**0.99**
PT_{00h} at Trappes	295.8 K	293.5 K	2.64 K	**-0.01**	**0.01**	**-0.01**	**0.01**	**0.99**
WS10 at Palaiseau	2.31 m/s	4.00 m/s	2.11 m/s	0.62	0.69	1.00	1.08	0.40
WS58 at Saclay	4.72 m/s	6.25 m/s	2.20 m/s	0.30	0.38	0.32	0.39	0.63
WS110 at Saclay	5.91 m/s	7.17 m/s	2.30 m/s	0.21	0.33	0.21	0.31	0.61
WS319 at Eiffel	6.38 m/s	8.32 m/s	3.37 m/s	0.25	0.38	0.30	0.43	0.59
WS_{12h} at Trappes	11.43 m/s	11.23 m/s	2.75 m/s	**0.07**	0.27	0.08	0.28	0.68
WS_{00h} at Trappes	12.17 m/s	12.17 m/s	2.57 m/s	0.05	0.24	0.12	0.28	**0.85**
RH at Palaiseau	0.65	0.78	0.18	0.21	0.24	0.22	0.25	0.70
SH_{12h} at Trappes	2.59 g/kg	2.80 g/kg	0.85 g/kg	0.14	0.36	0.08	0.26	0.93
SH_{00h} at Trappes	2.57 g/kg	2.62 g/kg	0.74 g/kg	0.10	0.32	0.05	0.23	**0.94**
$PBLH_{12h}$ at Trappes	1227 m	972 m	472 m	-0.32	0.45	-0.21	0.33	0.66
$PBLH_{00h}$ at Trappes	322 m	224 m	**224 m**	-0.41	**0.63**	**-0.30**	**0.54**	0.21
PBLH by lidar								
Palaiseau-Paris (24 May)	425 m	168 m	259 m	-0.86	0.86	-0.60	0.60	**0.44**
Palaiseau-Paris (25 May)	390 m	50 m	343 m	-1.55	1.55	-0.87	0.87	**0.88**
Paris before rush-hour	445 m	74 m	373 m	-1.43	1.43	-0.83	0.83	-0.42
Paris during rush-hour	376 m	97 m	282 m	-1.18	1.18	-0.74	0.74	-0.55

*: see Table 5.3a, †: see Tabel 5.2.
Values with boldface indicate best performance among the PBL schemes.

Table 5.3c: Comparison of modeled values with the MYJ PBL scheme to observations.

Variables*	Observed mean	Modeled mean	RMSE†	MFB†	MFE†	NMB†	NME†	Correlation†
T2 at Palaiseau	13.7 °C	11.8 °C	2.93 °C	-0.15	0.22	-0.13	0.19	0.83
T40 at Saclay	12.5 °C	9.8 °C	3.51 °C	-0.27	0.30	-0.22	0.23	0.86
T100 at Saclay	12.1 °C	9.5 °C	3.42 °C	-0.28	0.30	-0.21	0.23	0.86
T319 at Eiffel	13.0 °C	9.22 °C	4.71 °C	-0.41	0.42	-0.29	0.31	0.87
PT_{12h} at Trappes	296.4 K	294.2 K	2.63 K	**-0.01**	**0.01**	**-0.01**	**0.01**	0.98
PT_{00h} at Trappes	295.8 K	293.3 K	2.84 K	**-0.01**	**0.01**	**-0.01**	**0.01**	**0.99**
WS10 at Palaiseau	2.31 m/s	4.55 m/s	2.60 m/s	0.73	0.76	1.30	1.33	0.39
WS58 at Saclay	4.72 m/s	6.01 m/s	**1.99 m/s**	**0.28**	**0.34**	**0.27**	**0.35**	0.64
WS110 at Saclay	5.91 m/s	6.99 m/s	2.11 m/s	0.20	0.30	0.18	0.28	0.63
WS319 at Eiffel	6.38 m/s	8.03 m/s	3.12 m/s	0.22	0.34	0.26	0.39	0.60
WS_{12h} at Trappes	11.43 m/s	11.43 m/s	2.73 m/s	0.08	0.27	0.09	0.27	0.64
WS_{00h} at Trappes	12.17 m/s	11.69 m/s	**2.54 m/s**	**0.00**	0.24	**0.04**	**0.23**	0.84
RH at Palaiseau	0.65	0.76	0.17	0.18	0.23	0.19	0.24	0.66
SH_{12h} at Trappes	2.59 g/kg	2.65 g/kg	0.89 g/kg	**0.07**	0.37	**0.01**	0.28	0.91
SH_{00h} at Trappes	2.57 g/kg	2.41 g/kg	0.83 g/kg	**0.02**	0.31	-0.04	0.24	0.88
$PBLH_{12h}$ at Trappes	1227 m	1070 m	**384 m**	**-0.13**	**0.32**	**-0.12**	**0.26**	0.66
$PBLH_{00h}$ at Trappes	322 m	593 m	487 m	**0.30**	0.68	0.84	1.07	**0.53**
PBLH by lidar								
Palaiseau-Paris (24 May)	425 m	319 m	**113 m**	-0.28	**0.28**	-0.25	**0.25**	-0.15
Palaiseau-Paris (25 May)	390 m	63 m	330 m	-1.45	1.45	-0.84	0.84	0.44
Paris before rush-hour	445 m	50 m	397 m	-1.59	1.59	-0.89	0.89	-0.41
Paris during rush-hour	376 m	178 m	**214 m**	**-0.74**	**0.74**	**-0.53**	**0.53**	-0.64

*: see Table 5.3a, †: see Tabel 5.2.
Values with boldface indicate best performance among the PBL schemes.

Table 5.3d: Comparison of modeled values with the MYNN PBL scheme to observations.

Variables*	Observed mean	Modeled mean	RMSE†	MFB†	MFE†	NMB†	NME†	Correlation†
T2 at Palaiseau	13.7 °C	12.6 °C	**2.57 °C**	-0.07	**0.17**	**-0.05**	**0.16**	**0.86**
T40 at Saclay	12.5 °C	10.9 °C	**2.62 °C**	**-0.15**	**0.19**	**-0.13**	**0.17**	**0.88**
T100 at Saclay	12.1 °C	10.6 °C	**2.50 °C**	**-0.14**	**0.18**	**-0.13**	**0.16**	**0.89**
T319 at Eiffel	13.0 °C	10.3 °C	**3.80 °C**	**-0.24**	**0.27**	**-0.21**	**0.24**	**0.89**
PT_{12h} at Trappes	296.4 K	294.5 K	**2.33 K**	**-0.01**	**0.01**	**-0.01**	**0.01**	**0.99**
PT_{00h} at Trappes	295.8 K	293.5 K	**2.60 K**	**-0.01**	**0.01**	**-0.01**	**0.01**	**0.99**
WS10 at Palaiseau	2.31 m/s	3.96 m/s	**2.04 m/s**	**0.61**	**0.65**	**0.97**	**1.02**	**0.49**
WS58 at Saclay	4.72 m/s	6.24 m/s	2.18 m/s	0.30	0.35	0.32	0.37	**0.66**
WS110 at Saclay	5.91 m/s	7.18 m/s	2.28 m/s	0.21	0.30	0.21	0.30	0.64
WS319 at Eiffel	6.38 m/s	8.16 m/s	3.15 m/s	0.23	0.33	0.28	0.37	0.63
WS_{12h} at Trappes	11.43 m/s	11.39 m/s	2.69 m/s	0.08	0.26	0.07	0.25	**0.73**
WS_{00h} at Trappes	12.17 m/s	12.27 m/s	2.63 m/s	0.07	0.25	0.12	0.27	0.82
RH at Palaiseau	0.65	0.74	0.15	0.16	**0.20**	0.16	0.21	**0.74**
SH_{12h} at Trappes	2.59 g/kg	2.80 g/kg	**0.83 g/kg**	0.12	0.36	0.09	**0.25**	**0.94**
SH_{00h} at Trappes	2.57 g/kg	2.58 g/kg	**0.69 g/kg**	0.07	**0.28**	0.03	**0.20**	0.93
$PBLH_{12h}$ at Trappes	1227 m	891 m	471 m	-0.41	0.47	-0.27	0.32	**0.74**
$PBLH_{00h}$ at Trappes	322 m	150 m	247 m	-0.92	1.00	-0.53	0.62	0.47
PBLH by lidar								
Palaiseau-Paris (24 May)	425 m	104 m	327 m	-1.24	1.24	-0.76	0.76	0.07
Palaiseau-Paris (25 May)	390 m	43 m	351 m	-1.60	1.60	-0.89	0.89	0.85
Paris before rush-hour	445 m	51 m	395 m	-1.59	1.59	-0.89	0.89	-0.50
Paris during rush-hour	376 m	71 m	308 m	-1.36	1.36	-0.81	0.81	**-0.36**

*: see Table 5.3a, †: see Tabel 5.2.
Values with boldface indicate best performance among the PBL schemes.

Figure 5.4 shows the mean diurnal variations of 2-m temperature at Palaiseau, 40-m and 100-m temperatures at Saclay and 319-m temperature at the Eiffel Tower. The modeled values agree relatively well with the observations for all the PBL schemes even though the temperatures are underestimated, particularly during the day. The differences between the PBL schemes are small though the statistics obtained with the MYNN scheme are slightly better than others. The underestimations of the 2-m temperature are not important: for the PBL schemes the MFB varies from -0.06 (YSU) to -0.15 (MYJ) and the NMB varies from -0.05 (YSU and MYNN) to -0.13 (MYJ). However the underestimations tend to increase with altitude and they are significant at the Eiffel Tower (MFB: -0.24 for MYNN to -0.41 for MYJ, NMB: -0.21 for MYNN to -0.29 for MYJ).

Figure 5.5 presents the observed and simulated mean vertical profiles of potential temperature at Trappes at 0000 and 1200 UTC. All the schemes underestimate the potential temperature

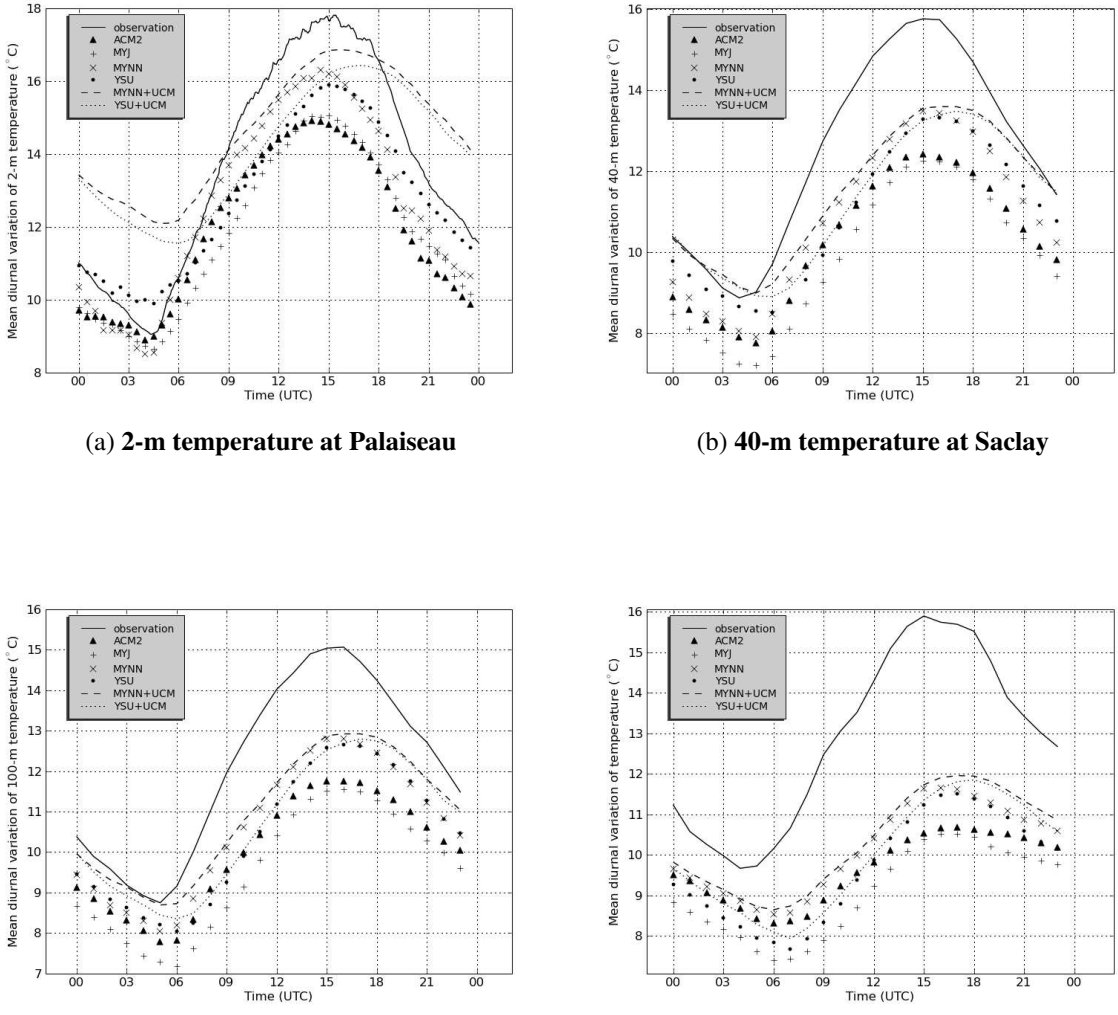

(a) **2-m temperature at Palaiseau**

(b) **40-m temperature at Saclay**

(c) **100-m temperature at Saclay**

(d) **319-m temperature at the Eiffel Tower**

Figure 5.4: Mean diurnal variation of observed and modeled temperatures.

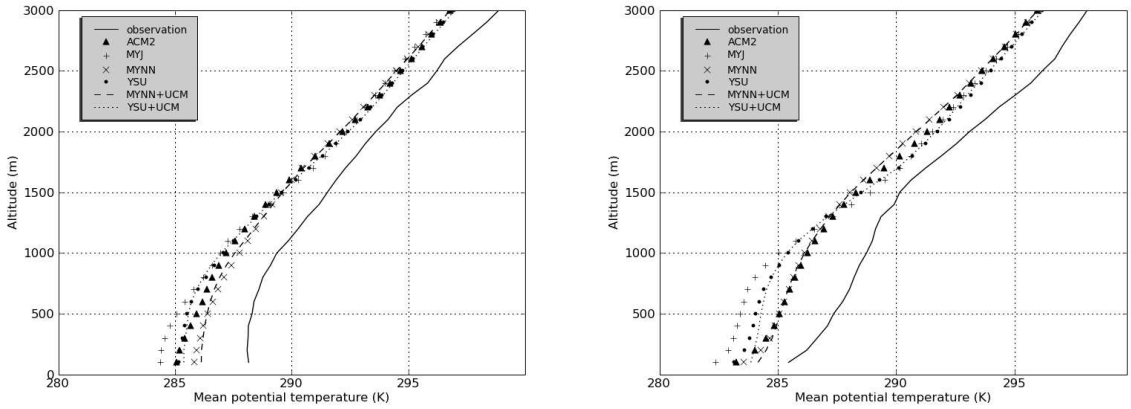

(a) **1200 UTC** (b) **0000 UTC**

Figure 5.5: Vertical profile of observed and modeled potential temperatures at Trappes.

for both the daytime and the nighttime observations. The MYNN scheme performs better than others under 1200 m height.

Figure 5.6 shows the mean diurnal variations of 10-m wind speed at Palaiseau, 58-m and 110-m wind speeds at Saclay and 319-m wind speed at the Eiffel Tower. The 10-m wind speed is overestimated with all the schemes. The overestimation of the MYJ scheme (MFB: 0.73) is higher than others (MFB: 0.66, 0.62 and 0.61 for YSU, ACM2 and MYNN respectively). The statistics obtained with the MYNN scheme are overall better than others. The diurnal variations of the 58-m and 110-m wind speed at Saclay compare better to observations than the 10-m wind speed at Palaiseau. Statistics obtained with the YSU scheme are the best among the schemes except RMSE, MFB/MFE and NMB of the 58-m wind speed, which are better with the MYJ scheme.

Figure 5.7 presents observed and simulated mean vertical profiles of wind speed at Trappes at 0000 and 1200 UTC. The four schemes overestimate the wind speed from the ground to around 1000 m in the daytime profile and they underestimate it above that height. The largest discrepancies between the different schemes are observed at night in the first 1000 m height. Close to the surface, the wind speed is underestimated by all schemes at night. The wind speed decreases near the surface with all the schemes and low-level jet develops around 500 m of height. The low-level jet with the ACM2 scheme and the MYNN scheme is stronger (11 m/s at peak) than that with the YSU scheme and the MYJ scheme (9 m/s at peak). The observed low-level jet has its peak of middle value between those of the simulations (about 10 m/s at peak) and the peak is vertically lower (200 m) than those of the modeled peaks (300 to 500 m). During daytime, except for the correlation coefficient, the YSU scheme shows the better statistics. During nighttime the YSU and the MYJ schemes show the best statistics.

Figure 5.8 displays the mean diurnal variations of surface relative humidity (RH) at Palaiseau. The modeled values agree well with observations for all the PBL schemes (about 20% of errors and biases). RH is slightly overestimated by all the schemes. The statistics obtained with the YSU scheme are slightly better than others, except the correlation coefficient.

Figure 5.9 presents observed and simulated mean vertical profiles of specific humidity (SH)

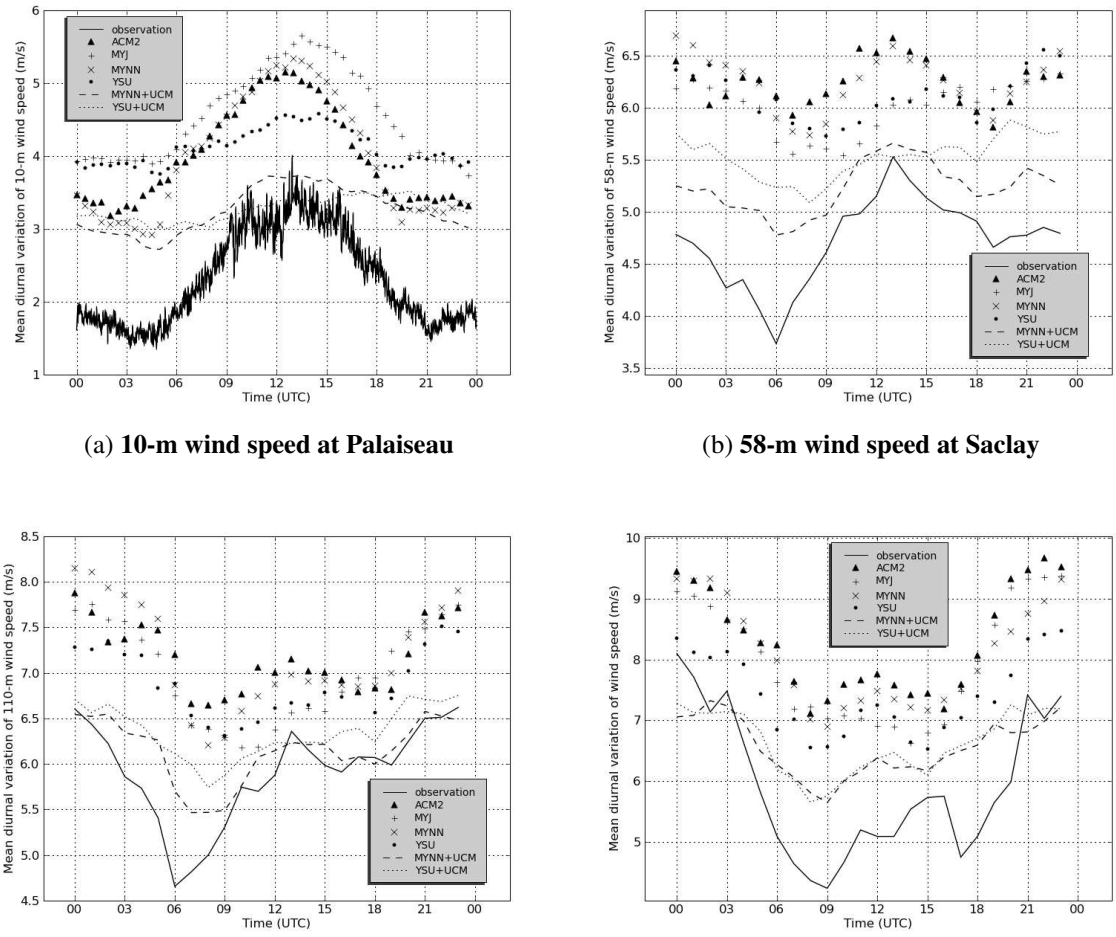

(a) **10-m wind speed at Palaiseau**

(b) **58-m wind speed at Saclay**

(c) **110-m wind speed at Saclay**

(d) **319-m wind speed at the Eiffel Tower**

Figure 5.6: Mean diurnal variation of observed and modeled wind speeds.

at Trappes. The four schemes overestimate SH during daytime. The SH simulated with the MYJ scheme is higher than others from the surface to 400 m, because of weaker vertical mixing in the MYJ scheme. The MYNN scheme, which has improved vertical mixing, simulates similar results to the two nonlocal schemes [Nakanishi et Niino, 2009]. The MFE of the YSU scheme is better than others while the RMSE and the NME of the MYNN scheme are the best. For the nighttime profile, the MYNN scheme has the smallest errors while the YSU and the MYJ schemes have the smallest biases.

The PBL heights modeled by the PBL schemes and retrieved by the radiosonde at Trappes are displayed in Figure 5.10. During daytime, the four schemes underestimate the PBL heights. The lowest monthly-mean error is obtained with the MYJ scheme. The maximum difference of modeled mean PBL heights among the PBL schemes is 20% (180 m between MYNN and MYJ). During nighttime, the YSU and the MYJ schemes overestimate the PBL heights while the ACM2 and the MYNN schemes underestimate them. Modeled mean PBL heights are significantly different among the schemes (from 150 m for MYNN to 652 m for YSU, 335%).

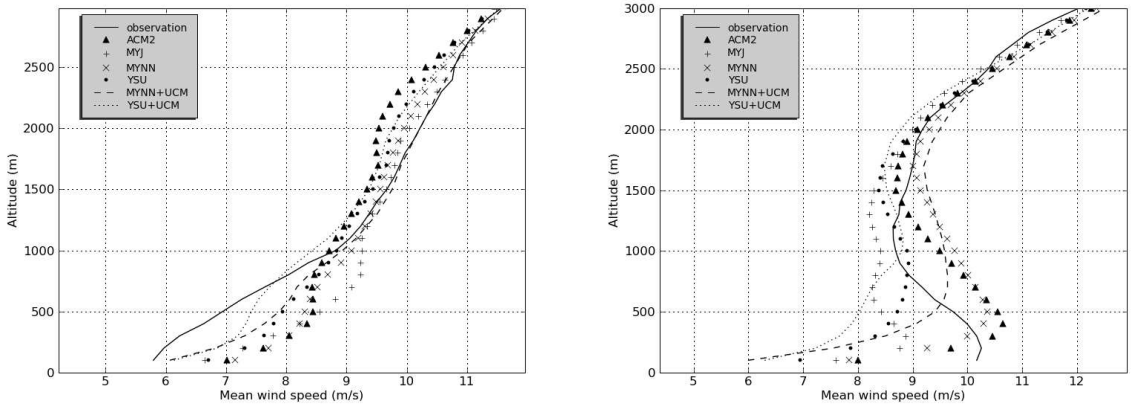

(a) **1200 UTC** (b) **0000 UTC**

Figure 5.7: Vertical profile of observed and modeled wind speeds at Trappes.

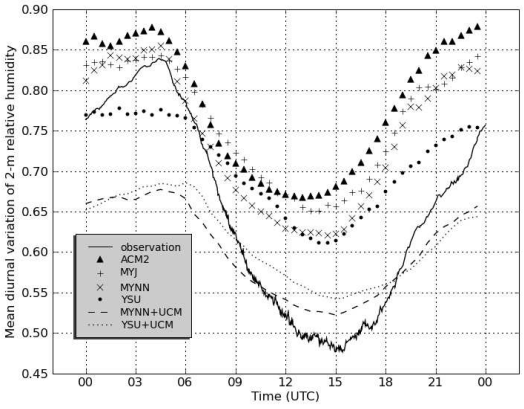

Figure 5.8: Mean diurnal variation of observed and modeled surface relative humidity at Palaiseau.

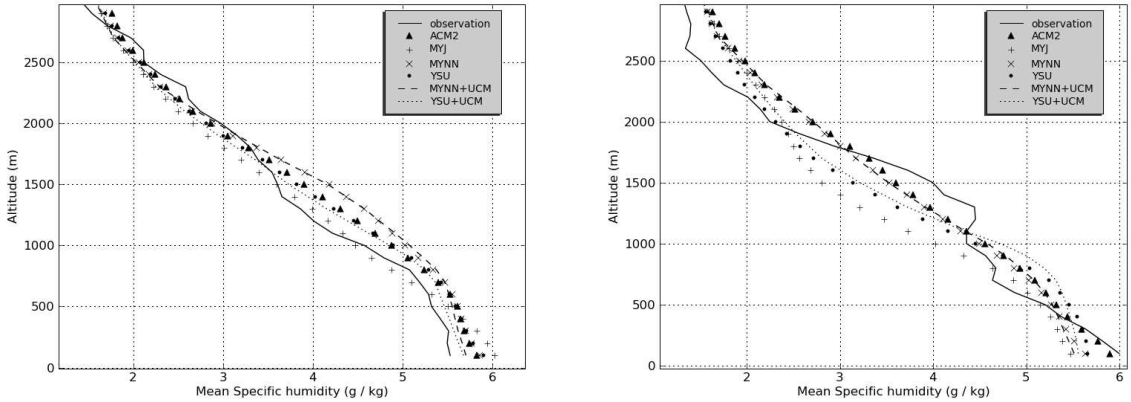

(a) **1200 UTC** (b) **0000 UTC**

Figure 5.9: Vertical profile of observed and modeled specific humidity at Trappes.

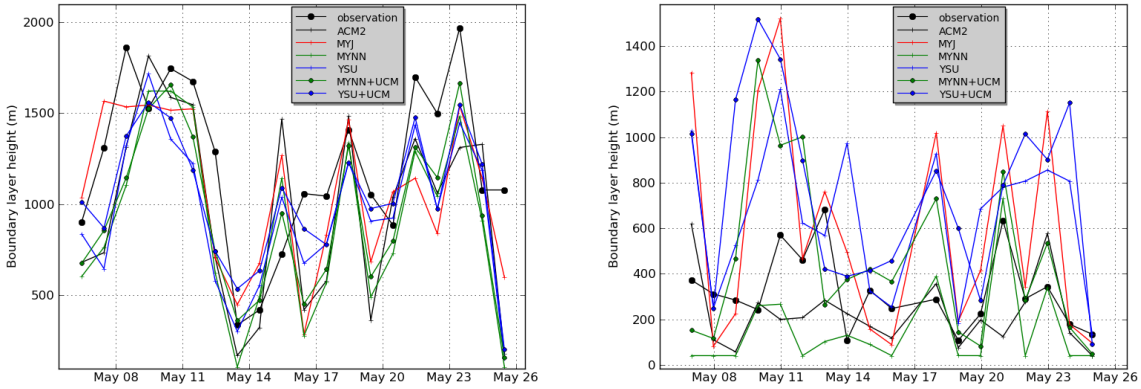

(a) **1200 UTC** (b) **0000 UTC**

Figure 5.10: PBL heights retrieved by the radiosonde and modeled heights at Trappes.

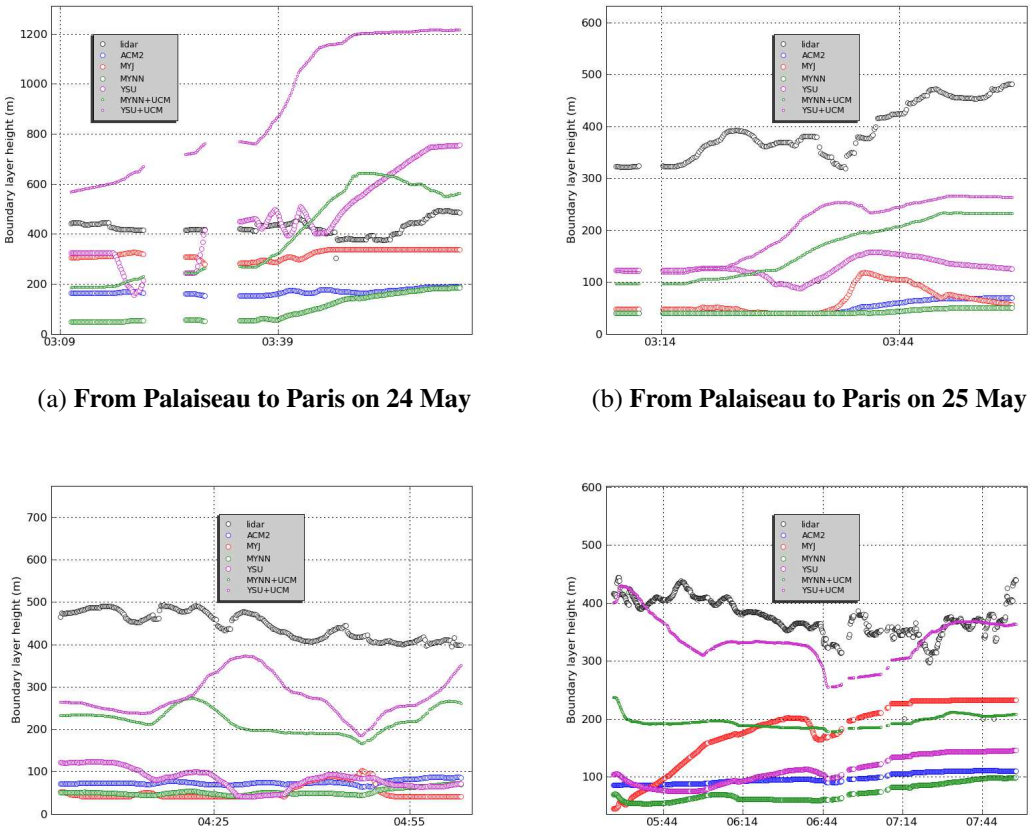

(a) **From Palaiseau to Paris on 24 May**

(b) **From Palaiseau to Paris on 25 May**

(c) **Main road and the beltway of Paris before rush-hour**

(d) **Main road and the beltway of Paris during rush-hour**

Figure 5.11: Boundary layer heights estimated by the GBML and modeled heights.

We compare the PBL heights estimated by the GBML measurements to the modeled PBL heights. Figure 5.11a and 5.11b present PBL heights estimated by the lidar from the suburbs of Paris (Palaiseau) to Paris center (Les Halles) on 24 May and 25 May, respectively. The heights do not significantly vary during the measurements on 24 May. The height at Palaiseau is 444 m while the height at Les Halles is 486 m. All the PBL schemes underestimate the PBL heights except for YSU for Paris center where the modeled heights increase to about 750 m. This increase of the modeled PBL height by YSU for Paris center is due to the unstable condition of temperature. A high potential temperature at ground is simulated with YSU (not shown here). The potential temperature is as high as that around 750 m of height leading to an increase of PBL height. The height at Palaiseau at 0300 UTC on 25 May is about 320 m while the height at Les Halles at 0400 UTC is about 480 m. The PBL height does not significantly increase from 0300 UTC to 0400 UTC because the sunrise hour at Paris at the end of May is about 0400 UTC. Therefore, the increase of the PBL height at Les Halles compared to that at Palaiseau is explained by the stronger urban heat release at Les Halles. All the PBL schemes significantly underestimate the PBL heights. The mean modeled PBL heights are lower than 100 m except for YSU (130 m) while the mean height observed by the lidar is about 390 m. This discrepancy

is mostly due to the nighttime heat flux from human activities in the urban region.

Figures 5.11c and 5.11d present the PBL heights along the main road and the beltway of Paris before rush-hour (from 0400 to 0500 UTC) and during rush-hour (from 0530 to 0800 UTC), respectively. The mean PBL heights estimated by the lidar are 445 m before rush-hour and 378 m during rush-hour while the mean modeled heights are less than 80 m before rush-hour and less than 180 m during rush-hour. All the PBL schemes underestimate the PBL heights. The YSU and the MYJ schemes perform slightly better before and during rush-hour than others.

The PBL heights along the GBML measurements vary greatly with the PBL scheme: the maximum difference between the mean PBL heights of the PBL schemes is important for the case of Palaiseau to Paris on 24 May (78%) compared to the others (66% for Palaiseau to Paris on 25 May, 40% for the beltway of Paris before rush-hour and 60% for the beltway of Paris during rush-hour).

To summarize, the temperature is relatively well modeled by all schemes, while larger discrepancies are found for wind speed, humidity and PBL height. For the temperature, the MYNN scheme presents the best performance. For the wind speed, the YSU and the MYNN schemes perform better than the others. The YSU and the MYNN schemes perform better for the relative humidity and the specific humidity, as well. For the PBL height, the YSU scheme performs better than the others but still underestimates significantly the PBL height.

5.5 Effects of urban canopy model and Corine land-use data

Impacts of UCM and Corine land-use data on the meteorological fields are studied by comparing the reference simulations of the previous section (hereafter Reference) to simulations that use UCM coupled to the Corine land-use data (hereafter UCM-Corine). Simulations are compared for the 2 PBL schemes that performed the best in the previous section (YSU and MYNN). Statistical indicators for the comparison to measurements of these simulations are given in Tables 5.4a-5.4b. As expected, the temperature of the UCM-Corine simulations are higher than the Reference simulations, especially during nighttime (+ 0.8 °C on average for both YSU and MYNN). Influences of UCM and Corine on the 40-m and 100-m temperatures are lower than on the 2-m temperature, partly because the 2-m temperature is inside the urban canopy. Outside the canopy (40-m and 100-m temperatures), the UCM-Corine performs better than the Reference, as the temperature is underestimated by the model. Although this underestimation is resolved using UCM-Corine during nighttime at Saclay, it persists at the Eiffel Tower. As shown in Figure 5.5, the influence of UCM-Corine on the mean vertical profiles of potential temperature at Trappes is low and confined to the lowest altitudes. The maximum differences between the UCM-Corine and the Reference at 100 m altitude are only 0.3 K during daytime and 0.5 K during nighttime (see Figure 5.5).

As shown in Figure 5.6, the 10-m wind speed at Palaiseau and 58-m and 110-m wind speeds at Saclay are much lower and closer to measurements in the UCM-Corine simulation than in the Reference simulation for both YSU and MYNN [Miao *et al.*, 2009]. The UCM-Corine simulation performs better for the 10-m wind speed, the 58-m wind speed and the 110-m wind speed, because the modeled wind speed is lower and in much better agreement with the measurements. As shown in Figure 5.7, for the vertical profiles at Trappes, influences of UCM-Corine on the wind speed during both daytime and nighttime are important below 1000 m height, especially

Table 5.4a: Comparison of modeled values with the YSU PBL scheme, the UCM model and the Corine land-use to observations.

Variables*	Observed mean	Modeled mean	RMSE†	MFB†	MFE†	NMB†	NME†	Correlation†
T2 at Palaiseau	13.7 °C	14.1 °C	2.87 °C	0.05	0.19	0.04	0.19	0.69
T40 at Saclay	12.5 °C	11.3 °C	2.79 °C	-0.11	0.20	-0.10	0.18	0.82
T100 at Saclay	12.1 °C	10.7 °C	2.82 °C	-0.14	0.22	-0.12	0.19	0.84
T319 at Eiffel	13.0 °C	10.1 °C	3.99 °C	-0.28	0.33	-0.22	0.26	0.87
PT_{12h} at Trappes	296.4 K	294.5 K	2.39 K	-0.01	0.01	-0.01	0.01	0.99
PT_{00h} at Trappes	295.8 K	293.6 K	2.57 K	-0.01	0.01	-0.01	0.01	0.99
WS10 at Palaiseau	2.31 m/s	3.27 m/s	1.64 m/s	0.47	0.58	0.69	0.82	0.25
WS58 at Saclay	4.72 m/s	5.52 m/s	1.59 m/s	0.19	0.28	0.17	0.27	0.69
WS110 at Saclay	5.91 m/s	6.34 m/s	1.63 m/s	0.11	0.24	0.07	0.22	0.71
WS319 at Eiffel	6.38 m/s	6.81 m/s	2.43 m/s	0.08	0.29	0.07	0.30	0.66
WS_{12h} at Trappes	11.43 m/s	11.11 m/s	2.51 m/s	0.05	0.26	0.04	0.25	0.68
WS_{00h} at Trappes	12.17 m/s	11.57 m/s	2.65 m/s	-0.01	0.24	0.03	0.24	0.83
RH at Palaiseau	0.65	0.61	0.12	-0.03	0.17	-0.04	0.16	0.63
SH_{12h} at Trappes	2.59 g/kg	2.70 g/kg	0.84 g/kg	0.07	0.34	0.04	0.25	0.94
SH_{00h} at Trappes	2.57 g/kg	2.55 g/kg	0.75 g/kg	0.06	0.29	0.02	0.22	0.92
$PBLH_{12h}$ at Trappes	1227 m	1036 m	369 m	-0.15	0.31	-0.16	0.25	0.70
$PBLH_{00h}$ at Trappes	322 m	753 m	586 m	0.68	0.80	1.34	1.46	0.20
PBLH by lidar								
Palaiseau-Paris (24 May)	425 m	964 m	596 m	0.73	0.73	1.27	1.27	-0.08
Palaiseau-Paris (25 May)	390 m	204 m	192 m	-0.65	0.66	-0.48	0.48	0.64
Paris before rush-hour	445 m	276 m	177 m	-0.48	0.48	-0.38	0.38	0.11
Paris during rush-hour	376 m	339 m	54 m	-0.11	0.13	-0.10	0.12	0.41

*: see Table 5.3a, †: see Tabel 5.2.

Table 5.4b: Comparison of modeled values with the MYNN PBL scheme, the UCM model and the Corine land-use to observations.

Variables*	Observed mean	Modeled mean	RMSE†	MFB†	MFE†	NMB†	NME†	Correlation†
T2 at Palaiseau	13.7 °C	14.6 °C	2.68 °C	0.10	0.18	0.09	0.18	0.83
T40 at Saclay	12.5 °C	11.5 °C	2.43 °C	-0.08	0.17	-0.08	0.16	0.85
T100 at Saclay	12.1 °C	11.0 °C	2.42 °C	-0.10	0.17	-0.10	0.16	0.87
T319 at Eiffel	13.0 °C	10.5 °C	3.64 °C	-0.22	0.26	-0.20	0.23	0.89
PT_{12h} at Trappes	296.4 K	294.5 K	2.29 K	-0.01	0.01	-0.01	0.01	0.99
PT_{00h} at Trappes	295.8 K	293.5 K	2.55 K	-0.01	0.01	-0.01	0.01	0.99
WS10 at Palaiseau	2.31 m/s	3.25 m/s	1.56 m/s	0.46	0.56	0.67	0.80	0.42
WS58 at Saclay	4.72 m/s	5.23 m/s	1.49 m/s	0.13	0.26	0.11	0.24	0.69
WS110 at Saclay	5.91 m/s	6.14 m/s	1.72 m/s	0.06	0.25	0.04	0.22	0.68
WS319 at Eiffel	6.38 m/s	6.63 m/s	2.32 m/s	0.04	0.28	0.04	0.29	0.69
WS_{12h} at Trappes	11.43 m/s	11.39 m/s	2.62 m/s	0.08	0.26	0.08	0.26	0.74
WS_{00h} at Trappes	12.17 m/s	12.19 m/s	2.76 m/s	0.06	0.26	0.11	0.28	0.78
RH at Palaiseau	0.65	0.60	0.12	-0.05	0.17	-0.06	0.16	0.69
SH_{12h} at Trappes	2.59 g/kg	2.79 g/kg	0.83 g/kg	0.11	0.35	0.08	0.25	0.94
SH_{00h} at Trappes	2.57 g/kg	2.59 g/kg	0.71 g/kg	0.07	0.29	0.03	0.20	0.93
$PBLH_{12h}$ at Trappes	1227 m	938 m	400 m	-0.29	0.34	-0.24	0.26	0.80
$PBLH_{00h}$ at Trappes	322 m	461 m	361 m	0.12	0.63	0.43	0.80	0.39
PBLH by lidar								
Palaiseau-Paris (24 May)	425 m	420 m	181 m	-0.10	0.42	-0.01	0.39	-0.19
Palaiseau-Paris (25 May)	390 m	165 m	228 m	-0.84	0.84	-0.58	0.58	0.77
Paris before rush-hour	445 m	219 m	228 m	-0.68	0.68	-0.51	0.51	0.39
Paris during rush-hour	376 m	195 m	184 m	-0.63	0.63	-0.48	0.48	0.22

*: see Table 5.3a, †: see Tabel 5.2.

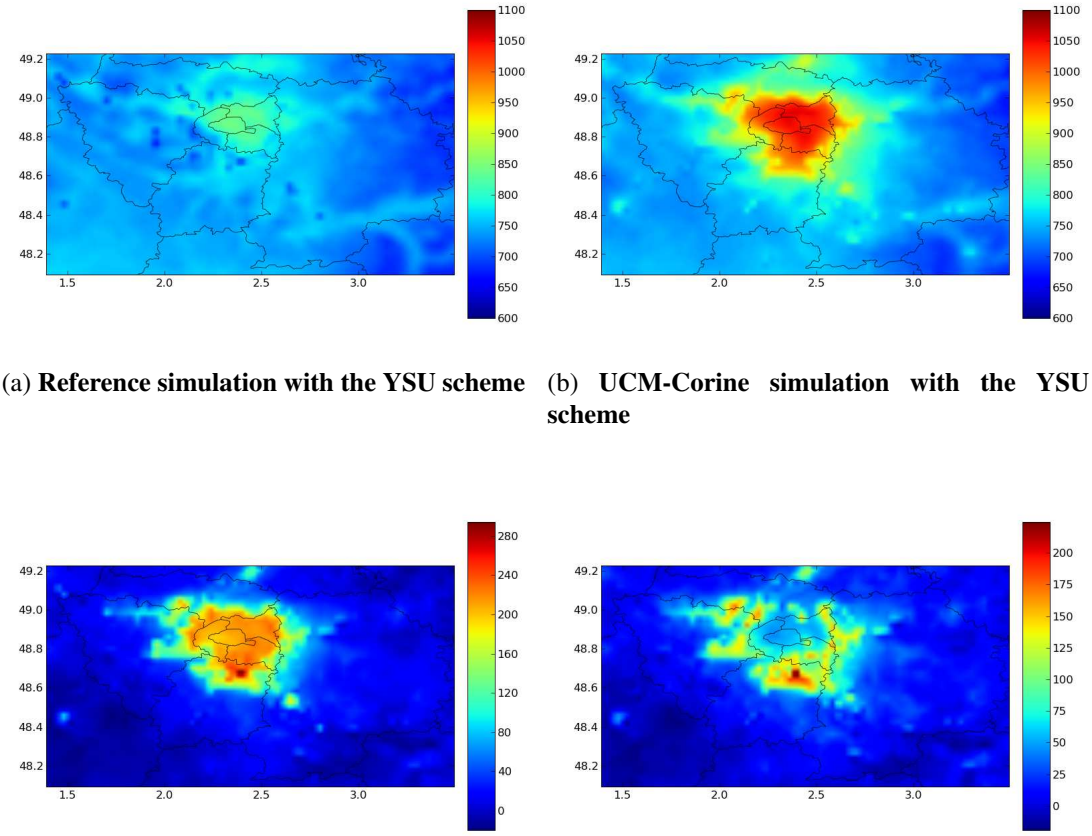

(a) **Reference simulation with the YSU scheme**

(b) **UCM-Corine simulation with the YSU scheme**

(c) **Differences between the UCM-Corine and the Reference**

(d) **Differences between the UCM-Corine and the simulation with UCM and the USGS land-use**

Figure 5.12: Modeled mean PBL heights from 6 May to 27 May (unit: m).

during nighttime. Maximum differences between the UCM-Corine and the Reference is 1 m/s for YSU and 2 m/s for MYNN at 100 m during nighttime.

For the relative humidity at Palaiseau, as shown in Figure 5.8, the differences between the UCM-Corine simulation and the Reference simulation are significant (about 15% of mean RH) for both YSU and MYNN. Lower relative humidity with UCM-Corine at the ground is due to stronger vertical mixing in the boundary layer influenced by the anthropogenic heat release in the UCM-Corine simulation. In the Reference simulations, RH at Palaiseau is well modeled at night but overestimated during daytime. In the UCM-Corine simulations, RH is underestimated at night but well modeled during daytime. As seen in Figure 5.9, the variations of the vertical profiles of specific humidity at Trappes is influenced by the stronger vertical mixing in the UCM-Corine simulation. Lower specific humidity is simulated by the UCM-Corine than by the Reference near the surface while the specific humidity with UCM-Corine at higher altitudes is slightly higher than the Reference.

The UCM model increases the PBL height over the urbanized surface. This increase is more

important during nighttime than during daytime. Accordingly, the increase by UCM-Corine of the PBL heights retrieved by the radiosonde at Trappes is 8% for YSU and 5% for MYNN during daytime while it is 15% for YSU and 200% for MYNN during nighttime. Figure 5.12a and 5.12b display the mean PBL heights from 6 May to 27 May over Greater Paris by simulations with and without UCM-Corine. The PBL heights are greater with the UCM-Corine simulation than with the Reference simulation in Paris and the near suburbs. The maximum difference of the mean PBL height is about 290 meters near Orly airport located south of Paris (see Figure 5.12c). The effect of using Corine land-use data rather than USGS is shown in Figure 5.12d, which shows differences of the PBL height between the UCM-Corine simulations and a simulation with UCM and the standard USGS land-use. Influence of Corine on the PBL height is not significant in Paris while it is significant over urbanized areas mostly between 10 km and 30 km from Paris.

Compared to the GBML measurements, modeled PBL heights are also significantly influenced by UCM-Corine (see Figure 5.11). For the measurement from Palaiseau to Paris center, as well as for the measurement at the main road and the beltway of Paris, the UCM-Corine simulations perform much better than the Reference simulations, as the modeled PBL heights are higher.

5.6 Conclusion

Numerical simulations of the nocturnal vertical dispersion of PM_{10} over Paris and the near suburbs are performed using off-line meteorology (WRF) and chemistry-transport (Polyphemus) models. In this Part I article, the WRF model evaluation is conducted for the period from 6 May to 27 May 2005. As ground PM_{10} concentrations have previously shown to be very sensitive to the eddy diffusivity parameterization, simulations were performed with various PBL schemes. Meteorological data obtained with the ACM2, MYJ, MYNN and YSU PBL schemes were compared to observations at various meteorological stations around Paris and its suburbs.

Temperature is relatively well modeled by all schemes and the MYNN scheme performs slightly better than others. However, the temperatures are underestimated, particularly during daytime and the underestimations tend to increase with altitude.

Larger discrepancies are found for the wind speed and the YSU and the MYNN schemes perform better than others. The wind speeds are overestimated, particularly near the ground and the overestimations decrease with altitude.

For humidity, the modeled values are in good agreement with the observed values for the four PBL schemes, although relative humidity tends to be overestimated. The YSU and the MYNN schemes perform better for the relative humidity at the ground station and the specific humidity of radiosonde profiles, as well.

Larger differences between the simulations are obtained for the PBL height. The YSU and the MYJ schemes overestimate the PBL heights while the ACM2 and the MYNN schemes underestimate them during nighttime. Mean PBL heights are also significantly different among them. The YSU scheme performs better than the others (maximum difference: 77%).

Including the urban canopy model (UCM) and the Corine land-use data makes modeled meteorological data more realistic. Improvements of the temperature and the specific humidity modeling using UCM-Corine are low because these variables are already well modeled without

UCM-Corine. The modeling of the wind speed, the relative humidity and the PBL height is significantly improved using UCM-Corine. In particular, modeled PBL heights with the MYNN scheme during nighttime are strongly influenced by UCM-Corine (200%).

Influences of using UCM-Corine on the differences of the modeled meteorological variables are greater than those of using different PBL schemes on the surface while the latter are greater for the upper air temperatures (above 40 meters) and the PBL heights estimated by radiosonde profiles at Trappes. For the PBL heights by lidar, the influences of using different PBL schemes at Palaiseau are more important than those of using UCM-corine while the latter are more important at Paris center. Further work will be devoted to evaluate the impact of the meteorological modeling on PM_{10} vertical distribution within the PBL.

Chapitre 6

Modélisation de la distribution verticale des PM_{10} : Comparaison avec la mesure

Résumé

La modélisation de la dispersion verticale des polluants est evaluée par comparaison à diverses observations pour comprendre l'influence des paramétrisations de la couche limite atmosphérique (CLA) et de la canopée urbaine dans le modèle météorologique. Les comparaisons sont effectuées en utilisant des observations obtenues par mesures au sol et à la Tour Eiffel, ainsi que par mesures lidar ("*Light detection and ranging*").

Polyphemus version 1.6 et son modèle de qualité de l'air Polair3D ont été utilisés. La matière particulaire (PM) est modélisée en utilisant le modèle d'aérosol SIREAM associé au module d'aérosols organiques secondaires (AOS) Super-SORGAM, au module thermodynamique pour la formation des aérosols minéraux ISORROPIA et au mécanisme chimique en phase gazeuse CB05. Trois domaines de modélisation emboîtés uni-directionnellement ont été utilisés : le plus grand domaine de résolution de 0,5 ° × 0,5 ° pour l'Europe occidentale et une partie de l'Europe orientale, le deuxième domaine de résolution 0,125 ° × 0,125 ° pour la France et le plus petit domaine de résolution 0,02 ° × 0,02 ° pour l'Île de France. La simulation pour l'Île de France a été réalisée du 9 mai au 27 mai 2005. Les émissions anthropiques ont été générées avec l'inventaire d'AIRPARIF (`http://www.airparif.asso.fr/`) pour l'année 2005 sur l'Île de France et avec l'inventaire d'EMEP pour le reste du domaine. Les champs météorologiques ont été obtenus avec le modèle météorologique WRF (Weather Research and Forecast) version 3.3. Deux paramétrisations de la CLA dans WRF (celles qui donnent les meilleurs résultats pour la modélisation météorologique, voir chapitre 5) ont été utilisées : YSU (the Yonsei University, une paramétrisation de fermeture non-locale) et MYNN (Mellor-Yamada-Nakanishi et Niino, une paramétrisation de fermeture locale). Des simulations avec et sans le modèle de canopée urbaine de WRF, appelé UCM ("*Urban Canopy Model*") sont effectutées en utilisant la base de données récente de l'occupation des sols "*Corine*". Par ailleurs, comme dans Polyphemus la diffusivité turbulente a été paramétrisée à partir des variables météorologiques obtenues des simulations de WRF, il est intéressant de tester la sensibilité à la modélisation de la diffusivité turbulente. En particulier, nous avons comparé des simulations utilisant la diffusivité paramétrisée dans Polyphemus et celle obtenue de manière directe dans WRF.

Les concentrations simulées de PM_{10}, $PM_{2.5}$ (particules de diamètre aérodynamique in-

férieur à 10 et 2,5 micromètres, respectivement), ozone (O_3) et dioxyde d'azote (NO_2) sont évaluées par comparaison aux mesures de stations de surface du réseau BDQA (Base de Données de la Qualité de l'Air). Les performances du modèle sont satisfaisantes pour PM_{10}, $PM_{2.5}$ et O_3 en utilisant les données météorologiques simulées avec les deux paramétrisations de CLA YSU et MYNN. En moyenne, les concentrations de PM_{10}, $PM_{2.5}$ et NO_2 sont plus grandes au sol avec MYNN qu'avec YSU. Ces différences sont dues à des différences de mélanges verticaux qui sont influencées par les différentes hauteurs de la CLA modélisées en utilisant YSU ou MYNN. Pour O_3, la concentration obtenue avec YSU est en moyenne plus élevée au sol que celle obtenue avec MYNN, car la concentration de NO_2 est plus faible avec YSU et le régime de formation d'ozone est COV-limité. L'influence du modèle de canopée urbaine UCM-Corine sur les concentrations de polluants est plus importante que celle des différentes paramétrisations de la CLA. Les différences de concentrations entre la simulation qui utilise YSU et celle qui utilise MYNN sont en moyenne 6% pour PM_{10} et $PM_{2.5}$, 2% pour O_3 et 4% pour NO_2 alors que les différences entre YSU avec ou sans UCM-Corine sont 14% pour PM_{10}, 20% pour $PM_{2.5}$, 12% pour O_3 et 28% pour NO_2 (les différences sont similaires si MYNN est utilisé à la place de YSU).

Les concentrations simulées sont également comparées à des mesures faites en altitude à la Tour Eiffel et à une station de surface proche de la Tour Eiffel, appelée Paris-7, pour évaluer la distribution verticale des polluants dans le modèle. Les concentrations de NO_2 à la station Paris-7 sont en moyenne plus élevées avec MYNN qu'avec YSU tandis que celles à la Tour Eiffel sont plus élevées avec YSU qu'avec MYNN ; cependant les différences entre YSU et MYNN à la Tour Eiffel ne sont pas significatives. Bien que les concentrations de NO_2 à la Tour Eiffel soient sous-estimées dans toutes les simulations, l'utilisation d'UCM-Corine diminue les concentrations de NO_2 à Paris-7 et augmente celles à la Tour Eiffel, conduisant à une meilleure représentation de la distribution verticale de NO_2.

Pour les comparaisons des distributions verticales de PM_{10} modélisées avec les distributions mesurées par le lidar, les concentrations de PM_{10} sont en général le plus souvent sous-estimées dans la couche résiduelle tandis qu'elles sont surestimées au-dessus de la couche résiduelle.

Aux Halles dans le centre de Paris, le 24 mai à 0357 UTC, les concentrations de PM_{10} sont surestimées dans la couche limite nocturne alors qu'elles sont sous-estimées dans la couche résiduelle pour toutes les simulations. L'utilisation d'UCM-Corine conduit à une augmentation du mélange vertical de PM_{10} qui est due à l'augmentation de la hauteur de la CLA et à l'augmentation de la diffusivité turbulente dans la CLA.

À Palaiseau en banlieue parisienne, le 25 mai à 0309 UTC, les concentrations de PM_{10} sont sous-estimées dans les couches limite et résiduelle. La paramétrisation de la CLA utilisée influence plus les concentrations de PM_{10} et leur répartition verticale que l'utilisation ou non du modèle de canopée urbaine.

Aux Halles, la CLA est plus basse le 25 mai à 0357 UTC que le 24 mai à 0357 UTC et les concentrations de PM_{10} au sol sont par conséquent plus élevées. Les concentrations au sol sont surestimées si UCM-Corine n'est pas utilisé, mais elles concordent bien avec les observations si UCM-Corine est utilisé. En revanche, les concentrations sont sous-estimées dans le reste de la couche limite et dans la couche résiduelle.

Aux Halles, le 24 mai à 0755 UTC, les concentrations simulées de PM_{10} augmentent fortement dans la couche limite par rapport aux concentrations à 0357 UTC. Cette augmentation est due aux émissions liées au trafic. Il y a une bonne concordance entre l'augmentation des concentrations simulées et mesurées de PM_{10} au sol. Mais les simulations ne reproduisent pas

quantitativement l'augmentation importante mesurée dans la CLA par le lidar, en partie à cause de sous-estimations des hauteurs de CLA.

Les faibles concentrations de PM_{10} simulées dans la couche résiduelle pourraient être dues, d'une part, à une sous-estimation des PM_{10} dans la couche limite pendant la journée et, d'autre part, à une surestimation du mélange au-dessus de la couche résiduelle pendant la nuit. Par exemple, la concentration maximale simulée pendant la journée du 24 mai n'est que de 16 $\mu g/m^3$ alors que la concentration maximale observée par lidar à 0300 UTC le 25 mai est d'environ 27 $\mu g/m^3$.

L'utilisation de la diffusivité turbulente (K_z) calculée dans WRF à la place de la diffusivité calculée par la méthode de Troen et Mahrt dans Polyphemus influence les concentrations, particulièrement quand la paramétrisation de CLA utilisée est MYNN. Par exemple, aux Halles, le 25 mai à 0755 UTC, la valeur maximale de K_z calculée par WRF est de 120 m^2/s et celle calculée par Polyphemus est inférieure à 10 m^2/s. La paramétrisation de la diffusivité turbulente dans Polyphemus influence autant les concentrations que la paramétrisation de CLA dans WRF.

Les résultats montrent que l'influence du modèle de canopée urbaine UCM-Corine sur la dispersion verticale des PM_{10} dans la CLA est plus importante que celle de la paramétrisation de la CLA au centre de Paris, tandis que l'influence de la paramétrisation de CLA est plus importante en banlieue de Paris. L'utilisation de la diffusivité turbulente (K_z) obtenue directement par le modèle météorologique est recommandée, en particulier quand la paramétrisation de la fermeture locale MYNN est utilisée. Par ailleurs, un traitement de l'occupation des sols plus détaillé dans UCM sera nécessaire pour améliorer la performance du modèle dans les régions semi-urbaines.

Ce chapitre est constitué de
Kim, Y. et Sartelet, K. (2011). **Evaluation of the modeling of the PM_{10} vertical distribution over Greater Paris : Part II - Comparison to measurements**. soumis à *Atmos. Environ.*

Sommaire

6.1 Introduction

Uncertainty of chemistry-transport models (CTM) has diverse origins: physico-chemical parameterizations (turbulence closure, deposition velocities, chemical mechanism, etc.), input data (land-use data, emission inventories, meteorological fields, chemical kinetic constants, etc.) and numerical approximations (grid sizes, time steps, etc.) [Mallet et Sportisse, 2006].

Previous studies have been performed to examine quantitatively the uncertainties on the modeling of atmospheric pollutants in CTM; they revealed that the turbulence closure scheme and the number of vertical levels used bring the largest uncertainties for ozone (O_3) and particulate matter (PM) concentrations [Mallet et Sportisse, 2006; Roustan *et al.*, 2010b; Tang *et al.*, 2011]. Several studies have investigated the influence of meteorological modeling on ozone and PM concentrations [e.g. de Meij *et al.*, 2009; Appel *et al.*, 2010]. The choice of the planetary boundary layer (PBL) scheme in the meteorological model plays an important role [Borge *et al.*, 2008; Kim *et al.*, 2010b; Kim et Sartelet, 2011a], as well as the urban canopy modeling [Lee *et al.*, 2010; Chen *et al.*, 2011; Kim et Sartelet, 2011a]. Dupont *et al.* [1999] showed that in Paris the urban influence is especially important during nighttime.

Various instrumented platforms have been used to investigate the vertical dispersion and chemical transformations of pollutants in the boundary layer: fixed platforms (surface stations) and mobile platforms (automobile, aircraft, balloon, satellite, etc). Because of their capabilities for tracking the evolution of pollutants over time, lidars are widely employed on fixed platforms [Menut *et al.*, 1999; Chen *et al.*, 2001; Guibert *et al.*, 2005; Chou *et al.*, 2007], aircraft [Flamant *et al.*, 1997], satellites [Kaufman *et al.*, 2003] or ground-based mobile platforms [Raut et Chazette, 2009; Royer *et al.*, 2011]. Some studies have included comparisons of measured and modeled vertical distribution of the pollutants over Europe or Paris and its suburbs (Greater Paris) [Guibert *et al.*, 2005; Royer *et al.*, 2011] during daytime. However, to our knowledge, there is no numerical study of the vertical distribution of pollutants in the nocturnal boundary layer and the residual layer over Greater Paris.

In a companion article [Part I, Kim et Sartelet, 2011a], meteorological modeling in the PBL was performed over Greater Paris in May 2005 using the Weather Research and Forecast model (WRF) and the simulated meteorological fields were evaluated by comparison to observational data. The uncertainties linked to the parameterization of the PBL as well as to the modeling of the urban canopy (UC) were investigated. As the next step, to understand the impacts of the meteorological modeling of the PBL and UC on the vertical dispersion of pollutants, this study focuses on the comparison of the modeled aerosol vertical distribution to the distribution retrieved by a ground-based mobile lidar (GBML) system over Greater Paris during nighttime and early morning. First, a description of the model and the modeling setup is given and followed by model evaluations through comparisons of pollutant concentrations to observational data obtained by a surface measurement network and data at an upper air monitoring station. Then, the PM vertical distribution retrieved by the lidar is compared to the modeled distribution. The influence of the PBL scheme versus the UC scheme is discussed.

6.2 Model description and setup

6.2.1 Model description: Polyphemus

The chemistry-transport model Polair3D [Sartelet *et al.*, 2007] of the air-quality platform Polyphemus version 1.6 [Mallet *et al.*, 2007] is used in this study (`http://cerea.enpc.fr/polyphemus`). PM is modeled using SIREAM (Size REsolved Aerosol Model) [Debry *et al.*, 2007a] coupled to the Super-SORGAM secondary organic aerosol module [Kim *et al.*, 2011] and the CB05 chemical kinetic mechanism [Yarwood *et al.*, 2005]. Polair3D/Polyphemus was used to model the PM_{10} (particles less than 10 µm of aerodynamic diameter) vertical distribution during the MEGAPOLI campaign during daytime [Royer *et al.*, 2011].

6.2.2 Modeling domain and setup

Three modeling domains are used with one-way nesting (see Figure 6.1). The largest domain covers western Europe and part of eastern Europe with a horizontal resolution of $0.5° \times 0.5°$ ($35.0°$N - $70.0°$N, $15.0°$W - $35.0°$E). The first nested domain covers France with a resolution of $0.125° \times 0.125°$ ($41.5°$N - $51.1°$N, $4.0°$W - $10.1°$E) and the smallest domain covers Greater Paris with a resolution of $0.02° \times 0.02°$ ($48.1°$N - $49.2°$N, $1.4°$E - $3.5°$E).

The simulation over Europe is carried out for one month from 1 May to 31 May 2005. The U.S. Geological Survey (USGS) land cover is used. Meteorological inputs are obtained from a reanalysis provided by the European Centre for Medium-Range Weather Forecasts (ECMWF). Anthropogenic emissions of gases and PM are generated with the European Monitoring and Evaluation Programme (EMEP) inventory for 2005. Biogenic emissions are com-

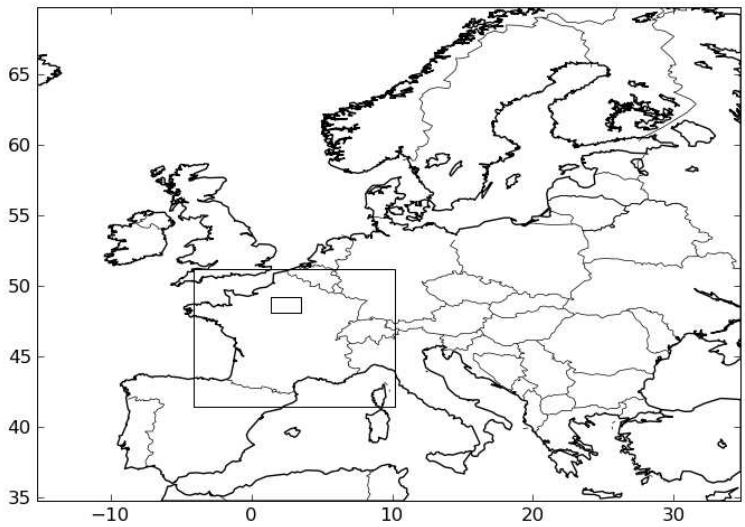

Figure 6.1: Three modeling domains for Polyphemus/Polair3D simulations.

puted as in Simpson *et al.* [1999] and sea-salt emissions as in Monahan *et al.* [1986]. For initial and boundary conditions, daily means are extracted from the outputs of the global chemistry and aerosol model, Interaction Chimie-Aérosols (INCA) coupled to the Laboratoire de Météorologie Dynamique general circulation model (LMDz) for this study (`http://www-lsceinca.cea.fr/`).

The nested simulation over France is performed from 7 May to 31 May 2005. Meteorological inputs are obtained from the Fifth-Generation NCAR/Penn State Mesoscale Model (MM5) [Dudhia, 1993], with a horizontal resolution of 12 km and a vertical resolution of 29 levels between 0 m and 13,700 m. Initial and boundary conditions are extracted from outputs of the simulation over Europe.

The nested simulation over Greater Paris is performed from 9 May to 27 May 2005. Anthropogenic emissions are generated with the AIRPARIF (air quality agency of the Paris region) inventory (`http://www.airparif.asso.fr/`) for 2005 over the Île de France region and with the EMEP inventory outside. Initial and boundary conditions are extracted from the outputs of the simulation over France. Meteorological inputs are obtained from the WRF model version 3.3, as detailed in the companion paper [Kim et Sartelet, 2011a]. Four WRF simulations are performed, changing the planetary boundary layer (PBL) scheme and with/without the urban canopy model [UCM, Kusaka *et al.*, 2001]. The two PBL schemes, which performed best in Kim et Sartelet [2011a] for meteorological modeling are used: the Yonsei University (YSU) scheme, a nonlocal closure scheme, and the Mellor-Yamada-Nakanishi and Niino (MYNN), a local closure scheme. The Polair3d/Polyphemus simulations are labelled Reference-YSU and Reference-MYNN when WRF meteorological fields are simulated without the urban module, but with the YSU and the MYNN PBL schemes respectively. When the urban module UCM with the Corine land-use data is used to compute the WRF meteorological fields, the Polyphemus simulations are labelled UCM-Corine-YSU and UCM-Corine-MYNN.

In all these four simulations, the eddy-diffusion coefficient K_z is parameterized following Troen et Mahrt [1986] and Louis [1979]. A minimum value of the coefficient is set to 0.2 m^2 s^{-1}. The parameterization of Louis [1979] is used to calculate the coefficients, except in the unstable convective boundary layer. The parameterization of Louis [1979] depends on the vertical gradient of the wind speed v as follows

$$K_z = l^2 F \left| \frac{\Delta v}{\Delta z} \right| \tag{6.1}$$

where l is the mixing length and F is the stability function. In the unstable convective boundary layer, the coefficients are calculated using the parameterization of Troen et Mahrt [1986], as it tends to be more robust for a fine discretization of vertical levels near the surface.

$$K_z = u_* \kappa z \Phi^{-1} \left(1 - \frac{z}{h}\right)^p \tag{6.2}$$

where u_* is the surface friction velocity, κ is the Von Kàrmàn constant set to 0.4, Φ is the non-dimensional shear, h is the planetary boundary layer height and the exponent p is set to 2 for this study.

To test the sensitivity to the modeling of the K_z in the CTM, Polair3D/Polyphemus simulations using the K_z of WRF are also performed. They are labelled UCM-Corine-YSU-Kz and UCM-Corine-MYNN-Kz. A minimum value of Kz is set to 0.2 m^2 s^{-1} below 200 m and to 10^{-6} m^2 s^{-1} in the upper layers [Pleim, 2011].

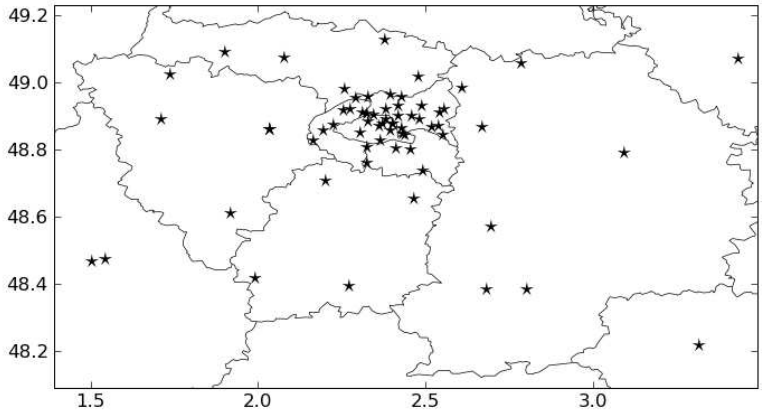

Figure 6.2: Locations of the BDQA stations over Greater Paris.

6.3 Comparisons to surface observational data

6.3.1 Surface observations

We compare pollutant concentrations obtained from the simulations over Greater Paris (9 May to 27 May) to a French observation database for air quality, "Base de Données de la Qualité de l'Air" (BDQA). Hourly observations of particulate matters (PM_{10} and $PM_{2.5}$) and gases (O_3 and NO_2) are available for 2005. Details on the measurements are presented at `http://www.atmonet.org/` and the locations of the BDQA observation stations are displayed in Figure 6.2. The statistical indicators used in this study are the root mean square error (RMSE), the mean fractional bias and error (MFB and MFE), the mean normalized bias and gross error (MNB and MNGE) and the correlation coefficient. They are defined in Table 6.1. Modeled concentrations are compared to observations from the BDQA database in Table 6.2.

For O_3, the MNGE of the four Polair3d/Polyphemus simulations varies between 0.14 and 0.17 using a 60 $\mu g/m^3$ threshold, while the MNB varies between -0.07 and 0.02. These results meet performance standards, typically MNGE $\leq$ 0.3 and -0.15 $\leq$ MNB $\leq$ +0.15 [Russell et Dennis, 2000]. For PM_{10}, following Boylan et Russell [2006], the model performance goal (-0.30 $\leq$ MFB $\leq$ +0.30 and MFE $\leq$ 0.50) is met for all four Polair3d/Polyphemus simulations. For $PM_{2.5}$, the model performance goal is met for 3 simulations (Reference-YSU, UCM-Corine-YSU and UCM-Corine-MYNN). The MFB varies between 0.09 and 0.26 and the MFE between 0.43 and 0.46. For the Reference-MYNN simulation, although the model performance goal is met for MFE, it is not met for MFB (0.32).

Using the MYNN rather than the YSU PBL scheme leads to higher surface concentrations for PM_{10}, $PM_{2.5}$ and NO_2, suggesting weaker vertical mixing near the surface. For $PM_{2.5}$,

Table 6.1: Definitions of the statistical indicators.

Indicators	Definitions
Root mean square error (RMSE)	$\sqrt{\frac{1}{n}\sum_{i=1}^{n}(c_i - o_i)^2}$
Mean fractional bias (MFB) and mean fractional error (MFE)	$\frac{1}{n}\sum_{i=1}^{n}\frac{c_i - o_i}{(c_i + o_i)/2}$ and $\frac{1}{n}\sum_{i=1}^{n}\frac{\mid c_i - o_i \mid}{(c_i + o_i)/2}$
Mean normalized bias (MNB) and mean normalized gross error (MNGE)	$\frac{1}{n}\sum_{i=1}^{n}\frac{c_i - o_i}{o_i}$ and $\frac{1}{n}\sum_{i=1}^{n}\frac{\mid c_i - o_i \mid}{o_i}$
Correlation coefficient	$\frac{\sum_{i=1}^{n}(c_i - \overline{c})(o_i - \overline{o})}{\sqrt{\sum_{i=1}^{n}(c_i - \overline{c})^2}\sqrt{\sum_{i=1}^{n}(o_i - \overline{o})^2}}$ with $\overline{o} = \frac{1}{n}\sum_{i=1}^{n} o_i$ and $\overline{c} = \frac{1}{n}\sum_{i=1}^{n} c_i$

c_i: modeled values, o_i: observed values, n: number of data.

except for the correlation, the statistics are better when YSU is used rather than MYNN because the over-estimation of $PM_{2.5}$ is lower with YSU. For O_3, PM_{10}, $PM_{2.5}$ and NO_2, the correlation is higher when using YSU rather than MYNN.

Differences between simulations using different PBL schemes (6% for PM_{10} and $PM_{2.5}$, 2% for O_3 and 4% for NO_2) are lower than differences between simulations with and without UCM-Corine (using YSU, 14% for PM_{10}, 20% for $PM_{2.5}$, 12% for O_3 and 28% for NO_2 and using MYNN, 12% for PM_{10}, 17% for $PM_{2.5}$, 10% for O_3 and 22% for NO_2). Lower concentrations are obtained for PM_{10}, $PM_{2.5}$ and NO_2 in the UCM-Corine simulations and the statistics are globally improved. The lower concentrations at the surface stations with the UCM-Corine simulations are due to stronger vertical mixing. For $PM_{2.5}$, the UCM-Corine simulations perform better than the Reference simulations, because the over-estimation of $PM_{2.5}$ is reduced. For PM_{10}, the UCM-Corine simulations give better statistics, except for the MFB and the correlation. The modeled mean is under-estimated in the UCM-Corine simulations, whereas it is well estimated in the Reference simulations. In opposite to PM_{10}, $PM_{2.5}$ and NO_2, for O_3 the UCM-Corine simulations leads to higher mean concentrations. This increase in O_3 concentration is due to the decrease in NO_2 concentration with UCM-Corine: over urbanized areas such as Paris, which are in a VOC-limited regime for O_3 formation, a decrease in NO_x concentration leads to an increase in O_3.

Table 6.2: Comparison of modeled concentrations to observations from the BDQA database ($\mu g/m^3$).

	Stations	Observed mean*†	Model	Modeled mean*†	RMSE*	MFB*	MFE*	MNB*	MNGE*	Correlation*
PM_{10}	17	17.0	Reference-YSU	17.0	9.5	-0.06	0.41	0.08	0.44	0.28
			Reference-MYNN	18.0	10.1	0.00	0.41	0.16	0.47	0.22
			UCM-Corine-YSU	14.6	8.4	-0.17	0.41	-0.05	0.39	0.23
			UCM-Corine-MYNN	15.9	8.6	-0.09	0.40	0.03	0.41	0.21
			UCM-Corine-YSU-Kz	14.1	8.3	-0.19	0.41	-0.08	0.39	0.22
			UCM-Corine-MYNN-Kz	13.9	8.5	-0.20	0.42	-0.08	0.39	0.16
$PM_{2.5}$	5	11.1	Reference-YSU	15.5	9.7	0.26	0.46	0.53	0.70	0.34
			Reference-MYNN	16.5	10.7	0.32	0.48	0.64	0.78	0.30
			UCM-Corine-YSU	12.4	6.9	0.09	0.43	0.27	0.53	0.23
			UCM-Corine-MYNN	13.7	7.8	0.17	0.45	0.40	0.62	0.22
			UCM-Corine-YSU-Kz	11.7	6.3	0.04	0.41	0.20	0.48	0.24
			UCM-Corine-MYNN-Kz	11.1	6.1	-0.01	0.41	0.14	0.47	0.17
O_3	30	56.4	Reference-YSU	61.9	22.6	-0.08	0.17	-0.05	0.15	0.63
			Reference-MYNN	60.9	23.3	-0.11	0.19	-0.07	0.17	0.59
			UCM-Corine-YSU	69.5	25.7	-0.02	0.15	0.00	0.14	0.58
			UCM-Corine-MYNN	66.7	24.7	-0.06	0.17	-0.03	0.16	0.57
			UCM-Corine-YSU-Kz	71.0	26.5	0.00	0.15	0.02	0.14	0.57
			UCM-Corine-MYNN-Kz	70.0	25.5	-0.01	0.15	0.01	0.15	0.60
NO_2	32	28.2	Reference-YSU	27.7	18.9	-0.15	0.54	0.14	0.64	0.50
			Reference-MYNN	28.8	19.0	-0.11	0.53	0.18	0.64	0.48
			UCM-Corine-YSU	19.9	18.0	-0.42	0.64	-0.15	0.57	0.43
			UCM-Corine-MYNN	22.5	17.8	-0.31	0.59	-0.05	0.57	0.42
			UCM-Corine-YSU-Kz	18.9	18.2	-0.47	0.66	-0.19	0.57	0.43
			UCM-Corine-MYNN-Kz	16.4	19.0	-0.55	0.69	-0.26	0.58	0.42

*: mean values over all stations, †: mean concentrations from 9 May to 27 May.

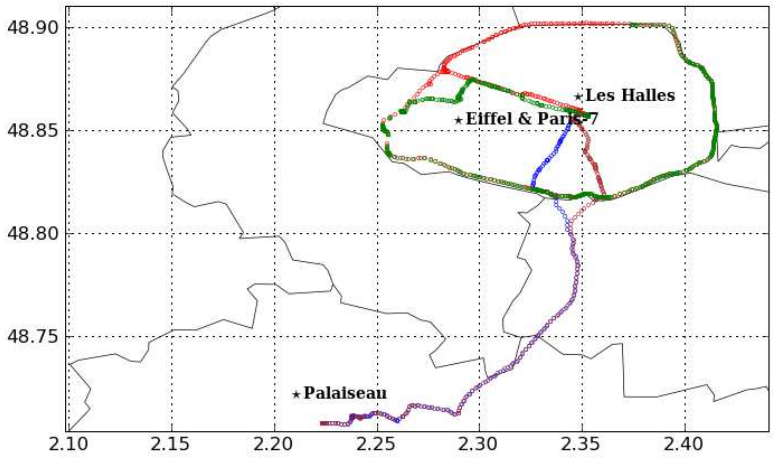

Figure 6.3: Locations of observation stations and route taken for the measurements of the GBML. Blue and brown marks show the route for the measurements from the suburbs of Paris to Paris center on 24 and 25 May, respectively. Red ones are for the measurements on the beltway of Paris before rush-hour and green ones are for the measurements on the beltway during rush-hour on 25 May.

6.3.2 Upper air observations: the Eiffel Tower

Although the stations included in the BDQA database are surface stations, AIRPARIF (`http://www.airparif.fr/`) monitors the upper air quality with a station located at the fourth floor (319 m) of the Eiffel Tower. It is useful to compare the concentration at the Eiffel Tower (hereafter Eiffel) to a nearby surface station (Paris-7, an urban background station) to diagnose the vertical distribution of pollutants, although only NO_2 is monitored at Paris-7. The locations of the monitoring stations are presented in Figure 6.3. Modeled concentrations are compared to observations at Eiffel and Paris-7 in Table 6.3.

The Reference-YSU and the Reference-MYNN simulations lead to similar NO_2 concentration at Eiffel. Statistics of YSU are better for the RMSE and the correlation, while statistics of MYNN are better for MFB, MFE, MNB and MNGE. Both simulations model well the observed mean NO_2 concentration at Paris-7 (43.8 $\mu g/m^3$ against 43.4 and 45.2 $\mu g/m^3$ modeled). However, NO_2 is strongly under-estimated at Eiffel. The observed mean concentration at Eiffel is about half that at Paris-7, while the modeled mean concentration at Eiffel is only 17-19% of the modeled mean at Paris-7, suggesting that vertical mixing is under-estimated in the Reference simulations. Vertical mixing is better modeled in the UCM-Corine simulations: the modeled mean of NO_2 at Eiffel is 33-35% of the modeled mean at Paris-7, but NO_2 concentrations are under-estimated at both Eiffel and Paris-7.

The Reference simulations over-estimate the concentrations of O_3 at Eiffel (MNB: 0.10 to

Table 6.3: Comparison of modeled concentrations to observations at the Eiffel tower and Paris-7 stations ($\mu g/m^3$).

	Stations	Observed mean*†	Model	Modeled mean*†	RMSE*	MFB*	MFE*	MNB*	MNGE*	Correlation*
O_3	Eiffel	55.9	Reference-YSU	77.4	31.3	0.08	0.18	0.11	0.19	0.34
			Reference-MYNN	77.9	32.2	0.07	0.18	0.10	0.19	0.26
			UCM-Corine-YSU	76.0	30.0	0.07	0.20	0.10	0.21	0.40
			UCM-Corine-MYNN	74.5	29.2	0.05	0.19	0.08	0.19	0.38
			UCM-Corine-YSU-Kz	76.5	30.9	0.07	0.21	0.10	0.22	0.36
			UCM-Corine-MYNN-Kz	74.5	30.0	0.05	0.21	0.08	0.21	0.32
NO_2	Eiffel	22.0	Reference-YSU	8.1	19.8	-0.83	0.88	-0.50	0.61	0.34
			Reference-MYNN	7.8	20.4	-0.89	0.94	-0.53	0.63	0.28
			UCM-Corine-YSU	11.2	16.4	-0.58	0.67	-0.36	0.51	0.56
			UCM-Corine-MYNN	11.7	16.7	-0.53	0.63	-0.32	0.49	0.48
			UCM-Corine-YSU-Kz	10.4	17.1	-0.66	0.75	-0.41	0.56	0.55
			UCM-Corine-MYNN-Kz	11.7	16.3	-0.56	0.67	-0.33	0.52	0.54
	Paris-7	43.8	Reference-YSU	43.4	21.5	-0.21	0.41	-0.11	0.34	0.60
			Reference-MYNN	45.2	22.6	-0.16	0.35	-0.07	0.31	0.56
			UCM-Corine-YSU	32.3	22.6	-0.54	0.58	-0.37	0.41	0.47
			UCM-Corine-MYNN	35.8	22.5	-0.47	0.52	-0.31	0.37	0.45
			UCM-Corine-YSU-Kz	31.2	22.9	-0.36	0.49	-0.22	0.40	0.46
			UCM-Corine-MYNN-Kz	25.5	26.0	-0.53	0.60	-0.35	0.45	0.43

*: mean values over all stations, †: mean concentrations from 9 May to 27 May.

0.11). The observed mean concentration of O_3 at Eiffel is similar to the concentration averaged over the BDQA surface stations (less than 1% of difference). However, the modeled mean concentration at Eiffel is significantly higher (77.4 $\mu g/m^3$) than the concentration averaged over surface stations (61.9 $\mu g/m^3$). Similarly to the increase of O_3 with the UCM-Corine simulations at BDQA ground stations (see Section 6.3.1), concentrations of O_3 are slightly lower than those of the Reference simulations when UCM-Corine is used (2% and 4% lower for YSU and MYNN respectively) because of the increase in NO_2 concentrations. With the UCM-Corine simulations, the O_3 concentration at Eiffel is closer to the O_3 concentration averaged over surface stations, suggesting that vertical mixing is better simulated even though it may still be under-estimated. This conclusion is in agreement with Kim et Sartelet [2011a] who found that UCM-Corine improved the modeling of the PBL height over Greater Paris.

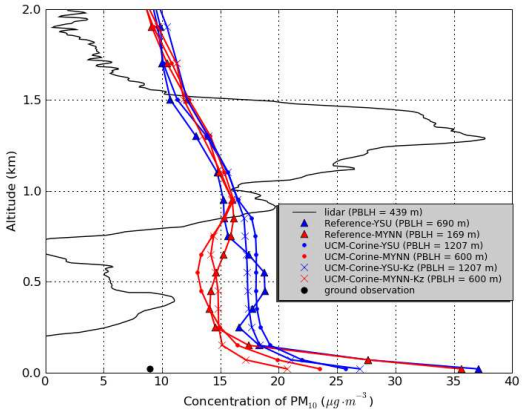

(a) PM$_{10}$ on 24 May, 0357 UTC at Paris, Les Halles (48.86°N, 2.35°E)

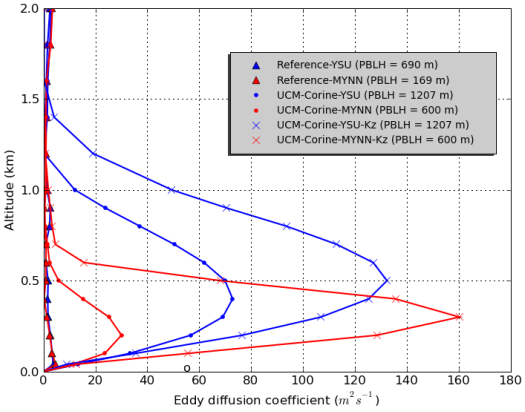

(b) Eddy-diffusion coefficient

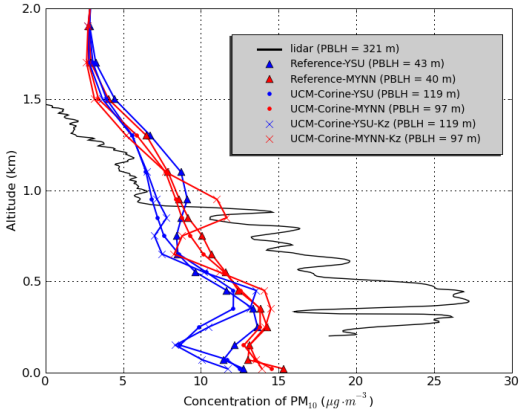

(c) PM$_{10}$ on 25 May, 0309 UTC at Palaiseau (48.71°N, 2.22°E)

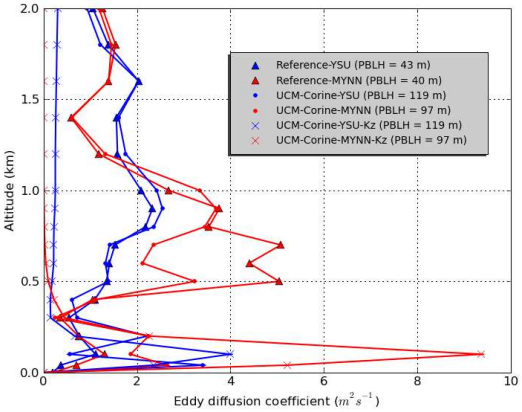

(d) Eddy-diffusion coefficient

Figure 6.4: Observed and modeled PM$_{10}$ vertical distributions are compared in the left column. PBLH are planetary boundary layer height estimated by the lidar or diagnosed in the simulations. Black circles in (a), (e) and (g) represent observed PM$_{10}$ at the surface stations. In the right column, modeled eddy-diffusion coefficients are shown.

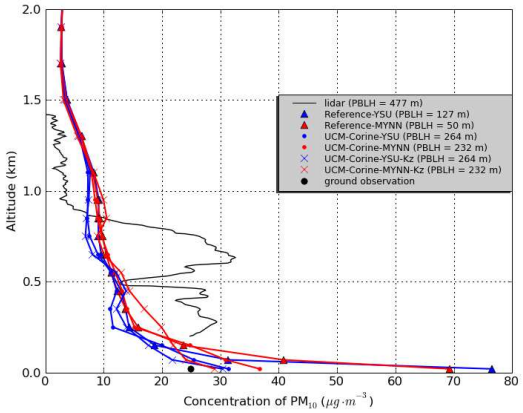

(e) PM_{10} on 25 May, 0357 UTC at Paris, Les Halles (48.86°N, 2.35°E)

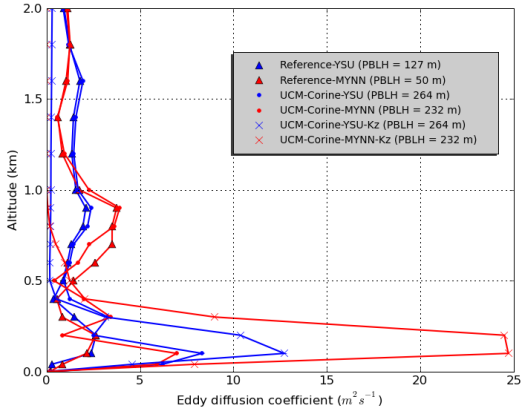

(f) Eddy-diffusion coefficient

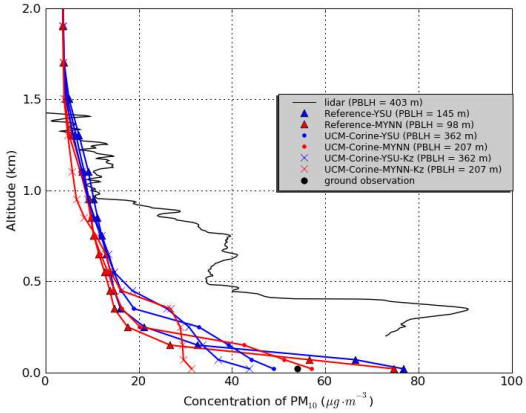

(g) PM_{10} on 25 May, 0755 UTC at Paris, Les Halles (48.86°N, 2.35°E)

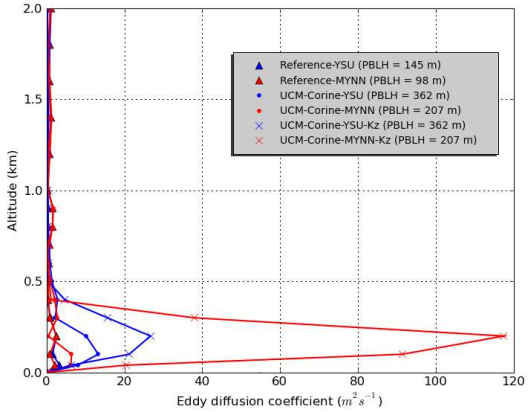

(h) Eddy-diffusion coefficient

Figure 6.4: Observed and modeled PM_{10} vertical distributions are compared in the left column. PBLH are planetary boundary layer height estimated by the lidar or diagnosed in the simulations. Black circles in (a), (e) and (g) represent observed PM_{10} at the surface stations. In the right column, modeled eddy-diffusion coefficients are shown.

6.4 PM_{10} vertical distribution

6.4.1 Comparisons to lidar measurements

The PM_{10} vertical distribution was measured using a GBML during the air quality observation campaign, "LIdar pour la Surveillance de l'AIR" (LISAIR) in Greater Paris from 24 May to 27 May 2005 [Raut et Chazette, 2009]. Observations of the aerosol extinction coefficients profiles by the GBML were performed to retrieve the multiple boundary layers in the free troposphere and in turn the vertical distribution of PM. Observations performed on 24 and 25 May at nighttime illustrate the presence of an inversion layer trapping pollutants at low altitude and the residual layer in altitude. Routes followed by the automobile embarking the lidar are presented in Figure 6.3. Details on the GBML measurements can be found in Raut et Chazette [2009]. PM_{10} concentrations are deduced from the lidar signal following Raut et Chazette [2009] by assuming that humidity does not influence much the extinction coefficients. A discussion on the influence of humidity and comparisons of extinction coefficients are presented in Appendix 6.A.

We compare the vertical concentrations of PM_{10} retrieved by the lidar to the modeled concentrations. Figure 6.4a presents the vertical distribution of PM_{10} at Les Halles, Paris center on 24 May at 0357 UTC. PM_{10} is over-estimated in the nocturnal boundary layer (NBL) with all the simulations while it is under-estimed in the residual layer and over-estimated above. PM_{10} modeled using Reference-YSU is higher than using Reference-MYNN between 0.2 km and 0.7 km because the PBL height computed by WRF for Reference-MYNN is lower (169 m) than the PBL height computed for Reference-YSU (690 m). Surface PM_{10} concentrations are over-estimated with Reference-MYNN and Reference-YSU. This over-estimation is reduced using UCM-Corine because of greater vertical mixing. Using UCM-Corine, the PBL heights increase by as much as 75% for YSU and by more than a factor 3 for MYNN, and the eddy-diffusion coefficients (K_z) increase in the PBL (see Figure 6.4b). In the first 200 meters, differences induced by using UCM-Corine or not are larger than differences induced by using different PBL schemes. However, the opposite is observed between 200 m and below the residual layer. Although PM_{10} concentrations tend to be under-estimated in the residual layer, UCM-Corine-MYNN, which estimates the PBL height fairly well (600 m against 439 m), manages to reproduce the observed residual layer between 800 and 1100 m. However, it under-estimates the concentrations between 1100 and 1500 m, which may be due to regional transport as suggested by Raut et Chazette [2009].

Figure 6.4c presents the vertical distribution of PM_{10} at Palaiseau, a suburb of Paris on 25 May at 0309 UTC. PM_{10} is under-estimated with the Reference-YSU simulation below 0.9 km. The PBL height is under-estimated in all simulations (119 m maximum for UCM-Corine-YSU against 321 m from the measurements). The maximum difference between modeled and measured PM_{10} is 15 $\mu g/m^3$ at around 0.4 km. The modeled PM_{10} is higher than the measured PM_{10} above 0.9 km. Modeled PM_{10} with the Reference-MYNN is higher than the Reference-YSU from 0.02 km to 0.75 km, with a maximum difference of 2 $\mu g/m^3$ at 0.02 km. PM_{10} with the UCM-Corine-MYNN and with the Reference-MYNN are not significantly different, however, PM_{10} with the UCM-Corine-YSU is slightly lower than with the Reference-YSU between 0.1 km and 0.4 km and between 0.6 km and 1.5 km. These differences of PM_{10} are linked to higher eddy diffusivity (K_z) with the UCM-Corine-YSU (see Figure 6.4d), which is itself linked to the vertical gradient of wind speed ($|\Delta v/\Delta z|$) in the formulation of Louis (see

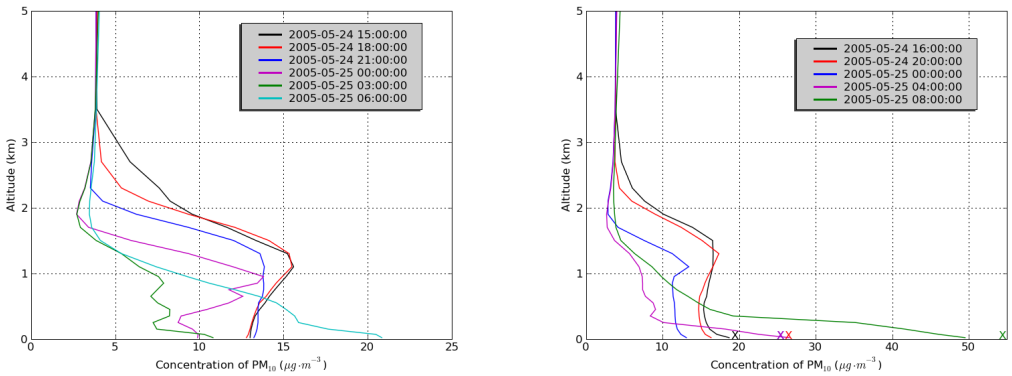

(a) **PM_{10} every three hours from 24 May 1500 UTC to 25 May 0600 UTC at Palaiseau (48.71°N, 2.22°E)**

(b) **PM_{10} every four hours from 24 May 1600 UTC to 25 May 0800 UTC at Paris, Les Halles (48.86°N, 2.35°E).**

Figure 6.5: Modeled PM_{10} vertical distributions using the YSU scheme. Cross marks are for the PM_{10} concentrations observed at the ground BDQA station (Les Halles) at the same hour as modeled PM_{10} (same color of marks used).

equation 6.1).

Figure 6.4e presents the vertical distribution of PM_{10} at Les Halles, Paris center on 25 May at 0357 UTC. Comparisons of Figures 6.4a and 6.4e allow one to compare the PM_{10} vertical distributions at the same place and same time on different days (i.e., different weather conditions). More developped PBL on 24 May results in lower surface PM_{10} concentrations (9 $\mu g/m^3$ from AIRPARIF measurements) than on 25 May (25 $\mu g/m^3$). The results obtained with UCM-Corine-YSU and -MYNN agree qualitatively well with the observed PM_{10}: modeled PM_{10} on 24 May and 25 May are about 25 $\mu g/m^3$ and 35 $\mu g/m^3$, respectively, while observed PM_{10} are 9 $\mu g/m^3$ on 24 May and 25 $\mu g/m^3$ on 25 May. As on 24 May, surface PM_{10} concentrations are over-estimated with Reference-MYNN and Reference-YSU, but this over-estimation is reduced using UCM-Corine. However, in contrast to 24 May, the PBL height is under-estimated in all simulations (264 m maximum for UCM-Corine-YSU against 477 m from the measurements), leading to an under-estimation of PM_{10} in the PBL between 200 m and 500 m. As on 24 May, PM_{10} in the residual layer tends to be under-estimated but over-estimated above.

To study how the influence of the automobile traffic on the concentration of PM_{10} is modeled, measurements performed at the same place (Les Halles) at 0357 UTC (before rush hour) and at 0755 UTC (during rush hour) are compared in Figures 6.4e and 6.4g. Surface PM_{10} concentrations measured by AIRPARIF increase from 26 $\mu g/m^3$ to 58 $\mu g/m^3$. At both 0357 UTC and 0755 UTC, surface PM_{10} concentrations are over-estimated with the Reference simulations, but they are well modeled with UCM-Corine (YSU and MYNN). Lidar measurements show a large increase of PM_{10} concentrations in the PBL, from concentrations lower than 30 $\mu g/m^3$ at 0357 UTC to concentrations higher than 90 $\mu g/m^3$ at 0755 UTC. Because the PBL height is strongly under-estimated in the Reference runs (145 m maximum for Reference-YSU against 403 m from the measurement), the PM_{10} concentrations are also under-estimated in the PBL below 400 m. However, they are better modeled with the UCM-Corine runs.

The residual layer observed by the lidar from about 0.5 km to 1 km of height is not well

simulated by the model. The low PM_{10} concentration in the residual layer may be partly due to difficulties to estimate the PBL height, an over-estimation of vertical mixing during nighttime at high altitudes, large-scale transport and under-estimation of PM_{10} in the boundary layer during daytime. Figures 6.5a and 6.5b present diurnal variations of the modeled PM_{10} vertical distribution at Palaiseau and Les Halles, respectively. The maximum PM_{10} concentration is about 16 $\mu g/m^3$ above 1 km between 24 May 1500 UTC and 1800 UTC at Palaiseau. The maximum PM_{10} concentration is much lower than the observed maximum PM_{10} (about 27 $\mu g/m^3$) in the residual layer on 25 May 0300 UTC (see Figure 6.4c). The modeled maximum PM_{10} during daytime is lower than observed maximum PM_{10} during nighttime, which partly explains the lower modeled maximum PM_{10} during nighttime. This lower maximum PM_{10} during daytime is also modeled at Les Halles during daytime on 24 May (about 18 $\mu g/m^3$). The observed maximum PM_{10} in the residual layer is 32 $\mu g/m^3$ at 0357 UTC and 41 $\mu g/m^3$ at 0755 UTC on 25 May (see Figures 6.4e and 6.4g). Compared to surface concentrations, modeled PM_{10} agrees well with observed PM_{10} at the BDQA surface station (Les Halles) at 1600 UTC on 24 May and 0400, 0800 UTC on 25 May (see Figure 6.5b), but it is under-estimated in the evening between 24 May 2000 UTC and 25 May 0000 UTC. This under-estimation may be a consequence of an over-estimation of the PBL height and mixing strength.

6.4.2 Sensitivity to the eddy-diffusion coefficient

In the Polair3D/Polyphemus simulations discussed in the previous sections, the vertical eddy-diffusion coefficient (K_z) in the boundary layer is parameterized following Troen et Mahrt [1986] (see section 6.2.2). A preprocessing tool calculates K_z from modeled meteorological variables, such as wind velocity and PBL height, which are obtained from WRF. To estimate the influence of the K_z parameterization on the PM_{10} vertical distribution, the K_z computed in the WRF model with the YSU and the MYNN schemes (eddy-diffusion coefficients for heat) are compared to the K_z obtained from the Polyphemus preprocessing tool. A minimum value of the coefficient is set to 10^{-6} m^2/s except in the lowest layers [Pleim, 2011] where it is set to 0.2 m^2/s. The simulations using K_z directly computed in WRF are labelled UCM-Corine-YSU-Kz and UCM-Corine-MYNN-Kz.

Modeled concentrations using UCM-Corine-YSU-Kz and UCM-Corine-MYNN-Kz are compared to observations from the BDQA database in Table 6.2 and observations at the Eiffel tower and Paris-7 in Table 6.3. The concentrations of PM_{10}, $PM_{2.5}$ and NO_2 with UCM-Corine-YSU-Kz and UCM-Corine-MYNN-Kz are systematically lower than those with UCM-Corine-YSU and UCM-Corine-MYNN, respectively. The concentrations of O_3 with UCM-Corine-YSU-Kz and UCM-Corine-MYNN-Kz are higher than (at the BDQA stations) or similar to (at the Eiffel tower) UCM-Corine-YSU and UCM-Corine-MYNN. At the surface, using the K_z from WRF with MYNN leads to significant differences of concentrations between UCM-Corine-MYNN-Kz and UCM-Corine-MYNN and the differences are higher than those simulated between UCM-Corine-MYNN and UCM-Corine-YSU.

Comparisons of surface PM_{10} concentrations to measurements at BDQA stations confirm that UCM-Corine-MYNN-Kz and UCM-Corine-YSU-Kz do not systematically perform better than UCM-Corine-MYNN and UCM-Corine-YSU. Although UCM-Corine-MYNN-Kz and UCM-Corine-YSU-Kz have slightly lower RMSE than UCM-Corine-MYNN and UCM-Corine-YSU, they also have higher bias as the mean PM_{10} concentrations are lower. However, for $PM_{2.5}$, UCM-Corine-MYNN-Kz and UCM-Corine-YSU-Kz perform better than UCM-

Corine-MYNN and UCM-Corine-YSU, as modeled concentrations are lower. The opposite is observed for O_3 and NO_2 with better performance of UCM-Corine-MYNN and UCM-Corine-YSU.

Figures 6.4b, 6.4d, 6.4f and 6.4h compare eddy-diffusion coefficients on 24 May 0357 UTC at Les Halles, on 25 May 0309 UTC at Palaiseau, on 25 May 0357 UTC and 0755 UTC at Les Halles respectively. At all places and times, the K_z computed in WRF with MYNN (WRF-MYNN) is significantly different from the K_z obtained using the method of Troen and Mahrt and WRF-MYNN meteorology. The differences are lower if the YSU scheme is used rather than MYNN in WRF, because the parameterization of K_z in the YSU scheme is based on the method of Troen and Mahrt.

Figures 6.4a, 6.4c, 6.4e and 6.4g compare the PM_{10} vertical distribution obtained using the different PBL schemes and K_z parameterizations on 24 May 0357 UTC at Les Halles, on 25 May 0309 UTC at Palaiseau, on 25 May 0357 UTC and 0755 UTC at Les Halles respectively. As expected, the influence of computing K_z in WRF on the PM_{10} vertical distribution is higher with MYNN than with YSU.

The differences of the PM_{10} concentrations between UCM-Corine-YSU and UCM-Corine-YSU-Kz are lower those between UCM-Corine-YSU and UCM-Corine-MYNN, suggesting that the impact of computing K_z in Polyphemus is low when the YSU PBL scheme is used in WRF. However, the differences of PM_{10} concentrations between UCM-Corine-MYNN and UCM-Corine-MYNN-Kz are higher than those between UCM-Corine-YSU and UCM-Corine-MYNN on 25 May 0357 UTC and on 25 May 0755 UTC at Les Halles: the RMSE between UCM-Corine-MYNN and UCM-Corine-MYNN-Kz is 8.45 $\mu g/m^3$ while the RMSE between UCM-Corine-YSU and UCM-Corine-MYNN is 3.80 $\mu g/m^3$ on 25 May 0755 UTC at Les Halles.

The differences between K_z computed by WRF-MYNN (max. 120 m^2/s) and K_z computed by Polyphemus/Troen and Mahrt (max. $\leq$ 10 m^2/s) are highest in Figure 6.4h (25 May 0755 UTC at Les Halles). As K_z by WRF-MYNN is higher than K_z by Troen and Mahrt, mixing is stronger and surface PM_{10} is lower with UCM-Corine-MYNN-Kz (30 $\mu g/m^3$) than with UCM-Corine-MYNN (55 $\mu g/m^3$). Compared to measurements, surface PM_{10} is significantly under-estimated with UCM-Corine-MYNN-Kz while it is well estimated with UCM-Corine-MYNN.

6.5 Discussion

Sensitivities of the vertical dispersion of pollutants to different meteorological and physical parameterizations (PBL schemes, urban canopy model (UCM) and eddy-diffusion coefficient) were studied using off-line meteorology (WRF) and chemistry-transport (Polair3D/Polyphemus) models. Two different PBL schemes were used (MYNN and YSU) and UCM was turned on and off. Pollutant concentrations were also compared to surface and lidar measurements.

Comparisons at surface stations (BDQA network) and at an upper air station (the Eiffel tower) show that simulations with UCM globally perform better. Higher surface concentrations are obtained for PM_{10}, $PM_{2.5}$ and NO_2 with the MYNN PBL scheme than the YSU PBL scheme, suggesting weaker vertical mixing in MYNN. Differences between simulations using different PBL schemes are lower than differences between simulations with and without UCM. The comparison of the NO_2 concentrations at the Eiffel tower and a surface station near the

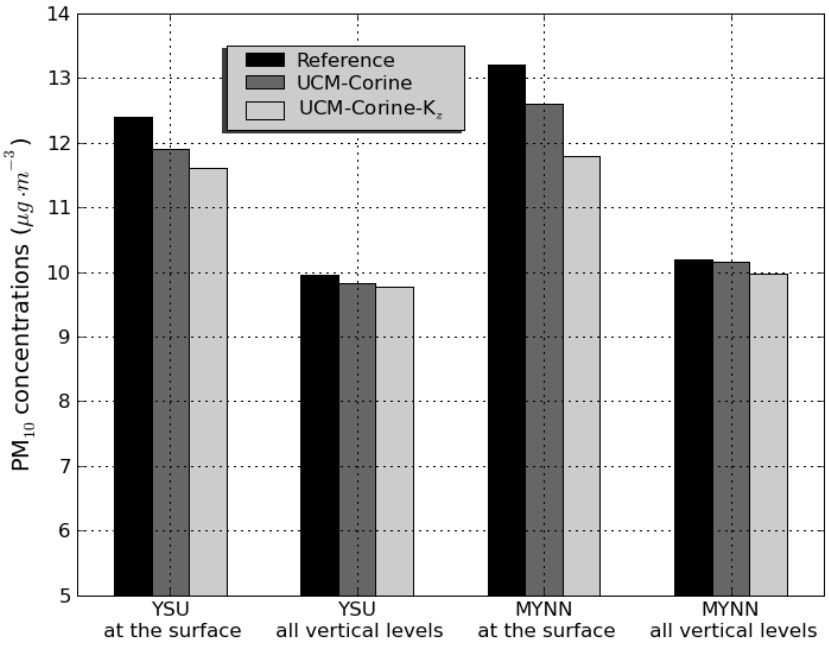

Figure 6.6: Domain-averaged PM_{10} concentrations over Greater Paris from 9 May to 27 May 2005 and differences between the simulations.

Eiffel tower shows an improvement in the modeled vertical mixing when UCM is used.

Concerning the comparisons of the modeled PM_{10} vertical distributions to the distributions obtained from lidar measurements, PM_{10} is under-estimated in the PBL on 25 May but over-estimated on 24 May, 0357 UTC at Les Halles. The concentrations of PM_{10} with YSU in the PBL are higher than those with MYNN because of the higher PBL heights with YSU, leading to a reduction of the under-estimations of PM_{10} in the PBL with YSU. However, as at surface stations, using UCM significantly influences the PM_{10} concentrations in the PBL, mostly because PBL heights and eddy-diffusion coefficients are higher. The influence of using UCM is greater than the influence of using different PBL schemes at Les Halles (Paris center).

PM_{10} concentrations tend to be under-estimated in the residual layer while they tend to be over-estimated over the residual layer. The under-estimations of PM_{10} during nighttime are related to the lower modeled PM_{10} in the convective boundary layer during daytime. Modeled maximum PM_{10} in the convective layer during daytime on 24 May is lower than observed maximum PM_{10} in the residual layer during nighttime and early morning on 25 May. The under-estimations of PM_{10} may also be related to an over-estimation of vertical mixing during nighttime at high altitudes.

The impact on PM_{10} of computing the eddy-diffusion coefficient K_z in Polyphemus (Troen and Mahrt parameterization) rather than using the one from WRF is larger for the MYNN scheme than the YSU scheme because the calculation of K_z in the YSU scheme is based on the method of Troen and Mahrt. PM_{10} surface concentrations are largely influenced by the computation of K_z for MYNN. For example, during the morning traffic rush hour, surface PM_{10} is reduced from 55 µg/m^3 to 30 µg/m^3 (45%) if K_z from WRF is used. However, using K_z

from WRF does not systematically perform better than using preprocessed K_z in Polyphemus.

Averaged over the whole domain and the three weeks of simulations, differences induced by PBL and UCM parameterizations have a stronger impact on surface PM_{10} than on PM_{10} at higher altitudes, as shown in Figure 6.6. For PM_{10} surface concentrations, the impact of the PBL parameterization is about 6% on average and the impact of the UCM model is 4 to 5%.

The results of this work imply that the model performance for the PM_{10} vertical dispersion is improved using UCM and updated Corine land-use over urbanized areas. In particular, the vertical mixing strength in the nocturnal boundary layer is significantly improved over the semi-urban and urban regions. However, the diagnosis of nocturnal boundary layer heights, which is related to PBL energy budget modeling, still needs to be improved, particularly over semi-urban regions. In this study, only one urban category of land-use data was used. More categories of urban land-use data would be required to take into account more accurate geometric and thermal characteristics in the WRF model.

Appendix 6.A Comparison of extinction coefficients

In the comparisons of particle vertical profiles of section 6.4.1, PM_{10} concentrations were derived from lidar measurements by Raut et Chazette [2009] using an empirical optical-to-mass relationship between dry PM_{10} concentrations in the PBL and dry extinction coefficients. This relationship was established from nephelometer and TEOM (Tapered element oscillating microbalance) in-situ measurements [Raut et Chazette, 2009]. However, depending on the relative humidity (RH) and their chemical composition, particles may absorb water vapor. The extinction coefficient obtained from lidar measurements is a wet one, that is, it takes into account all chemical components of particles including water. This wet extinction coefficient was used instead of the dry one to derive PM_{10} concentrations.

To assess the role of water in the comparisons of the vertical PM_{10} profiles, wet (α_{wet}) and dry (α_{dry}) extinction coefficients computed from the simulations were compared to each other and to extinction coefficients obtained from lidar measurements in Figure 6.A.1. The

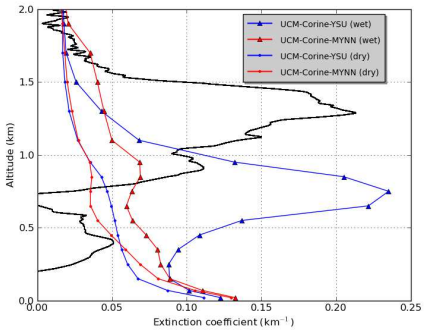

(a) α **(km^{-1}) on 24 May, 0357 UTC at Paris, Les Halles (48.86°N, 2.35°E)**

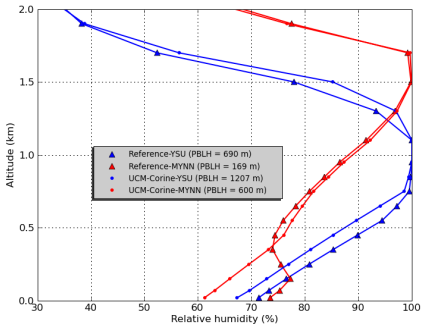

(b) **Relative humidity (%)**

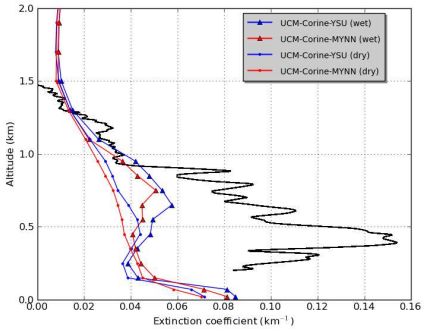

(c) α **(km^{-1}) on 25 May, 0309 UTC at Palaiseau (48.71°N, 2.22°E)**

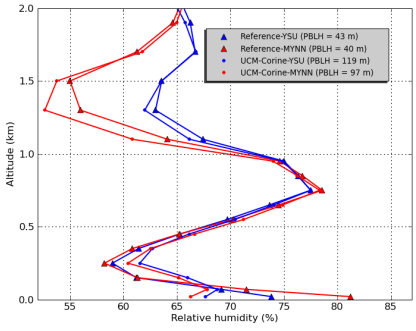

(d) **Relative humidity (%)**

Figure 6.A.1: Observed and modeled extinction coefficients are compared in the left column. Modeled relative humidities are shown in the right column.

computation of the α_{wet} and α_{dry} from the simulation was done using a postprocessing tool of Polyphemus [Real et Sartelet, 2011].

The comparison of α_{wet} to observation (Figure 6.A.1) exhibits similar patterns to the comparison of PM_{10} concentrations (Figure 6.4). On 24 May 0357 UTC at Les Halles, they are slightly over-estimated in the PBL under 0.7 km and under-estimated above 0.8 km. They are under-estimated on 25 May in both the PBL and the residual layer.

The differences between the simulated α_{dry} and α_{wet} are not significant for the three profiles of 25 May while they are important on 24 May 0357 UTC at Les Halles, especially between 0.5 km and 1 km height when the YSU PBL scheme is used to compute meteorological fields (Figure 6.A.1). The low differences between α_{dry} and α_{wet} are due to relatively low RH on 25 May: the RH peak is equal to 77% on 25 May 0309 UTC and 0357 UTC, 62% at 0755 UTC (see Figures 6.A.1d, 6.A.1f and 6.A.1h). The higher differences between α_{dry} and α_{wet} on 24 May 0357 UTC are a consequence of high RH. When the YSU PBL scheme is used, RH reaches a value of almost 100% in the residual layer (see Figure 6.A.1b). However, this high

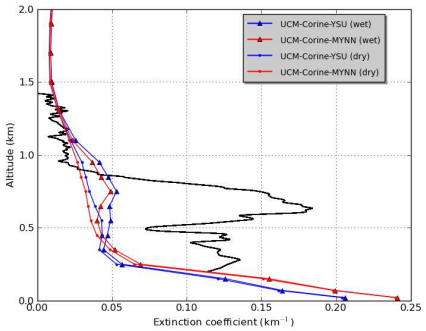

(e) α **(km^{-1}) on 25 May, 0357 UTC at Paris, Les Halles (48.86°N, 2.35°E)**

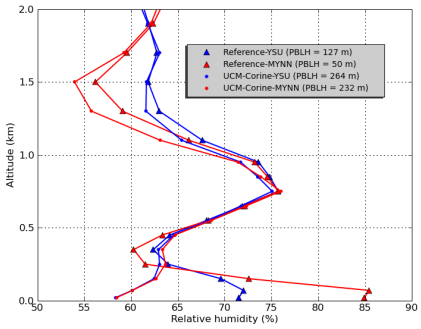

(f) **Relative humidity (%)**

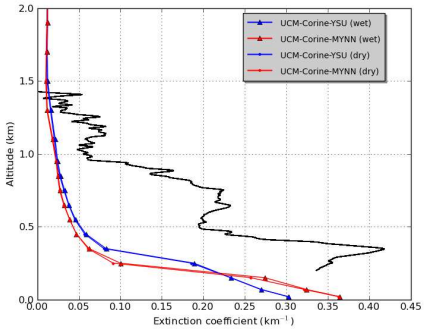

(g) α **(km^{-1}) on 25 May, 0755 UTC at Paris, Les Halles (48.86°N, 2.35°E)**

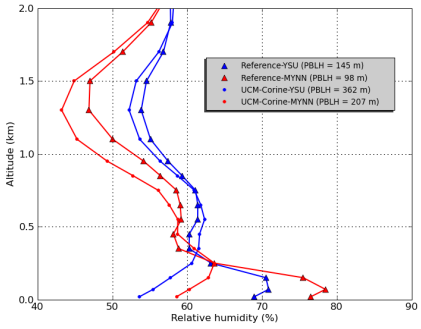

(h) **Relative humidity (%)**

Figure 6.A.1: Observed and modeled extinction coefficients are compared in the left column. Modeled relative humidities are shown in the right column.

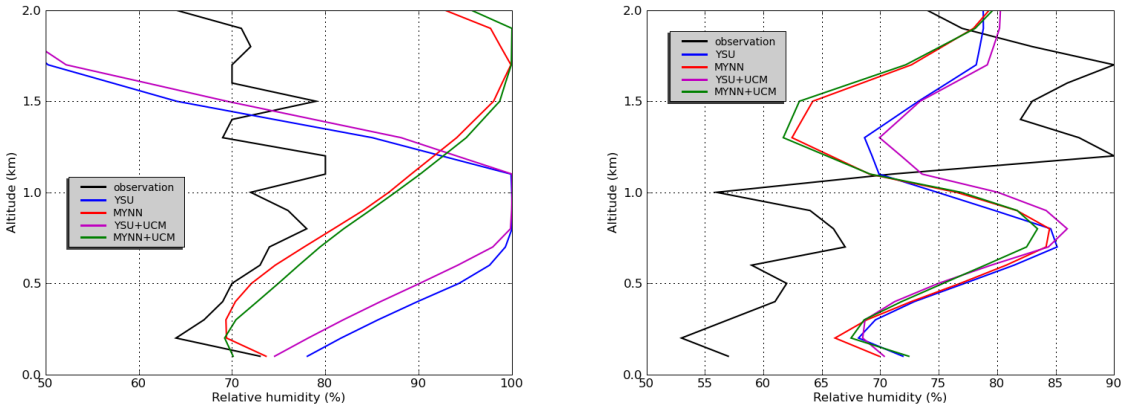

(a) **RH on 23 May 2305 UTC at Trappes**

(b) **RH on 24 May 2330 UTC at Trappes**

Figure 6.A.2: Vertical profiles of observed and modeled relative humidity. Observations are performed using the radiosonde at Trappes.

RH is not observed by the radiosonde at Trappes on 23 May 2305 UTC. Figure 6.A.2 compares the modeled and observed RH using the radiosonde at Trappes on 23 May 2305 UTC and on 24 May 2330 UTC, respectively. The RH are over-estimated between the surface and about 1 km height, suggesting an over-estimation of α_{wet} below 1km height, in particular on 24 May 0357 UTC at Les Halles.

In conclusion, α_{wet} should not be significantly different from α_{dry} for the vertical profiles of 24 May and 25 May, and the empirical optical-to-mass relationship used to derive PM_{10} concentrations from extinction coefficients may be used.

Chapitre 7

Conclusion et perspective

7.1 Conculsion

Les modèles de qualité de l'air (MQA) sont utilisés afin de décrire les processus de l'atmosphère qui influencent les concentrations de polluants. En raison de la complexité des processus physiques et chimiques concernés, certains processus doivent être paramétrisés, et le choix de la paramétrisation peut avoir une influence forte sur les concentrations. Dans cette thèse, nous avons étudié deux processus connus pour influencer les concentrations calculées des polluants de manière significative : le mécanisme chimique et la paramétrisation de la diffusivité turbulente verticale.

L'influence de deux mécanismes chimiques (CB05 et RACM2) sur la formation des polluants secondaires, l'ozone (O_3) et les particules fines ($PM_{2.5}$, particules de diamètre aérodynamique inférieur à 2,5 micromètres), a été évaluée. Les résultats de simulations sur l'Europe montrent que les différences sont faibles en moyenne pour les concentrations obtenues en utilisant CB05 et RACM2. Les différences moyennées sur le domaine sont de seulement 5% pour O_3 et 6% pour $PM_{2.5}$. Cependant, localement, les différences peuvent être plus importantes. Par exemple, des différences de 9% pour O_3 et de 15% pour $PM_{2.5}$ sont simulées sur des régions où les émissions anthropiques et biogéniques sont grandes. De fortes différences sont obtenues pour certains composés minéraux et organiques des $PM_{2.5}$. Plus particulièrement, les différentes concentrations d'O_3 et de $PM_{2.5}$ entre CB05 et RACM2 sont dues à :

- des incertitudes dans nos connaissances de la chimie (e.g., la cinétique des réactions d'oxydation de NO et l'importance relative des voies chimiques pour l'oxydation de composés aromatiques)

- des approximations nécessaires pour simplifier la chimie organique (e.g., selon le schéma chimique, il y a des différences d'émission des espèces du modèle dues aux différences d'agrégation des composés organiques volatils (COV), ainsi que des différences de cinétique d'oxydation).

Non seulement le choix du schéma chimique gazeux influence les concentrations de polluants, mais également le choix du schéma de modélisation des aérosols organiques secondaires (AOS). Les résultats de simulations de $PM_{2.5}$ en utilisant deux modules différents d'AOS (SORGAM et AEC) montrent que l'influence du module d'aérosols est due à plusieurs éléments :

- la liste des précurseurs (par exemple, isoprène et sesquiterpènes absents dans SORGAM mais présents dans AEC)
- l'oligomérisation de certains AOS de type aldéhyde
- l'effet des régimes en haut-NO_x et bas-NO_x (l'oxydation des précurseurs gazeux d'AOS ne varie pas avec les concentrations de NO_x dans SORGAM).

L'étude de la sensibilité conjointe des concentrations de particules aux deux modules d'AOS et aux deux mécanismes chimiques montre que les influences de ces deux éléments sur les concentrations d'AOS ne sont pas additives mais non-linéaires. Ceci est dû principalement au fait que la formation des AOS est très sensible aux concentrations de NO_x et, par conséquent, à la chimie de la phase gazeuse.

Les influences de la paramétrisation de la couche limite atmosphérique (CLA) et de l'effet de l'urbanisation sur les champs météorologiques et sur les concentrations de polluants en Île de France ont ensuite été estimées. Les champs météorologiques ont été calculés en utilisant le modèle météorologique WRF (Weather Research and Forecast). L'influence de la paramétrisation de la CLA sur les champs météorologiques est importante pour tous les champs étudiés (température, vitesse du vent, humidité et hauteur de CLA). Par exemple, la différence maximale de hauteurs de la CLA pendant la nuit entre les différentes paramétrisations de CLA est en moyenne d'un facteur trois. Pour l'effet de l'urbanisation, le modèle de canopée urbaine UCM de WRF et la base de données Corine pour l'occupation des sols sont utilisés. En général, l'influence de l'utilisation d'UCM-Corine sur les champs météorologiques simulés est supérieure à celle de la paramétrisation de la CLA. Pour les hauteurs de la CLA, l'influence du choix de la paramétrisation de la CLA est plus importante que celle de UCM-Corine dans la banlieue de Paris, tandis que cette dernière est plus importante au centre de Paris.

En ce qui concerne les concentrations de particules, les résultats de simulations avec le MQA Polair3d/Polyphemus confirment l'influence plus grande d'UCM-Corine par rapport aux paramétrisations de la CLA près du sol. Les concentrations verticales sont surtout influencées par la paramétrisation de la CLA en régions rurale et semi-urbaine alors que l'influence d'UCM-Corine est plus important en région urbaine. Non seulement la paramétrisation de la CLA dans le modèle météorologique influence les champs météorologiques et les concentrations de polluants, mais la paramétrisation utilisée pour représenter la diffusivité turbulente dans le MQA est également importante.

Des comparaisons entre les concentrations à la station de la Tour Eiffel et celles à la station au sol près de la Tour Eiffel (Paris-7) montrent que les influences de la chimie et de la météorologie sont difficilement dissociables pour les composés secondaires. L'utilisation d'UCM-Corine diminue les concentrations moyennes de NO_2 au sol (Paris-7) et augmente celles en hauteur (Tour Eiffel), par augmentation du mélange vertical (météorologie). Cette augmentation de NO_2 en hauteur est associée à une diminution de l'ozone par titration (chimie).

7.2 Perspectives

Dans cette thèse, plusieurs voies d'amélioration des mécanismes chimiques ont été proposées. Des données expérimentales sont nécessaires pour réduire les incertitudes actuelles en phase gazeuse, en particulièr pour la cinétique d'oxydation de NO par O_3 et par les radicaux péroxyles et pour les voies majeures d'oxydation des composés aromatiques (conservation versus scission du noyau). Des études récentes liées aux incertitudes pour les réactions en phase gazeuse pour l'oxydation minérale [Mollner *et al.*, 2010] et l'oxydation organique [Whitten *et al.*, 2010] vont dans ce sens.

Plusieurs étapes d'oxydation devraient être prises en compte pour améliorer la formation des PM car les AOS sont formés au fil d'étapes d'oxydation successive des COV et les voies d'oxydations sont sensibles au niveau des NO_x. Dans cette thèse, les deux étapes d'oxydation sont utilisées seulement pour le toluène et le xylène grâce aux résultats disponibles des études expérimentales. Donc, des études expérimentales supplémentaires sont nécessaires pour prendre en compte plusieurs étapes d'oxydation pour d'autres COV.

Pour améliorer la modélisation de la dispersion verticale des polluants, il faudrait des catégories détaillées d'occupation des sols urbanisés, qui devraient être mises à jour pour prendre en compte l'évolution des zones urbaines. Les champs météorologiques modélisés sont très sensibles aux paramètres dans le modèle urbain (e.g., la hauteur du bâtiment, le rapport des largeurs du bâtiment et de la rue, l'évolution diurne de la chaleur anthropique, etc). Les catégories détaillées pourraient permettre d'utiliser les paramètres appropriés pour divers types de régions (urbain, semi-urbain et rural). Il est encore difficile de choisir les paramètres représentantes pour un type de région.

L'utilisation du modèles urbains en multi-couches serait utile pour la modélisation du champ météorologique sur la région urbaine parce que les hauteurs de bâtiment sont variables dans cette région. Le modèle en multi-couche permettra de modéliser des échanges thermiques aux différents niveaux verticaux liés aux hauteurs de bâtiment. Cependant, la chaleur anthropique devrait préalablement être explicitement représentée dans le modèle en multi-couche.

Il faudrait aussi améliorer la modélisation de la hauteur de la couche limite nocturne dans le modèle météorologique. L'origine de l'incertitude liée aux hauteurs de la couche limite selon les paramétrisations est encore un sujet important.

Finalement, il vaut mieux garder la plus grande cohérence possible entre les champs météorologiques calculés par le modèle météorologique et ceux utilisés par les MQA (ou l'utilisation de modèles "en ligne" qui intègrent météorologie et transformations chimiques).

Bibliographie

Ansari, A. S. et Pandis, S. N. (1998). Response of inorganic PM to precursor concentrations. *Environ. Sci. Technol.*, 32(18):2706–2714. 18, 75

Appel, K., Roselle, S., Gilliam, R. et Pleim, J. (2010). Sensitivity of the Community Multiscale Air Quality (CMAQ) model v4.7 results for the eastern United States to MM5 and WRF meteorological drivers. *Geosci. Model Dev.*, 3(1):169–188. 125

Argentini, S., Mastrantonio, G. et Lena, F. (1999). Case studies of the wintertime convective boundary-layer structure in the urban area of Milan, Italy. *Bound.-Lay. Meteorol.*, 93:253–267. 98

Arnold, D., Schicker, I. et Seibert, P. (2010). High-resolution atmospheric modelling in complex terrain for future climate simulations (HiRmod). VSC report 2010 available at `http://www.boku.ac.at/met/envmet/hirmod.html`. 101

Arteta, J., Cautenet, S., Taghavi, M. et Audiffren, N. (2006). Impact of two chemistry mechanisms fully coupled with mesoscale model on the atmospheric pollutants distribution. *Atmos. Environ.*, 40(40):7983–8001. 27

Atkinson, R., Baulch, D. L., Cox, R. A., Crowley, J. N., Hampson, R. F., Hynes, R. G., Jenkin, M. E., Rossi, M. J. et Troe, J. (2005). Evaluated kinetic and photochemical data for atmospheric chemistry - IUPAC subcommittee on gas kinetic data evaluation for atmospheric chemistry. available at : `http://www.iupac-kinetic.ch.cam.ac.uk/`. 28

Atkinson, R., Baulch, D. L., Cox, R. A., Crowley, J. N., Hampson, R. F., Hynes, R. G., Jenkin, M. E., Rossi, M. J. et Troe, J. (2006). Evaluated kinetic and photochemical data for atmospheric chemistry - IUPAC subcommittee on gas kinetic data evaluation for atmospheric chemistry. available at : `http://www.iupac-kinetic.ch.cam.ac.uk/`. 28

Aumont, B., Szopa, S. et Madronich, S. (2005). Modelling the evolution of organic carbon during its gas-phase tropospheric oxidation : development of an explicit model based on a self generating approach. *Atmos. Chem. Phys.*, 5(9):2497–2517. 27

Bailey, E., Gautney, L., Kelsoe, J., Jacobs, M., Mao, Q., Condrey, J., Pun, B., Wu, S.-Y., Seigneur, C., Douglas, S., Haney, J. et Kumar, N. (2007). A comparison of the performance of four air quality models for the Southern Oxidants Study episode in July 1999. *J. Geophys. Res.*, 112, D05306. 67, 83, 86

Bessagnet, B., Menut, L., Curci, G., Hodzic, A., Guillaume, B., Liousse, C., Moukhtar, S., Pun, B., Seigneur, C. et Schulz, M. (2008). Regional modeling of carbonaceous aerosols over Europe—focus on secondary organic aerosols. *J. Atmos. Chem.*, 61:175–202. 12, 84

Blanchard, C. L., Roth, P. M., Tanenbaum, S. J., Ziman, S. D. et Seinfeld, J. H. (2000). The use of ambient measurements to identify which precursor species limit aerosol nitrate formation. *J. Air & Waste Manage. Assoc.*, 50(12):2073–2084. 18

Bloss, C., Wagner, V., Jenkin, M. E., Volkamer, R., Bloss, W. J., Lee, J. D., Heard, D. E., Wirtz, K., Martin-Reviejo, M., Rea, G., Wenger, J. C. et Pilling, M. J. (2005). Development of a detailed chemical mechanism (MCMv3.1) for the atmospheric oxidation of aromatic hydrocarbons. *Atmos. Chem. Phys.*, 5(3):641–664. available at : `http://mcm.leeds.ac.uk/MCM/`. 28

Borge, R., Alexandrov, V., Josedelvas, J., Lumbreras, J. et Rodríguez, E. (2008). A comprehensive sensitivity analysis of the WRF model for air quality applications over the Iberian Peninsula. *Atmos. Environ.*, 42(37):8560–8574. 98, 125

Bowman, F. M., Pilinis, C. et Seinfeld, J. H. (1995). Ozone and aerosol productivity of reactive organics. *Atmos. Environ.*, 29:579–589. 33

Boylan, J. W. et Russell, A. G. (2006). PM and light extinction model performance metrics, goals, and criteria for three-dimensional air quality models. *Atmos. Environ.*, 40(26):4946–4959. 65, 85, 128

Byun, D. et Schere, K. L. (2006). Review of the governing equations, computational algorithms, and other components of the Models-3 Community Multiscale Air Quality (CMAQ) modeling system. *Appl. Mech. Rev.*, 59(2):51–77. 12

Cai, H. et Xie, S. D. (2010). A modelling study of air quality impact of odd-even day traffic restriction scheme before, during and after the 2008 Beijing Olympic Games. *Atmos. Chem. Phys. Discuss.*, 10(2):5135–5184. 11

Calvert, J. G., Atkinson, R., Becker, K. H., Kamens, R. M., Seinfeld, J. H., Wallington, T. J. et Yarwood, G. (2002). *The Mechanisms of Atmospheric Oxidation of Aromatic Hydrocarbons*. Oxford University Press, New York. 44

Calvert, J. G., Derwent, R. G., Orlando, J. J., Tyndall, G. S. et Wallington, T. J. (2008). *Mechanisms of Atmospheric Oxidation of the Alkanes*. Oxford University Press, New York. 46

Carlton, A. G., Bhave, P. V., Napelenok, S. L., Edney, E. O., Sarwar, G., Pinder, R. W., Pouliot, G. A. et Houyoux, M. (2010). Model representation of secondary organic aerosol in CMAQv4.7. *Environ. Sci. Technol.*, 44(22):8553–8560. 83

Carlton, A. G., Turpin, B. J., Altieri, K. E., Seitzinger, S. P., Mathur, R., Roselle, S. J. et Weber, R. J. (2008). CMAQ model performance enhanced when in-cloud secondary organic aerosol is included : Comparisons of organic carbon predictions with measurements. *Environ. Sci. Technol.*, 42(23):8798–8802. 94

Carter, W. P. L. (1995). Computer modeling of environmental chamber measurements of maximum incremental reactivities of volatile organic compounds. *Atmos. Environ.*, 29:2513–2527. 33

Carter, W. P. L. (2000). Implementation of the SAPRC-99 chemical mechanism into the models-3 framework. Report to the United States Environmental Protection Agency, available at : http://www.cert.ucr.edu/~carter/pubs/s99mod3.pdf. 57

Carter, W. P. L. (2008). Development of an improved chemical speciation database for processing emissions of volatile organic compounds for air quality models. available at : http://www.engr.ucr.edu/~carter/emitdb/. 30, 64

Carter, W. P. L. (2010). Development of the SAPRC-07 chemical mechanism and updated ozone reactivity scales. Report to the California Air Resources Board, available at : http://www.engr.ucr.edu/~carter/SAPRC/saprc07.pdf. 57

Carter, W. P. L., Pierce, J. A., Dongmin, L. et Malkina, I. L. (1995). Environmental chamber study of maximum incremental reactivities of volatile organic compounds. *Atmos. Environ.*, 29:2499–2511. 33

Carvalho, A., Monteiro, A., Solman, S., Miranda, A. et Borrego, C. (2010). Climate-driven changes in air quality over Europe by the end of the 21st century, with special reference to Portugal. *Environ. Sci. Policy*, 13(6):445–458. 12

Castell, N., Stein, A. F., Salvador, R., Mantilla, E. et Millán, M. (2008). The impact of biogenic VOC emissions on photochemical ozone formation during a high ozone pollution episode in the Iberian Peninsula in the 2003 summer season. *Adv. Sci. Res.*, 2:9–15. 49

Chen, F. et Dudhia, J. (2001). Coupling an advanced land surface-hydrology model with the Penn State-NCAR MM5 modeling system. Part I : Model implementation and sensitivity. *Mon. Wea. Rev.*, 129:569–585. 99

Chen, F., Kusaka, H., Bornstein, R., Ching, J., Grimmond, C., Grossman-Clarke, S., Loridan, T., Manning, K., Martilli, A., Miao, S., Sailor, D., Salamanca, F., Taha, H., Tewari, M., Wang, X., Wyszogrodzki, A. et Zhang, C. (2011). The integrated WRF/urban modeling system : development, evaluation, and applications to urban environmental problems. *Int. J. Climatol.*, 31(2):479–492. 125

Chen, W., Kuze, H., Uchiyama, A., Suzuki, Y. et Takeuchi, N. (2001). One-year observation of urban mixed layer characteristics at Tsukuba, Japan using a micro pulse lidar. *Atmos. Environ.*, 35(25):4273–4280. 125

Chin, M., Rood, R. B., Lin, S.-J., Müller, J.-F. et Thompson, A. M. (2000). Atmospheric sulfur cycle simulated in the global model GOCART : Model description and global properties. *J. Geophys. Res.*, 105(D20):24671–24687. 65

Chou, C. C.-K., Lee, C.-T., Chen, W.-N., Chang, S.-Y., Chen, T.-K., Lin, C.-Y. et Chen, J.-P. (2007). Lidar observations of the diurnal variations in the depth of urban mixing layer : a case study on the air quality deterioration in Taipei, Taiwan. *Sci. Total Environ.*, 374(1):156–166. 125

Chou, M.-D. et Suarez, M. J. (1994). An efficient thermal infrared radiation parameterization for use in general circulation models. *NASA Tech. Memo. 104606*, 3:85. available at : http://citeseerx.ist.psu.edu/viewdoc/download?doi=10.1.1.26.4850&rep=rep1&type=ps. 99

Chow, J. C., Watson, J. G., Crow, D., Lowenthal, D. H. et Merrifield, T. (2001). Comparison of improve and niosh carbon measurements. *Aerosol Sci. Technol.*, 34(1):23–34. 68

Curci, G., Beekmann, M., Vautard, R., Smiatek, G., Steinbrecher, R., Theloke, J. et Friedrich, R. (2009). Modelling study of the impact of isoprene and terpene biogenic emissions on European ozone levels. *Atmos. Environ.*, 43(7):1444–1455. 36

de Meij, A., Gzella, A., Cuvelier, C., Thunis, P., Bessagnet, B., Vinuesa, J., Menut, L. et Kelder, H. (2009). The impact of MM5 and WRF meteorology over complex terrain on CHIMERE model calculations. *Atmos. Chem. Phys.*, 9:6611–6632. 125

Debry, É., Fahey, K., Sartelet, K., Sportisse, B. et Tombette, M. (2007a). Technical Note : A new SIze REsolved Aerosol Model (SIREAM). *Atmos. Chem. Phys.*, 7(6):1537–1547. 17, 58, 126

Debry, É., Seigneur, C. et Sartelet, K. (2007b). Organic aerosols in the air quality platform Polyphemus : oxidation pathways, hydrophilic/hydrophobic partitioning and oligomerization. International Aerosol Modeling Algorithms. University of California, Davis, available at : `http://mae.ucdavis.edu/wexler/IAMA/ppts/VIIB/debry_iama.pdf`. 58, 60, 61, 71, 83, 84, 87, 91

Deguillaume, L., Tilgner, A., Schrödner, R., Wolke, R., Chaumerliac, N. et Herrmann, H. (2009). Towards an operational aqueous phase chemistry mechanism for regional chemistry-transport models : CAPRAM-RED and its application to the COSMO-MUSCAT model. *J. Atmos. Chem.*, 64:1–35. 94

Demuzere, M., De Ridder, K. et Van Lipzig, N. P. M. (2008). Modeling the energy balance in Marseille : Sensitivity to roughness length parameterizations and thermal admittance. *J. Geophys. Res.*, 113(D16120). 101

Dennis, R. L., Byun, D. W., Novak, J. H., Galluppi, K. J., Coats, C. J. et Vouk, M. A. (1996). The next generation of integrated air quality modeling : EPA's models-3. *Atmos. Environ.*, 30(12):1925–1938. 27

Derwent, R. G., Jenkin, M. E., Passant, N. R. et Pilling, M. J. (2007). Reactivity-based strategies for photochemical ozone control in Europe. *Environ. Sci. Policy*, 10(5):445–453. 33

Djouad, R., Sportisse, B. et Audiffren, N. (2002). Numerical simulation of aqueous-phase atmospheric models : use of a non-autonomous Rosenbrock method. *Atmos. Environ.*, 36(5): 873–879. 30

Dodge, M. C. (2000). Chemical oxidant mechanisms for air quality modeling : critical review. *Atmos. Environ.*, 34:2103–2130. 27, 28

Dommen, J., Prévôt, A., Neininger, B. et Bäumle, M. (2002). Characterization of the photooxidant formation in the metropolitan area of Milan from aircraft measurements. *J. Geophys. Res.*, 107(D22):8197. 36

Doran, J. C., Fast, J. D. et Horel, J. (2002). The VTMX 2000 campaign. *Bull. Am. Meteorol. Soc.*, 83(4):537–551. 98

Dudhia, J. (1993). A nonhydrostatic version of the Penn State NCAR Mesoscale Model : Validation tests and simulation of an Atlantic cyclone and cold front. *Mon. Wea. Rev.*, 121: 1493–1513. 127

Duhanian, N. et Roustan, Y. (2011). Below-cloud wet scavenging coefficients for atmospheric gases and particulates. *Atmos. Environ.* in press. 17

Dupont, E., Menut, L., Carissimo, B., Pelon, J. et Flamant, P. (1999). Comparison between the atmospheric boundary layer in Paris and its rural suburbs during the ECLAP experiment. *Atmos. Environ.*, 33:979–994. 98, 102, 125

Dupont, S., Otte, T. L. et Ching, J. K. S. (2004). Simulation of meteorological fields within and above urban and rural canopies with a mesoscale model. *Bound.-Lay. Meteorol.*, 113:111–158. 98

El Haddad, I., Liu, Y., Nieto-Gligorovski, L., Michaud, V., Temime-Roussel, B., Quivet, E., Marchand, N., Sellegri, K. et Monod, A. (2009). In-cloud processes of methacrolein under simulated conditions - Part 2 : Formation of secondary organic aerosol. *Atmos. Chem. Phys.*, 9:5107–5117. 94

Ervens, B., Carlton, A. G., Turpin, B. J., Altieri, K. E., Kreidenweis, S. M. et Feingold, G. (2008). Secondary organic aerosol yields from cloud-processing of isoprene oxidation products. *Geophys. Res. Lett.*, 35:L02816. 94

Fan, H. et Sailor, D. J. (2005). Modeling the impacts of anthropogenic heating on the urban climate of philadelphia : a comparison of implementations in two pbl schemes. *Atmos. Environ.*, 39(1):73–84. 98

Faraji, M., Kimura, Y., McDonald-Buller, E. et Allen, D. (2008). Comparison of the carbon bond and SAPRC photochemical mechanisms under conditions relevant to southeast Texas. *Atmos. Environ.*, 42(23):5821–5836. 27, 44

Fast, J., Doran, J., Shaw, W., Coulter, R. et Martin, T. (2000). The evolution of the boundary layer and its effect on air chemistry in the Phoenix area. *J. Geophys. Res.*, 105(D18):22833–22848. 98

Finlayson-Pitts, B. J. et Pitts, Jr., J. N. (2000). *Chemistry of the upper and lower atmosphere*. Academic Press, San Diego. 17, 27, 57

Flamant, C., Pelon, J., Flamant, P. H. et Durand, P. (1997). Lidar determination of the entrainment zone thickness at the top of the unstable marine atmospheric boundary layer. *Bound.-Lay. Meteorol.*, 83:247–284. 125

Gaydos, T. M., Pinder, R., Koo, B., Fahey, K. M., Yarwood, G. et Pandis, S. N. (2007). Development and application of a three-dimensional aerosol chemical transport model, PMCAMx. *Atmos. Environ.*, 41(12):2594–2611. 83

Gerber, H. (1985). Relative-humidity parameterization of the Navy Aerosol Model (NAM). Technical Report 8956, Natl. Res. Lab., Washington D.C., available at `http://handle.dtic.mil/100.2/ADA163209`. 64

Gery, M. W., Whitten, G. Z., Killus, J. P. et Dodge, M. C. (1989). A photochemical kinetics mechanism for urban and regional scale computer modeling. *J. Geophys. Res.*, 94(D10): 12925–12956. 28, 57, 59

Goliff, W. S. et Stockwell, W. R. (2008). The Regional Atmospheric Chemistry Mechanism, version 2, an update. University of California, Davis. International conference on Atmospheric Chemical Mechanisms. available at : `http://airquality.ucdavis.edu/pages/events/2008/acm/Goliff.pdf`. 28, 57, 59, 83

Goliff, W. S. et Stockwell, W. R. (2010). The Regional Atmospheric Chemistry Mechanism, version 2. 1. Description and Evaluation. *in preparation, to be submitted to J. Geophys. Res*. 28, 29, 30, 59

Grell, G. A. et Devenyi, D. (2002). A generalized approach to parameterizing convection combining ensemble and data assimilation techniques. *Geophys. Res. Lett.*, 29(14):38.1–38.4. 99

Grell, G. A., Emeis, S., Stockwell, W. R., Schoenemeyer, T., Forkel, R., Michalakes, J., Knoche, R. et Seidl, W. (2000). Application of a multiscale, coupled MM5/chemistry model to the complex terrain of the VOTALP valley campaign. *Atmos. Environ.*, 34(9):1435–1453. 12

Grell, G. A., Peckham, S. E., Schmitz, R., McKeen, S. A., Frost, G., Skamarock, W. C. et Eder, B. (2005). Fully coupled "online" chemistry within the WRF model. *Atmos. Environ.*, 39(37):6957–6975. 12

Griffin, R. J., Dabdub, D. et Seinfeld, J. H. (2002). Secondary organic aerosol 1. atmospheric chemical mechanism for production of molecular constituents. *J. Geophys. Res.*, 107(D17). 58, 78

Gross, A. et Stockwell, W. R. (2003). Comparison of the EMEP, RADM2 and RACM Mechanisms. *J. Atmos. Chem.*, 44:151–170. 21

Guibert, S., Matthias, V., Schulz, M., Bösenberg, J., Eixmann, R., Mattis, I., Pappalardo, G., Perrone, M. R., Spinelli, N. et Vaughan, G. (2005). The vertical distribution of aerosol over Europe–synthesis of one year of EARLINET aerosol lidar measurements and aerosol transport modeling with LMDzT-INCA. *Atmos. Environ.*, 39(16):2933–2943. 125

Haeffelin, M., Barthès, L., Bock, O., Boitel, C., Bony, S., Bouniol, D., Chepfer, H., Chiriaco, M., Cuesta, J., Delanoë, J., Drobinski, P., Dufresne, J.-L., Flamant, C., Grall, M., Hodzic, A., Hourdin, F., Lapouge, F., Lemaître, Y., Mathieu, A., Morille, Y., Naud, C., Noël, V., O'Hirok, W., Pelon, J., Pietras, C., Protat, A., Romand, B., Scialom, G. et Vautard, R. (2005). SIRTA, a ground-based atmospheric observatory for cloud and aerosol research. *Ann. Geophys.*, 23(2):253–275. 102

Hakami, A., Bergin, M. S. et Russell, A. G. (2004). Ozone formation potential of organic compounds in the eastern United States : A comparison of episodes, inventories, and domains. *Environ. Sci. Technol.*, 38(24):6748–6759. 33, 46

Han, Z., Ueda, H. et Matsuda, K. (2005). Model study of the impact of biogenic emission on regional ozone and the effectiveness of emission reduction scenarios over eastern China. *Tellus B*, 57:12–27. 46

Hedegaard, G. (2007). Impacts of climate change on air pollution levels in the northern hemisphere. National Environmental Research Institute, University of Aarhus. Denmark - Research Notes from NERI No. 240 available at : `www.dmu.dk/Pub/AR240.pdf`. 12

Hering, S. et Cass, G. (1999). The magnitude of bias in the measurement of $PM_{2.5}$ arising from volatilization of particulate nitrate from teflon filters. *J. Air Waste Manage. Assoc.*, 49:725–733. 67

Holtslag, A. A. M., Meijgaard, E. et Rooy, W. C. (1995). A comparison of boundary layer diffusion schemes in unstable conditions over land. *Bound.-Lay. Meteorol.*, 76:69–95. 98

Hong, S.-Y., Noh, Y. et Dudhia, J. (2006). A new vertical diffusion package with an explicit treatment of entrainment processes. *Mon. Wea. Rev.*, 134(9):2318–2341. 98, 100

Hong, S.-Y. et Pan, H.-L. (1996). Nonlocal boundary layer vertical diffusion in a medium-range forecast model. *Mon. Wea. Rev.*, 124(10):2322–2339. 98, 100

Honoré, C., Rouïl, L., Vautard, R., Beekmann, M., Bessagnet, B., Dufour, A., Elichegaray, C., Flaud, J.-M., Malherbe, L., Meleux, F., Menut, L., Martin, D., Peuch, A., Peuch, V.-H. et Poisson, N. (2008). Predictability of European air quality : Assessment of 3 years of operational forecasts and analyses by the PREV'AIR system. *J. Geophys. Res.*, 113, D04301. 32

Honoré, C., Vautard, R. et Beekmann, M. (2000). Photochemical regimes in urban atmospheres : The influence of dispersion. *Geophys. Res. Lett.*, 27(13):1895–1898. 36

Horowitz, L. W., Walters, S., Mauzerall, D. L., Emmons, L. K., Rasch, P. J., Granier, C., Tie, X., Lamarque, J.-F., Schultz, M. G., Tyndall, G. S., Orlando, J. J. et Brasseur, G. P. (2003). A global simulation of tropospheric ozone and related tracers : Description and evaluation of MOZART, version 2. *J. Geophys. Res.*, 108(D24):4784. 65

Hu, X.-M., Nielsen-Gammon, J. W. et Zhang, F. (2010). Evaluation of three planetary boundary layer schemes in the WRF model. *J. Appl. Meteorol. Climatol.*, 49(9):1831–1844. 98, 100

Jacob, D. J. (2000). Heterogeneous chemistry and tropospheric ozone. *Atmos. Environ.*, 34(12-14):2131–2159. 60

Jacobson, M. Z. (2001). GATOR-GCMM : A global- through urban-scale air pollution and weather forecast model 1. Model design and treatment of subgrid soil, vegetation, roads, rooftops, water, sea ice, and snow. *J. Geophys. Res.*, 106:5385–5401. 12

Jacobson, M. Z. (2005). *Fundamentals of Atmospheric Modeling*. Cambridge University Press, 2nd edition, Cambridge. 10

Janjic, Z. I. (2001). Nonsingular implementation of the Mellor-Yamada level 2.5 scheme in the NCEP Meso model. National Centers for Environmental Prediction, Office Note 437, available at : `http://www.emc.ncep.noaa.gov/officenotes/newernotes/on437.pdf`. 100

Johnson, D., Utembe, S. R., Jenkin, M. E., Derwent, R. G., Hayman, G. D., Alfarra, M. R., Coe, H. et McFiggans, G. (2006). Simulating regional scale secondary organic aerosol formation during the TORCH 2003 campaign in the southern UK. *Atmos. Chem. Phys.*, 6:403–418. 30

Junier, M., Kirchner, F., Clappier, A. et van den Bergh, H. (2005). The chemical mechanism generation programme CHEMATA–Part 2 : Comparison of four chemical mechanisms for mesoscale calculation of atmospheric pollution. *Atmos. Environ.*, 39(6):1161–1171. 27, 36

Kaufman, Y., Tanré, D., Léon, J.-F. et Pelon, J. (2003). Retrievals of profiles of fine and coarse aerosols using lidar and radiometric space measurements. *IEEE Trans. Geosci. Remote Sens.*, 41(8):1743–1754. 125

Keck, L. et Wittmaack, K. (2005). Effect of filter type and temperature on volatilisation losses from ammonium salts in aerosol matter. *Atmos. Environ.*, 39:4093–4100. 67

Kessler, E. (1969). On the distribution and continuity of water substance in atmospheric circulation. *Meteor. Monogr.*, 32:84. 99

Kim, Y., Couvidat, F., Sartelet, K. et Seigneur, C. (2011). Comparison of different gas-phase mechanisms and aerosol modules for simulating particulate matter formation. *J. Air Waste Manage. Assoc.*, 61:1–9. 126

Kim, Y., Fu, J. S. et Miller, T. L. (2010a). Improving ozone modeling in complex terrain at a fine grid resolution : Part I – examination of analysis nudging and all PBL schemes associated with LSMs in meteorological model. *Atmos. Environ.*, 44(4):523–532. 98

Kim, Y., Fu, J. S. et Miller, T. L. (2010b). Improving ozone modeling in complex terrain at a fine grid resolution – Part II : Influence of schemes in MM5 on daily maximum 8-h ozone concentrations and RRFs (Relative Reduction Factors) for SIPs in the non-attainment areas. *Atmos. Environ.*, 44(17):2116–2124. 125

Kim, Y. et Sartelet, K. (2011a). Evaluation of the modeling of the PM_{10} vertical distribution over Greater Paris : Part I - Meteorological evaluation. *Atmos. Environ.*, submitted. 125, 127, 132

Kim, Y. et Sartelet, K. (2011b). Evaluation of the modeling of the PM_{10} vertical distribution over Greater Paris : Part II - Comparison to measurements. *Atmos. Environ.*, submitted. 103

Kim, Y., Sartelet, K. et Seigneur, C. (2009). Comparison of two gas-phase chemical kinetic mechanisms of ozone formation over Europe. *J. Atmos. Chem.*, 62(2):89–119. 57, 59, 63, 65, 69, 83, 84, 92

Kleindienst, T. E., Lewandowski, M., Offenberg, J. H., Jaoui, M. et Edney, E. O. (2009). The formation of secondary organic aerosol from the isoprene + OH reaction in the absence of NO_x. *Atmos. Chem. Phys.*, 9(17):6541–6558. 91

Kuebler, J., Giovannoni, J. M. et Russell, A. G. (1996). Eulerian modeling of photochemical pollutants over the Swiss Plateau and control strategy analysis. *Atmos. Environ.*, 30(6):951–966. 36

Kuhn, M., Builtjes, P. J. H., Poppe, D., Simpson, D., Stockwell, W. R., Andersson-Skold, Y., Baart, A., Das, M., Fiedler, F., Hov, Ø., Kirchner, F., Makar, P. A., Milford, J. B., Roemer, M. G. M., Ruhnke, R., Strand, A., Vogel, B. et Vogel, H. (1998). Intercomparison of the gas-phase chemistry in several chemistry and transport models. *Atmos. Environ.*, 32:693–709. 27

Kusaka, H., Kondo, H., Kikegawa, Y. et Kimura, F. (2001). A simple single-layer urban canopy model for atmospheric models : comparison with multi-layer and slab models. *Bound.-Lay. Meteorol.*, 101:329–358. 100, 101, 127

Lam, Y. F., Fu, J. S., Wu, S. et Mickley, L. J. (2011). Impacts of future climate change and effects of biogenic emissions on surface ozone and particulate matter concentrations in the United States. *Atmos. Chem. Phys.*, 11(10):4789–4806. 12

Lee, S.-H., Kim, S.-W., Angevine, W., Bianco, L., McKeen, S., Senff, C., Trainer, M., Tucker, S. et Zamora, R. (2010). Evaluation of urban surface parameterizations in the WRF model using measurements during the Texas Air Quality Study 2006 field campaign. *Atmos. Chem. Phys.*, 11:2127–2143. 125

Lim, H.-J., Carlton, A. G. et Turpin, B. J. (2005). Isoprene forms secondary organic aerosol through cloud processing : Model simulations. *Environ. Sci. Technol.*, 39(12):4441–4446. 94

Lin, C.-Y., Chen, F., Huang, J., Chen, W.-C., Liou, Y.-A., Chen, W.-N. et Liu, S.-C. (2008). Urban heat island effect and its impact on boundary layer development and land-sea circulation over northern Taiwan. *Atmos. Environ.*, 42(22):5635–5649. 98

Louis, J.-F. (1979). A parametric model of vertical eddy fluxes in the atmosphere. *Bound.-Lay. Meteorol.*, 17(2):187–202. 30, 127

Luecken, D. J. (2008). Comparison of atmospheric chemical mechanisms for regulatory and research applications. *In Simulation and Assessment of Chemical Processes in a Multiphase Environment*, pages 95–106. Springer, The Netherlands. 27, 57, 83

Luecken, D. J., Phillips, S., Sarwar, G. et Jang, C. (2008). Effects of using the CB05 vs. SAPRC99 vs. CB4 chemical mechanism on model predictions : Ozone and gas-phase photochemical precursor concentrations. *Atmos. Environ.*, 42(23):5805–5820. 27, 29, 32, 36, 44

Makar, P., Gravel, S., Chirkov, V., Strawbridge, K., Froude, F., Arnold, J. et Brook, J. (2006). Heat flux, urban properties, and regional weather. *Atmos. Environ.*, 40(15):2750–2766. 101

Mallet, V., Quélo, D., Sportisse, B., Ahmed de Biasi, M., Debry, É., Korsakissok, I., Wu, L., Roustan, Y., Sartelet, K., Tombette, M. et Foudhil, H. (2007). Technical Note : The air quality modeling system Polyphemus. *Atmos. Chem. Phys.*, 7(20):5479–5487. 12, 30, 57, 83, 126

Mallet, V. et Sportisse, B. (2006). Uncertainty in a chemistry-transport model due to physical parameterizations and numerical approximations : An ensemble approach applied to ozone modeling. *J. Geophys. Res.*, 111:D01302. 21, 125

Martien, P. T., Harley, R. A., Milford, J. B. et Russell, A. G. (2003). Evaluation of incremental reactivity and its uncertainty in southern California. *Environ. Sci. Technol.*, 37(8):1598–1608. 33

Martilli, A., Clappier, A. et Rotach, M. W. (2002). An urban surface exchange parameterisation for mesoscale models. *Bound.-Lay. Meteorol.*, 104:261–304. 100

Mellor, G. L. et Yamada, T. (1974). A hierarchy of turbulence closure models for planetary boundary layers. *J. Atmos. Sci.*, 31:1791–1806. 100

Menut, L., Flamant, C., Pelon, J. et Flamant, P. H. (1999). Urban boundary-layer height determination from lidar measurements over the Paris area. *Appl. Opt.*, 38(6):945–954. 125

Menut, L., Vautard, R., Beekmann, M. et Honoré, C. (2000). Sensitivity of photochemical pollution using the adjoint of a simplified chemistry-transport model. *J. Geophys. Res.*, 105(D12):15379–15402. 36

Miao, S., Chen, F., Lemone, M. A., Tewari, M., Li, Q. et Wang, Y. (2009). An observational and modeling study of characteristics of urban heat island and boundary layer structures in Beijing. *J. Appl. Meteorol. Climatol.*, 48:484–501. 115

Mlawer, E. J., Taubman, S. J., Brown, P. D., Iacono, M. J. et Clough, S. A. (1997). Radiative transfer for inhomogeneous atmospheres : RRTM, a validated correlated-k model for the longwave. *J. Geophys. Res.*, 102(D14):16663–16682. 99

Mollner, A. K., Valluvadasan, S., Feng, L., Sprague, M. K., Okumura, M., Milligan, D. B., Bloss, W. J., Sander, S. P., Martien, P. T., Harley, R. A., McCoy, A. B. et Carter, W. P. L. (2010). Rate of gas phase association of hydroxyl radical and nitrogen dioxide. *Science*, 330(6004):646–649. 147

Monahan, E. C., Spiel, D. E. et Davidson, K. L. (1986). A model of marine aerosol generation via whitecaps and wave disruption. *In Oceanic Whitecaps and their role in air-sea exchange processes*, pages 167–174. D. Reidel, Netherlands. 64, 127

Morris, R., Yarwood, G., Emery, C., Koo, B. et Wilson, G. M. (2003). Development of the CAMx one-atmosphere air quality model to treat ozone, particulate matter, visibility and air toxics and application for State Implementation Plans (SIPs). AWMA specialty conference, Guideline on air quality models : The path forward, available at `http://www.camx.com/publ/pdfs/AWMA_AQGuidelines03_Paper9_CAMx.pdf`. 12

Morris, R. E., Koo, B., Guenther, A., Yarwood, G., McNally, D., Tesche, T., Tonnesen, G., Boylan, J. et Brewer, P. (2006). Model sensitivity evaluation for organic carbon using two multi-pollutant air quality models that simulate regional haze in the southeastern United States. *Atmos. Environ.*, 40(26):4960–4972. 83

Ménard, S. (2007). Development of a new Canadian operational air quality forecast model GEM-MACH. National air quality conferences : air quality forecasting, mapping, and monitoring and communicating air quality and communities in motion, Orlando, available at : http://www.epa.gov/airnow/2007conference/wednesday/menard_s.ppt. 12

Nakanishi, M. et Niino, H. (2004). An improved Mellor Yamada Level-3 model with condensation physics : its design and verification. *Bound.-Lay. Meteorol.*, 112:1–31. 100

Nakanishi, M. et Niino, H. (2009). Development of an improved turbulence closure model for the atmospheric boundary layer. *J. Meteorol. Soc. Jpn*, 87(5):895–912. 98, 111

Nenes, A., Pandis, S. N. et Pilinis, C. (1998). ISORROPIA : A new thermodynamic equilibrium model for multiphase multicomponent inorganic aerosols. *Aquat. Geochem.*, 4(1):123–152. 58

Nenes, A., Pandis, S. N. et Pilinis, C. (1999). Continued development and testing of a new thermodynamic aerosol module for urban and regional air quality models. *Atmos. Environ.*, 33(10):1553–1560. 83

Ng, N. L., Chhabra, P. S., Chan, A. W. H., Surratt, J. D., Kroll, J. H., Kwan, A. J., McCabe, D. C., Wennberg, P. O., Sorooshian, A., Murphy, S. M., Dalleska, N. F., Flagan, R. C. et Seinfeld, J. H. (2007a). Effect of NO_x level on secondary organic aerosol (SOA) formation from the photooxidation of terpenes. *Atmos. Chem. Phys.*, 7(19):5159–5174. 88, 91

Ng, N. L., Kroll, J. H., Chan, A. W. H., Chhabra, P. S., Flagan, R. C. et Seinfeld, J. H. (2007b). Secondary organic aerosol formation from m-xylene, toluene, and benzene. *Atmos. Chem. Phys.*, 7:3909–3922. 59, 88

Odum, J. R., Hoffmann, T., Bowman, F., Collins, D., Flagan, R. C. et Seinfeld, J. H. (1996). Gas/particle partitioning and secondary organic aerosol yields. *Environ. Sci. Technol.*, 30(8): 2580–2585. 18, 83

Oke, T. R. (1987). *Boundary layer climates, 2nd edition*. Routledge, London. 98

Olson, J. B. et Brown, J. M. (2009). A comparison of two mellor-yamada-based pbl schemes in simulating a hybrid barrier jet. 23rd conference on weather analysis and forecasting/19th conference on numerical weather prediction, Omaha, available at http://ams.confex.com/ams/pdfpapers/154321.pdf. 98, 100

Pan, Y., Zhang, Y. et Sarwar, G. (2008). Impact of gas-phase chemistry on WRF/CHEM predictions of O_3 and $PM_{2.5}$: Mechanism implementation and comparative evaluation. 7th annual CMAS conference, Chapel Hill, available at : http://www.cmascenter.org/conference/2008/abstracts/pan_impact_gas-phase_cmas08.pdf. 27, 57

Pankow, J. F. (1994a). An absorption model of gas/particle partitioning of organic compounds in the atmosphere. *Atmos. Environ.*, 28(2):185–188. 77

Pankow, J. F. (1994b). An absorption model of the gas/aerosol partitioning involved in the formation of secondary organic aerosol. *Atmos. Environ.*, 28(2):189–193. 77

Park, R. J., Jacob, D. J., Field, B. D., Yantosca, R. M. et Chin, M. (2004). Natural and transboundary pollution influences on sulfate-nitrate-ammonium aerosols in the United States : Implications for policy. *J. Geophys. Res.*, 109, D15204. 75

Passant, N. (2002). Speciation of UK emissions of non-methane volatile organic compounds. AEA Technology, AEAT/ENV/0545, available at : `http://uk-air.defra.gov.uk/reports/empire/AEAT_ENV_0545_final_v2.pdf`. 30, 64

Pigeon, G., Legain, D., Durand, P. et Masson, V. (2007). Anthropogenic heat release in an old European agglomeration (Toulouse, France). *Int. J. Climatol.*, 27:1969–1981. 98, 101

Pilinis, C., Capaldo, K. P., Nenes, A. et Pandis, S. N. (2000). MADM-A new Multicomponent Aerosol Dynamics Model. *Aerosol Sci. Technol.*, 32(5):482–502. 17

Pineda, N., Jorba, O., Jorge, J. et Baldasano, J. M. (2004). Using NOAA AVHRR and SPOT VGT data to estimate surface parameters : application to a mesoscale meteorological model. *Int. J. Remote Sens.*, 25(1):129–143. 101

Pleim, J. E. (2007). A combined local and nonlocal closure model for the atmospheric boundary layer. Part I : Model description and testing. *J. Appl. Meteorol. Climatol.*, 46(9):1383–1395. 98, 100

Pleim, J. E. (2011). Comment on "Simulation of surface ozone pollution in the Central Gulf Coast region using WRF/Chem model : sensitivity to PBL and land surface physics. *Adv. Meteorol.*, 2011, article ID 464753, 3 pages. 127, 137

Pleim, J. E. et Chang, J. S. (1992). A non-local closure model for vertical mixing in the convective boundary layer. *Atmos. Environ.*, 26A:965–981. 98, 100

Poulet, D., Caro, D., Buisson, E., Leroy, D., Donnat, L., Duclaux, O. et Puel, C. (2008). Local-scale weather forecasts for pollution peak prediction system. 8th EMS annual meeting & 7th European conference on applied climatology, Amsterdam, available at : `http://www.emetsoc.org/annual_meetings/documents/sessionA11-1_Poulet-et-al.pdf`. 11

Pun, B. K. (2008). Development and initial application of the sesquiversion of MADRID. *J. Geophys. Res.*, 113:D12212. 91, 92, 94

Pun, B. K., Griffin, R. J., Seigneur, C. et Seinfeld, J. H. (2002). Secondary organic aerosol 2. thermodynamic model for gas/particle partitioning of molecular constituents. *J. Geophys. Res.*, 107(D17):4333. 58

Pun, B. K. et Seigneur, C. (2007). Investigative modeling of new pathways for secondary organic aerosol formation. *Atmos. Chem. Phys.*, 7:2199–2216. 58, 59, 61, 92

Pun, B. K. et Seigneur, C. (2008). Organic aerosol spatial/temporal patterns : Perspectives of measurements and model. *Environ. Sci. Technol.*, 42(19):7287–7293. 88

Pun, B. K., Seigneur, C., Grosjean, D. et Saxena, P. (2000). Gas-phase formation of water-soluble organic compounds in the atmosphere : A retrosynthetic analysis. *J. Atmos. Chem.*, 35:199–223. 94

Pun, B. K., Seigneur, C. et Lohman, K. (2006). Modeling secondary organic aerosol formation via multiphase partitioning with molecular data. *Environ. Sci. Technol.*, 40(15):4722–4731. 58, 83, 87, 91

Pun, B. K., Wu, S.-Y., Seigneur, C., Seinfeld, J. H., Griffin, R. J. et Pandis, S. N. (2003). Uncertainties in modeling secondary organic aerosols : Three-dimensional modeling studies in Nashville/Western Tennessee. *Environ. Sci. Technol.*, 37(16):3647–3661. 83, 86

Putaud, J.-P., Van Dingenen, R., Alastuey, A., Bauer, H., Birmili, W., Cyrys, J., Flentje, H., Fuzzi, S., Gehrig, R., Hansson, H., Harrison, R., Herrmann, H., Hitzenberger, R., Hüglin, C., Jones, A., Kasper-Giebl, A., Kiss, G., Kousa, A., Kuhlbusch, T., Löschau, G., Maenhaut, W., Molnar, A., Moreno, T., Pekkanen, J., Perrino, C., Pitz, M., Puxbaum, H., Querol, X., Rodriguez, S., Salma, I., Schwarz, J., Smolik, J., Schneider, J., Spindler, G., ten Brink, H., Tursic, J., Viana, M., Wiedensohler, A. et Raes, F. (2010). A European aerosol phenomenology - 3 : Physical and chemical characteristics of particulate matter from 60 rural, urban, and kerbside sites across Europe. *Atmos. Environ.*, 44(10):1308–1320. 57

Putaud, J.-P., Van Dingenen, R., Mangoni, M., Virkkula, A., Raes, F., Maring, H., Prospero, J. M., Swietlicki, E., Berg, O. H., Hillamo, R. et Mäkelä, T. (2000). Chemical mass closure and assessment of the origin of the submicron aerosol in the marine boundary layer and the free troposphere at Tenerife during ACE-2. *Tellus B*, 52(2):141–168. 67

Raut, J.-C. (2008). *Synergie expérimentale impliquant la mesure lidar pour la caractérisation optique et microphysique de l'aérosol : applications à la qualité de l'air et au transfert radiatif*. Thèse de doctorat, Université Paris VI. available at `http://tel.archives-ouvertes.fr/tel-00323901/en/`. 103

Raut, J.-C. et Chazette, P. (2009). Assessment of vertically-resolved PM_{10} from mobile lidar observations. *Atmos. Chem. Phys.*, 9(21):8617–8638. 103, 125, 135, 141

Real, E. et Sartelet, K. (2011). Modeling of photolysis rates over Europe : impact on chemical gaseous species and aerosols. *Atmos. Chem. Phys.*, 11:1711–1727. 142

Rotach, M. W. (1995). Profiles of turbulence statistics in and above an urban street canyon. *Atmos. Environ.*, 29(13):1473–1486. 98

Roustan, Y., Pausader, M. et Seigneur, C. (2010a). Estimating the effect of on-road vehicle emission controls on future air quality in Paris, France. *Atmospheric Environment*, 45(37): 6828–6836. 12

Roustan, Y., Sartelet, K., Tombette, M., Debry, É. et Sportisse, B. (2010b). Simulation of aerosols and gas-phase species over Europe with the Polyphemus system. Part II : Model sensitivity analysis for 2001. *Atmos. Environ.*, 44(34):4219–4229. 21, 98, 125

Royer, P., Chazette, P., Sartelet, K., Zhang, Q. J., Beekmann, M. et Raut, J.-C. (2011). Lidar-derived PM_{10} and comparison with regional modeling in the frame of the MEGAPOLI Paris summer campaign. *Atmos. Chem. Phys. Discuss.*, 11:11861–11909. 125, 126

Russell, A. et Dennis, R. (2000). NARSTO critical review of photochemical models and modeling. *Atmos. Environ.*, 34:2283–2324. 30, 84, 128

Russell, A. G. (2008). EPA Supersites program-related emissions-based particulate matter modeling : initial applications and advances. *J. Air Waste Manage. Assoc.*, 58:289–302. 67, 86

Sailor, D. et Lu, L. (2004). A top-down methodology for developing diurnal and seasonal anthropogenic heating profiles for urban areas. *Atmos. Environ.*, 38(17):2737–2748. 98

Salamanca, F., Krpo, A., Martilli, A. et Clappier, A. (2010). A new building energy model coupled with an urban canopy parameterization for urban climate simulations—part I. formulation, verification, and sensitivity analysis of the model. *Theor. Appl. Climatol.*, 99:331–344. 100

Sander, S. P., Friedl, R. R., Golden, D. M., Kurylo, M. J., Huie, R. E., Orkin, V. L., Moortgat, G. K., Ravishankara, A. R., Kolb, C. E., Molina, M. J. et Finlayson-Pitts, B. J. (2003). Chemical kinetics and photochemical data for use in atmospheric studies, evaluation number 14. NASA Jet Propulsion Laboratory, available at : `http://jpldataeval.jpl.nasa.gov/previous_evaluations.html`. 28

Sander, S. P., Friedl, R. R., Golden, D. M., Kurylo, M. J., Moortgat, G. K., Keller-Rudek, H., Wine, P. H., Ravishankara, A. R., Kolb, C. E., Molina, M. J., Finlayson-Pitts, B. J., Huie, R. E. et Orkin, V. L. (2006). Chemical kinetics and photochemical data for use in atmospheric studies, evaluation number 15. NASA Jet Propulsion Laboratory, available at : `http://jpldataeval.jpl.nasa.gov/download.html`. 28

Sarkar, A. et De Ridder, K. (2011). The urban heat island intensity of Paris : a case study based on a simple urban surface parametrization. *Bound.-Lay. Meteorol.*, 138:511–520. 98, 101

Sarrat, C., Lemonsu, A., Masson, V. et Guedalia, D. (2006). Impact of urban heat island on regional atmospheric pollution. *Atmos. Environ.*, 40(10):1743–1758. 98

Sartelet, K. N., Debry, É., Fahey, K., Roustan, Y., Tombette, M. et Sportisse, B. (2007). Simulation of aerosols and gas-phase species over Europe with the Polyphemus system : Part I–Model-to-data comparison for 2001. *Atmos. Environ.*, 41(29):6116–6131. 30, 32, 57, 63, 70, 75, 83, 84, 126

Sarwar, G., Luecken, D., Yarwood, G., Whitten, G. Z. et Carter, W. P. L. (2008). Impact of an updated carbon bond mechanism on predictions from the CMAQ modeling system : Preliminary assessment. *J. Appl. Meteor. Climatol.*, 47:3–14. 27, 57, 83

Saxena, P., Hudischewskyj, A. B., Seigneur, C. et Seinfeld, J. H. (1986). A comparative study of equilibrium approaches to the chemical characterization of secondary aerosols. *Atmos. Environ.*, 20(7):1471–1483. 18

Schell, B., Ackermann, I. J., Hass, H., Binkowski, F. S. et Ebel, A. (2001). Modeling the formation of secondary organic aerosol within a comprehensive air quality model system. *J. Geophys. Res.*, 106:28275–28293. 83, 84, 87

Seinfeld, J. et Pandis, S. (1998). *Atmospheric Chemistry and Physics : From Air Pollution to Climate Change*. Wiley-Interscience, New York. 27, 57, 64

Seinfeld, J. et Pandis, S. (2006). *Atmospheric Chemistry and Physics : From Air Pollution to Climate Change*. Wiley-Interscience, Hoboken, 2nd edition. 16, 17, 18

Sillman, S. (1999). The relation between ozone, NO_x and hydrocarbons in urban and polluted rural environments. *Atmos. Environ.*, 33:1821–1845. 34, 44, 46

Sillman, S. et He, D. (2002). Some theoretical results concerning O_3-NO_x-VOC chemistry and NO_x-VOC indicators. *J. Geophys. Res.*, 107(D22):4659. 36

Sillman, S., Vautard, R., Menut, L. et Kley, D. (2003). O_3-NO_x-VOC sensitivity and NO_x-VOC indicators in Paris : Results from models and atmospheric pollution over the Paris area (ESQUIF) measurements. *J. Geophys. Res.*, 108(D17). 36

Simpson, D., Winiwarter, W., Börjesson, G., Cinderby, S., Ferreiro, A., Guenther, A., Hewitt, C. N., Janson, R., Aslam, M., Khalil, K., Owen, S., Pierce, T. E., Puxbaum, H., Shearer, M., Skiba, U., Steinbrecher, R., Tarrasón, L. et Öquist, M. G. (1999). Inventorying emissions from nature in Europe. *J. Geophys. Res.*, 104((D7)):8113–8152. 20, 30, 37, 64, 127

Simpson, D., Yttri, K. E., Klimont, Z., Kupiainen, K., Caseiro, A., Gelencsér, A., Pio, C., Puxbaum, H. et Legrand, M. (2007). Modeling carbonaceous aerosol over Europe : Analysis of the CARBOSOL and EMEP EC/OC campaigns. *J. Geophys. Res.*, 112:D23S14. 84

Skamarock, W. C., Klemp, J. B., Dudhia, J., Gill, D. O., Barker, D. M., Duda, M. G., Huang, X.-Y., Wang, W. et Powers, J. G. (2008). A description of the Advanced Research WRF version 3. NCAR Technical note-475+STR available at : `http://www.mmm.ucar.edu/wrf/users/docs/arw_v3.pdf`. 98

Sportisse, B. (2007). A review of parameterizations for modelling dry deposition and scavenging of radionuclides. *Atmos. Environ.*, 41(13):2683–2698. 16

Sportisse, B. (2008). *Pollution atmosphérique : des processus à la modélisation*. Springer-Verlag France, Paris. 12, 13, 36

Srinivas, C., Venkatesan, R. et Singh, A. B. (2007). Sensitivity of mesoscale simulations of land-sea breeze to boundary layer turbulence parameterization. *Atmos. Environ.*, 41(12): 2534–2548. 98

Stockwell, W. R. (2009). Peer review of the SAPRC-07 chemical mechanism of Dr. William Carter. California Air Resources Board available at : `http://www.arb.ca.gov/research/reactivity/3-25-2009/stockwell-present.pdf`. 28

Stockwell, W. R., Kirchner, F., Kuhn, M. et Seefeld, S. (1997). A new mechanism for regional atmospheric chemistry modeling. *J. Geophys. Res.*, 102(D22):25847–25879. 28, 57, 59

Stull, R., Santoso, E., Berg, L. et Hacker, J. (1997). Boundary Layer Experiment 1996 (BLX96). *Bull. Am. Meteorol. Soc.*, 78(6):1149–1158. 98

Stull, R. B. (1988). *An introduction to boundary layer meteorology*. Kluwer Academic Publishers, Dordrecht. 14, 22, 98, 100

Tang, W., Cohan, D. S., Morris, G. A., Byun, D. W. et Luke, W. T. (2011). Influence of vertical mixing uncertainties on ozone simulation in CMAQ. *Atmos. Environ.*, 45:2898–2909. 21, 125

Troen, I. B. et Mahrt, L. (1986). A simple model of the atmospheric boundary layer ; sensitivity to surface evaporation. *Bound.-Lay. Meteorol.*, 37(1):129–148. 30, 127, 137

Tulet, P., Crassier, V. et Rosset, R. (2000). Air pollution modelling at a regional scale. *Environ. Modell. Softw.*, 15:693–701. 36

Ulden, A. P. et Wieringa, J. (1996). Atmospheric boundary layer research at Cabauw. *Bound.-Lay. Meteorol.*, 78:39–69. 98

van Loon, M., Vautard, R., Schaap, M., Bergström, R., Bessagnet, B., Brandt, J., Builtjes, P. J. H., Christensen, J. H., Cuvelier, C., Graff, A., Jonson, J. E., Krol, M., Langner, J., Roberts, P., Rouil, L., Stern, R., Tarrasón, L., Thunis, P., Vignati, E., White, L. et Wind, P. (2007). Evaluation of long-term ozone simulations from seven regional air quality models and their ensemble. *Atmos. Environ.*, 41(10):2083–2097. 32

Wesely, M. (1989). Parameterization of surface resistances to gaseous dry deposition in regional-scale numerical models. *Atmos. Environ.*, 23(6):1293–1304. 16

Whitten, G. Z., Heo, G., Kimura, Y., McDonald-Buller, E., Allen, D. T., Carter, W. P. et Yarwood, G. (2010). A new condensed toluene mechanism for Carbon Bond : CB05-TU. *Atmos. Environ.*, 44(40):5346–5355. 78, 147

Wild, O., Zhu, X. et Prather, M. J. (2000). Fast-J : Accurate simulation of in- and below-cloud photolysis in tropospheric chemical models. *J. Atmos. Chem.*, 37(3):245–282. 30

Yarwood, G., Rao, S., Yocke, M. et Whitten, G. (2005). Updates to the carbon bond chemical mechanism : CB05 final report to the US EPA, RT-0400675. available at `http://www.camx.com/publ/pdfs/CB05_Final_Report_120805.pdf`. 28, 29, 30, 57, 59, 126

Zhang, L., Moran, M. D., Makar, P. A., Brook, J. R. et Gong, S. (2002). Modelling gaseous dry deposition in AURAMS : a unified regional air-quality modelling system. *Atmos. Environ.*, 36(3):537–560. 30

Zhang, Y., Huang, J.-P., Henze, D. K. et Seinfeld, J. H. (2007). Role of isoprene in secondary organic aerosol formation on a regional scale. *J. Geophys. Res.*, 112, D20207. 58, 87, 88, 91

Zhang, Y., Liu, P., Liu, X.-H., Jacobson, M. Z., McMurry, P. H., Yu, F., Yu, S. et Schere, K. L. (2010a). A comparative study of nucleation parameterizations : 2. three-dimensional model application and evaluation. *J. Geophys. Res.*, 115:D20213. 17

Zhang, Y., Liu, P., Queen, A., Misenis, C., Pun, B., Seigneur, C. et Wu, S.-Y. (2006). A comprehensive performance evaluation of MM5-CMAQ for the Summer 1999 Southern Oxidants Study episode–Part II : Gas and aerosol predictions. *Atmos. Environ.*, 40(26):4839–4855. 67

Zhang, Y., McMurry, P. H., Yu, F. et Jacobson, M. Z. (2010b). A comparative study of nucleation parameterizations : 1. examination and evaluation of the formulations. *J. Geophys. Res.*, 115:D20212. 17

Zhang, Y., Pan, Y., Wang, K., Fast, J. D. et Grell, G. A. (2010c). WRF/Chem-MADRID : Incorporation of an aerosol module into WRF/Chem and its initial application to the TexAQS2000 episode. *J. Geophys. Res.*, 115:D18202. 83, 84

Zhang, Y., Pun, B., Vijayaraghavan, K., Wu, S.-Y., Seigneur, C., Pandis, S. N., Jacobson, M. Z., Nenes, A. et Seinfeld, J. H. (2004). Development and application of the Model of Aerosol Dynamics, Reaction, Ionization, and Dissolution (MADRID). *J. Geophys. Res.*, 109:D01202. 84

Zhang, Y., Vijayaraghavan, K. et Seigneur, C. (2005). Evaluation of three probing techniques in a three-dimensional air quality model. *J. Geophys. Res.*, 110, D02305. 36

Résumé

L'influence des paramétrisations chimiques et météorologiques sur les concentrations de polluants calculées avec un modèle de qualité de l'air est étudiée. L'influence des différences entre deux mécanismes chimiques de la phase gazeuse sur la formation d'ozone et d'aérosols en Europe est faible en moyenne. Pour l'ozone, les fortes différences observées localement proviennent principalement de l'incertitude associée à la cinétique des réactions d'oxydation du monoxyde d'azote (NO) d'une part et de la représentation des différents chemins d'oxydation des composés aromatiques d'autre part. Les concentrations d'aérosols sont surtout influencées par la prise en compte des précurseurs majeurs d'aérosols secondaires et le traitement explicite des régimes chimiques correspondant au niveau d'oxydes d'azote (NO_x). L'influence des paramétrisations météorologiques sur les concentrations d'aérosols et leur répartition verticale est évaluée sur l'Île de France par comparaison à des données lidar. L'influence de la paramétrisation de la dynamique de la couche limite atmosphérique est importante ; cependant, c'est l'utilisation d'un modèle de canopée urbaine qui permet d'améliorer considérablement la modélisation de la répartition verticale des polluants.

Abstract

The influence of chemical mechanisms and meteorological parameterizations on pollutant concentrations calculated with an air quality model is studied. The influence of the differences between two gas-phase chemical mechanisms on the formation of ozone and aerosols in Europe is low on average. For ozone, the large local differences are mainly due to the uncertainty associated with the kinetics of nitrogen monoxide (NO) oxidation reactions on the one hand and the representation of different pathways for the oxidation of aromatic compounds on the other hand. The aerosol concentrations are mainly influenced by the selection of all major precursors of secondary aerosols and the explicit treatment of chemical regimes corresponding to the nitrogen oxides (NO_x) levels. The influence of the meteorological parameterizations on the concentrations of aerosols and their vertical distribution is evaluated over the Paris region in France by comparisons to lidar data. The influence of the parameterization of the dynamics in the atmospheric boundary layer is important ; however, it is the use of an urban canopy model that improves significantly the modeling of the pollutant vertical distribution.